THE UNIVERSITY OF HULL

Signatures of i-process Nucleosynthesis

being a Thesis submitted for the Degree of Master of Science (by Research) Physics

in the University of Hull

by

Kate Alice Womack, B.Sc.

September 2021

Acknowledgements

I would like to express my sincere gratitude to Dr. Richard Stancliffe, without whom I would not have made it to this point, for all the valuable help and support he has given me. I would like to thank my second supervisor Dr. Marco Pignatari for his guidance and my head of department Prof. Brad Gibson for being a supporter of me and my work throughout my time at university.

A special thank you to Dr James Keegans for his insights in assisting with the methodology of Chapter 3 of this thesis. Thanks to all my friends and colleagues at the E.A.Milne centre for all their encouragement, including Leah Cox, Kiri Newson, Emily Shelton and Oliver Bartlett for being a listening ear whenever I needed it. Thanks to Dr Yjan Gordon for this excellent LaTeX thesis template and to Thomas Lawson for all the python help over the years.

I would also like to thank the friends in my life who have been there for me and have seen the journey to this point from the very beginning: Emily Neal and Kate Berry. Also, thanks to Claire Buffey and Demi Wright who were always in my corner throughout my academic journey and loaded me with tea whenever I needed it.

I am privileged to be able to acknowledge my family Stephen, Julie and Ella Womack who have been incredibly supportive throughout this process and have given me laughs and joy when I needed it most. Finally, I am grateful to my partner Jack Tinegate for allowing me to talk at him about this thesis at great length and always reassuring me that I would eventually get to this point.

Declaration of Originality

This thesis is submitted in partial fulfilment of the degree of M.Sc. (by Research) Physics (Research) from the University of Hull. I declare that the work undertaken in this thesis is original and my own and was carried out under the supervision of Dr. Richard Stancliffe and Dr. Marco Pignatari. Where work, results, or ideas have been taken from other sources, those sources are explicitly referenced.

Kate Alice Womack

Date: 2nd September 2021

Abstract

Neutron capture nucleosynthesis is responsible for the production of heavy elements. Three neutron capture processes are currently known, each occurring at their own characteristic neutron density and operating in different ways. The slow neutron capture process operates at neutron densities of $n \approx 10^7 - 10^{10}\,\mathrm{cm}^{-3}$, the rapid at neutron densities of $n \gtrsim 10^{20}\,\mathrm{cm}^{-3}$ and the intermediate at neutron densities of $n = 10^{12}$ - $10^{15}\,\mathrm{cm}^{-3}$. The intermediate neutron capture process (i process) is the focus of this work.

The i process is now widely accepted to be the process that produces the unusual abundances of carbon-enhanced metal-poor (CEMP) -r/s stars. A challenge in recent years has been constraining a site for the i process. Given the large range in potential neutron densities, many astrophysical sites have the potential to host i-process conditions. Two of the most promising sites for the i process are: the intershell regions of low-mass, low-metallicity asymptotic giant branch stars and on rapidly accreting white dwarfs. This work provides abundance analyses of models of the two different scenarios.

I first look at comparing both models to a sample of CEMP-r/s stars using χ^2 fitting. From this I was able to determine the abundance signatures that can make one model fit an i-process pattern more closely than another. I used this fitting technique to fit i-process models to other objects in the literature, including to phosphorus-rich stars. χ^2 fitting is also used to show that stellar models can be used to make predictions of the Th and U we would expect to see from the i process.

I move on to investigating elemental abundance ratios that may help us distinguish an s process from an i process by using three-element plots. From this, I came up with four abundance ratios that have the potential to be useful as an i-process signature.

Contents

List of Figures

List of Tables

1. Introduction

In the first few seconds after the Big Bang, the only elements made in abundance were hydrogen and helium. It was from this initial hydrogen-rich environment that the first stars were made (Coc & Vangioni, 2017).

To produce elements heavier than hydrogen and helium, stars undergo fusion which converts H and He into heavier and heavier elements up to iron. It is energetically unfavourable for iron fusion to occur because nuclear binding energy is at a maximum at the iron group. Therefore, energy would need adding to the system for fusion to occur, instead of fusion releasing energy. For larger nuclei (beyond iron), it is difficult for charged particles to make heavier elements because the Coulomb barrier is too large to overcome. So the question becomes: how are elements heavier than iron made without charged particle reactions? The answer is neutron captures, as a neutral particle neutrons do not experience Coulomb repulsion. Therefore, a nucleus can capture a neutron to make the next heaviest isotope of the same element without adding charge. The study of one particular neutron capture process, the intermediate neutron capture process, will be the focus of this work.

1.1 Neutron Captures: The s and r process

Burbidge et al. (1957) (hereafter B^2FH) proposed that there were two different neutron capture processes that could occur in stars: the slow (s) and the rapid (r) neutron capture process. At the time of B^2FH, knowledge of stellar physics was limited but we did know about nuclear physics such as: the structure of the atom and the formation of isotopes; the decay of nuclei through β decays and the production and annihilation of nucleons at high energies. Using their understanding of nuclear physics B^2FH were able to propose a number of processes, including the s and the r process, as a way to explain the features of the Solar abundance curve.

Figure 1.1 shows this curve of logarithmic relative abundance against atomic weight using

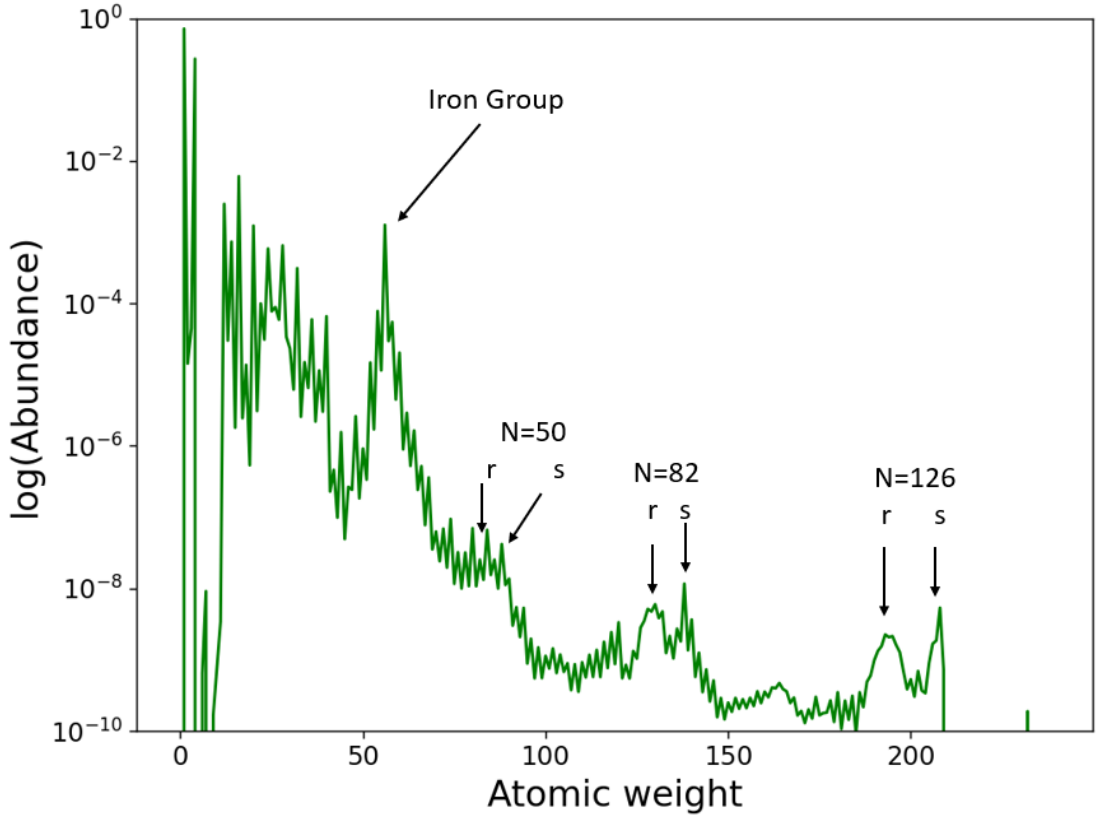

Figure 1.1: Logarithmic abundance against atomic weight for the Solar abundance pattern with the iron group and s- and r- process peaks marked on the line.

the Solar abundances of Asplund et al. (2009) in the style of figure I,1 of Burbidge et al. (1957). We can see a large spike in abundance around the iron group elements, which we expect because the end of the fusion stage occurs here. After the iron group, we see a series of double peaks at A = 80 and 90, A = 130-138 and A = 194-208. These are the s- and r-process peaks. The peaks represent nuclei with neutron numbers N = 50, 82 and 126 respectively, which are neutron magic numbers. Neutron magic nuclei have full neutron shells (this can be though of as analogous to electron shells) which means these nuclei are more stable than those without full neutron shells so it is difficult for further neutron captures onto these nuclei to take place. Having a full neutron shell means that neutron magic nuclei have low neutron capture cross sections. Neutron capture cross section is a measure of how easily a nucleus can capture a neutron so a low cross section indicates a low probability of neutron capture onto this nucleus. This means that these nuclei are often responsible for forming a bottleneck during neutron captures and hence we see these abundance peaks forming.

When a neutron is captured by a nucleus, the next heaviest isotope of that element is produced. If the next isotope is unstable it will either β-decay or capture another neutron. Which of these two processes will occur depends both on the neutron density of the system and on the half life of the isotope. However, if the next isotope is stable, it will eventually capture a neutron as stable isotopes do not decay.

B^{2}FH characterized the s and the r process by the timescale over which a neutron capture occurs compared to a β decay. The s process operates at low neutron densities of $n \approx 10^7 - 10^{10}\,\mathrm{cm}^{-3}$ (Busso, Gallino & Wasserburg, 1999) so it is more likely that an unstable nucleus will β decay than capture a neutron. Hence, neutrons are captured slowly relative to the rate of β decay. On the other hand, the r process operates at neutron densities of higher than $n \approx 10^{20}\,\mathrm{cm}^{-3}$ (e.g. Lugaro 2005). Therefore it is much more likely for a nucleus to capture neutrons than decay, hence it occurs rapidly.

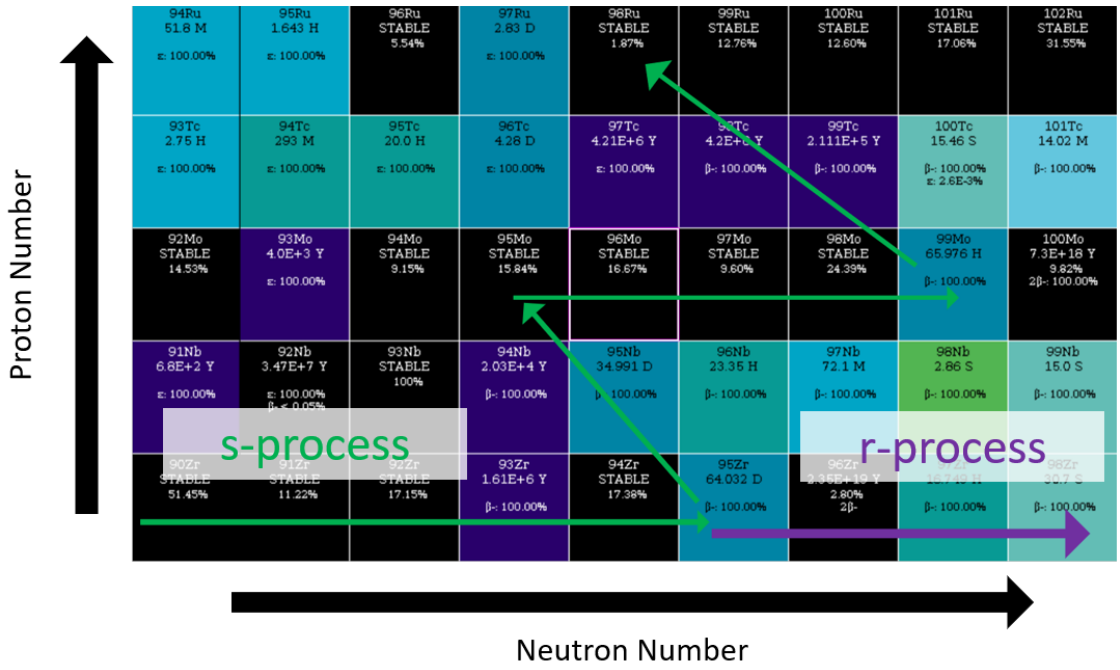

Figure 1.2: A section of the nuclide chart from The National Nuclear Data Center, Brookhaven National Laboratory (National Nuclear Data Centre, 2021). The green arrows represent the s-process path and the purple arrows show the r-process path.

To illustrate the paths of these processes, Figure 1.2 shows how the s and r process behave for the same section of the nuclide chart. A nuclide chart places isotopes as a function of

their neutron (x-axis) and proton number (y-axis). The s-process path shows stable nuclei capturing a neutron and moving right - along the neutron number axis. The unstable isotope ^{93}Zr has a long enough half-life for neutron captures to continue to ^{95}Zr when it β-decays back towards stability. When the r-process path reaches ^{95}Zr, neutrons continue to be captured towards neutron rich zirconium isotopes and eventually to the neutron drip line.

As Figure 1.2 shows, the two timescales for β decay versus neutron capture mean the s and r process have very different neutron capture paths. The decay of an unstable nucleus is more likely during the s process so the nuclei produced tend to stay closer to the region of the nuclide chart where most stable isotopes are located, the so-called 'valley of stability'. The r process can produce isotopes all the way up to the neutron drip-line as neutron capture is much more likely. The neutron drip line is the region at the edge of the nuclide chart and is populated by very neutron-rich isotopes. The drip line denotes the point at which another neutron is unable to bind to the nucleus due to a decrease in separation energy (the amount of energy needed to remove a nucleon from a nucleus) that occurs as a nucleus becomes more neutron-rich (Iliadis, 2015). The isotopes on the drip-line are so short-lived and have such low separation energy that neutron captures cannot take place, so no heavier elements can be made after this point. More information on how the r process proceeds can be found in section 1.1.2.

1.1.1 The s process

The isotopes and elements that neutron capture processes make not only depend on the neutron density of the region of the star in question but also on the neutron exposure. This is a measure of the time-integrated neutron density, in other words - how many neutrons are 'hitting' a given unit surface area over a period of time. The neutron exposure is given by

$$\tau = \int n v_{\mathrm{T}} dt, \tag{1.1}$$

where n is the neutron density and v_{T} is the thermal velocity of a neutron. Neutron exposure is measured in the inverse surface unit, mbarn^{-1}, where 1 mbarn = 10^{-31} m^2.

The concept of neutron exposure is important when considering the s process because a different component of the s process is activated depending on the neutron exposure.

There are three components to the s process: the weak, main and strong components. The weak component operates at neutron exposures of $\tau \approx 0.05$ mbarn^{-1} and mainly produces elements with atomic mass $A \leq 88$ (Käppeler, Beer & Wisshak, 1999). The main component operates at exposures of $\tau \approx 0.3$ mbarn^{-1} and produces elements with atomic masses between $88 \leq A \leq 204$. Finally, the strong s-process component operates at exposures of $\tau \approx 7$ mbarn^{-1} and produces the heavier elements with atomic masses $204 \leq A \leq 209$ (Busso, Gallino & Wasserburg 1999, Sneden, Cowan & Gallino 2008). These numbers correspond with the s-process peaks that we see in Figure 1.1. Knowledge of how these peaks are formed allows us to put together a picture of the isotopes and elements we should be looking for as evidence of the s process having taken place.

The two main s-process peaks we see correspond to the 'light' and 'heavy' s-process. The light s (ls) peak (first peak) is at N = 50 and elemental signatures of this process are Sr, Y, Zr, while the heavy s (hs) peak (second peak) is at N = 82 with elemental signatures Ba, La, Ce. Lead (Pb) is the last stable element of the s-process path at N = 126 and corresponds to the final s-process peak (Sneden et al. 2008, Karakas & Lattanzio 2014) along with bismuth (Bi) which has quasi-stable isotope ^{209}Bi. The stable isotopes of the s-process elements at their respective peaks are neutron magic, therefore they have low neutron capture cross sections and they become a bottleneck for the neutron captures (Cowan & Thielemann, 2004).

The most commonly used elemental signature for the s process is barium because stable ^{138}Ba falls at neutron magic number N = 82. Another signature of the s process which is unrelated to the neutron magic numbers is technetium (Tc). If Tc is present in the abundances of a star it means there is active s process occurring (Merrill, 1952). This is because the half life of ^{99}Tc is so long that we are able to observe Tc in stellar abundances before it has had a chance to β decay.

We cannot make anything beyond lead with the s process because lead is the last element with stable isotopes. Thorium (Th) and uranium (U) do have quasi-stable isotopes which can be made by the r process but they cannot be made by the s process because there are too many short-lived radioactive isotopes between Pb and Th. In this region of the nuclide chart α decays are occurring, this reaction makes it more challenging for the s-process path to get

from Pb up to Th.

Understanding the physical conditions required for the s process means we can narrow down where the s process might take place. The main proposed site for the s process are asymptotic giant branch (AGB) stars (Käppeler et al., 2011). Neutron densities of $n \approx 10^7 - 10^{10}\,\mathrm{cm}^{-3}$, as is required for the s process, are found mainly in the intershell region (the region between the hydrogen and heium burning shells see section 1.3) of thermally pulsing, low mass AGB stars and also in massive stars undergoing core helium burning (Iliadis, 2015).

1.1.2 The r process

Much like the s process, there are isotopes and elements that we can use as tracers that the r process has taken place. The main r-process signature we look for is europium (Eu). Europium is used as a signature for the r process because over 90% of the solar europium is made in the r process. Exactly how much solar europium is made in the r process varies between authors (e.g. Sneden, Cowan & Gallino 2008 estimate 98%, Bisterzo et al. 2011 estimate 94% and Travaglio et al. 2004 estimate 95%). It should be noted that unlike Ba and the s process, Eu is not an r-process peak element. Other elements that indicate an r process are osmium (Os) and platinum (Pt), these are r-process peak elements.

As stated above (section 1.1), the r process can produce neutron-rich isotopes all the way up to the neutron drip line. However, these isotopes are very short-lived. Therefore, once the neutron source has been turned off, the unstable nuclei will decay towards stable nuclei of the same atomic mass. A notable feature of the Solar abundance curve (Figure 1.1) is that the r-process peaks occur at mass numbers of approximately 10 less than the s-process peaks. This is due to the fact that, as the neutron rich isotopes decay, the r-process path will reach isotopes with closed neutron shells at smaller mass numbers than the s process. Most of these neutron magic isotopes are unstable, therefore, instead of causing a build-up of abundance at the neutron magic nuclei, the build-up will occur at the next stable isotope of the same mass number. Thus, the build-up in abundance occurs at lower mass numbers than that of the s process (Sneden, Cowan & Gallino, 2008).

To achieve neutron densities as high as is needed for the r process, very energetic events are

required. Some proposed sites of the r process include magneto-rotationally driven supernovae (Ono et al. 2012, Winteler et al. 2012, Nishimura et al. 2015, Nishimura et al. 2017) and neutron star mergers (NSM) (e.g. Lattimer & Schramm 1974, Iliadis 2015, Ishimaru et al. 2015, Ji et al. 2016, Thielemann et al. 2017, Kilpatrick et al. 2017, Côté et al. 2018b). Neutron star mergers became an even more promising candidate in 2017 when the first neutron star merger (NSM), GW170817 was detected using gravitational waves (Abbott et al., 2017a). It was found that the gamma ray burst detection GRB 170817A 1.7 s after the merger detection was similar to GW170817 in terms of its emission. The merging of two neutron stars results in a kilonova. Kilonova can emit gamma ray bursts and are powered by the decay of r-process nuclei. The gravitational wave and gamma ray burst detection were determined to be signatures of the same neutron star merger event, confirming NSMs as a site for the r-process (Abbott et al., 2017b).

1.2 The i process

The intermediate neutron capture process (i process) is another neutron capture process and was proposed by Cowan & Rose (1977). They modelled mixing H-rich material into the convective intershell region of a red giant star undergoing helium shell flashes (also known as thermal pulses). They calculated the neutron density for one of the models and found a neutron density of $n \approx 10^{15}$-10^{17} cm^{-3}. This is intermediate to the values required for the s and r processes proposed by B^{2}FH, hence it was named the intermediate or i process. Asplund et al. (1999) found the first observational evidence for the i process in the born-again, very late thermal pulse (VLTP) object, Sakurai's object, which was then confirmed with stellar models by Herwig et al. (2011).

The i process works in a similar fashion to the s process. When an unstable isotope is reached, what happens next depends upon the neutron density of the system and the half life of the isotope. However, a higher neutron density allows the neutron capture path to deviate further from stability than the s process, producing a larger swathe of elements rather than a single path up the nuclide chart, as is the case for the s process. Figure 1 of Hampel et al. (2016) demonstrates this concept and is included in this thesis as Figure 1.3. Figure 1.3 shows

the neutron capture paths of an s-process model at $n = 10^7\,\mathrm{cm}^{-3}$ and an i-process model at $n = 10^{15}\,\mathrm{cm}^{-3}$ for the same section of the nuclide chart. We can see that the neutron capture path for the i process is much broader and further from stability. This means bottlenecks at the magic numbers appear at lower atomic weights. For example, this leads to a build up of abundance at the neutron magic, unstable isotope ^{135}I (deep red isotope at N = 82 and Z = 53 in the i-process path of Figure 1.3) which will decay back to ^{135}Ba. Figure 1.4 illustrates this. Each of the panels is a section of the nuclide chart around I and Ba. The colour of each square indicates how abundant that particular isotope is, as shown by the colourbar. Figure 1.4a is representative of an i-process pattern at neutron densities of $n \approx 10^{14}\,\mathrm{cm}^{-3}$. Each subsequent panel is the abundance of the isotopes as they are allowed to decay over a timescale of approximately 10 Gyr. We can see that ^{135}I becomes much less abundant by Figure 1.4b which is 0.1 yrs after initial production, ^{135}Xe has also become less abundant as they have both β decayed to ^{135}Cs. The half life for ^{135}Cs to β decay is 2.3×10^6 yrs, therefore it continues to stay highly abundant through Figures 1.4c, 1.4d and 1.4e, while the abundance of ^{135}Ba starts to increase as the β decays occur. By Figure 1.4f we can see that ^{135}I, ^{135}Xe and ^{135}Cs have all decayed back to ^{135}Ba because it is the closest stable isotope along the β decay pathway. We can use a high abundance of ^{135}I in our models as a signature that the i process is occurring.

It should be noted that B^{2}FH did not propose the i process in 1957 because it was not needed to explain the Solar abundance curve - which was the goal of their research. So if it is not needed to explain the Solar abundance, one may ask the question: why do we need the i process at all? Research into the i process has become more active in the last couple of decades and has shown us that the i process can be used to explain anomalous abundance patterns. Some of these abundances are believed to have been produced in the site itself and others are simply signatures of the i process having occurred somewhere else.

Pre-solar grains have been suggested as a place where we see signatures that the i process has previously occurred (e.g. Fujiya et al. 2013, Jadhav et al. 2013, Liu et al. 2014). As the name would suggest, pre-solar grains are grains of material created before the sun so we cannot be entirely certain of their origins. It is thought that the grains which display i-process

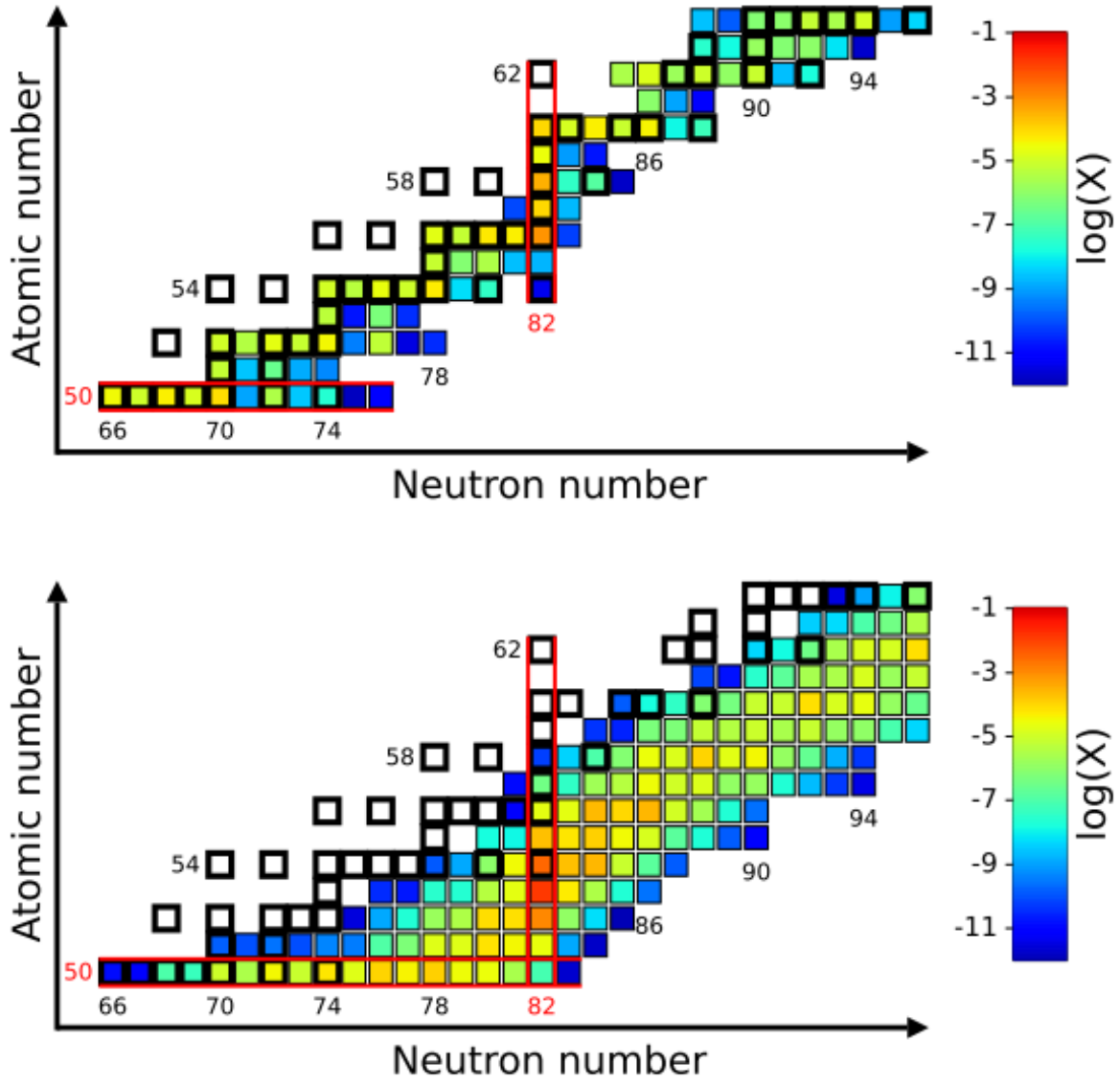

Figure 1.3: s- and i-process neutron capture paths for the same section of the nuclide chart (Figure 1 of Hampel et al. (2016)). Neutron and proton magic numbers are bordered in red, stable isotopes are bordered in black and the colour of each isotope represents how abundant it is.

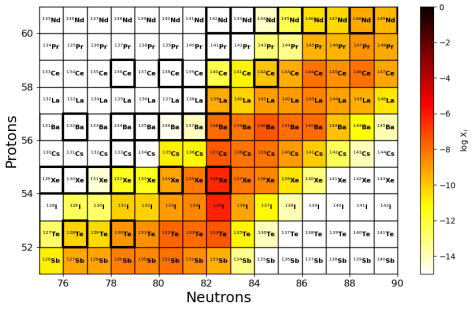

(a) t = 0 yrs after production

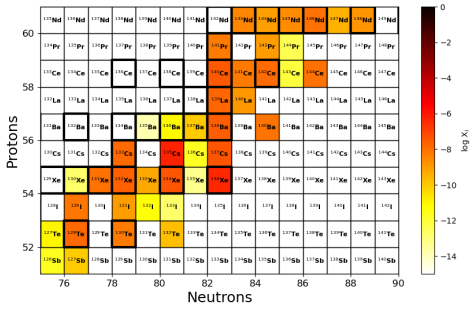

(b) t = 0.1 yrs after production

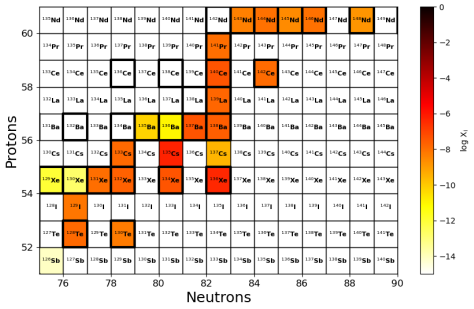

(c) t = 332 yrs after production

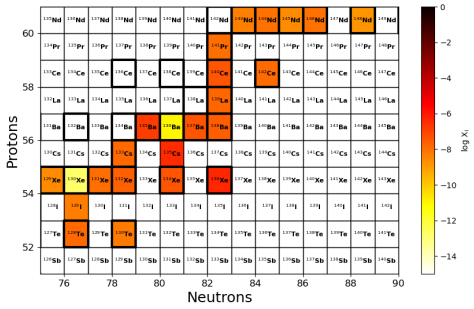

(d) t = 1.1×10^6 yrs after production

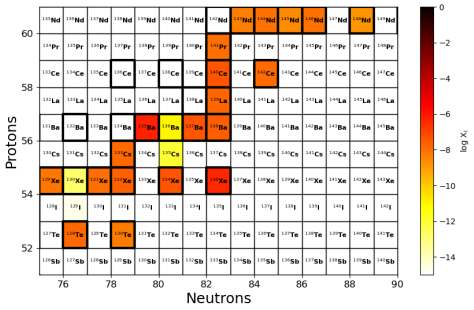

(e) t = 6.4×10^7 yrs after production

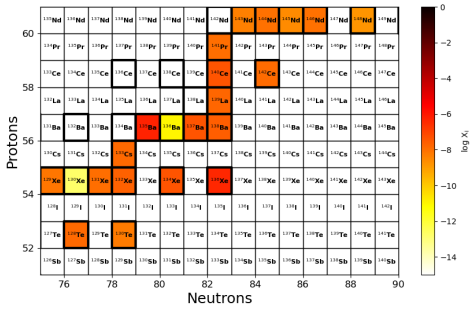

(f) t = 3.4×10^9 yrs, after production

Figure 1.4: Evolution of isotopes with atomic weight A = 135 as they decay shown on a series of nuclide charts from t = 0 years to t = 3.4×10^9 yrs after initial production. The abundance of each isotope is indicated by the colour of the box, the darker the colour the more abundant the isotope.

signatures have come from AGB and post-AGB stars. For example, Jadhav et al. (2013) compared grain data to models of VLTP events in post-AGB stars and found that the i process can explain the anomalous abundance ratios of carbon (C), calcium (Ca) and titanium (Ti) in high density graphite grains. This gives us evidence that the i process has occurred but unless we can extract extra information from the grains, such as an abundance ratio that could only have occurred at a specific temperature or metallicity, they are not necessarily useful for providing us with the information needed to narrow down a site for the i process.

Another group of objects that displays signatures of the i process are carbon-enhanced, metal-poor (CEMP) -r/s stars. A CEMP star is a very metal-poor star which typically has [Fe/H] < -2 and [C/Fe] > 1 (Beers & Christlieb, 2005)[1]. There are a few different classifications of CEMP stars, see section 1.6 for details. For a star to be a CEMP-r/s star it must show enrichment in both barium and europium which are the two main signatures of the s and r process respectively. This would imply that the s and r process are occurring in the same site, which is extremely unlikely given the neutron densities required for each process and the highly energetic conditions needed for the r-process to occur. Dardelet et al. (2015) and Hampel et al. (2016) demonstrated that i-process nucleosynthesis can be used to explain the abundance patterns of CEMP-r/s stars. However, it is not believed that the i process is occurring in these stars but that the material is being accreted from elsewhere (Abate, Stancliffe & Liu, 2016). More detail on the types of CEMP stars and how the i-process material is accreted by the CEMP-r/s stars is presented in section 1.6.

Naturally, for pre-solar grains and CEMP-r/s stars to display signatures of the i process, there must be astrophysical sites which are undergoing or have undergone the i process. To understand why these objects are sites for the i process, we must first understand how neutrons are produced.

[1]Abundances are typically represented in this square-bracket notation where:

$[\frac{A}{B}] = \log_{10}(\frac{X_A}{X_B})_* - \log_{10}(\frac{X_A}{X_B})_\odot$ where X is the abundance by mass fraction of the element in question.

1.3 Fundamentals of Neutron Production

For neutron captures to take place in a star it must first have a source of neutrons. The neutrons required for i-process nucleosynthesis to occur are believed to be produced in regions of high helium abundance by Proton Ingestion Episodes (PIEs) (e.g. Stancliffe et al. 2011). For proton ingestion to occur, the helium rich region must be convective as the convection is what pulls (ingests) protons from the above hydrogen-rich region into the region of high helium abundance. Fujimoto, Iben & Hollowell (1990) and Hollowell, Iben & Fujimoto (1990) first explored mixing events in low mass stars by modelling ingestion of hydrogen (protons) by convection into the carbon rich region of a population-III star during a core helium flash. Since then, the modelling of proton ingestion by convection has been extended far beyond population-III stars. The most commonly used example is ingestion of protons into the helium rich intershell region of a low-mass, low-metallicity AGB star, where it is believed the neutron density can get high enough for the i process to occur (e.g. Cristallo et al. 2009, Campbell et al. 2010, Stancliffe et al. 2011).

An AGB star has a CO core, a helium burning region, a convective helium rich intershell, a hydrogen burning shell and a hydrogen rich envelope, Figure 1.5 illustrates this structure. The intershell becomes convective when the helium burning shell is ignited and the energy generated from this burning is too great to be transported radiatively and must instead be transported by convection. This is known as a thermal pulse (or helium shell flash). The convection allows the helium-rich region to penetrate the hydrogen burning shell and ingest protons. There is an entropy barrier between the hydrogen burning shell and the helium-rich intershell region. For the intershell region to penetrate the hydrogen burning shell, energy must be put into the system in order to raise the entropy of the intershell region. At low metallicity, the gradient of the entropy barrier is shallow and therefore more mass can be ingested.

The proton ingestion triggers a series of reactions, the consequence of which is neutron production and therefore neutron captures. Helium burning enriches the intershell region with ^{12}C and hydrogen ingestion into the intershell region causes proton captures onto ^{12}C giving rise to $^{12}\mathrm{C} + p \rightarrow {}^{13}\mathrm{N}$. ^{13}N has a half-life of around 10 minutes and will decay into ^{13}C as

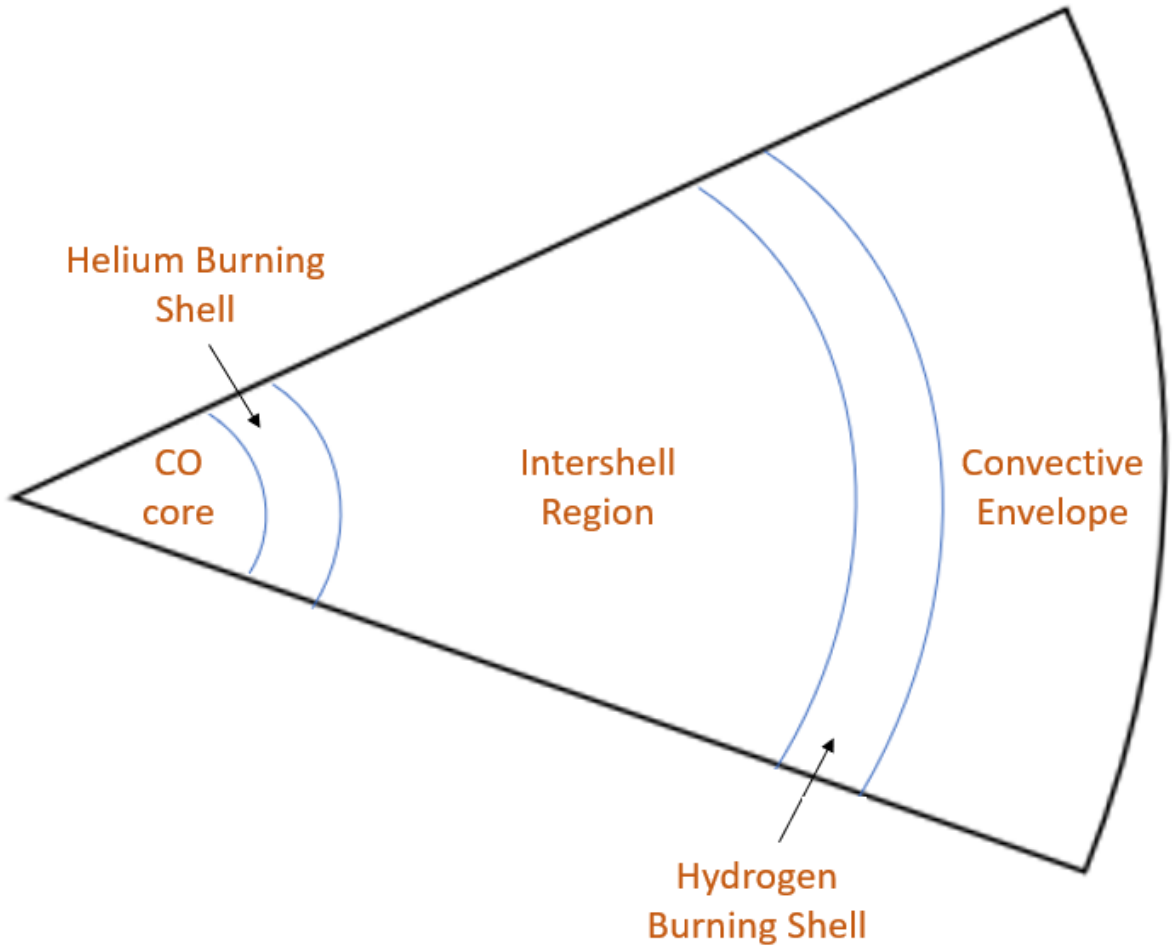

Figure 1.5: Structure of the interior of an AGB star (not to scale).

it is mixed downwards. As the intershell region is rich in helium, alpha captures onto ^{13}C can occur at the bottom of the convective region and neutrons are produced via the ^{13}C(α,n)^{16}O reaction [2].

Malaney (1986) aimed to investigate the processes that produce neutrons in AGB and post-AGB stars. In order to do this, he used the models of Schönberner (1979) and took the 13th thermal pulse as representative of a mixing event in the AGB and the 24th thermal pulse as representative of a mixing event in the post-AGB phase. The neutron densities of these models were found to be comparable with that of the i process ($n \approx 10^{11}$ cm^{-3} - 10^{14} cm^{-3}). This was an important result because it was confirmation how of i-process neutron densities in AGB and post-AGB stars are produced. Since then, other works (which will be discussed in the following section 1.4) have modelled proton ingestion to investigate other sites of i-process nucleosynthesis.

1.4 Sites of i-process nucleosynthesis

PIEs have also been found to occur in other stellar regions with high ^{4}He which make these sites potential candidates for the i process to be taking place. Some of these sites include the 'dual core-flash' in low-mass stars of low-metallicity, hyper metal-poor stars ([Fe/H] < -5), post-AGB stars, super-AGB stars, rapidly accreting white dwarfs, population III stars and lead poor AGB stars.

Lugaro, Campbell & De Mink (2009) build upon the previous work of Campbell (2007) to try to come up with a progenitor for CEMP-r/s stars. Campbell (2007) showed that a 'neutron superbust' can be produced in low-mass stars of low-metallicity due to a dual core-flash (PIE). A dual core-flash is described in Lugaro, Campbell & De Mink (2009) as an event in which protons are ingested in the helium flash region producing a hydrogen flash. Lugaro, Campbell & De Mink (2009) then went on to use the 0.85M$_\odot$ star at zero initial metallicity of Campbell (2007) to investigate the nucleosynthesis occurring in the model. They found that the neutron density of the model stayed above 6×10^{13} cm^{-3}, with peak neutron density of

[2]We should note that neutrons can also be produced via the ^{22}Ne (α,n) ^{25}Mg reaction. However, it is not believed this reaction is significant in producing neutrons for the i process.

$n = 2\times10^{14}$ cm^{-3}. Neutron densities in this range are characteristic of the i process. Therefore, calculating neutron densities of the model around 10^{13}-10^{14} cm^{-3} is indicative of the i process occurring in this site.

Campbell, Lugaro & Karakas (2010) modelled the proton ingestion of a star with metallicity [Fe/H] = -6.5 during the core helium flash phase. They found it undergoes a 'neutron superburst' at t = 0 - 1.2 yr, producing peak neutron densities of $n \approx 10^{15}$ cm^{-3}. This neutron density is indicative of the i process having occurred. The modelled abundances were diluted and compared to metal-poor halo star HE1327-2326, which has Sr overabundance. The model was able to reproduce the abundances of C, N, O and Sr but overproduced Ba. However, the modelled [Ba/Sr] ratio of [Ba/Sr] < 0.19 was consistent with the observation of [Ba/Sr] < 0.23. This showed that i-process neutron densities are able to replicate heavy element overabundance at neutron capture peaks.

Herwig et al. (2011) demonstrated that i-process neutron densities of $n \approx 10^{15}$ cm^{-3} can also be achieved in the VLTP of post-AGB stars like Sakurai's object. To do this they used three-dimensional (3D) calculations in order to study the entrainment of H into the convective zone of a post-AGB star. By introducing a delay of approx 1 day between the last thermal pulse and the splitting of the convective zone they found that heavy element production only went as far as the light-s peak, finding [hs/ls][3] ratios of -1.5 < [hs/ls] < -0.9. Using this model the authors were able to reproduce the observed [hs/ls] ratio within uncertainties, the Li abundance and low ^{12}C/^{13}C ratio of Sakurai's object.

Jones et al. (2016) propose that super-AGB stars could be a potential site for the i process. A super-AGB star is differentiated from an AGB star because carbon burning can be ignited, leading to the production of an oxygen-neon (ONe) core not present with regular AGB evolution (Garcia-Berro & Iben Jr, 1994). This is because they believe that the hydrodynamics induced by H-ingestion in the super-AGB dredge-out helium-buring convection zone would behave similarly to the H ingestion event of Sakurai's object (Herwig et al., 2011). However, in order to confirm this, three-dimensional (3D) simulations of the H ingestion are needed.

[3][hs/ls] here means the ratio of heavy s-process to light s-process elements. Different authors have different definitions but here it means [ls/Fe] = $\frac{1}{3}$([Sr/Fe]+[Y/Fe]+[Zr/Fe]), [hs/Fe] = $\frac{1}{2}$([Ba/Fe]+[La/Fe])

Denissenkov et al. (2019) modelled a series of rapidly accreting white dwarfs (RAWDs) undergoing multiple helium shell flashes. They found that models at low metallicity can reproduce the heavy element abundances of CEMP-r/s stars. More detail on the i process in rapidly accreting white dwarfs can be found in 1.5.

Clarkson, Herwig & Pignatari (2018) proposed that population-III (Pop-III) metal-poor stars were a site for the i process. They did this by performing one-zone nucleosynthesis calculations of the convective-reactive environment of a 45 $M_{\odot}$ Pop III model. They found their one-dimensional model of the Pop III star reaches neutron densities of 10^{13}cm^{-3}. Though we cannot observe these stars, the most metal-poor stars we can observe today may carry their signature and it was found that the model can reproduce their high abundances of [Na/Mg] and [Mg/Al]. The heavy element production was not discussed in this work. However, figure 4 of Clarkson, Herwig & Pignatari (2018) shows a decrease in abundance at the iron group which suggests that there are not a lot of iron seeds in the model for neutron captures to happen.

Hampel et al. (2019) provided further evidence that AGB stars are promising candidate sites for the i process by investigating i-process nucleosynthesis at various neutron densities and exposures, ranging from $n = 10^{11}$ cm^{-3} - 10^{15} cm^{-3} and $\tau = 0.9$ - 23.2. These one-dimensional, single-zone calculations were compared with a sample of CEMP-i (CEMP-r/s) and post-AGB stars. They found that the fits to the abundances of the stars were good and that the i process can be used to explain the low Pb abundance of low mass-AGB and lead-poor post-AGB stars.

It should be noted that most of the works discussed above use one-dimensional (1D) calculations (the exception being Herwig et al. 2011) in order to study proton ingestion and the subsequent nucleosynthesis. However, 1D simulations cannot fully describe the physics occurring because the way protons are mixed is tied to the treatment of convection in the models. Convection is a three-dimensional (3D) problem, so for a complete picture we must turn to 3D simulations like those of Herwig et al. (2011, 2014) and Stancliffe et al. (2011). Herwig et al. (2011) proposed that the increase in entropy of the convective zone caused by the entrainment of hydrogen would cause the convective zone to split in to two regions. Herwig

et al. (2014) built upon this work by studying Global Oscillations of Shell H-ingestion (GOSH) during hydrogen ingestion flash of a post-AGB star like Sakurai's object. Global Oscillations of Shell H-ingestion refers to the process occurring in post-AGB stars by which one violent fuel ignition event causes an upwelling, which causes a circumfrential flow down to the point of the first ignition and the process begins again. More detail can be found in Herwig et al. (2014). They showed the GOSH proceeds until enough entropy is ingested such that the GOSH is quenched and the convective zone splits. This is in contrast to the 3D simulations of Stancliffe et al. (2011) which find that protons are ingested in plumes all the way to the bottom of the convective zone with no splitting present. This goes to show that although 3D simulations should be closer to real life, their results can differ significantly. This is because 3D scenarios are much more complicated to model, as well as being computationally both expensive and time consuming. As a result, 3D models are rarely used despite a need for them in order to verify much of what has already been proposed after 1D simulations.

1.5 Rapidly Accreting White Dwarfs - RAWDs

As stated in section 1.4 rapidly accreting white dwarfs are a potential site for i-process nucleosynthesis. RAWDs are carbon-oxygen (CO) white dwarfs in a close binary system that are rapidly accreting material from their companion star. The burning of accreted hydrogen on the RAWD occurs at a rate of approximately 10^{-7} $M_{\odot}$ yr^{-1}. Rapid accretion at this rate has to occur because this allows the accreted hydrogen to burn as it arrives on the stellar surface. This creates a layer of helium upon which a layer of hydrogen forms in order to create the structure which allows for proton ingestion. If the accretion were to occur any slower, the stable burning expected at the higher rates would cease and make way for thermonuclear runaway associated with novae (Nomoto, 1982).

In a binary system the RAWD starts as an intermediate mass star which arrives at the AGB phase and fills its Roche Lobe. When this happens, it goes through a common envelope event with its companion and a CO white dwarf is left. The companion star is likely to be a main sequence, sub-giant or red giant branch star. The companion star will then evolve and fill its Roche lobe and donate material from a hydrogen-rich envelope to the white dwarf.

When a star is burning material on its surface, the convective envelope surrounding that star will expand. There is an equipotential surface around a star at the boundary of which the envelope cannot expand any further without material being transferred to its companion, which is called the Roche lobe. Therefore, when a star fills its Roche lobe and material begins to be accreted by its companion, it is called Roche lobe overflow (RLOF). In some cases, the companion cannot accrete all the material being transferred to it. In these cases, the star can become engulfed in the envelope of the primary in what is known as a common envelope event. A common envelope event is when two stars in a binary system share the same envelope. Due to their complex nature, common envelope (CE) events are still a widely researched and contested area of stellar evolution. However, we do have a basic understanding of how a CE event typically occurs. (Ivanova et al., 2013) states that CE events happen in four stages:

1. Loss of corotation leading to spiralling-in binary. In a RAWD binary system described above, loss of corotation occurs due to unstable mass transfer from RLOF.

2. Plunge-in and its termination. During this stage, there is rapid spiralling in of the binary system. The orbital energy is deposited in the envelope which causes further envelope expansion.

3. Self-regulating spiral in. The envelope expands to the point where the spiralling slows down.

4. Termination of the self regulating phase. The envelope is ejected and a close binary system remains.

The accreted hydrogen on the RAWD will form a hydrogen burning layer around the star and a structure will form similar to that of an AGB star described in section 1.3. Helium burning drives convection in the intershell during which protons are ingested and neutrons are produced. The neutron density in the intershell region can reach values of $n \approx 10^{12}$ - $10^{15}\,\mathrm{cm}^{-3}$ (Denissenkov et al., 2019) which is characteristic of the i process. This means i-process nucleosynthesis could occur in the intershell region of a RAWD.

As the star continues to accrete material from the companion there will come a point where the RAWD will fill its Roche Lobe and throw off material which gets transferred back to the companion or ejected from the system, thus the cycle starts again. This cycle of accretion, to helium shell flash, to i process, to RLOF can occur dozens of times before accretion ceases. The formation sequence of a RAWD is shown in Figure 1.6.

Denissenkov et al. (2017) used the MESA stellar evolution code (Paxton et al., 2013) to model He shell flashes in RAWDs. They found that the RAWD ejecta was enriched with first-peak (light-s) heavy elements by 2.5 - 3.5 dex. It was calculated that 0.001 $M_{\odot}yr^{-1}$ of i-process enriched material was returned by RAWDs. Côté et al. (2018a) used the galactic chemical evolution code OMEGA (Côté et al., 2017) to investigate the contribution of RAWDs to the solar composition of first-peak neutron capture elements. They found that the RAWD contribution to the abundance of the first peak elements Kr, Rb, Sr, Y, Zr, Nb, and Mo can vary between 2% - 45% depending on the element. Work carried out by Denissenkov et al. (2019) showed that a low metallicity RAWD model (their model F, [Fe/H] = -2.3) can reproduce the abundances of a CEMP-r/s star. They did this by modelling multiple cycles of helium shell flashes and picking out a representative cycle, again using MESA. They then post-processed this using the NuGrid code mppnp (Pignatari et al., 2016) in order to find the i-process abundances.

1.6 Carbon-Enhanced Metal-Poor (CEMP) Stars

Carbon-enhanced metal-poor stars have carbon abundance [C/Fe] $\gtrsim$ 1 (Beers & Christlieb, 2005), though the exact definition varies between authors (e.g. Masseron et al. (2010) gives a value of [C/Fe] > 0.9). There are four types of CEMP stars:

- CEMP-s, which display enrichment of s-process elements. Namely, [Ba/Fe] > 1 and [Eu/Fe] > 0.
- CEMP-r which display enrichment of r-process elements. All CEMP-r stars have [Ba/Eu] < 0, CEMP-r I have [Eu/Fe] < 1 and CEMP-r II have [Eu/Fe] > 1.
- CEMP-r/s which display enrichment of both s and r-process elements. Namely,

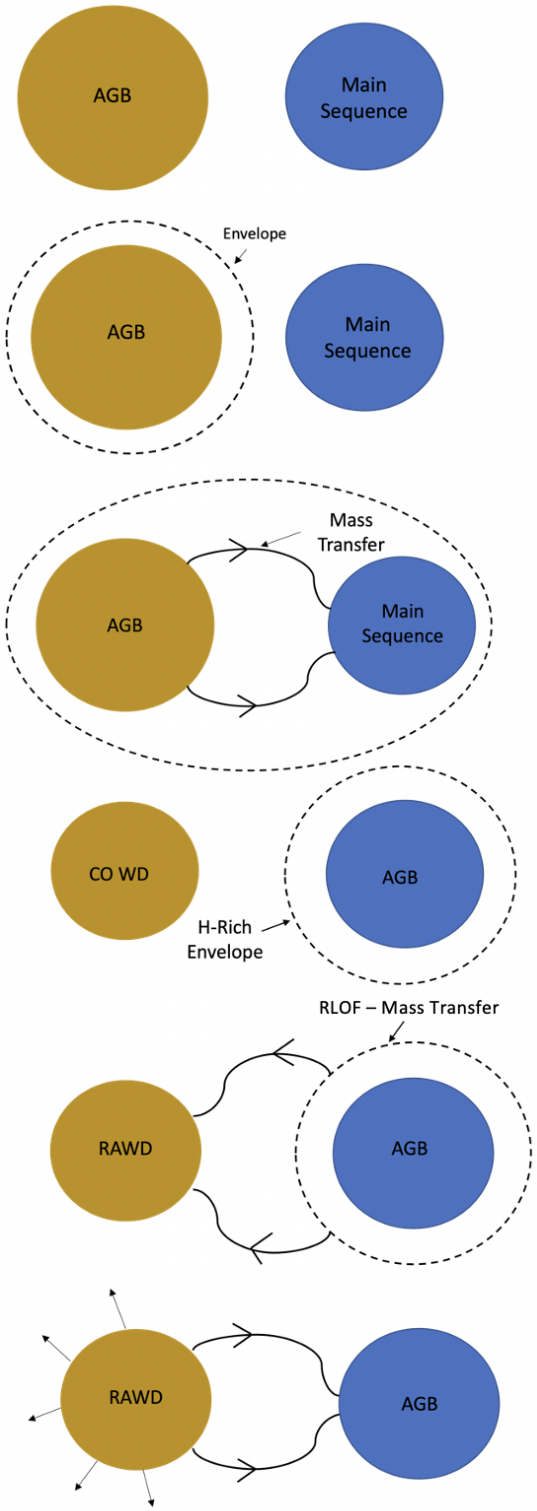

Figure 1.6: Formation of a RAWD in a binary system. The yellow circle is the star that will eventually become the RAWD and the blue circle is the companion star. Dashed lines represent stellar envelopes and the lines with arrows represent mass transfer and the direction of the mass transfer. RLOF here stands for Roche Lobe Over Flow.

[Ba/Eu] > 0 and [Eu/Fe] > 1.

- CEMP-no which display no enrichment of neutron capture elements i.e. [Ba/Fe] < 0

The abundance definitions given here are the same as those given in Masseron et al. (2010) and are the definitions that I will be adopting in the present work. More details on the properties of each of these stars as well as a graphical representation of these classifications can be found in Masseron et al. (2010).

In this work we will be focusing on CEMP-r/s stars, as they have been shown to have signatures of the i process (section 1.2). A CEMP-r/s star has enrichment of both barium and europium but the exact definition for how much of these elements should be present varies between authors (e.g. Beers & Christlieb 2005, Jonsell et al. 2006, Masseron et al. 2010). Masseron et al. (2010) defines a CEMP-r/s star as a star with [C/Fe] > 0.9, [Ba/Eu] > 0 and [Eu/Fe] > 1. However, Beers & Christlieb (2005) define a CEMP-r/s star as a star with [C/Fe] > 1 and 0 < [Ba/Eu] < 0.5 but this more restrictive definition means stars are misclassified as CEMP-s when their heavy element abundances would better fit an i process (Hampel et al., 2016).

The i process helps us to explain the enrichment of both barium and europium that we see in CEMP-r/s stars. Hampel et al. (2016) investigates this by creating a range of i-process models with neutron densities between $n \approx 10^{12}$ cm^{-3} and $n \approx 10^{15}$ cm^{-3} and comparing the nucleosynthetic signatures with the abundances of CEMP-r/s stars. They found that models with neutron density $n \approx 10^{14}$ cm^{-3} fit CEMP-r/s abundances so well that it was proposed they be renamed CEMP-i stars.

Though many formation scenarios have been proposed (e.g. Lugaro, Campbell & De Mink 2009 and Jonsell et al. 2006), Abate, Stancliffe & Liu (2016) suggest that a complete formation scenario for CEMP-r/s stars has not yet been achieved. However, arguably the most likely scenario for forming a CEMP-r/s star is for the star to be part of a system in which it is accreting material from a companion. It is widely accepted that CEMP-s form in this way (e.g. McClure & Woodsworth 1990, Aoki et al. 2007 and Hansen et al. 2016), therefore it is likely that CEMP-r/s stars will too (e.g. Abate et al. 2015, Hansen et al. 2016), though a more detailed study into the binary nature of CEMP-r/s stars is yet to be done. In this work the two

scenarios that are most relevant are an AGB star or a RAWD transferring i-process material onto a CEMP star.

Section 1.3 detailed the structure of AGB stars which allows for proton ingestion episodes. In a similar scenario to that of the RAWDs described previously, the AGB is in a binary system with the soon to be CEMP star. The AGB star will undergo a proton ingestion episode triggered by helium burning driven convection and begin to produce neutrons and i-process material. The envelope of the AGB star will expand to a point where it has filled its Roche lobe and the soon to be CEMP star will begin to accrete carbon-rich and i-process rich material.

For a CEMP-r/s star to gain material from a RAWD, the scenario is slightly more complicated. Denissenkov et al. (2019) proposed the CEMP-r/s star is a tertiary star in a triple system with the RAWD and its companion. Within this triple system, there are two potential scenarios. The first, the RAWD explodes as a supernova Ia, ejecting material into the ISM and landing on the CEMP. Or, the CEMP star is sufficiently close enough to the system that some of the material thrown off the RAWD would enrich the CEMP, rather than being transferred onto the companion. However, in this particular scenario the CEMP would also have to be far enough away that it is not influenced by the gravity of the initial binary system. Another thing to consider in this scenario is the fact that in a triple system, we expect the orbital period of the CEMP star to be different than that of a CEMP in a binary system. However, CEMP-s stars (which we know are formed in binary systems with an AGB companion) and CEMP-r/s stars have similar orbital periods, coupled with the rarity of triple systems, this formation scenario is thrown into question.

1.7 Summary of thesis aims

This thesis focuses on an abundance analysis of two i-process models compared to observations. The two models in question are an AGB intershell model and a RAWD model (sections 2.1.1 and 2.1.2).

I will compare each model to a sample of CEMP-i stars in order to try and predict the most likely formation scenario. Here χ^2 analysis is used to find the best fitting part of the model to the data. This technique is then applied in order to try and explain the strange abundance

patterns of two phosphorus rich stars and to make predictions of the thorium and uranium abundances we might expect the i process to produce.

As a continuation of the abundance analysis, the work will then move on to use three-element plots to find trends in the i-process models that cannot be replicated by the observational data or vice versa. The aim of this being to try to find abundance ratios and therefore potential observational signatures that are indicative of the i process.

2. Detailed Modelling of Stellar Abundance Patterns

In order to explore the nucleosynthesis of the i process, we first need to be able to model it. There are two i-process models which will be used in this work. The first is a one-zone AGB intershell model and the second is a RAWD model from Denissenkov et al. (2019). In this chapter, I will use χ^2 fitting to find out how well the i-process models fit a series of different objects and I will discuss what constitutes a 'good' fit when using this technique. I will aim to fit the abundances of a sample of CEMP-i stars and also show how robust the i-process model fitting technique is by fitting to objects that have already been classified. I will fit an i-process model to phosphorus-rich stars first identified by Masseron et al. (2020a,b). Finally, I will investigate how i-process models can be used to make observational predictions of thorium and uranium.

2.1 Models

2.1.1 One-Zone AGB intershell model

I used `ppn` (post processing network), a code produced by the NuGrid collaboration (Herwig et al., 2009), to compute the nucleosynthesis in conditions similar to those found in the intershell region of a 1.65 $M_\odot$ AGB star with metallicity $Z = 1\times10^{-4}$ ([Fe/H] $\approx$ -2.26). The code tracks 5627 isotopes and uses a network of 67,377 reactions to simulate stellar nucleosynthesis. The initial temperature of the model was T=2×10^8 K, with an initial density of ρ=2×10^3 g cm^{-3} and an initial helium abundance of X(^{4}He)=0.556, which are initial conditions from one of the stars modelled in Ritter et al. (2018). The initial chemical composition of the model is based on the abundances of an intershell region of an AGB star with high abundance by mass fraction of $^1H = 0.0104$ and $^{12}C = 0.37$ to mimic proton ingestion and generate the series of reactions that will produce neutrons, described in section 1.3. To create

the run I used a nuclear reaction network which runs up to astatine (At). The reaction rates here are taken from a range of sources. The neutron source reaction ^{13}C (α, n) ^{16}O is taken from Heil et al. (2008) and the ^{22}Ne (α, n) ^{25}Mg reaction from Jaeger et al. (2001). Neutron capture rates are taken from the KADoNIS compilation (Dillmann et al., 2006). Where the rate is not available from KADoNIS it is taken from Basel REACLIB database, revision 20090121 (Rauscher & Thielemann, 2000) instead. Details of other reaction rate sources can be found in Pignatari et al. (2016). The model is evolved over approximately 15300 years and the data is outputted in cycles (timesteps). Once the initial nucleosynthesis has settled, the time-step between the previous and current cycle increases by a fixed factor. For this model the factor is 1.05. Figure 2.1 shows how the increase in time corresponds to an increase in cycle. The slope of this figure is 0.05, which corresponds with the 1.05 multiplication factor on the time-step for each cycle.

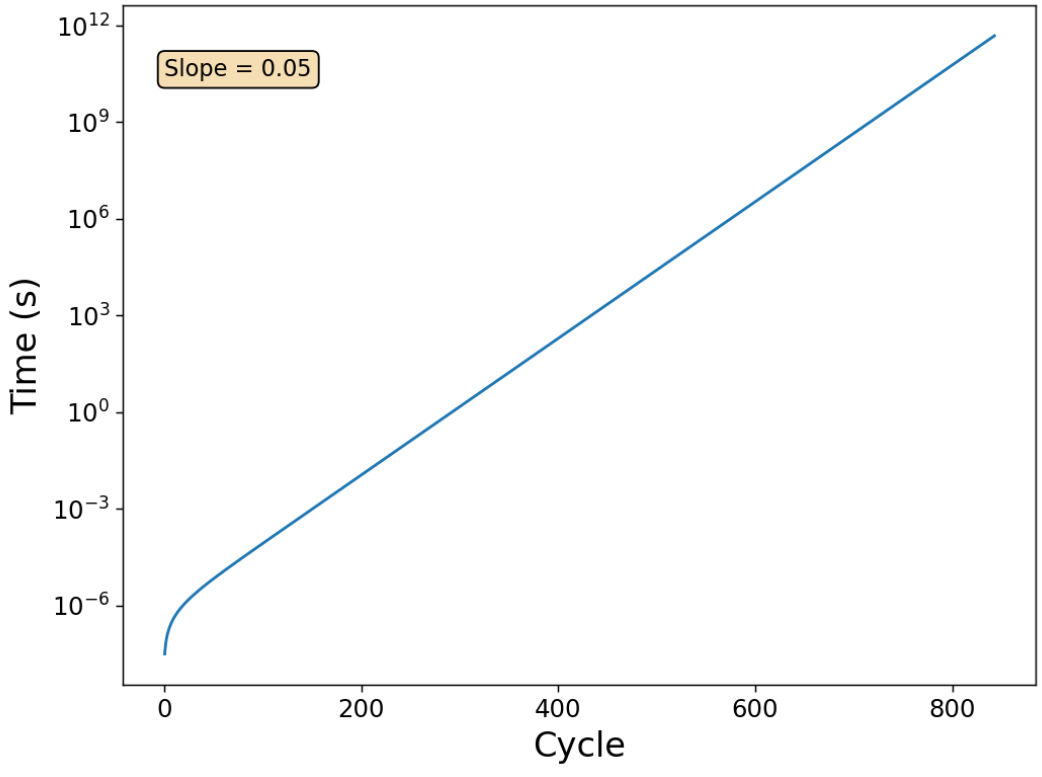

Figure 2.1: Cycle number versus time for the intershell model. Here the slope of the line is 0.05 and indicates the factor by which the timestep increases from one cycle to the next.

The model varies in neutron density throughout the evolution, where neutrons are generated by ingesting hydrogen into a helium rich intershell region (e.g. Dardelet et al. 2015). The model has i-process neutron densities of $n = 10^{12}$ - 10^{15} cm^{-3} at cycles 400 to 570 (t = 6.28×10^{-6} yrs to t = 0.025 yrs). Figure 2.2 shows the variation of neutron density through the evolution of the model. The red dotted lines represent the cycles at which i-process neutron densities begin and end. At cycle 570 the neutron exposure is 11.2 mbarn^{-1}.

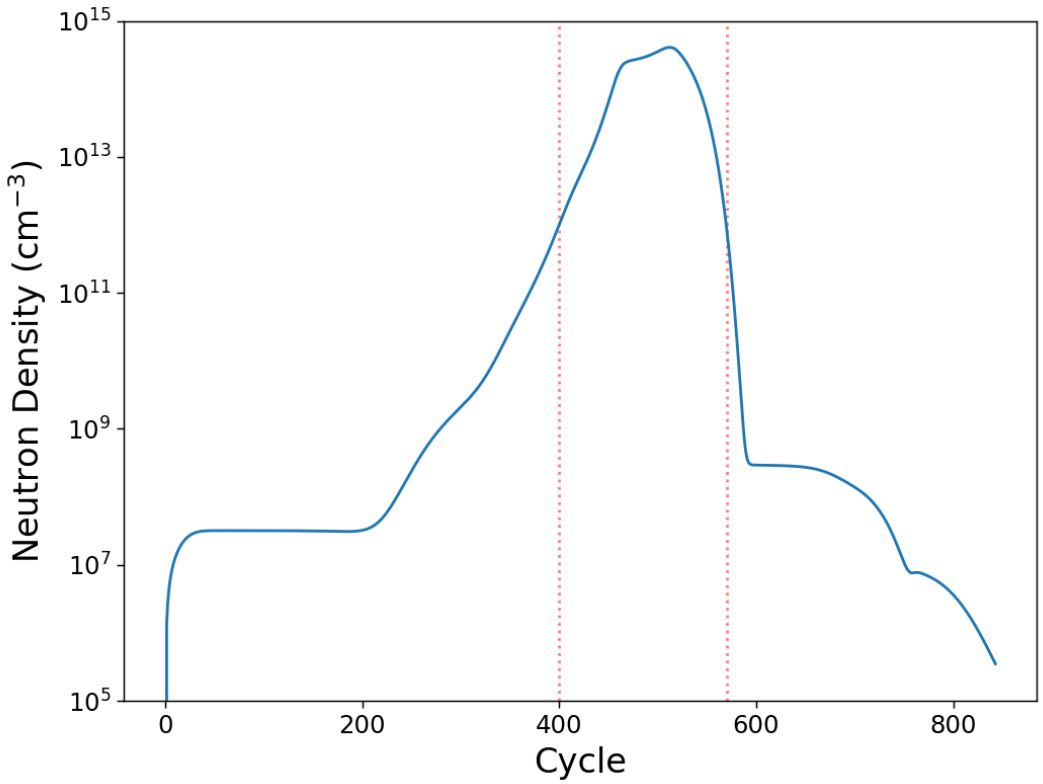

Figure 2.2: Variation of neutron density throughout the evolution of the one-zone intershell model (blue line). Red dotted lines are shown at cycles 400 (t = 6.28×10^{-6} yrs) and 570 (t = 0.025 yrs) to show where i-process neutron densities begin and end.

The exact range of exposures expected for the i process is yet to be constrained. However, the maximum value of 11.2 mbarn^{-1} found here falls within the range of 10 - 50 mbarn^{-1} found by Dardelet et al. (2015). When exploring fitting the Pb abundance of a sample of CEMP-i stars with a one-zone AGB model, Hampel et al. (2019) found exposures between 1.1 - 23.2 mbarn^{-1}, which again includes our maximum value. The reason expected i-process

exposures can range so much is due to the way in which crucial nuclear reactions are treated in their networks. For example, Dardelet et al. (2015) get a much higher range of exposures than Hampel et al. (2019) because the network prevents destruction of ^{13}N via the ^{13}N (p, γ) ^{14}O reaction but allows neutron release via ^{13}C (α, n) ^{16}O. Therefore, more neutrons are produced than would be expected if ^{13}N (p,γ)^{14}O was in operation.

2.1.2 RAWD model

The RAWD model is model F ([Fe/H] = -2.3) of Denissenkov et al. (2019). The RAWD models in this work were created using the MESA stellar evolution code (Paxton et al., 2011, 2013). Then the i process was simulated using the NuGrid post-processing code `mppnp` (multi-zone post processing network parallelized) (Pignatari et al., 2016). To do this, the abundances from a 'representative' helium-shell flash were taken during the evolution of the model and used as the initial abundances for the `mppnp` run. The conditions for the run are taken from a MESA model in the middle of a H-ingestion phase. Again, these calculations included a network of 5627 isotopes and 67,377 reactions. Details of exactly how the models, including model F, were created can be found in Denissenkov et al. (2019).

The RAWD model is a 1D multi-zone model this means the mass of the star is split into 'zones' with identical thermodynamic conditions. At each timestep, the nucleosynthesis for each zone is calculated and then mixing occurs between zones. This happens at each timestep until the model has completed the run. Each zone will have its own set of final abundances, therefore in order to compare the abundances to observation the model was reduced to a single set of abundances. The abundance calculated for each isotope was the mass weighted average of that isotope in each zone at each timestep. The data was outputted every 100 cycles over a 1673280 second period starting from $1.9864908728\times10^{16}$ s, which is the time through the evolution of the stellar model that the selected He-shell flash begins. Every 100 cycles represents 33600 seconds.

This model is also being used alongside the one-zone AGB intershell model because Denissenkov et al. (2021) state that their RAWD model F is a better fit for the heavy element abundances of a CEMP-i star than the low-mass, low-metallicity AGB scenario. This is

because they have found the RAWD model can reproduce the second peak to first peak ratio of the abundances more closely than the AGB intershell models of Karinkuzhi et al. (2021) and Choplin, Siess & Goriely (2021). We are assuming that when the RAWD throws off its material, it is able to eject all, or at least a significant fraction, of the material it processes.

2.2 Abundance Fitting

We often observe stellar abundance patterns which cannot immediately be identified as being a result of one process or another. In recent years the i process has been crucial in explaining some previously unexplained and strange abundance patterns such as Pop.III metal-poor stars, pre-solar grains and CEMP-i stars (see section 1.4). This is because the i process can operate at a wider range of neutron densities and exposures compared to the s process, allowing us to tweak i-process models to fit a range of scenarios.

2.2.1 Fitting a model to observations

When we observe a star, the abundances we extract from observational data come from the stellar surface. The material on the surface of a star is not pure material from the site of production, it has been diluted by any transport through the layers of the star or any accretion events that may have occurred e.g. accretion by a companion. The abundances on the surface of a star are also a result of nuclear decay which has taken place after production of various unstable isotopes in the interior layers.

Unlike observed abundances, modelled abundances are not necessarily decayed or diluted but are purely a result of the nucleosynthesis that has occurred in the simulations. In both scenarios studied, we are looking at a binary system where dilution would have occurred when the material was accreted by the companion. In the case of the AGB model, dilution would have occurred both as the intershell material is being transported to the stellar surface and as a consequence of accretion of material by the companion (that will eventually become a CEMP-i) (Stancliffe, 2009). For the RAWD model, dilution happens when the envelope material thrown off the RAWD is transferred onto the tertiary star in the system (again, eventually becoming the CEMP-i). Therefore, before comparing theoretical models to observations, two

things must happen. First, the abundances from the model must be decayed. This is because the time between the production of unstable isotopes and us observing the abundances of a star is such that any unstable isotopes produced have decayed to something stable. Here, the decay is an approximation to leaving the isotopes to decay for gigayears. Each unstable isotope is allowed to β decay until a stable isotope is reached, regardless of the unstable isotope's half-life. The assumption made by doing the decay in this way is that the only decays occurring are β decays. This assumption is justifiable because the the majority of the unstable isotopes included in the reaction network will decay by β decay. Secondly, we must dilute the material from the stellar interior with solar scaled material in order to replicate the binary nature of the systems. In this work the abundances I aim to study are metal poor and therefore I dilute the intershell abundances with solar material (Asplund et al., 2009) scaled to a metallicity of [Fe/H] = -2.

To find a model which matches the stellar abundances we need to know two things: 1) how much scaled solar material has been mixed with the pure i-process material i.e. the dilution factor, d and 2) when in the evolution of the model do the decayed abundances fit best (i.e. the best fitting cycle after decay has happened). To find this information I take the decayed data at each cycle and dilute by a range of 1000 dilution factors from d = 0.001 - 1, where the diluted abundances are calculated as follows:

$$X = X_i\, d + X_{\text{scaled}}\,(1 - d) \tag{2.1}$$

X is the abundance post-dilution, X_i is the abundance from the simulations after decay, d is the dilution factor and X_{scaled} is the scaled Solar abundance. In all of these cases X is the abundance by mass fraction of whichever element or isotope is being considered. The dilution factor d, is made physically meaningful by considering conservation of mass, where M_i is the mass of the unprocessed material, M_{scaled} is the mass of the scaled solar material and M is the total mass post-dilution. If:

$$M_{\text{scaled}} + M_i = \text{M}$$
$$\frac{M_{\text{scaled}}}{M} + \frac{M_i}{M} = 1$$

Let $d = \frac{M_i}{M}$:

$$\frac{M - M_i}{M} + d = 1$$

Therefore if:

$$\begin{aligned} X_{\text{scaled}}\, M_{\text{scaled}} + X_i\, M_i &= X\, M \\ \frac{X_{\text{scaled}}\, M_{\text{scaled}}}{M} + \frac{X_i\, M_i}{M} &= X \\ X_{\text{scaled}}\, \frac{M - M_i}{M} + X_i\, d &= X \\ X_{\text{scaled}}\, (1 - d) + X_i\, d &= X \end{aligned}$$

Here, X is again the abundance by mass fraction.

After each cycle has been mixed by each dilution factor, the final abundances (X) can be compared to observational data. To do this, we use a χ^2 fit as a measure of how closely the modelled abundances match the observed abundances. For this work χ^2 is defined as

$$\chi^2 = \sum_Z \frac{([\mathrm{X_Z/Fe}]_{\text{obs}} - [\mathrm{X_Z/Fe}]_{\text{mod}})^2}{\sigma^2_{\text{Z,obs}}} \tag{2.2}$$

where $[\mathrm{X_Z/Fe}]_{\text{obs}}$ and $[\mathrm{X_Z/Fe}]_{\text{mod}}$ are the observed and modelled abundances of element X with atomic number Z and $\sigma^2_{\text{Z,obs}}$ is the observational error on the observed abundances.

χ^2 fits are most useful for independent data points with Gaussian errors which is not the case here. However, we can still use this as a good statistical approximation of how well the models fit the abundances and other examples of this approach can be found in across the literature (e.g. Hampel et al. 2016, 2019, Karinkuzhi et al. 2021, Goswami & Goswami 2020, Goswami et al. 2021, Choplin, Siess & Goriely 2021). Some of these authors use a reduced χ^2 value, χ^2_ν, which is defined as $\frac{\chi^2}{N}$ where N is the number of degrees of freedom (which in this case is generally the number of observational data points). In theory, this allows for direct comparison between the χ^2 values of two different sets of observations because it has removed the dependence on how many data points are in the data set. However, given that the use of χ^2 as an indicator of fit is already not ideal due to the non-Gaussian errors, the reduced χ^2 will not be used in this work.

When I use equation 2.2, I only fit the abundances from Zn (Z = 30) onward for a few reasons. First, the abundances from the lower part of the ppn network (Z<10) are incorrect

because there is significant hydrogen burning happening elsewhere in the star that cannot be accounted for in a one-zone code in the same way it could be in a full model. Secondly, the initial ^{12}C is much higher in the intershell region of the star that it would be in other regions, therefore even with the dilution of the abundances, the C remains high. Lastly, the light element (elements lighter than iron) abundance pattern is often explained by other processes and I am mostly interested in how the neutron captures produce the heavy elements.

2.2.2 CEMP-i abundance fitting

Here the sample of CEMP-i (CEMP-r/s) stars are 17 of the same stars used in Hampel et al. (2016, 2019), which is in turn from Abate et al. (2015). The stars were selected from the SAGA database (Suda et al., 2008) (a database of Milky Way stars) in the metallicity range -2.8 ≤ [Fe/H] ≤ -1.8, however for the sample used in this thesis, the metallicity does not exceed [Fe/H] = -2.1. As stated in Abate et al. (2015) the selected stars have observed carbon and barium abundances and no upper or lower limits to the abundances. When this sample was collected by Abate et al. (2015) any stars that appeared multiple times (i.e. abundances had been calculated more than once by different authors) were dealt with by making sure the abundances agreed within error bars. If they did not, an average of the measurements was taken, with an error bar given as half the difference between the two values. Table 2.1 shows the properties of the stars in this sample including the surface gravity log g, effective temperature T_{eff}, metallicity ([Fe/H]) and some stellar abundances. The surface gravity and effective temperature have been shown here to provide more detail on the properties and evolutionary stages of the stars in the sample. The abundances are shown in order to understand the enhancements in C, Ba and Eu of the sample of stars.

Throughout this work I will be using samples of stars that have been put together using abundance databases. It should be noted that these abundances will have been measured by different authors using different techniques. Therefore, one author's measurement of one star could be different than another for the same star. This idea will be returned to when discussing the work of Karinkuzhi et al. (2021) in section 2.2.2.4.

Name	log g	T_{eff} (K)	Number of Elements Measured	[Fe/H]	[C/Fe]	[Ba/Fe]	[Eu/Fe]
HD187861	2.0±0.35	4960	14	-2.4	2.0	1.9	1.3
HD224959	1.9±0.25	5050	14	-2.1	1.8	2.2	1.7
CS31062-050	2.9±0.24	5489	37	-2.5	1.9	2.4	2.0
CS31062-012	4.2±0.38	6099	24	-2.8	2.3	2.1	1.6
CS29526-110	3.2±0.1	6500	18	-2.4	2.3	2.1	1.8
CS29497-030	4.0±0.5	6966	33	-2.5	2.4	2.3	1.7
CS22948-027	1.8±0.4	4800	21	-2.5	2.4	2.4	1.9
CS22898-027	3.7±0.28	6110	22	-2.3	2.0	2.3	2.0
CS22881-036	4.0±0.1	6200	14	-2.1	2.1	1.9	1.0
HE0131-3953	3.8±0.1	5928	16	-2.7	2.5	2.2	1.7
HE0143-0441	4.0±0.35	6305	22	-2.4	2.0	2.4	1.7
HE0338-3945	4.1±0.33	6161	32	-2.5	2.1	2.4	2.0
HE1105+0027	3.5±0.1	6132	16	-2.5	2.0	2.4	1.9
HE1305+0007	1.5±0.5	4655	21	-2.2	2.1	2.6	2.2
HE2148-1247	3.9±0.1	6380	25	-2.4	2.0	2.4	2.0
HE2258-6358	1.6±0.1	4900	31	-2.7	2.4	2.3	1.7
LP625-44	2.6±0.3	5500	31	-2.8	2.3	2.8	1.9

Table 2.1: Properties of the 17 CEMP-i stars in my sample.

2.2.2.1 One-Zone AGB intershell vs RAWD model

The aim of this section is to build upon the work of Hampel et al. (2016, 2019). Hampel et al. (2016) used models with constant neutron density and artificially high exposure of $\tau = 495$ mbarn^{-1} to show that an i-process model can reproduce the abundances of CEMP-r/s stars. Hampel et al. (2019) built upon this and used one-dimensional, single-zone models with varying exposures to show that the production of lead (Pb) in AGB and post-AGB stars is exposure dependent.

I can compare the sample of CEMP-i stars described in section 2.2.2 with the two models described in section 2.1 and use a χ^2 fit to see how well the models reproduce the abundances. This is useful to do because both scenarios are a plausible explanation of the abundances of CEMP-i stars. By comparing the same sample to the two different models, we can see if one model gives a lower χ^2 fit than the other (implying a better fit) and how much 'better' the fit is by looking at variations in the χ^2 value as the parameters change. This means we can also go on to make comment on what a 'good' fit looks like.

For each CEMP-i star, I found the best χ^2 fit for both the one-zone AGB intershell and RAWD model, using the method described in section 2.2.1. Tables 2.2 and 2.3 show which properties best reproduce the stellar abundances for each model. Each table shows the dilution factor and cycle number that belong to the best fitting model and the χ^2 value for that model is shown in the right hand column on each table. Table 2.2 also shows the neutron density and exposure for the best fitting model but Table 2.3 does not. Neutron density and thus neutron exposure cannot be calculated for the RAWD model because in order to count the number of neutrons available, we would have to average over the whole mass range of the model. This would not be a realistic count of the neutrons because some regions will be more neutron dense than others.

From these tables we can find the stars where one model is clearly a better fit than the other (a much smaller χ^2) and the stars for which the χ^2 values are close enough together that its hard to say conclusively which model is a better fit. For two χ^2 values to be close together they must be within 5 of each other. On some level, this is an arbitrary value. The idea here is that a small difference in χ^2 does not make a big difference in terms of fit so having a

Star	Dilution factor	Cycle Number	Neutron Density (cm^{-3})	Exposure ($mbarn^{-1}$)	χ^2 value
HD187861	0.013	566	2.51×10^{12}	11.2	1.7
HD224959	0.034	530	2.32×10^{14}	6.47	7.0
CS31062-050	0.034	520	3.61×10^{14}	4.18	15.9
CS31062-012	0.021	517	3.90×10^{14}	3.55	4.5
CS29526-110	0.033	532	2.07×10^{14}	6.93	7.4
CS29497-030	0.048	532	2.07×10^{14}	6.93	6.1
CS22948-027	0.03	516	3.97×10^{14}	3.35	17.5
CS22898-027	0.057	529	2.44×10^{14}	6.24	22.1
CS22881-036	0.009	569	1.15×10^{12}	11.2	6.36
HE0131-3953	0.033	532	2.07×10^{14}	6.93	0.9759
HE0143-0441	0.046	534	1.83×10^{14}	7.38	7.6
HE0338-3945	0.058	529	2.44×10^{14}	6.24	16.9
HE1105+0027	0.052	531	2.19×10^{14}	6.70	0.92
HE1305+0007	0.09	517	3.90×10^{14}	3.55	25.9
HE2148-1247	0.054	523	3.23×10^{14}	4.85	56.4
HE2258-6358	0.017	519	3.72×10^{14}	3.96	49.3
LP625-44	0.088	532	2.07×10^{14}	6.93	16.6

Table 2.2: Summary of the best fit properties of stars in the CEMP-i sample for the one-zone model. The right hand column shows the smallest χ^2 value for each star in the sample compared to the one-zone intershell model. The other two columns show the dilution factor and cycle number which corresponds to the best fit.

Star	Dilution factor	Cycle Number	χ^2 value
HD187861	0.011	5000	9.4
HD224959	0.008	3700	5.0
CS31062-050	0.006	2300	20.0
CS31062-012	0.003	2400	3.5
CS29526-110	0.008	4100	17.2
CS29497-030	0.014	4800	22.2
CS22948-027	0.007	2100	14.8
CS22898-027	0.009	2000	8.0
CS22881-036	0.003	1600	14.2
HE0131-3953	0.005	1800	0.9761
HE0143-0441	0.022	5000	27.7
HE0338-3945	0.009	2000	16.6
HE1105+0027	0.007	1800	2.13
HE1305+0007	0.024	1900	9.53
HE2148-1247	0.013	2100	28.2
HE2258-6358	0.004	2100	53.6
LP625-44	0.014	1900	7.8

Table 2.3: Summary of the best fit properties of stars in the CEMP-i sample for the RAWD model. The right hand column shows the smallest χ^2 value for each star in the sample compared to the i-process RAWD model. The other two columns show the dilution factor and cycle number which corresponds to the best fit.

difference in χ^2 of < 5 is not going to tell us one way or another which model fits better. For example, HD224959 has a χ^2 value of 7.0 for the one-zone intershell model and 5.0 for the RAWD model. On visual inspection of Figures 2.12a and 2.12b, we can see that there is no noticeable difference between the two models in reproducing the abundances, which raises the question: when can a fit be considered better than another and what is a 'good' fit? This will be discussed in more detail in section 2.2.2.2

The stars for which the abundances are best reproduced by the one-zone AGB intershell model are: HD187861, CS29526-110, CS29497-030, CS22881-036 and HE0143-0441. Figures 2.3 to 2.7 show these fits. Each of these figures shows the abundance of each element ([X/Fe]) for the model versus that element's proton number (blue line) plotted next to the observational data for that star (red circles) and the error bars associated with it (grey lines).

- **HD187861**: Figure 2.3 shows the fits for HD187861. The one-zone model provides a much closer fit to Zr (Z = 40), Eu (Z = 63) and Pb (Z = 82). The RAWD model overproduces Eu and Pb by about 0.3 and 0.5 a dex respectively and underproduces Zr by about 0.4 dex. These differences in fit is what makes the χ^2 value for the one-zone model so much smaller.

- **CS29526-110**: Figure 2.4 shows the fits for CS29526-110. Here, the first peak elements Sr (Z = 38) and Zr (Z = 40) fit closely in the one-zone intershell model fit but are underproduced by about 0.6 and 0.35 dex respectively in the RAWD model. Though the lead and most of the heavy s-process (second peak) elements fit within error bars in both models, we can see that the one-zone model reproduces the second peak abundances more closely.

- **CS29497-030**: Figure 2.5 shows the fits for star CS29486-030. Both models have similar challenges in fitting Sr and Eu, with the the one-zone model underproducing Sr by about 0.35 dex and overproducing Eu by about 0.2 dex (though they both fit within error bars), while the RAWD model underproduces Sr by about 0.7 dex and overproduces Eu by about 0.15 dex. The RAWD model does not fit the first peak abundances as well as the one-zone model with Zr and Nb being underproduced by about

0.25 and 0.8 dex respectively. Though the RAWD model does fit the Pb observation within the error bar, the one-zone fit is much closer. Overall, this means that the one-zone model fit gives us the smallest χ^2.

- **CS22881-036**: Figure 2.6 shows the fits for CS22881-036, which has a sparse amount of data in comparison to some of the other stars in the sample. We can see that the one-zone intershell model comes closer to reproducing Nd (Z = 60) and Eu (Z = 63) than the RAWD model. Hence, the one-zone intershell model has the lower χ^2 even though the rest of the pattern looks largely similar between the two models.

- **HE0143-0441**: Figure 2.7 shows the fits for HE0143-0441. The fits between the two models appear largely similar until the lead abundance. We can see that the first – Sr (Z = 38) - Zr (Z = 40) – and second – Ba (Z = 56) - Nd (Z = 60) – peak elements are fit slightly better by the one-zone intershell model. Though, both the one-zone and RAWD model underproduce Nd, the better fit to Nd is achieved by the RAWD model. The RAWD model overproduces the lead by about 0.5 dex, this is the main reason the χ^2 is much smaller for the one-zone model.

What is notable here is that for 4 of the 5 stars, the model that best replicates the observed abundances is the model which can fit the Pb abundances closest.

The stars for which the abundances are best reproduced by the i-process RAWD model are CS22898-027, HE1305+0007, HE2148-1247 and LP625-44. Figures 2.8 to 2.11 show these fits.

- **CS22898-027**: Figure 2.8 shows the fits for CS22898-027. The two models fit most of the elements within error bars. However, the RAWD model gives a closer fit to the Er (Z = 68) than the one-zone model, which underproduces it by about 0.3 dex. The one-zone intershell model overproduces lead by about 0.8 dex, while the RAWD model underproduces it by 0.4 dex. Therefore, the better fit is achieved by the RAWD model overall.

- **HE1305+0007**: Figure 2.9 shows the fits for HE1305+0007. Here, the fit for elements Ba - Eu (Z = 56 - 63) is closer for the RAWD model, though both models fit everything

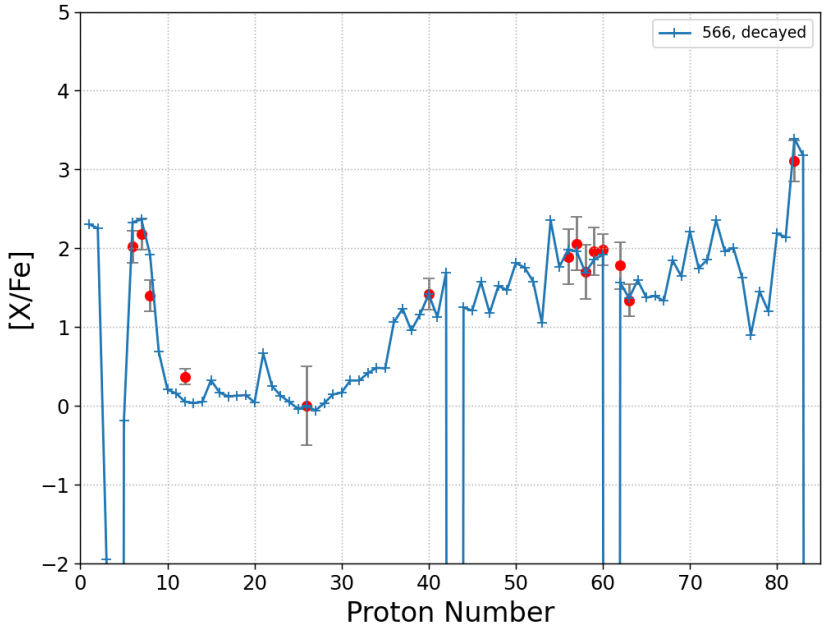

(a) One-zone AGB intershell model compared with the abundances of HD187861. The fitting parameters are: d = 0.013 at cycle 566, resulting in $\chi^2 = 1.7$.

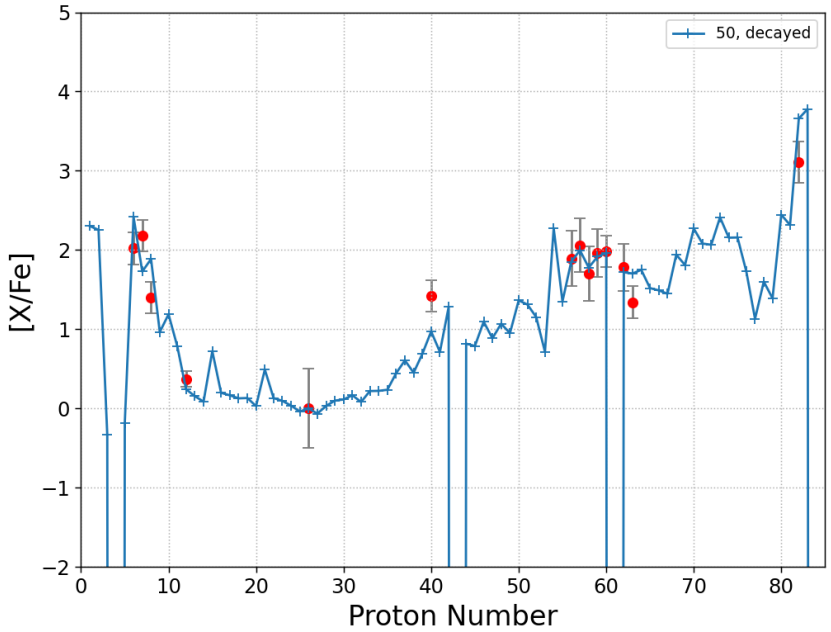

(b) RAWD model compared with the abundances of HD187861. The fitting parameters are d = 0.011 at cycle 5000, resulting in $\chi^2 = 9.4$.

Figure 2.3: Best fitting models for HD187861. The red circles show the observed data with the error bars in grey.

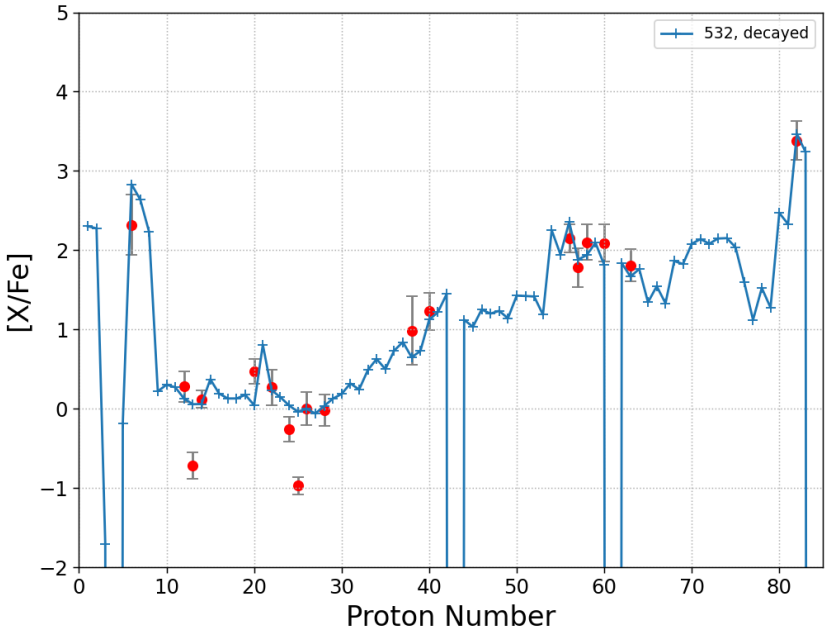

(a) One-zone AGB intershell model compared with the abundances of CS29526-110. The fitting parameters are d = 0.033 at cycle 532 resulting in $\chi^2 = 7.4$.

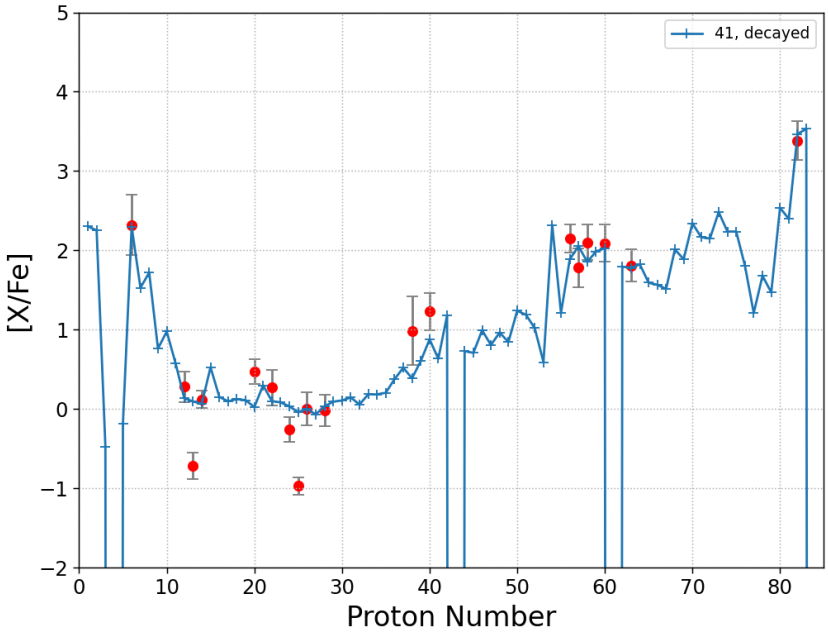

(b) RAWD model compared with the abundances of CS29526-110. The fitting parameters are d = 0.008 at cycle 4100, resulting in $\chi^2 = 17.2$.

Figure 2.4: Best fitting models for CS29526-110. The observations are shown in red with the error bars in grey.

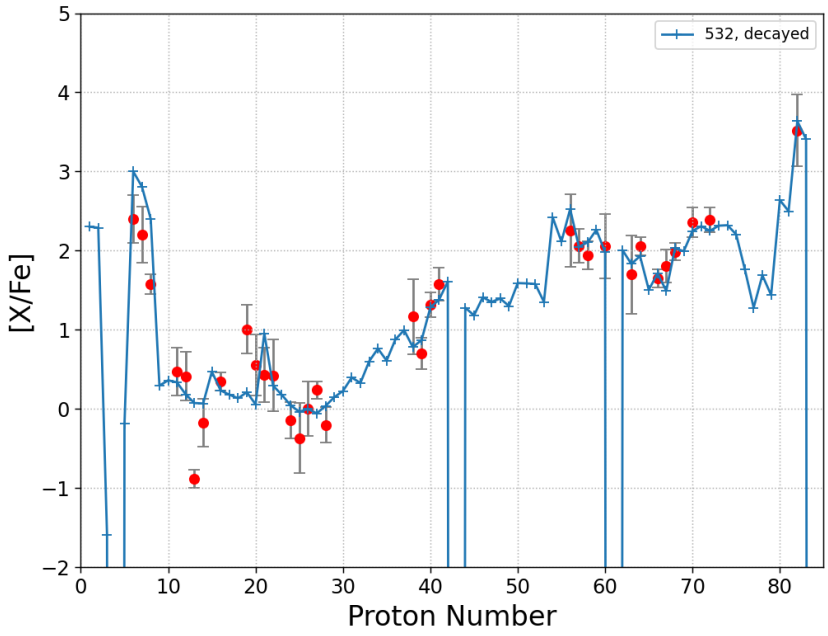

(a) One-zone AGB intershell model compared with the abundances of CS29497-030. The fitting parameters are d = 0.048 at cycle 532 resulting in $\chi^2 = 6.1$.

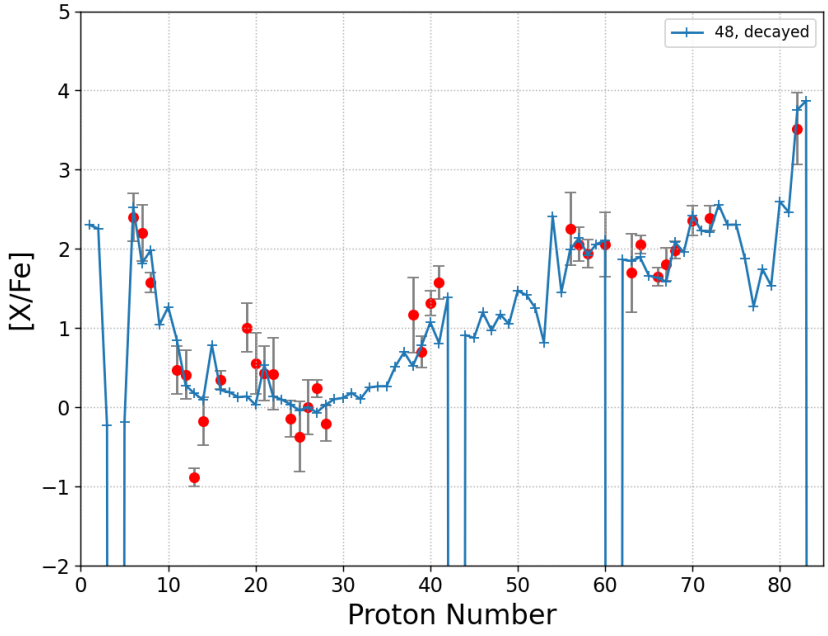

(b) RAWD model compared with the abundances of CS29497-030. The fitting parameters are d = 0.014 at cycle 4800, resulting in $\chi^2 = 22.2$.

Figure 2.5: Best fitting models for CS29497-030. The observations are shown in red with the error bars in grey.

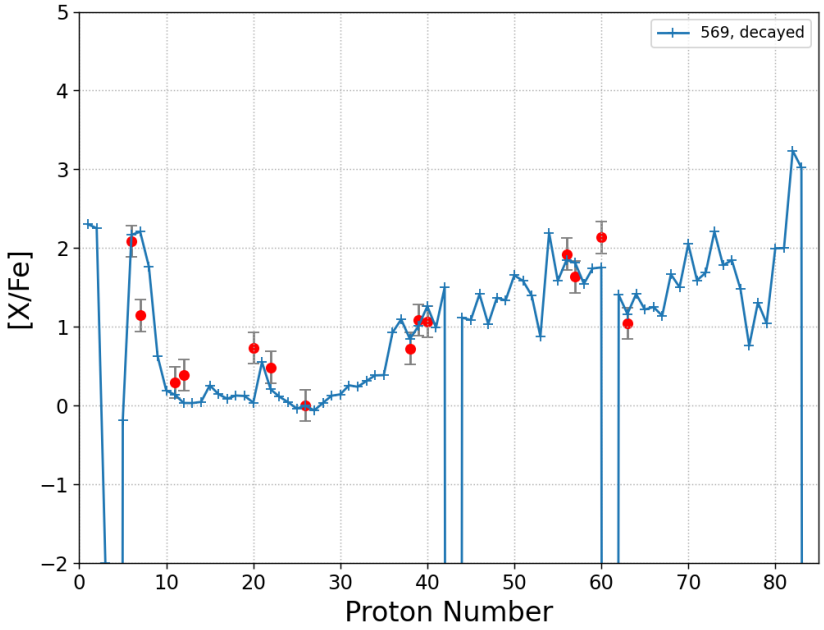

(a) One-zone AGB intershell model compared with the abundances of CS22881-036. The fitting parameters are d = 0.009 at cycle 569 resulting in $\chi^2 = 6.36$. The observations are shown in red with the error bars in grey.

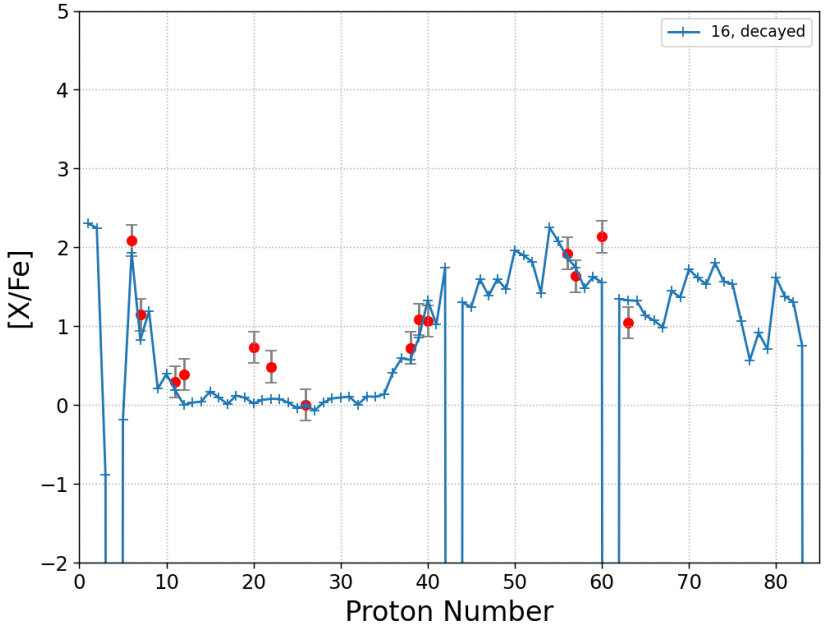

(b) RAWD model compared with the abundances of CS22881-036. The fitting parameters are d = 0.003 at cycle 1600, resulting in $\chi^2 = 14.2$.

Figure 2.6: Best fitting models for CS22881-036. The observations are shown in red with the error bars in grey.

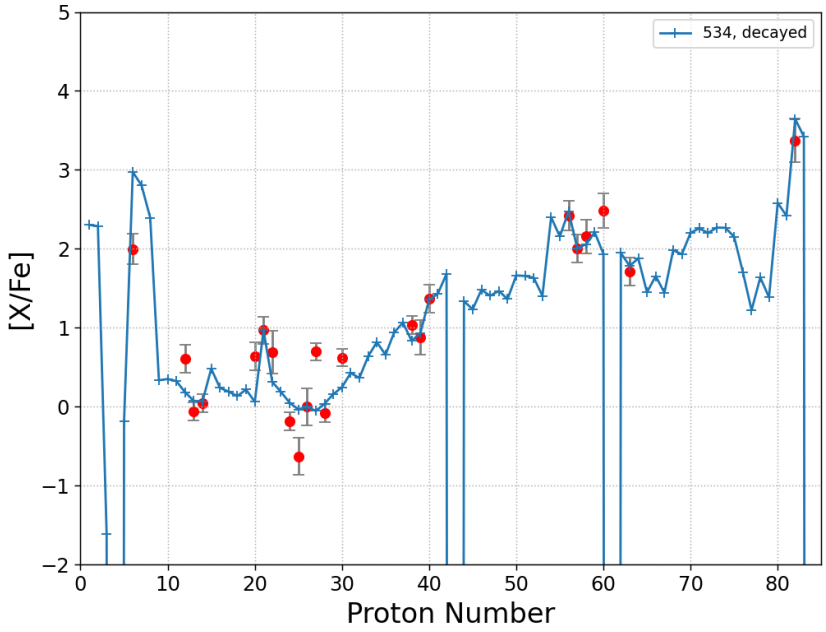

(a) One-zone AGB intershell model compared with the abundances of HE0143-0441. The fitting parameters are d = 0.046 at cycle 534, resulting in $\chi^2 = 7.6$.

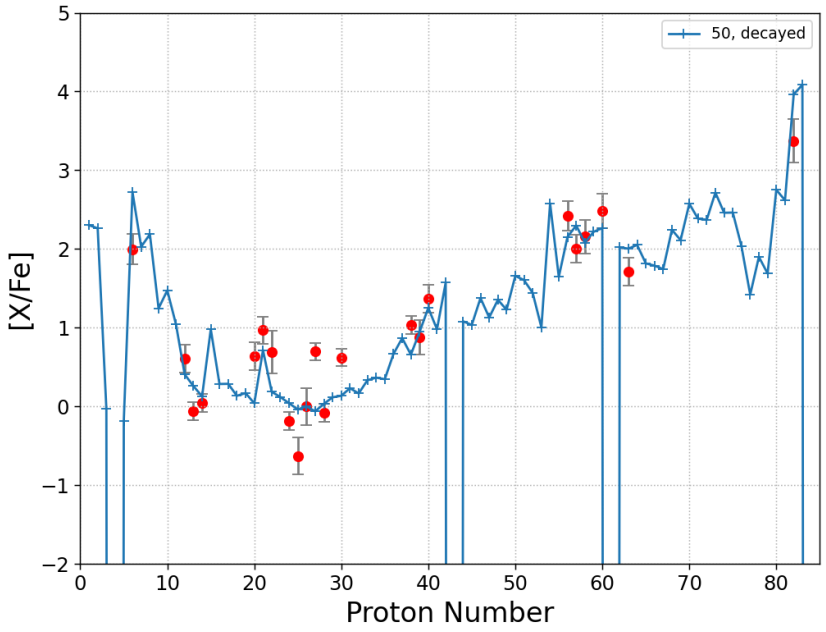

(b) RAWD model compared with the abundances of HE0143-0441. The fitting parameters are d = 0.022 at cycle 5000, resulting in $\chi^2 = 27.7$.

Figure 2.7: Best fitting models for HE0143-0441. The observations are shown in red with the error bars in grey.

but Sm within error bars. The lead is also a better fit, with the RAWD model underproducing it by about 0.2 dex and the one-zone model overproducing by about 0.7 dex.

- **HE2148-1247**: Figure 2.10 shows the fits for HE2148-1247 where both models have large χ^2 values relative to some of the other fits. This is likely due to the fact that this star has a larger number of data points clustered between Ba (Z = 56) and Ho (Z = 67). These elements appear to broadly fit the RAWD model more closely. Zr (Z = 40) also fits the RAWD model much more closely. Lead is overproduced by about 0.4 dex for the one-zone but under-produced by about 0.3 dex for the RAWD model, this shows that lead is not as much of deciding factor for these fits as it has been in other stars (e.g. HD187861, CS29497-030 and LP625-44) but the RAWD model does match a bit more closely.

- **LP625-44**: Figure 2.11 shows the fits for LP625-44. These fits are interesting because the pattern for both of the models is largely similar until we reach Pb, at which point the one-zone model overproduces lead by about 1.2 dex while the RAWD model replicates the abundance closely.

A trend with most of the stars discussed so far (Figures 2.3 to 2.11) is that where lead is present in the abundances, whichever model reproduces the lead abundance more closely is the model with the smallest χ^2. Another commonality between some of these fits is, in stars where the one-zone model fits best, [Pb/hs][1] is higher than in stars where the RAWD model fits best. The average [Pb/hs] for stars where the one-zone model is deemed the best fit is [Pb/hs] = 1.27 ± 0.577, whereas the average [Pb/hs] for stars where the RAWD model fits best is [Pb/hs] = 0.318 ± 0.492.

2.2.2.2 What makes a 'good' fit?

There are several stars in this sample for which deciding which model fits best is more difficult. This is because the χ^2 values are close enough together that either model provides a good

[1][Pb/hs] is the abundance of lead over the heavy s-process peak elements relative to solar. Where [hs/Fe] is as defined in section 1.4.

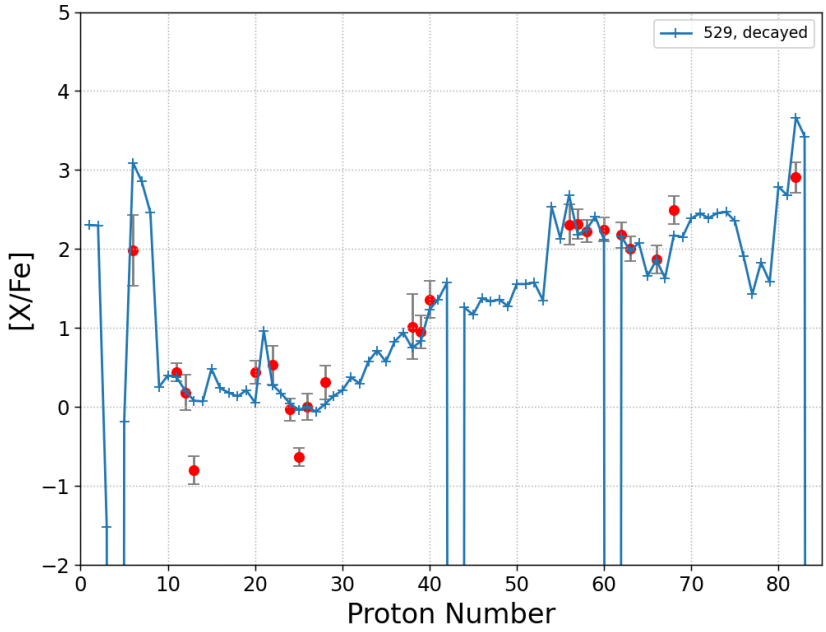

(a) One-zone AGB intershell model compared with the abundances of CS22898-027. The fitting parameters are d = 0.057 at cycle 529, resulting in $\chi^2 = 22.1$.

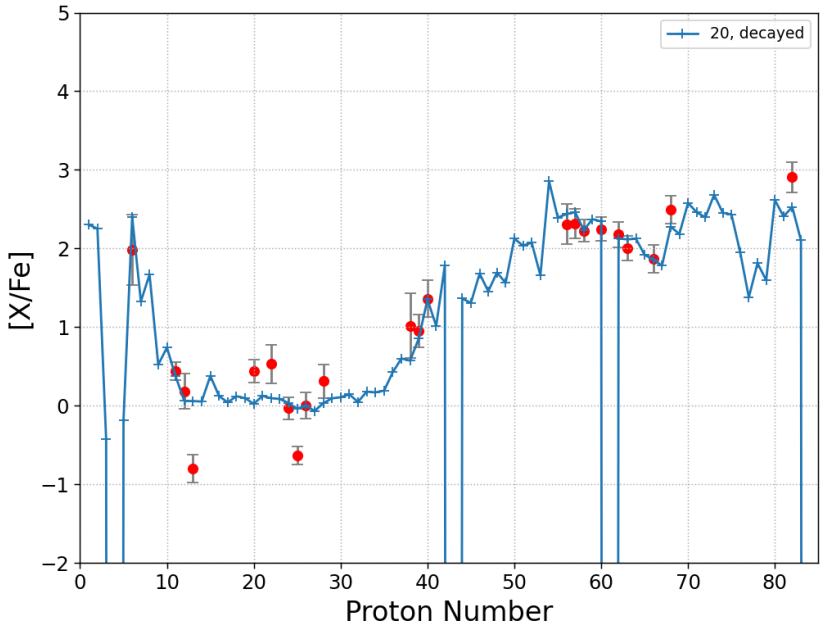

(b) RAWD model compared with the abundances of CS22898-027. The fitting parameters are d = 0.009 at cycle 2000, resulting in $\chi^2 = 8.0$.

Figure 2.8: Best fitting models for CS22898-027. The observations are shown in red with the error bars in grey.

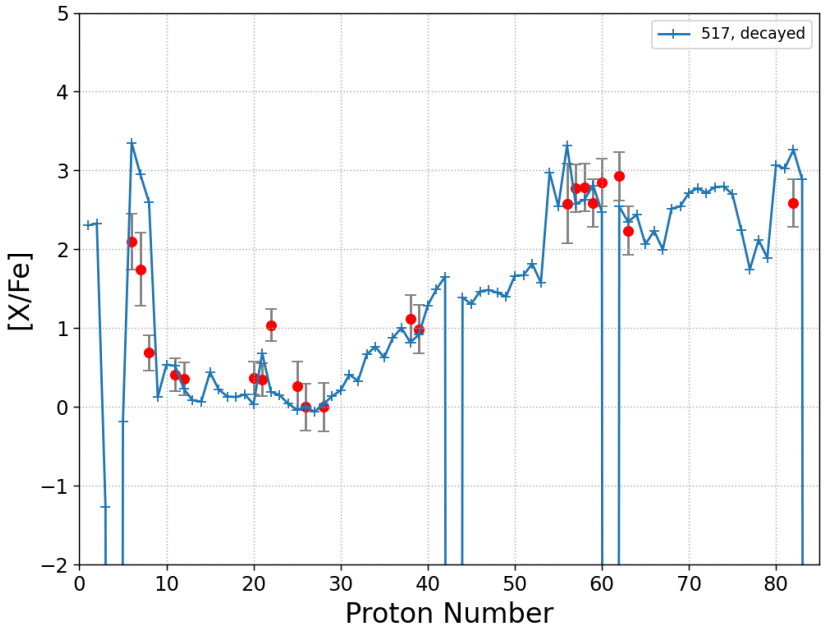

(a) One-zone AGB intershell model compared with the abundances of HR1305+0007. The fitting parameters are d = 0.09 at cycle 517, resulting in $\chi^2 = 25.9$.

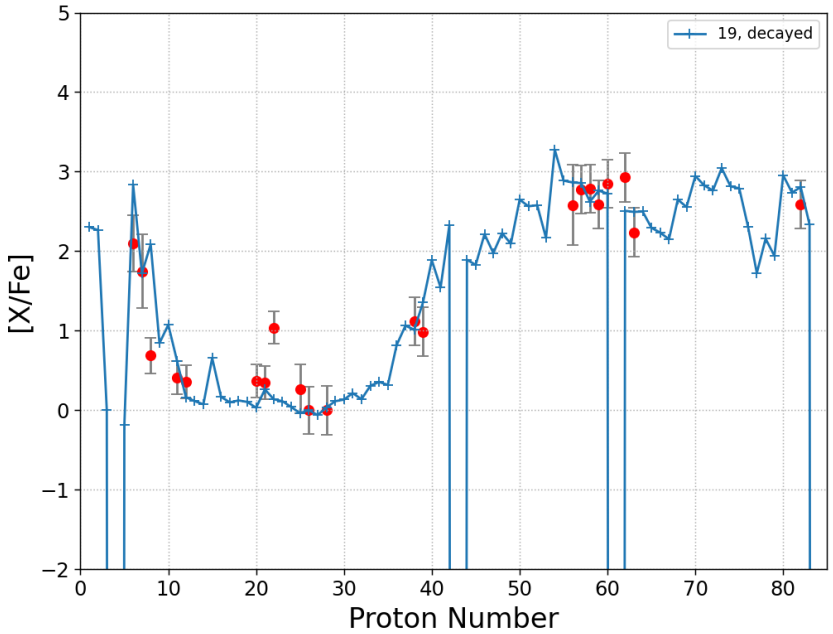

(b) RAWD model compared with the abundances of HE1305+0007. The fitting parameters are d = 0.024 at cycle 1900, resulting in $\chi^2 = 9.53$.

Figure 2.9: Best fitting models for HE1305+0007. The observations are shown in red with the error bars in grey.

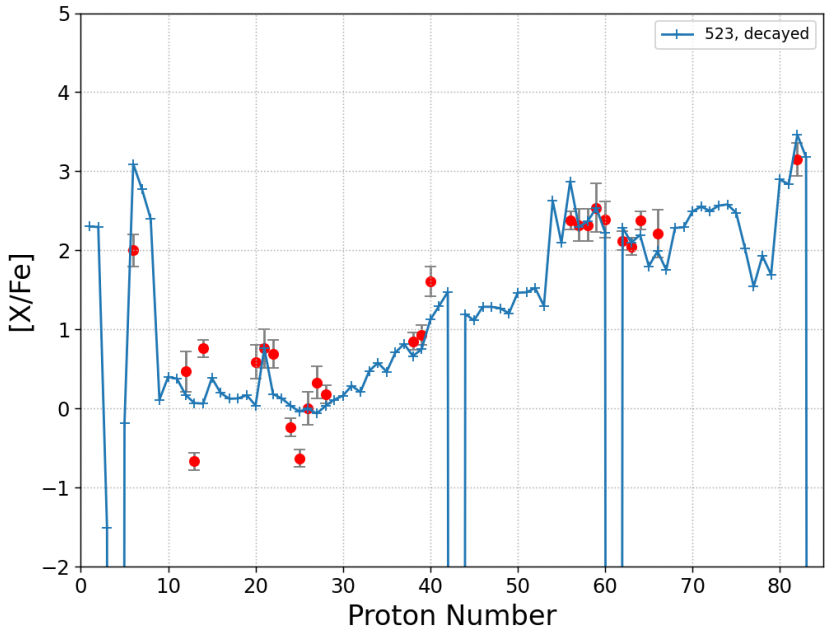

(a) One-zone AGB intershell model compared with the abundances of HE2148-1247 The fitting parameters are d = 0.054 at cycle 523, resulting in $\chi^2 = 56.4$.

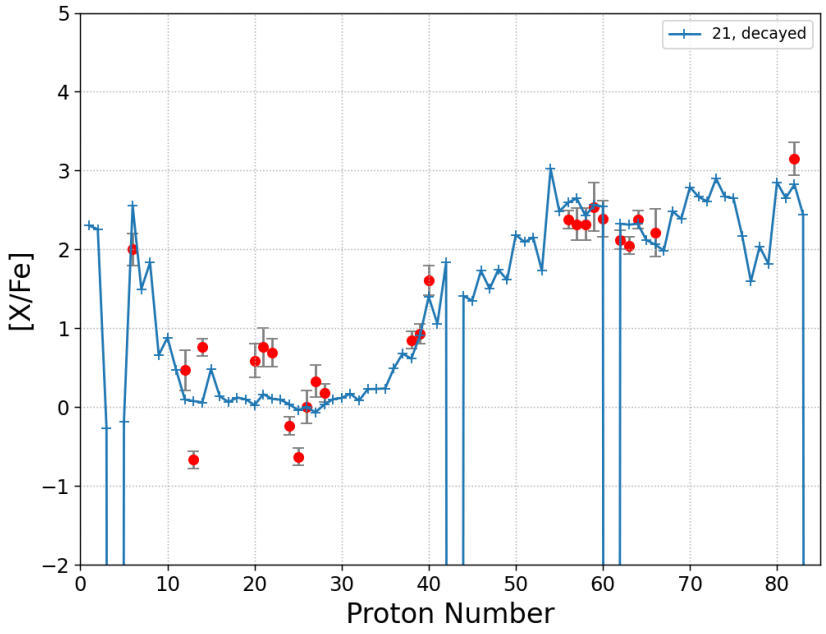

(b) RAWD model compared with the abundances of HE2148-1247. The fitting parameters are d = 0.013 at cycle 2100, resulting in $\chi^2 = 28.2$.

Figure 2.10: Best fitting models HE2148-1247. The observations are shown in red with the error bars in grey.

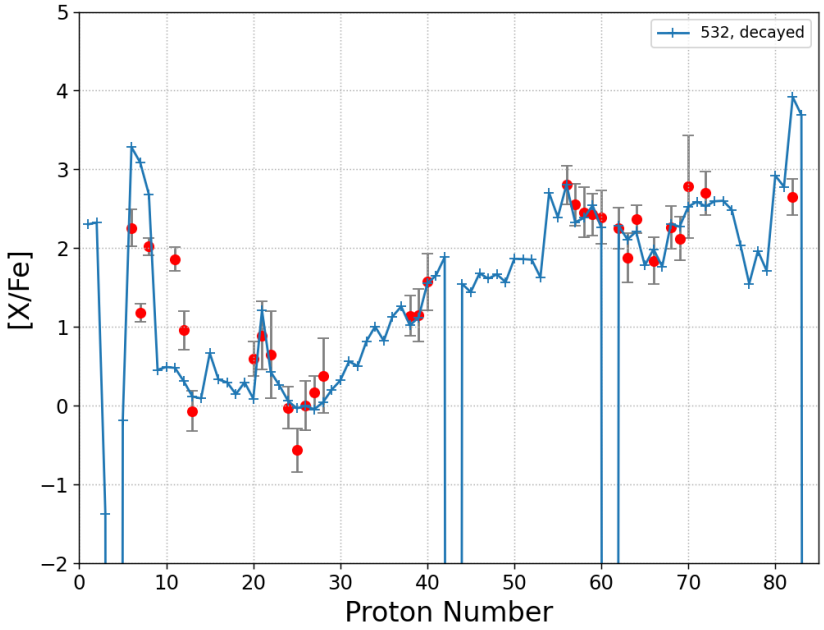

(a) One-zone AGB intershell model compared with the abundances of LP625-44. The fitting parameters are d = 0.088 at cycle 532, resulting in $\chi^2 = 16.6$. The observations are shown in red with the error bars in grey.

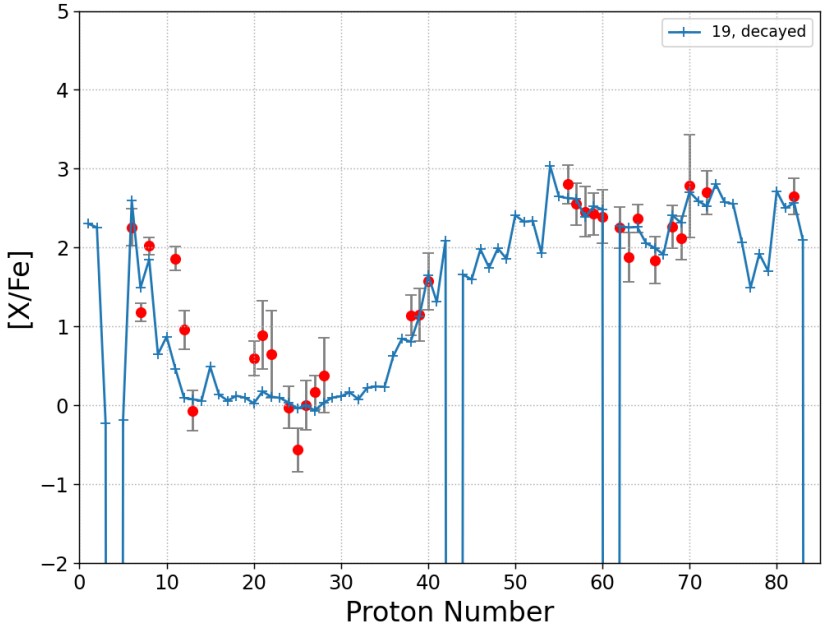

(b) RAWD model compared with the abundances of LP625-44. The fitting parameters are d = 0.014 at cycle 1900, resulting in $\chi^2 = 7.8$.

Figure 2.11: Best fitting models for LP625-44. The observations are shown in red with the error bars in grey.

enough fit to the abundances that it could be considered a likely formation scenario. These stars are HD224959, CS31062-050, CS31062-012, CS22948-027, HE0131-3953, HE0338-3945, HE1105+0027 and HE2258-6358. For a lot of these stars, the pattern for both of the models is largely similar, so saying conclusively which model fits best is not as straightforward as previous cases. The fits can be found in panels a and b of Figures 2.12 to 2.19.

To decide if the smallest χ^2 value really is the best fit we must consider what a constitutes a good fit and when that fit is no longer good. To do this, I use contour plots of χ^2 as a function of dilution factor and cycle number. The contour plots can be found in panels c and d of Figures 2.12 to 2.19. By making these plots we can see what combination of parameters gives us a high χ^2 value. Each region is coloured depending on the χ^2 value that would be found by fitting that set of parameters to the observations, the lighter the region the smaller the χ^2 value, as illustrated by the colour-bar on the side of each of the figures. The purple contour denotes the 'full-width double-minimum' (FWDM). This is the point at which the χ^2 is double its minimum value. The blue cross in the centre of each of the FWDM regions shows the parameters which give the smallest χ^2 value. Where the contour plot has two FWDM regions, an orange circle shows the minimum χ^2 in the second region.

The best χ^2 fits and the contour plots can now be used in combination to determine which model provides the better fit to the abundances. First we will consider the star HD224959, the fits and contour plots for this star can be found in Figure 2.12. From sub-figures 2.12a and 2.12b we can see that it would be difficult to pick out which model fits the best despite the smallest χ^2 value from the RAWD model. When we look at the contour plots for this star, we can see that the full-width double-minimum region is narrower in both cycle number and dilution for the one-zone intershell model. If the region is smaller and narrower this suggests there is a narrower range of parameters that can create a 'good' fit to the abundances. We would expect that if the region is wider then the fits would deteriorate and become much worse much quicker than if the region was narrower. However, the range in cycle number is not directly comparable between the two models because the time between cycles is different. For HD224959, the time encompassed by the FWDM region of the one-zone model (Figure 2.12c) is 0.037 years and the time covered by the FWDM region of the RAWD model is 0.032 years.

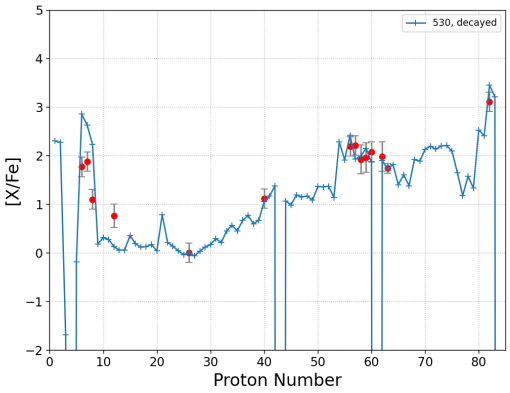

(a) One-zone AGB intershell model compared with the abundances of HD224959. The fitting parameters are d = 0.034 at cycle 530, resulting in $\chi^2 = 7.0$.

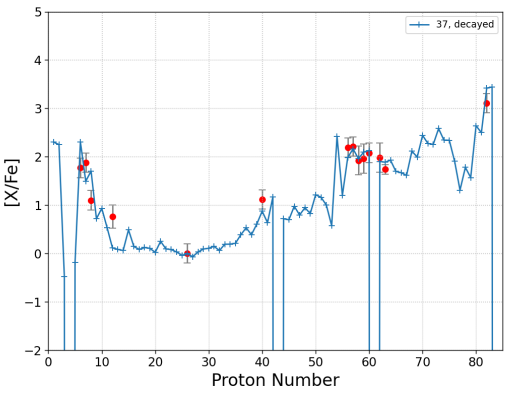

(b) RAWD model compared with the abundances of HD224959. The fitting parameters are d = 0.008 at cycle 3700, resulting in $\chi^2 = 5.0$.

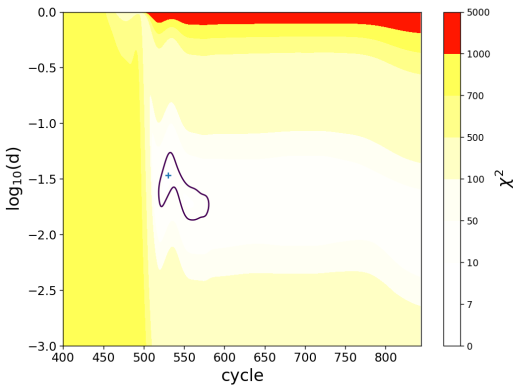

(c) Contour plot showing the variation of χ^2 with dilution factor and cycle number for the one-zone intershell model.

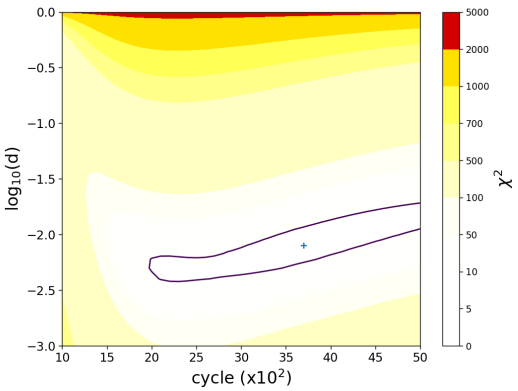

(d) Contour plot showing the variation of χ^2 with dilution factor and cycle number for the RAWD model.

Figure 2.12: Upper panels: Best [X/Fe] fits for each of the models. The observations are shown in red with the error bars in grey. Lower panels: Contour plots of χ^2 for the two models (HD224959). The region enclosed in the purple is the full-width double-minimum and the blue cross is the point of the smallest χ^2.

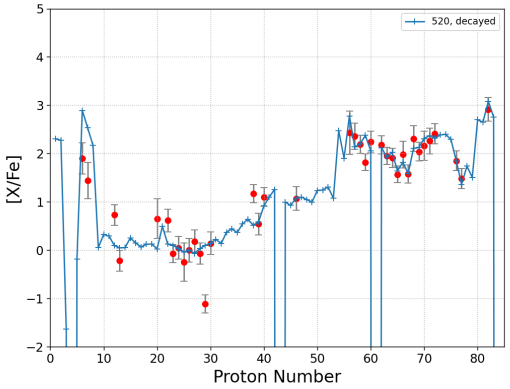

(a) One-zone AGB intershell model compared with the abundances of CS31062-050. The fitting parameters are d = 0.034 at cycle 520, resulting in $\chi^2 = 15.9$.

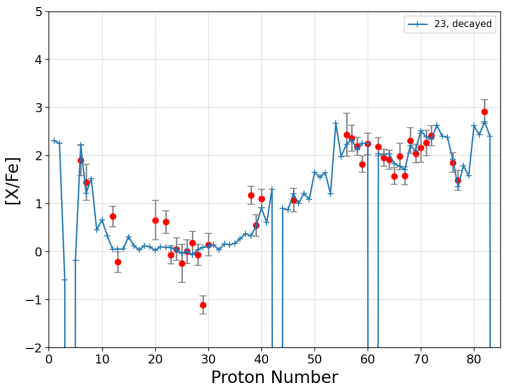

(b) RAWD model compared with the abundances of CS31062-050. The fitting parameters are d = 0.006 at cycle 2300, resulting in $\chi^2 = 20.0$.

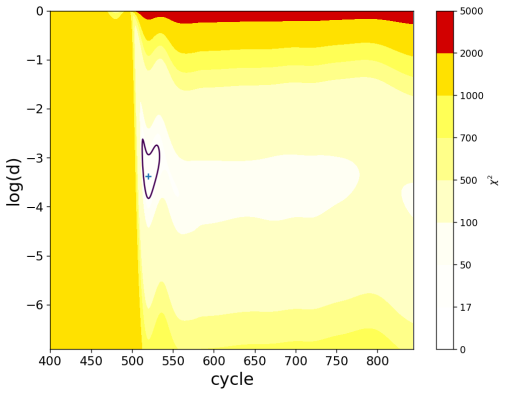

(c) Contour plot showing the variation of χ^2 with dilution factor and cycle number for the one-zone intershell model.

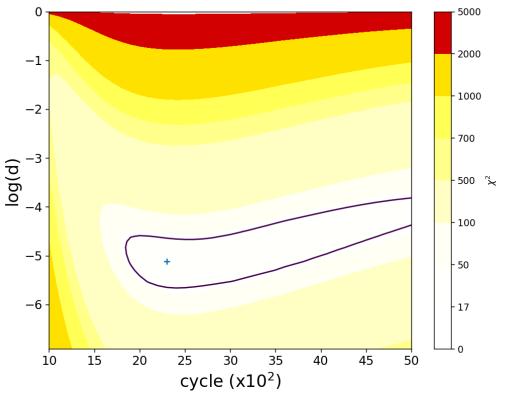

(d) Contour plot showing the variation of χ^2 with dilution factor and cycle number for the RAWD model.

Figure 2.13: Upper panels: Best [X/Fe] fits for each of the models. The observations are shown in red with the error bars in grey. Lower panels: Contour plots of the χ^2 for the two models (CS31062-050). The region enclosed in the purple is the full-width double-minimum and the blue cross is the point of the smallest χ^2.

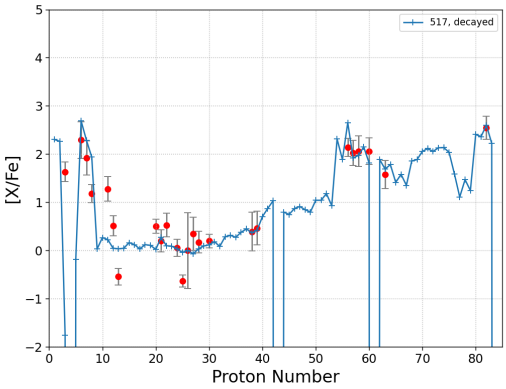

(a) One-zone AGB intershell model compared with the abundances of CS31062-012. The fitting parameters are d = 0.021 at cycle 517, resulting in $\chi^2 = 4.5$.

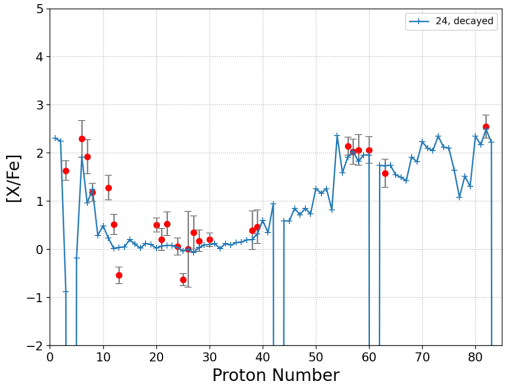

(b) RAWD model compared with the abundances of CS31062-012. The fitting parameters are d = 0.003 at cycle 2400, resulting in $\chi^2 = 3.5$.

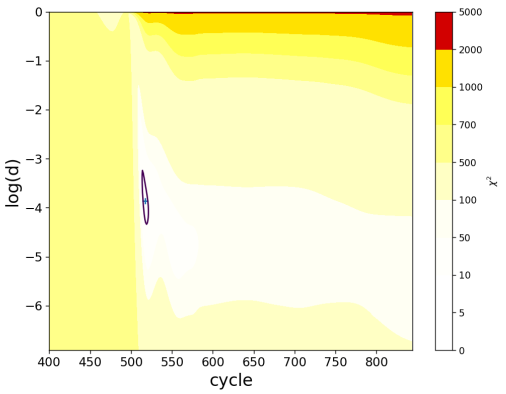

(c) Contour plot showing the variation of χ^2 with dilution factor and cycle number for the one-zone intershell model.

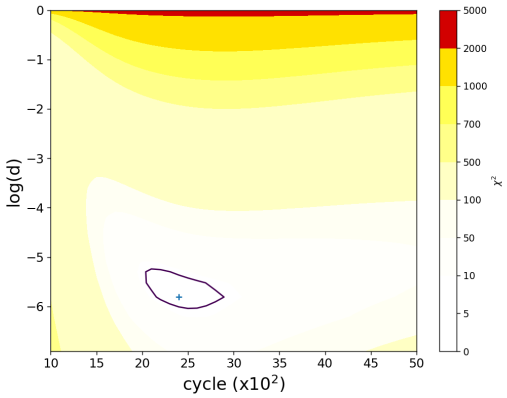

(d) Contour plot showing the variation of χ^2 with dilution factor and cycle number for the RAWD model.

Figure 2.14: Upper panels: Best [X/Fe] fits for each of the models. The observations are shown in red with the error bars in grey. Lower panels: Contour plots of the χ^2 for the two models (CS31062-012). The region enclosed in the purple is the full-width double-minimum and the blue cross is the point of the smallest χ^2.

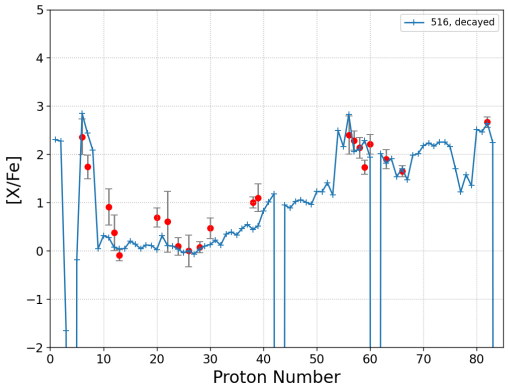

(a) One-zone AGB intershell model compared with the abundances of CS22948-027. The fitting parameters are d = 0.03 at cycle 516, resulting in $\chi^2 = 17.5$.

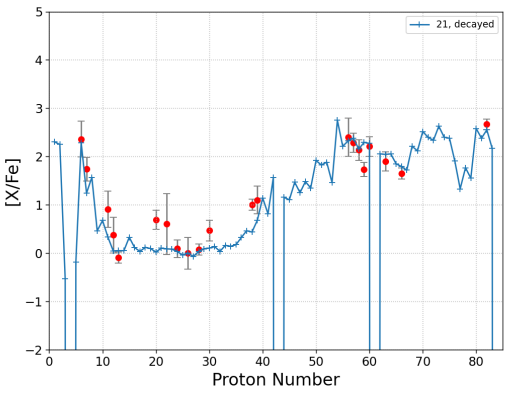

(b) RAWD model compared with the abundances of CS22948-027. The fitting parameters are d = 0.007 at cycle $\chi^2 = 14.8$.

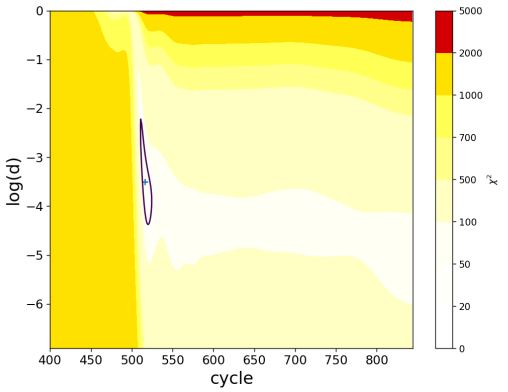

(c) Contour plot showing the variation of χ^2 with dilution factor and cycle number for the one-zone intershell model.

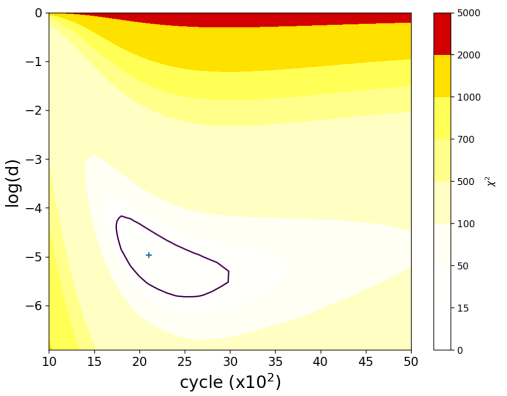

(d) Contour plot showing the variation of χ^2 with dilution factor and cycle number for the RAWD model.

Figure 2.15: Upper panels: Best [X/Fe] fits for each of the models. The observations are shown in red with the error bars in grey. Lower panels: Contour plots for the two models (CS22948-027). The region enclosed in the purple is the full-width double-minimum and the blue cross is the point of the smallest χ^2.

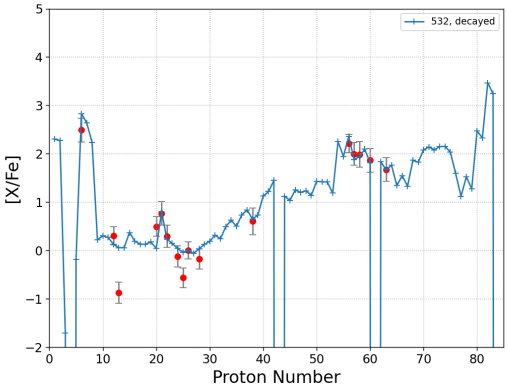

(a) One-zone AGB intershell model compared with the abundances of HE0131-3953. The fitting parameters are d = 0.033 at cycle 532, resulting in $\chi^2 = 0.9759$.

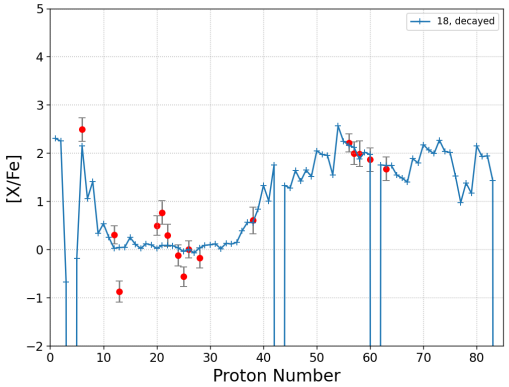

(b) RAWD model compared with the abundances of HE0131-3953. The fitting parameters d = 0.005 at cycle 1800, resulting in $\chi^2 = 0.9761$.

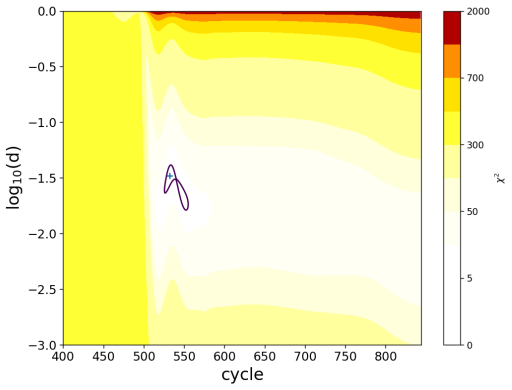

(c) Contour plot showing the variation of χ^2 with dilution factor and cycle number for the one-zone intershell model.

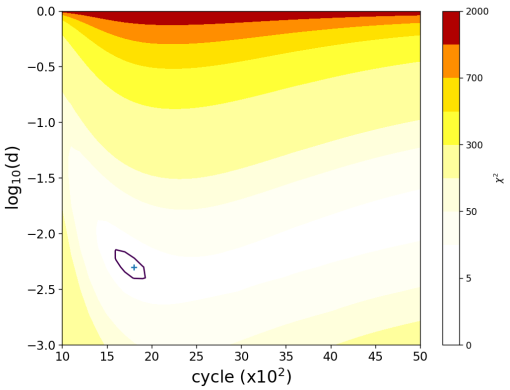

(d) Contour plot showing the variation of χ^2 with dilution factor and cycle number for the RAWD model.

Figure 2.16: Upper panels: Best [X/Fe] fits for each of the models. The observations are shown in red with the error bars in grey. Lower panels: Contour plots of χ^2 for the two models (HE0131-3953). The region enclosed in the purple is the full-width double-minimum and the blue cross is the point of the smallest χ^2.

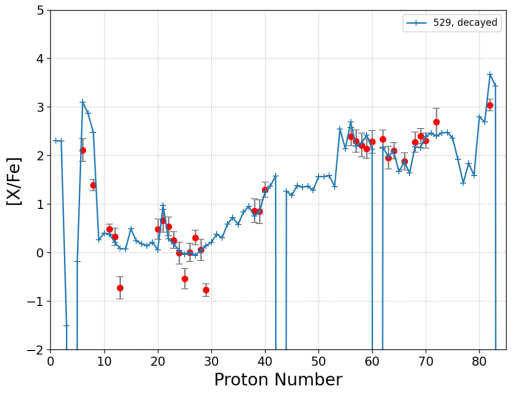

(a) One-zone AGB intershell model compared with the abundances of HE0338-3945. The fitting parameters are d = 0.058 at cycle 539, resulting in $\chi^2 = 16.9$.

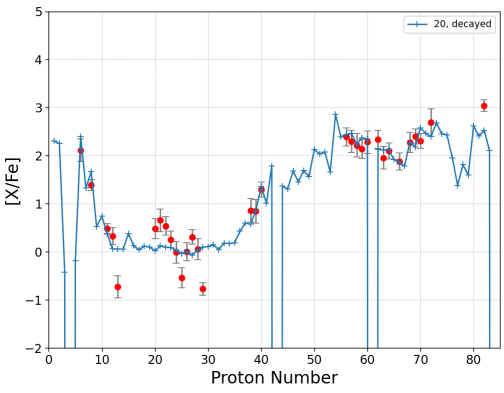

(b) RAWD model compared with the abundances of HE0338-3945. The fitting parameters are d = 0.009 at cycle 2000, resulting in $\chi^2 = 16.6$.

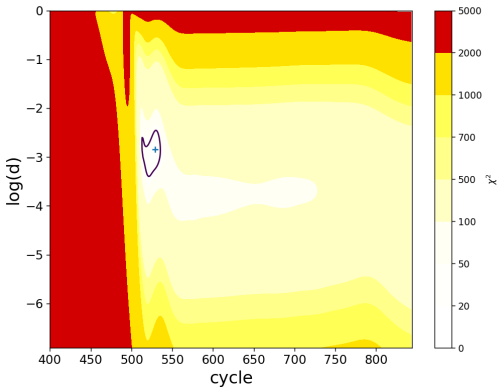

(c) Contour plot showing the variation of χ^2 with dilution factor and cycle number for the one-zone intershell model.

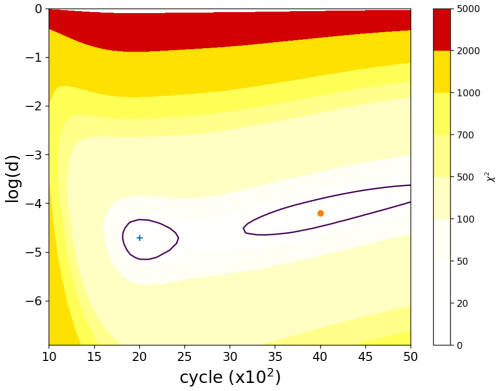

(d) Contour plot showing the variation of χ^2 with dilution factor and cycle number for the RAWD model.

Figure 2.17: Upper panels: Best [X/Fe] fits for each of the models. The observations are shown in red with the error bars in grey. Lower panels: Contour plots of χ^2 for the two models (HE0338-3945). The region enclosed in the purple is the full-width double-minimum, the blue cross is the point of the smallest χ^2 and the orange circle is the point of the smallest χ^2 in the second region.

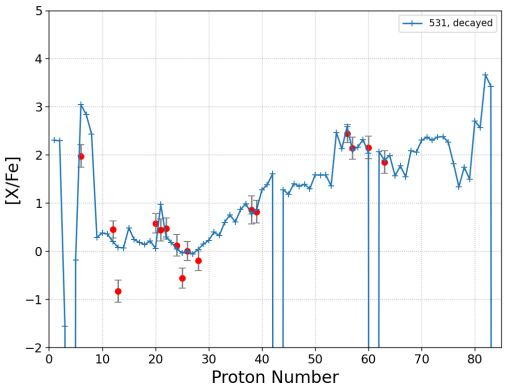

(a) One-zone AGB intershell model compared with the abundances of HE1105+0027. The fitting parameters are d = 0.052 at cycle 531, resulting in $\chi^2 = 0.92$.

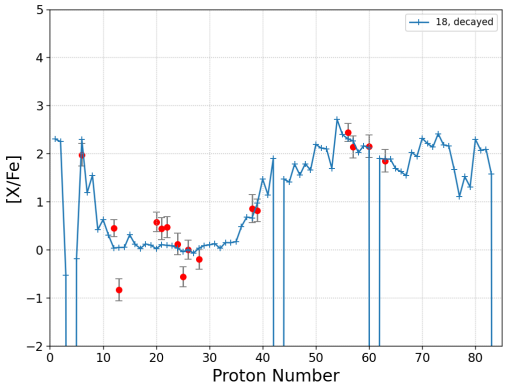

(b) RAWD model compared with the abundances of HE1105+0027. The fitting parameters are d = 0.007 at cycle 1800, resulting in $\chi^2 = 2.13$.

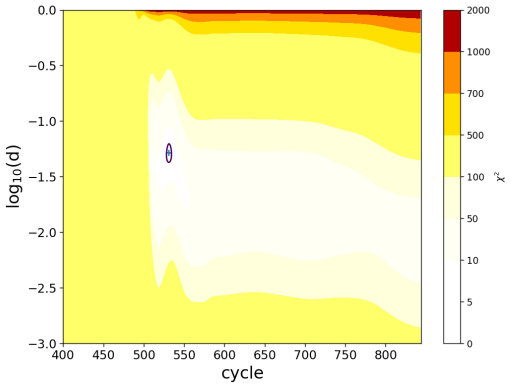

(c) Contour plot showing the variation of χ^2 with dilution factor and cycle number for the one-zone intershell model.

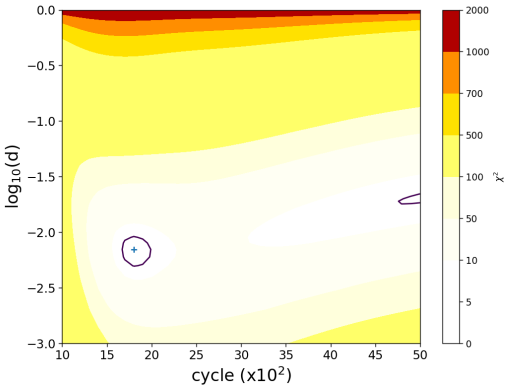

(d) Contour plot showing the variation of χ^2 with dilution factor and cycle number for the RAWD model.

Figure 2.18: Upper panels: Best [X/Fe] fits for each of the models. The observations are shown in red with the error bars in grey. Lower panels: Contour plots of χ^2 for the two models (HE1105+0027). The region enclosed in the purple is the full-width double-minimum and the blue cross is the point of the smallest χ^2.

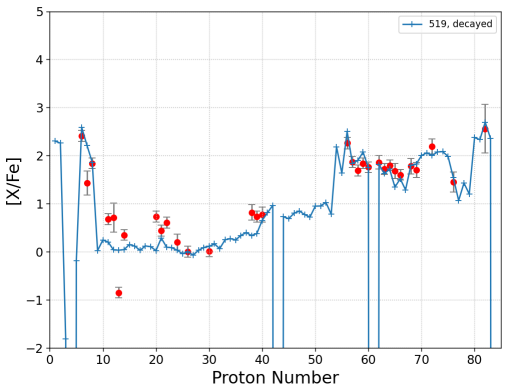

(a) One-zone AGB intershell model compared with the abundances of HE2258-6358. The fitting parameters are d = 0.017 at cycle 519, resulting in $\chi^2 = 49.3$.

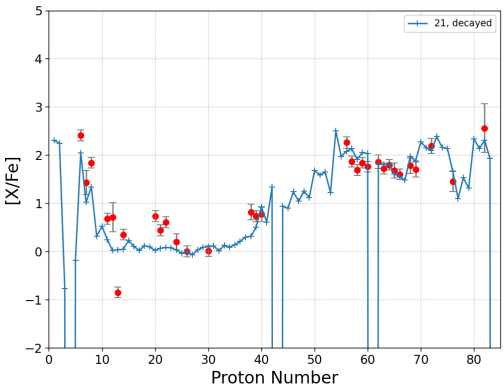

(b) RAWD model compared with the abundances of HE2258-6358. The fitting parameters are d = 0.004 at cycle 2100, resulting in $\chi^2 = 53.6$.

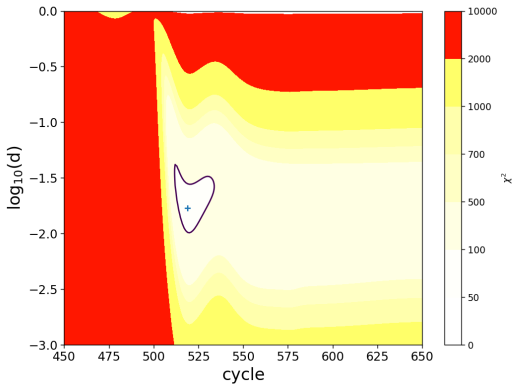

(c) Contour plot showing the variation of χ^2 with dilution factor and cycle number for the one-zone intershell model.

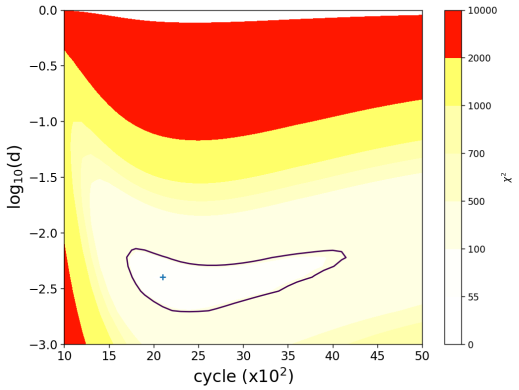

(d) Contour plot showing the variation of χ^2 with dilution factor and cycle number for the RAWD model.

Figure 2.19: Upper panels: Best [X/Fe] fits for each of the models. The observations are shown in red with the error bars in grey. Lower panels: Contour plots of χ^2 for the two models (HE2258-6358). The region enclosed in the purple is the full-width double-minimum and the blue cross is the point of the smallest χ^2.

These times are similar which makes sense given the two models are performing the same nucleosynthesis in comparable conditions. This effect is the same for the other contour plots in this section, where even though the range in time (cycle) looks significantly larger for the RAWD compared to the one-zone, the two are largely comparable. However, for HD224959 the range in dilution factors is smaller for the one-zone model. For this reason, the one-zone model may generally provide a better fit than the RAWD model. Of the remaining contour plots one more (CS31062-050) follows the same trend as HD224959 with the FWDM region being narrower in its range of dilution factors. Four have a smaller range of dilution factors in the RAWD model than the one-zone model, these stars are: CS31062-012, CS22948-027, HE0131-3953, HE2258-6358. We see double FWDM regions in Figures 2.17d and 2.18d (HE0338-3945 and HE1105+0027) for the RAWD model only, suggesting that there are two points in the RAWD evolution at which the abundances match the observations. Therefore, these stars will be attributed to the one-zone AGB intershell model for this work, as the variation in the FWDM regions is much less.

The eight stars discussed in this section could feasibly be attributed to either model. However, for the purposes of this work I will attribute each to the scenario for which the range in dilution factor was narrowest.

Overall, this means of the sample of 17 CEMP-i stars, I have attributed the heavy element abundances of 8 to an i-RAWD triple system and 9 to have come from a PIE in an AGB intershell. However, 4 of the stars attributed to the RAWD model and 4 attributed to the one-zone model are more uncertain due to the FWDM regions of the contour plots being so similar between the two models.

Something that each of the stars had in common is that the dilution factors for the RAWD model best fit are around a factor of 10 of more lower than the dilution factors for the one-zone intershell model. A lower dilution factor means that the material in the best fit abundances has been diluted with more solar scaled material. A lower dilution factor for the RAWD model is to be expected because it is a multi-zone model so more mixing occurs throughout the evolution of the model. More mixing means more processing of the material and therefore higher i-process abundances in general, leading to more dilution required in order to replicate

the observed abundances in comparison to a one-zone model.

As stated in section 2.2.2.1 above, there are some notable trends with the abundance fitting in this section. Firstly, whichever model fits the [Pb/Fe] abundance the closest, is the model that fits the abundances best overall. Secondly, the [Pb/hs] abundance is higher on average for the stars where the one-zone intershell model fits best compared to the RAWD model.

2.2.2.3 Comparison to other work

There are 14 stars in the set of CEMP-r/s stars in Choplin, Siess & Goriely (2021). Of these 14, there are 7 in common with my sample. These stars are CS22948-027, CS29497-030, CS31062-050, HD187861, HD224959, HE0338-3945 and HE2148-1247. The abundance data for these stars has come from either the SAGA database or Karinkuzhi et al. (2021). See section 2.2.2.4 for a discussion of the abundances found by Karinkuzhi et al. (2021) for HD187861 and HD224959, which are also the abundances used by Choplin, Siess & Goriely (2021). Choplin, Siess & Goriely (2021) uses a $1M_{\odot}$ AGB model and dilutes it with interstellar material for which the dilution factor ,f, is freely varied to find a best χ^2 fit, in similar fashion to the methods described in the present work. Given that Choplin, Siess & Goriely (2021) uses a different mass model and a reduced χ^2 (which I do not use for reasons outlined in section 2.2.1), the properties of their fits and mine are not directly comparable. However, the shape of the fits can be compared. Here, I will be comparing the one-zone intershell AGB model fits to the Choplin, Siess & Goriely (2021) (C21) fits (their figure A.1) because this model is more similar to their model than the RAWD model.

- **CS22948-027**: This object was one for which either model produced a good fit to the abundances. My one-zone model gives a much closer fit to the lead abundance than the C21 fit, which over produces the lead by around 1 dex. Everything else in both models is reproduced within error bars, except the Pr (Z = 59) which is overproduced in both the one-zone model and the model of C21.

- **CS29497-030**: Here, C21 includes some upper limit abundances that are not included in my sample. For the one-zone model in my work all elements are reproduced within error bars with the exception of Ho (Z = 67) which is slightly underproduced by the

model. In the case of C21, not all the elements where we have a definite abundance and not just an upper limit are reproduced within error bars. The Y is overproduced and Ba is underproduced. We can also see that again the lead abundance is better reproduced by the one-zone model, with the model of C21 underproducing Pb.

- **CS31062-050**: The shape of the two fits are largely similar for this object. We can see again that the lead fit is much better in the case of the one-zone model, with C21 overproducing the lead abundance. Though the shape of the fit around the light-s peak is similar, the better fit to Y, Zr and Pd comes from the one-zone model, with C21 overproducing the abundances for each of these elements.

- **HD187861 and HD224959**: The overall fit to HD187861 appears to be better for the one-zone model of this work than for the model of C21 due to the closer fit of the Pb, Y and Zr abundance. The better fit to HD224959 also appears to be with the one-zone model due to the closer fit to the lead abundance. A full comparison of the one-zone fit vs the C21 fits for these stars will be discussed in section 2.2.2.4.

- **HE0338-3945**: The shape of the fits here are largely similar, with both models overproducing the lead abundance. The fit to the light-s elements is closer with my one-zone model while the fit to all other elements seems to reproduce the abundance within error bars for both models.

- **HE2148-1247**: The lead in both of these fits is similar, with both models only just fitting the abundance within error bars. Here, the model of C21 matches the abundances of Zr and Ba slightly better than the one-zone model of my work which underproduces the Zr abundance but overproduces the Ba.

Overall, the two models appear to provide similar fits in terms of fit to the abundances. Of the seven objects discussed above, six of those are better fit by the one-zone intershell model in this work. However given most of the abundances are still reproduced within error bars for both models we cannot firmly say that this model provides a better fit to CEMP-i stars compared to the model of C21. Though some individual elements are clearly a better fit to one model than the other, it appears to hold that whichever model provides the closest fit to

the lead abundances also seems to provide the best fit to the rest of the elements. The reason that the one-zone model presented in this work may provide a closer fit to the lead than the work of Choplin, Siess & Goriely (2021) is because mixing isn't considered in a one-zone model. This will allow abundances to be built-up towards heavier nuclei. Whereas, when mixing is considered and nucleosynthesis is done across the whole of the evolution (as is the case for the C21 model), the neutron to seed ratio will decrease and it will be more difficult to produce a high lead abundance. From this, we can say that a one-zone model can do a reasonable job of reproducing i-process abundances and shows how difficult it is to produce a detailed AGB model that can replicate observations as well as a one-zone model can. In order to have a more detailed AGB model match the observations more closely, we would need a way to increase the number of neutrons in the system e.g. increasing the temperature or the ^{13}C abundance.

I can also compare my fits, to those of Hampel et al. (2016, 2019) in order to compare my one-zone model with theirs. In this case, it is more straightforward to compare the modelled fits from these works to those of the present work because the stellar abundances are from the same sample. Also included in the modelled fits of Hampel et al. (2016, 2019) are neutron densities and exposures of the best fitting models. This means that here I am able to compare the physical properties of the two models. Table 2.4 shows the neutron density, exposure, dilution and chi squared for each of the stars in this work and the work of Hampel et al. (2016, 2019). Only three stars have a lower χ^2 in this work compared to Hampel et al. (2016, 2019). However, 9 of the 17 stars have a χ^2 within 5 of the value found in Hampel et al. (2016, 2019) (H16 and H19) which is the metric I have used previously to decide if we can definitely say one model fits better than another. The 8 stars in this sample that have notably different physical properties between the two models are: HD224959, CS22948-027, CS22898-027, HE0338-3945, HE1305+0007, HE2148-1247, HE2258-6358 and LP625-44. For each of these stars the model which reproduces the lead abundance more closely is the model with the largest exposure. This is not surprising given that we know that lead abundance is exposure dependent (Hampel et al., 2019). There are no stars for which one model significantly over or underproduces an abundance while another does not but there are some for which one

Star	Dilution Factor This Work	Dilution Factor (1-d) H16, H19	Neutron Density (cm^{-3}) This Work	Neutron Density (log(n) cm^{-3}) H16, H19	Exposure ($mbarn^{-1}$) This Work	Exposure ($mbarn^{-1}$) H16, H19	χ^2 value This Work	χ^2 value H16, H19
HD187861	0.013	0.004 (H19)	2.51×10^{12}	10^{11}	11.2	2.5	1.7	2.2
HD224959	0.034	0.008 (H19)	2.32×10^{14}	10^{13}	6.47	3.0	7.0	1.1
CS31062-050	0.034	0.003 (H19)	3.61×10^{14}	10^{14}	4.18	3.4	15.9	11.9
CS31062-012	0.021	0.001 (H19)	3.90×10^{14}	10^{14}	3.55	3.0	4.5	1.3
CS29526-110	0.033	0.007 (H19)	2.07×10^{14}	10^{13}	6.93	3.4	7.4	3.9
CS29497-030	0.048	0.002 (H19)	2.07×10^{14}	10^{14}	6.93	23.2	6.1	8.7
CS22948-027	0.03	0.004 (H19)	3.97×10^{14}	10^{13}	3.35	2.0	17.5	10.8
CS22898-027	0.057	0.007 (H19)	2.44×10^{14}	10^{13}	6.24	2.4	22.1	2.1
CS22881-036	0.009	0.015 (H16)	1.15×10^{12}	10^{12} (H16)	11.2	N/A	6.36	5.08 (H16)
HE0131-3953	0.033	0.031 (H16)	2.07×10^{14}	10^{14} (H16)	6.93	N/A	0.976	0.41 (H16)
HE0143-0441	0.046	0.008 (H19)	1.83×10^{14}	10^{12}	7.38	2.7	7.6	5.9
HE0338-3945	0.058	0.005 (H19)	2.44×10^{14}	10^{13}	6.24	2.4	16.9	10.5
HE1105+0027	0.052	0.047 (H16)	2.19×10^{14}	10^{14} (H16)	6.70	N/A	0.92	1.17 (H16)
HE1305+0007	0.09	0.020 (H19)	3.90×10^{14}	10^{14}	3.55	2.4	25.9	6.6
HE2148-1247	0.054	0.007 (H19)	3.23×10^{14}	10^{13}	4.85	2.4	56.4	6.2
HE2258-6358	0.017	0.002 (H19)	3.72×10^{14}	10^{15}	3.96	7.7	49.3	28.8
LP625-44	0.088	0.003 (H19)	2.07×10^{14}	10^{13}	6.93	2.0	16.6	4.2

Table 2.4: Summary of the best fit properties of stars in the CEMP-i sample, for the one-zone model compared to the best fit properties of Hampel et al. (2016, 2019) for the same group of stars.

model does reproduce some key elements better than the other. For example, H19 reproduces the Sr, Y and Ba abundance of CS22948-027 more closely than the one-zone model of the present work, HE2148-1247's Ba and Zr is better replicated by H19 but the Ba abundance of LP625-44 is better matched by my model. There are also some objects, such as: HD187861 and CS29497-030, for which the χ^2 value is similar but the exposure associated to the two models is very different. For these two objects, the neutron densities found are similar between this work and H19. This suggests that the two fits have similar abundances but the different exposures mean that the two fits come from different points in the evolution of the two models. All of this goes to show that whether a set of abundances can be reproduced or not is extremely model dependent. The model of Hampel et al. (2019) uses a one-dimensional, single-zone nuclear reaction network with constant neutron density to model the intershell of a low-mass, low metallicity AGB star, while my model varies the neutron density throughout the evolution of the model. Both models seem to provide good fits to the sample, with some abundances being replicated more closely by one model than another. However, neither model stands out as being significantly better or worse than the other. This can help to give us an idea of the uncertainties associated to performing abundance fits like this.

2.2.2.4 Karinkuzhi et al 2021: HD224959 and HD187861

In this section, I will find the best fits to two of the stars in the sample of Karinkuzhi et al. (2021) which also appear in my sample. These stars are HD187861 and HD224959. However, the abundances given in Karinkuzhi et al. (2021) have been calculated differently to the abundances in my sample. Being able to see how fits to the same star but using two different sets of abundances compare to one another allows us to see how robust the abundance fitting is when the set of abundances for the same star is changed. This allows me to see how much variation in abundance measurements for the same object affects the prediction.

HD187861 and HD224959 appear in both my sample and in the sample of Karinkuzhi et al. (2021) and have been classified as CEMP-r/s (CEMP-i) in both cases. However, the spectra of these stars were re-analysed and the abundances re-calculated by Karinkuzhi et al. (2021) as part of an attempt to find a more robust CEMP classification system using a wider

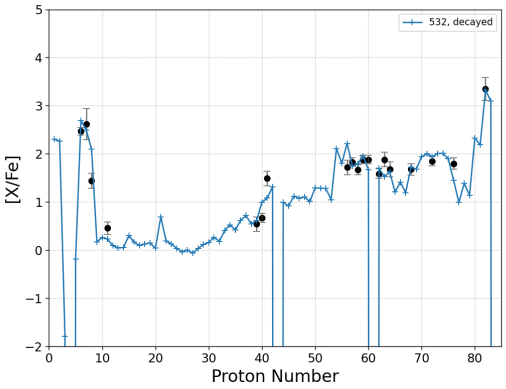

(a) One-zone AGB intershell model compared with the abundances of HD187861 of Karinkuzhi et al. (2021). The fitting parameters are d = 0.024 at cycle 532, resulting in $\chi^2 = 47.9$.

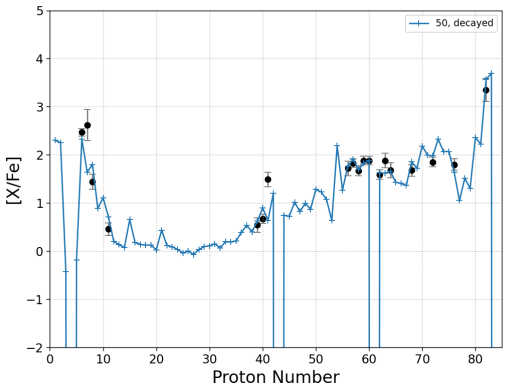

(b) RAWD model compared with the abundances of HD187861 Karinkuzhi et al. (2021). The fitting parameters are d = 0.009 at cycle 5000, resulting in $\chi^2 = 44.0$.

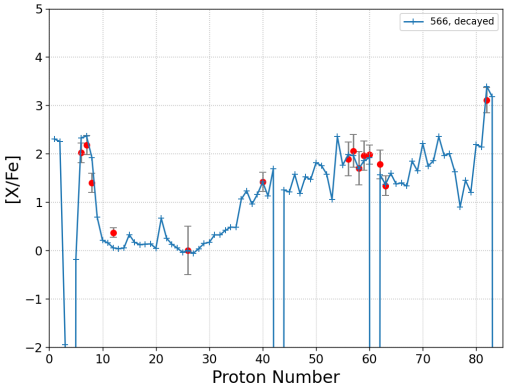

(c) Same as Figure 2.3a. The fitting parameters are d = 0.013 at cycle 566, resulting in $\chi^2 = 1.7$.

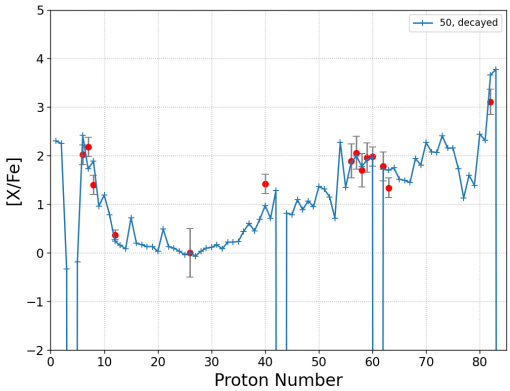

(d) Same as Figure 2.3b. The fitting parameters are d = 0.011 at cycle 5000, resulting in $\chi^2 = 9.4$.

Figure 2.20: The upper panels a and b show abundances for HD187861 from Karinkuzhi et al. (2021) and the best fitting one-zone intershell and RAWD model for these abundances, the NLTE values for strontium and lead are used where applicable. The observations are shown in black with the error bars in grey. The lower two panels c and d show the abundances from the original CEMP-i sample and the best fit for each of the two models. The observations are shown in red with the error bars in grey.

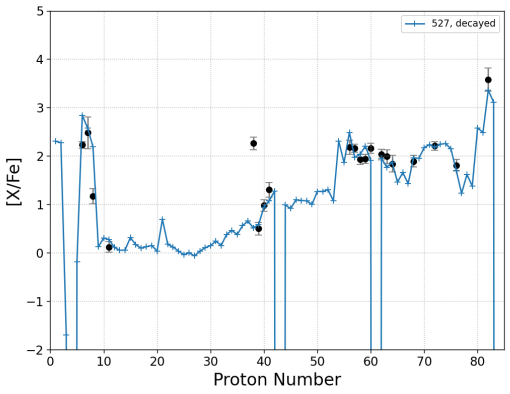

(a) One-zone AGB intershell model compared with the abundances of HD224959 of Karinkuzhi et al. (2021). The fitting parameters are d = 0.032 at cycle 527, resulting in $\chi^2 = 26.9$.

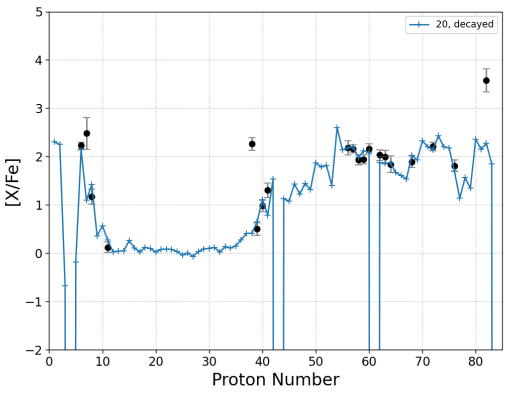

(b) RAWD model compared with the abundances of HD224959 of Karinkuzhi et al. (2021). The fitting parameters are d = 0.005 at cycle 2000, resulting in $\chi^2 = 22.9$.

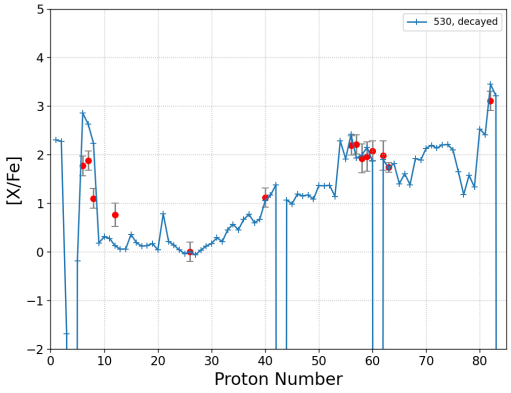

(c) Same as Figure 2.12a. The fitting parameters are d = 0.034 at cycle 530, resulting in $\chi^2 = 7.0$.

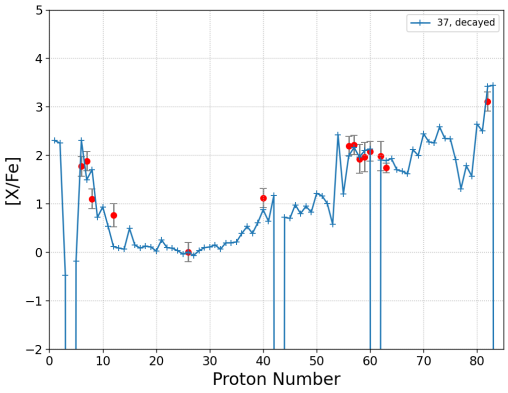

(d) Same as Figure 2.12b. The fitting parameters are d = 0.008 at cycle 3700, resulting in $\chi^2 = 5.0$.

Figure 2.21: The upper panels a and b show the abundances for HD224959 from Karinkuzhi et al. (2021) and the best fitting one-zone intershell and RAWD model for these abundances, the NLTE values for strontium and lead are used where applicable. The observations are shown in black with the error bars in grey. The lower two panels c and d show the abundances from the original CEMP-i sample and the best fit for each of the two models. The observations are shown in red with the error bars in grey.

range of elements. The abundance data of the original sample (the sample of 17 CEMP-i stars outlined at the start of section 2.2.2) for HD187861 and HD224959 contains 14 elements for each data-set, whereas the data of Karinkuzhi et al. (2021) contains 19 and 20 elements respectively. Therefore, the χ^2 value for both models is naturally going to be larger. The error bars on associated with the Karinkuzhi et al. (2021) abundance data are around at least 0.5 dex smaller than the error bars on the original set of abundances. A smaller error bar will also increase the χ^2 value of the Karinkuzhi et al. (2021) abundances. This means the χ^2 values for the abundances of Karinkuzhi et al. (2021) and of the original sample cannot be directly compared. However, we can compare both the shape of each of the fits for both models and the physical properties of the best fit models.

For HD187861 (Figure 2.20), the one-zone AGB intershell model gives a χ^2 value of 47.9 at cycle 532 ($n = 2.07\times10^{14}$ cm^{-3}), $\tau = 6.93$ mbarn^{-1} and d = 0.024. The RAWD fit gives $\chi^2 = 44.0$ at cycle 5000 and d = 0.011. The abundances of Karinkuzhi et al. (2021) have high Nb (Z = 41) that cannot be replicated by either model and which is not present in the abundances in my sample. Nb is produced via decay of ^{93}Zr, therefore the model cannot be producing enough ^{93}Zr to be able to decay and reproduce the Nb abundance. The one-zone AGB intershell model overproduces the Ba (Z = 56) abundance and underproduces the Os (Z = 76) abundance, whereas Ba is matched well in the original fit while Os isn't included in the abundances. The RAWD model overproduces Pb compared to the Karinkuzhi et al. (2021) abundance, which is also true for the RAWD model fit for the original set of abundances, though the two lead measurements are different. The properties of the best one-zone fit for the original set of abundances were: cycle 566 ($n = 2.51\times10^{12}$ cm^{-3}), $\tau = 11.2$ mbarn^{-1}, d = 0.013 and $\chi^2 = 1.7$ while for the RAWD model: d = 0.011 and $\chi^2 = 9.4$. Therefore, there are different physical properties associated with the models that best fit the two sets of abundances even though they are measurements of the same star. The exposure required of the one-zone model to fit the abundances of K21 is lower than what is required to fit the original set of abundances but the dilution factor required is higher. This would suggest that one of these fits is to a star that has more i-process material (longer exposure, less dilution), while one is not as enriched with i-process material (lower exposure, more dilution). However, these abundances are for

the same object which makes it harder to be certain of what conditions have produced the abundances because it all depends on the way the abundances are calculated. We can agree that the abundances of this object are likely i-process and that both the one-zone and RAWD models can fit both sets of abundances well. However, to be more specific about physical conditions is difficult. The best fit models of Figure 2.20a can also be compared to the best fit model found for this object in Choplin, Siess & Goriely (2021) as the same set of abundances was used. The lead abundance is replicated much more closely with the one-zone model in this work compared to the C21 fit, where it is slightly underproduced. The overall fit to the abundances appears better for the one-zone model of this work with Y and Zr being reproduced more closely than C21 where they are overproduced. This is in keeping with the conclusions drawn previously.

For HD224959 (Figure 2.21), the one-zone AGB intershell model gives a χ^2 value of 26.9 at cycle 527 ($n = 2.71\times10^{14}$ cm^{-3}), $\tau = 5.77$ mbarn^{-1} and d = 0.032. The RAWD fit gives $\chi^2 = 22.9$ at cycle 2000 and dilution factor 0.005. The observed abundances of Karinkuzhi et al. (2021) for this star show high Sr (Z = 38). The non-local thermodynamic equilibrium (NLTE) value for Sr is used for the abundance pattern. The authors state that this is because the line the abundance is derived from (Sr I line at 4607.327 Å) is known to show large NLTE corrections at low metallicities. This high Sr is the main reason why the models cannot reproduce the abundances of this star. If we were to ignore the Sr abundance, we can see that the one-zone model appears to fit the abundances well but does not quite replicate the abundances of Ba and Nd within error bars, which it does do for the original set of abundances. However, the effect of Sr on the overall modelled fit is so small that it does not need to be removed from the best fit calculations. The RAWD model is still under-producing the Pb abundance by 1.2 dex. This means the one-zone model is likely the better fit to this set of abundances despite the higher χ^2 value. The properties of the best fitting one-zone and RAWD models for the original set of abundances were as follows: d = 0.034 at cycle 530 ($n = 2.32\times10^{14}$ cm^{-3}), $\tau = 6.47$ with a $\chi^2 = 7.0$ for the one-zone model and d = 0.008 at cycle 3700 with $\chi^2 = 5.0$ for the RAWD model. Again, these different properties would suggest that the abundances are from two different objects when we know that is not the case. This adds

another level of uncertainty when we discuss abundance fitting because the modelled fit to the abundances is dependent upon the way the abundances themselves were calculated. The fit to the abundances of Karinkuzhi et al. (2021) can again be compared to the fit of Choplin, Siess & Goriely (2021) given the same set of abundances was used. The majority of first peak elements are more closely reproduced by the one-zone model, with Sr, Y, Zr and Nd being overproduced by C21. The Sr in both cases is underproduced by both the one-zone model and the model of C21 but is more closely matched by C21. Some of the second peak elements are more closely replicated by Choplin, Siess & Goriely (2021), while the lead abundance is matched a little closer by the one-zone model. The better fit appears to be with the one-zone model, further showing that the model which reproduces the lead abundance tends to fit best.

2.2.3 Other fits from literature

The one-zone AGB and RAWD models can also be compared to other stars from the literature using the same χ^2 fitting technique. In this section, the two models are compared to a typical CEMP-s and CEMP-no star. This is done as a check to make sure that the fitting in the previous section works as it should. The abundances that the models have been compared with so far in this work are likely from an i-process event so we would expect the models to fit the abundances reasonably well. Therefore, it is important to make sure that the modelled abundances can't be 'made' to fit any scenario. If the i-process models don't provide a strong fit to the CEMP-s and CEMP-no stars, then we know that the models are fitting an an i-process pattern properly.

2.2.3.1 Thompson et al 2008: the CEMP-s star CS22964-161

CS22964-161 is a binary star system detailed in Thompson et al. (2008). This system contains a primary star and secondary companion that are both on the 'metal poor main sequence turnoff' and both display carbon and neutron capture element enrichment. It is thought that the enhanced C and n-capture elements present in the system have come from mass-accretion of an AGB star previously in a triple system with CS22964-161. The abundances used here are from table 5 of Thompson et al. (2008).

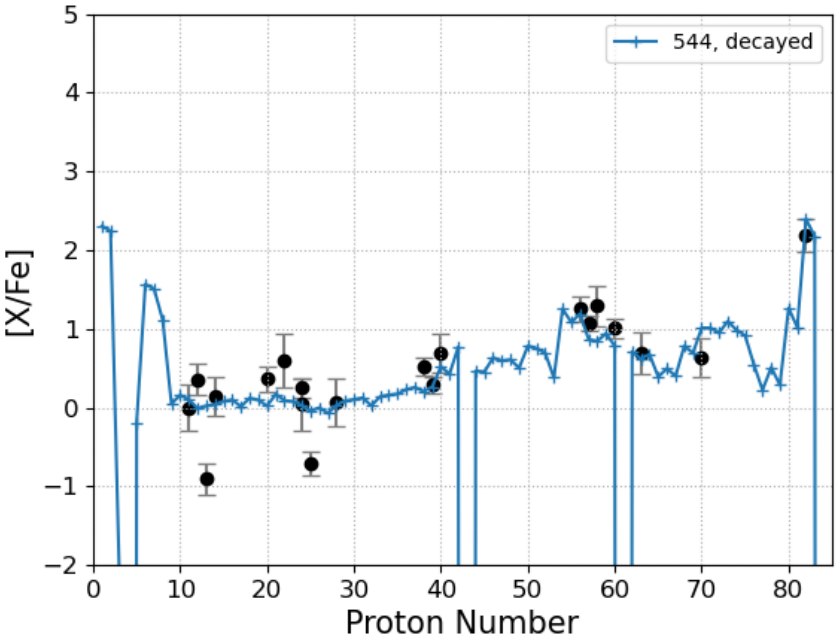

(a) One-zone AGB intershell model compared with the abundances of CS22964-161 of Thompson et al. (2008). The fitting parameters are d = 0.002 at cycle 544, resulting in $\chi^2 = 12.7$.

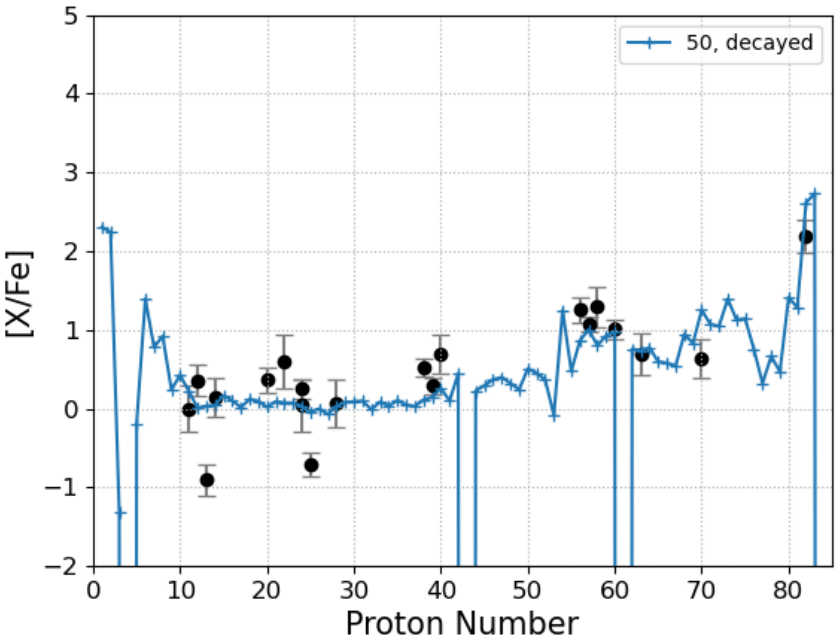

(b) RAWD model compared with the abundances of CS22964-161 of Thompson et al. (2008). The fitting parameters are d = 0.001 at cycle 5000, resulting in $\chi^2 = 30.6$.

Figure 2.22: Best [X/Fe] fits for each of the models to CEMP-s star CS22964-161. The observations are shown in black with the error bars in grey.

When fitting the one-zone AGB intershell model we get χ^2 of 12.7 at cycle 544 (τ = 9.37 mbarn^{-1}, $n = 8.29\times10^{13}$) and dilution 0.002. When fitting the RAWD model we get χ^2 of 30.6, at cycle 5000 and dilution 0.001. The high neutron density of the one-zone fit would suggest an i-process pattern. However, the dilution factors of 0.001 and 0.002 are the two lowest factors that can be chosen. By equation 2.1 those dilution factors would produce modelled abundances of almost entirely solar scaled material. The low dilution factors are in contrast to the factors from section 2.2.2.1 of about 0.040 on average for the one-zone intershell model and about 0.010 on average for the RAWD model, which give a much higher fraction of i-process material. The lower dilution factors are not surprising for a CEMP-s star, given that CEMP-s stars have a lower abundance of barium than CEMP-i stars and therefore i-process material would require more dilution to give an s-process pattern. The χ^2 values here are fairly low and the heavy element fits replicate the abundances well, especially for the one-zone intershell model (Figure 2.22a). This is perhaps to be expected given that the s process and i process capture neutrons in a similar way. What distinguishes the two processes is the origin of Ba. In the i process the majority of the Ba comes from ^{135}Ba due to β decays of unstable but highly abundant ^{135}I. However, in the s process the majority of the Ba comes from ^{138}Ba due to β decays of ^{138}Ce, ^{138}Xe and surrounding isotopes. Therefore, until ^{135}I becomes highly abundant, the dominant Ba isotope is still ^{138}Ba. Thus, we can achieve i-process like neutron densities and replicate i-process like patterns, with s-process like behaviour. This means that the s process can be capable of producing patterns similar to the patterns we would expect for the i process. Therefore, the model providing a reasonably good fit to the CEMP-s abundances is not of great concern, especially given the low dilution factors required of the best fit models.

2.2.3.2 BS16077-077: a CEMP-no star

CEMP-no stars do not show any evidence of heavy element neutron capture nucleosynthesis so the models should not be able to reproduce the abundances. To find a CEMP-no star, I searched the SAGA database (the search took place on 14/06/2021, with the last major update at that time occurring on 07/04/2021) (Suda et al., 2008) for a star with -3 < [Fe/H] < -2,

[Ba/Fe] < 1 and [C/Fe] > 1 and chose one from the sample selected. The star I am using is BS16077-077 (Allen et al., 2012). The modelled fits for this star can be found in Figure 2.23. The best fit for the one-zone AGB intershell model occurs at cycle 534 ($n = 1.83\times10^{14}$ cm^{-3}, $\tau = 7.38$ mbarn^{-1}) and dilution factor 0.001, this gives $\chi^2 = 12.9$. While the best fit for the RAWD model occurs at cycle 5000 and dilution factor 0.001, this gives $\chi^2 = 47.7$. Here, what is important is the fact that both fits use the lowest possible dilution factor. This is the smallest amount of i-process material that the model can be enriched with. This result is what we would expect given that the models are i-process models being fit to a star which does not show heavy element enrichment. The heavy element abundances are are flat (i.e. [X/Fe] = 0) for the light s elements as well as Eu (Z = 63) and Gd(Z = 64). What is being picked up in the fit and why we are getting a small χ^2 for the one-zone model is because we have abundances around the second peak elements (Z = 56 - 58 and Z = 60) of around 0.7 dex. Therefore, the i-process models are successful in replicating the CEMP-no abundances due to the small enhancement in some of the heavy element abundances if the model is significantly diluted, as is the case here. This again shows that if the smallest dilution factors are used, abundance patterns with small heavy element enhancements can be replicated due to the heavy element enhancement in the models. However, the dilution factors required are small and are not comparable to those required in order to reproduce the i-process abundance patterns of the CEMP-i stars previously.

2.2.4 Phosphorus-rich stars

Masseron et al. (2020a) identified a group of 15 stars as being rich in phosphorus. Phosphorus is important scientifically because it plays a role in DNA and in exchange of energy in cells (e.g. Gulick 1955). This provides extra importance for understanding the origins of P (along with C, N, O and S) because it is key to life. We think ^{31}P, which is the only stable isotope of phosphorus, is primarily produced via neutron captures onto ^{29}Si and ^{30}Si. This is expected to occur mainly in massive stars (Cescutti et al., 2012), which are a known site of the slow neutron capture process. Observations of P-rich stars are important because most galactic chemical evolution (GCE) models under-predict the phosphorus that we observe in the Solar

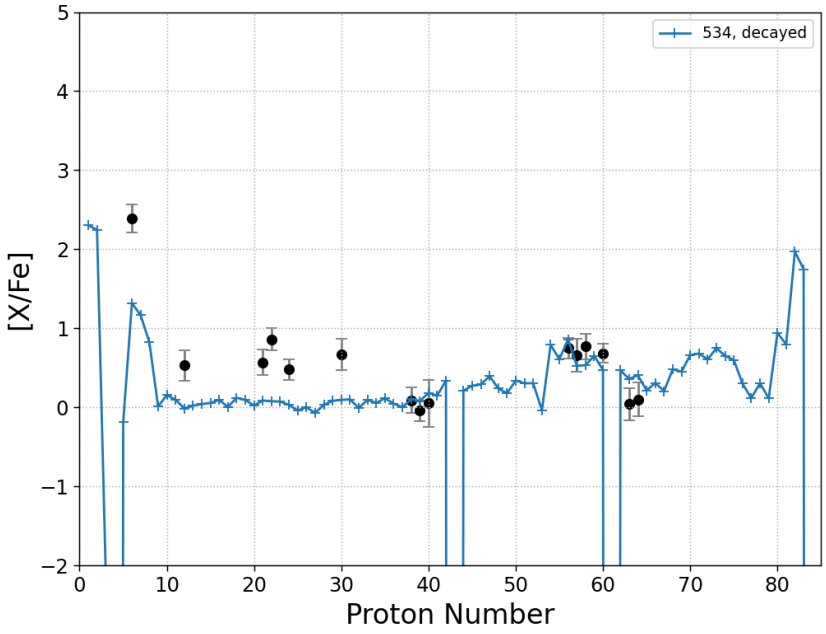

(a) One-zone AGB intershell fit to the CEMP-no star BS16077-077. The fitting parameters are d = 0.001 at cycle 534, resulting in $\chi^2 = 12.9$.

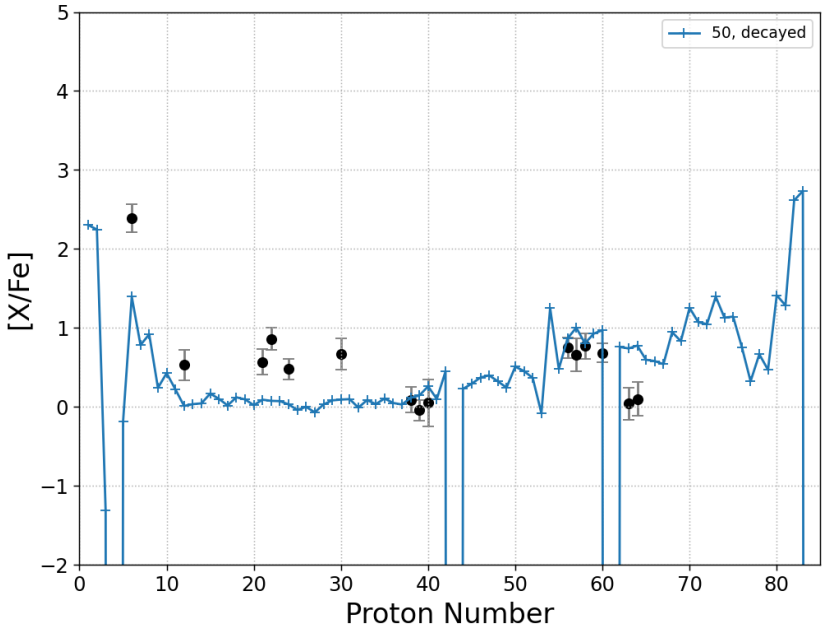

(b) RAWD model fit to the CEMP-no star BS16077-077. The fitting parameters are d = 0.001 at cycle 5000, resulting in $\chi^2 = 47.7$.

Figure 2.23: Best [X/Fe] model fits to CEMP-no star BS16077-077. The observations are shown in black with the error bars in grey.

System (e.g. figure 1 Masseron et al. 2020a). This under-prediction is illustrated in figure 13 of Prantzos et al. (2018) which shows a galactic chemical evolution model compared to some observations of phosphorus. We can see that the model underproduces P compared to all of the observations but also that the observational data for phosphorus is sparse compared to other light elements with only a small amount of data around -0.8 < [Fe/H] < 0.2. Cescutti et al. (2012) shows that in order to reproduce the observations of phosphorus with GCE models, the P yields of massive stars must be increased by a factor of 3. Therefore, having a P-rich source might be able to bridge that gap between the GCE models and Solar System observations. However, Kobayashi et al. (2020) showed that their chemical evolution models of the solar neighbourhood can reproduce the observations of P, though the number of observations is still sparse compared to the other elements included in that work.

Masseron et al. (2020b) obtained heavy element abundances for two P-rich stars, one of which was in the original Masseron et al. (2020a) sample, and investigated them in more detail. These stars were 2M13535604+4437076 and 2M22045404-1148287 hereafter 2M13535604 and 2M22045404 respectively. They compared the abundances of these stars to two CH (s process) stars, a CEMP-r/s star and a metal poor star with r-process enhancement and found that the abundances did not match any of these types of star. The light element abundances of the original P-rich sample of 15 stars ruled out a potential AGB progenitor scenario (Masseron et al., 2020a). Therefore, they ultimately concluded that the abundance pattern could not be explained but postulated that this could be a new mode of operation for the s process. The heavy element abundances of the two P-rich stars in question are particularly difficult to constrain due to the high [Ba/La] ratio ([Ba/La] = 0.76 for both 2M13535604 and 2M22045404), given Ba and La should be produced in similar quantities in the s process. This is demonstrated in figure 5 of Mishenina et al. (2014) where the pure s-process value of [Ba/La] from Bisterzo et al. (2014) and Travaglio et al. (2004) is shown to fall below 0.15. Low [Rb/Sr] in 2M22045404 suggests a low neutron density in this star but not the other.

Figure 2.24 shows the nuclide chart around ^{31}P for my one-zone AGB intershell model described in section 2.1.1. The nuclide chart plotted here is 5.07×10^{-4} years through the evolution at a neutron density of 3.05×10^{14} cm^{-3}, which is 9.76×10^{-4} years before peak

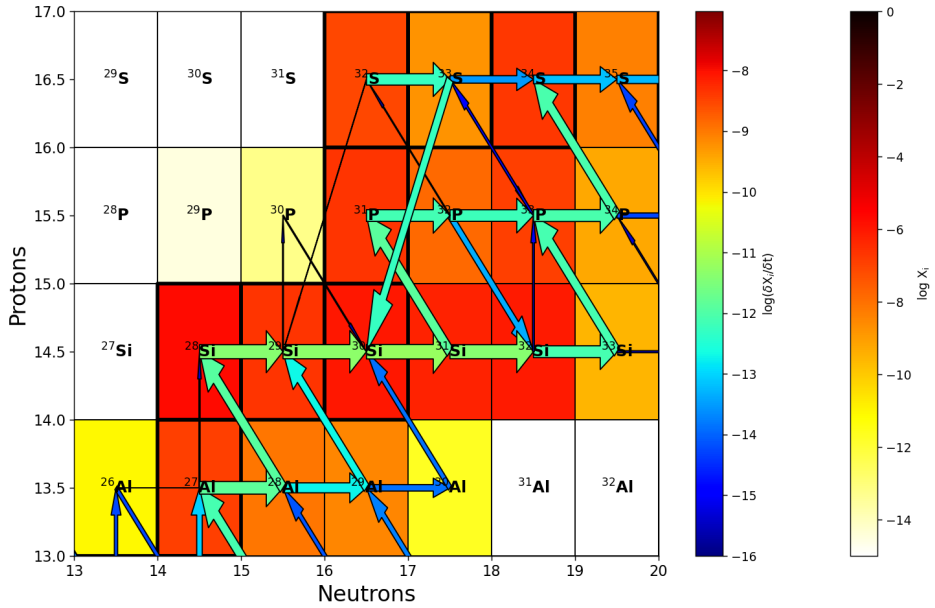

Figure 2.24: Nuclide chart showing the production of phosphorus 9.76×10^{-4} years before peak neutron density (cycle 490). Isotopes are placed as a function of their proton and neutron number, while their colour represents how abundant they are. The colour of the arrows represents the strength of the flux of the reaction that is taking place.

neutron density. Here each isotope is coloured based on how abundant it is and the arrows indicate the flux of the reaction from the isotope at the base of the arrow to the isotope at the top. We can see that ^{31}P is very abundant as are 4 of the isotopes of Si. As we expect, ^{31}P is being produced via β decay of ^{31}Si due to neutron captures onto the stable ^{29}Si and ^{30}Si. Given the high abundance of ^{31}P and flux of the β decay of ^{31}Si to ^{31}P due to neutron captures, I felt it was important to study the two P-rich stars with heavy element abundances to see if my i-process model could explain them, especially given that Masseron et al. (2020b) could not find an adequate solution.

Figures 2.25 and 2.26 show the best fit by each model to each star. Here, I have performed the same fitting that was performed on the sample of CEMP-i stars in section 2.2.2.1. Therefore, Figures 2.25 and 2.26 were the smallest χ^2 fits for the heavy element (Z $\geq$ 30) abundance pattern for each star.

For star 2M13535604 the values for the intershell model are $\chi^2 = 99$ at a dilution of d

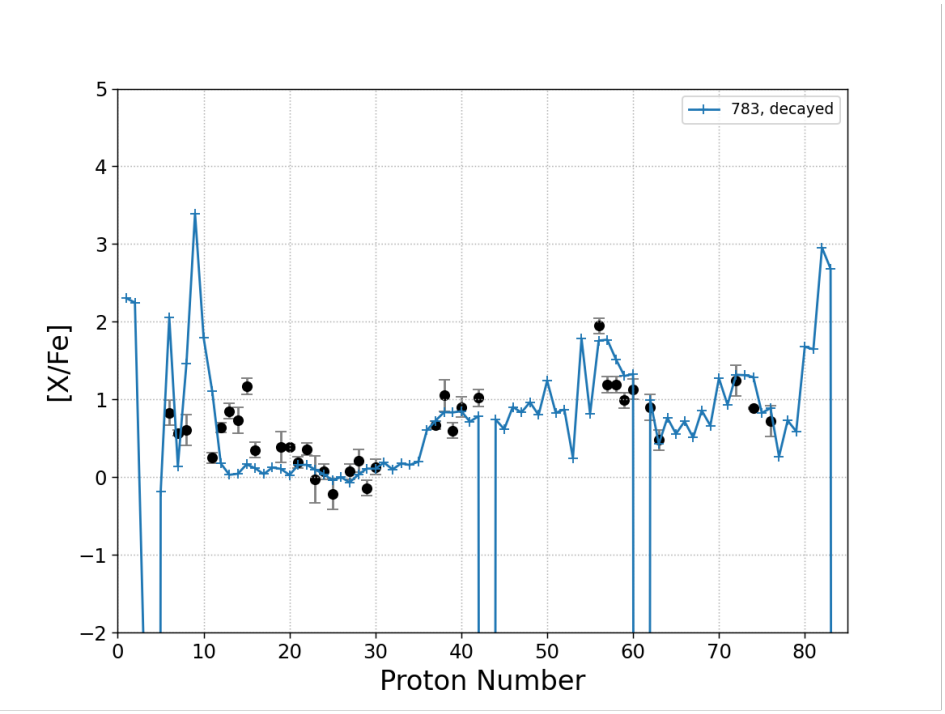

(a) Abundances of 2M13535604 compared with the one-zone AGB intershell model. The fitting parameters are d = 0.004 at cycle 783, resulting in $\chi^2 = 99$.

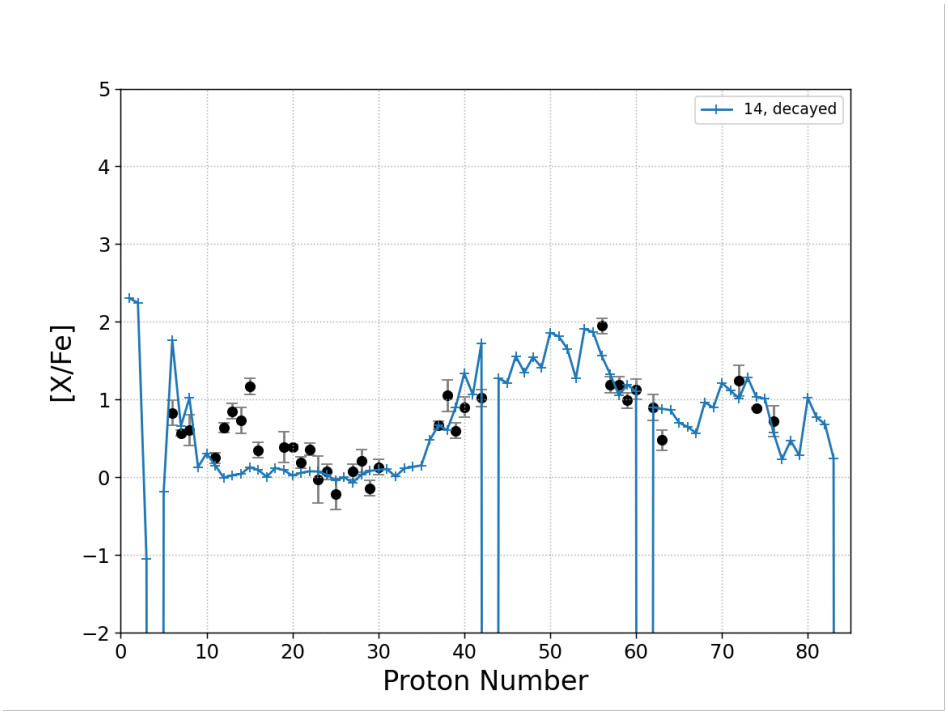

(b) Abundances of 2M13535604 compared with RAWD model. The fitting parameters are d = 0.002 at cycle 1400, resulting in $\chi^2 = 366$.

Figure 2.25: Best [X/Fe] fit for each model to P-rich star 2M13535604. The observations are shown in black with the error bars in grey.

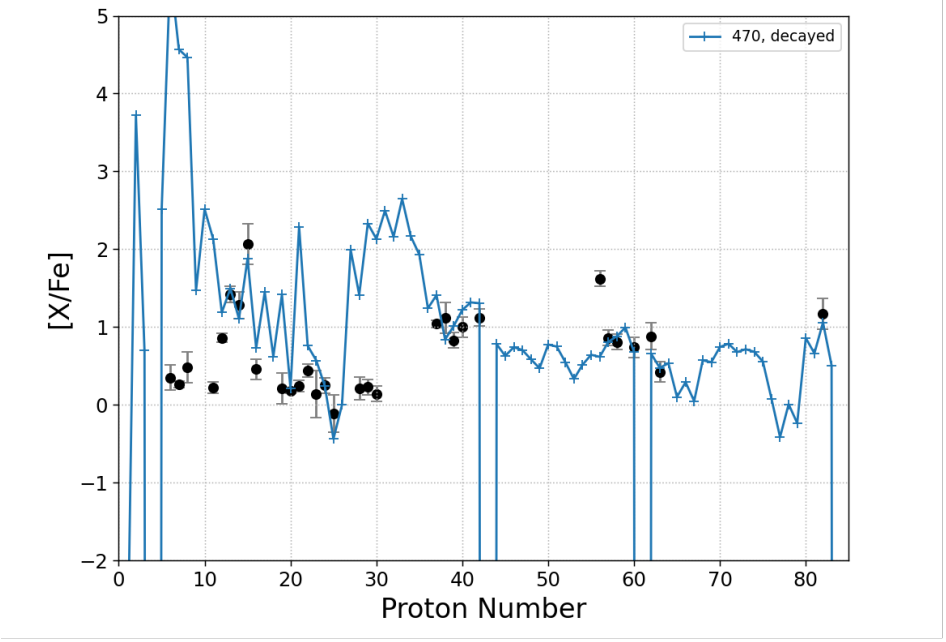

(a) Abundances of 2M22045404 compared with the one-zone AGB intershell model. The fitting parameters are d = 1.0 at cycle 470, resulting in $\chi^2 = 182$.

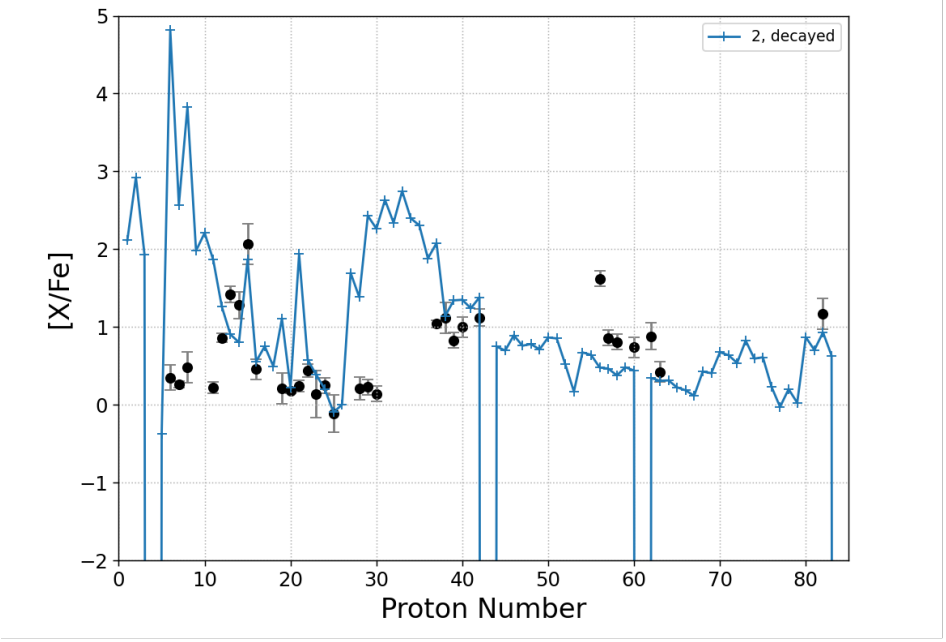

(b) Abundances of 2M22045404 compared with RAWD model. The fitting parameters are d = 0.765 at cycle 200, resulting in $\chi^2 = 269$.

Figure 2.26: Best [X/Fe] fit for each model to P-rich star 2M22045404. The observations are shown in black with the error bars in grey.

= 0.004 and cycle of 783 which corresponds to a neutron density of $n = 5.88\times10^{6}\,\mathrm{cm}^{-3}$ and exposure of $\tau = 11.31\,\mathrm{mbarn}^{-1}$. The values for the RAWD model are $\chi^2 = 366$ at dilution d = 0.002 and cycle 1400. Figure 2.25 shows neither i-process model is a good fit for the abundances of 2M13535604 and cannot replicate the enhanced P abundance. In both cases the dilution factors are some of the lowest that can be selected by the fitting script. From the one-zone intershell fit, we can see that the model reproduces the observations fairly well but fails around the second peak elements. Lanthanum (Z = 57) is overproduced by about 0.5 dex, while cerium (Z = 58) is overproduced by about 0.3 dex. The RAWD model fits closely around most of the second peak elements but Ba is under-produced by about 0.4 dex. The majority of the first peak elements are not reproduced well by the model, especially molybdenum (Z = 42) which is overproduced by about 0.7 dex. Given the low neutron density of the intershell model being much more like an s-process neutron density, I concur with previous findings that this abundance pattern is most likely from an unusual mode of neutron capture nucleosynthesis.

For star 2M22045404 the values for the intershell model are $\chi^2 = 182$ at a dilution of d = 1.0 and cycle of 470 which corresponds to a neutron density of $n = 2.54\times10^{14}\,\mathrm{cm}^{-3}$ and an exposure of $\tau = 0.129\,\mathrm{mbarn}^{-1}$. The values for the RAWD model are $\chi^2 = 269$ at dilution d = 0.765 and cycle 200. The heavy element abundances of this star are well reproduced by the one-zone intershell model, with the exception of Ba which is under-produced by about 1 dex. The RAWD model fit does not work well for most of the heavy element abundances, there is a poor fit of both the first and second peak elements. Though the χ^2 of both the intershell model and RAWD model fits are large, what is interesting about the intershell fit in particular is the match to the phosphorus peak and the d = 1 dilution factor. This factor means that no solar-scaled dilution is included in the model and the material is pure i-process material.

What is especially striking is I fit only to the heavy elements (Z ≥ 30) because we care mostly about the heavy element production when considering neutron capture processes. Therefore, the fact that in fitting to the heavy elements I have inadvertently fitted to the P peak of these abundances is surprising. This suggests that the i process can produce the abundance of phosphorus observed in these stars. However, from Figure 2.26a we can see there are going

to be some immediate challenges to fitting some sections of the abundance pattern. Firstly, the observed scandium (Sc) (Z = 21) abundance is low, whereas the modelled abundance is high. This is challenging because whenever we produce P, we also expect to produce Sc. There is also a high barium abundance of [Ba/Fe] = 1.62, which the initial fits (Figure 2.26) cannot reproduce. However, the [Ba/La] ratio for this star is [Ba/La] = 0.76 which is in the range of [Ba/La] that i-process models have reached (figure 6 Mishenina et al. 2014). Therefore, an i-process model could potentially fit this ratio. Our final issue is that Ni (Z = 28), Cu (Z = 29), and Zn (Z = 30) are low when the model predicts high abundance of these elements due to neutron captures onto iron. We can see this pattern in the modelled abundances where we have a low iron abundance which is replicated in the observations, followed by a peak in the iron group elements that follow. That being said, it was important to try and replicate the abundances of this star using the i process given that the P-rich peak can be reached. Therefore, this star warranted further investigation to try and reduce the χ^2 value and improve the fit. For the investigations that follow, the one-zone AGB intershell model will be used because this is the model with the d = 1 dilution factor and the match to the P abundance, as well as the fact it is a good fiducial model for the i process (see section 2.2.2.1) and is easy to manipulate.

I first wanted to see if the full abundance pattern would fit with one i-process exposure. Here, I will be fitting from Z = 10 rather than Z = 0 because, as previously mentioned in section 2.2.1, the way the lower portion of the nuclear network treats H burning is incorrect as there is significant hydrogen burning happening elsewhere in the star that cannot be accounted for. Doing this gave me values of $\chi^2 = 1075.4$ and d = 0.955 at cycle number 467, this corresponds to neutron density of $n = 2.42\times10^{14}$ cm^{-3} and an exposure of $\tau = 0.093$ mbarn^{-1}. Figure 2.27 shows this fit. The main feature we are looking for is a match to the high P abundance. Though there is a peak in the modelled abundances at phosphorus, we do not see the same match we did previously due to the dilution in this model. We can see that the fit is also underproducing the abundances of all the heavy elements, especially Ba and lead. This is likely because the exposure in this model is lower than the previous model so the heavy element abundances haven't had time to build up, coupled with more dilution than the previous model. All these

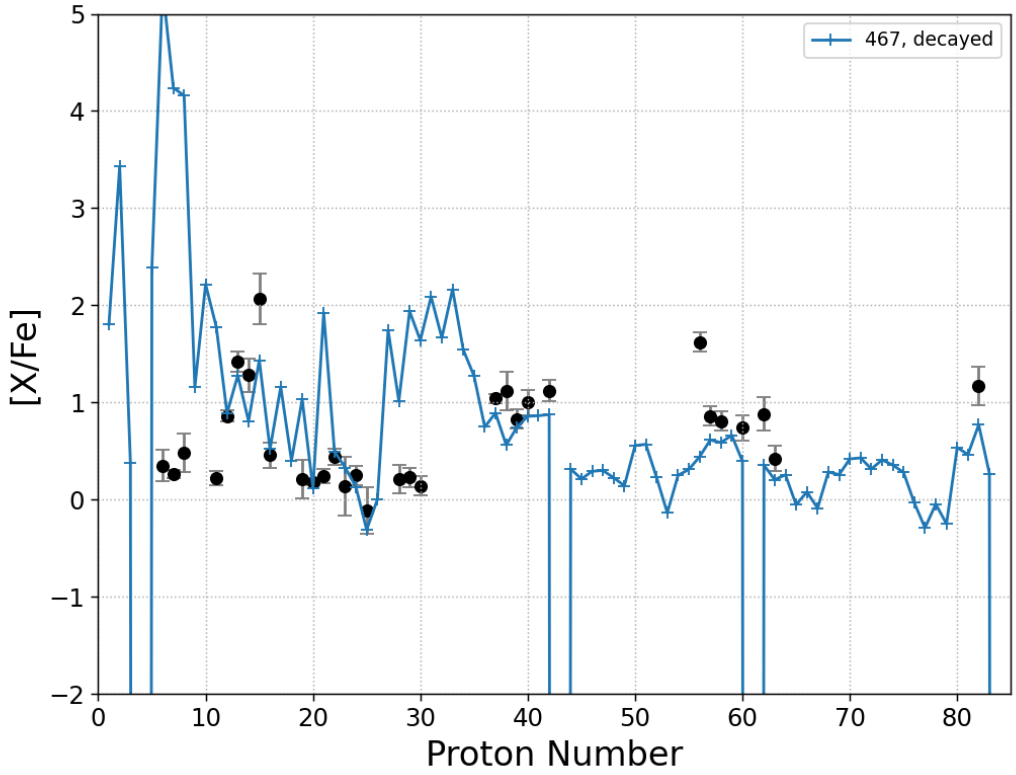

Figure 2.27: Best fit of the one-zone model to the observations of 2M22045404 from Z = 10. The fitting parameters are d = 0.955 at cycle 467, resulting in $\chi^2 = 1075.4$. The observations are shown in black with the error bars in grey.

factors contribute to a high χ^2 and shows how difficult getting a good fit to these abundances is going to be.

I also considered what would happen by just fitting to the light elements $10 \leq Z < 30$. When I did this I got values of $\chi^2 = 656.4$ and d = 0.599 at cycle number 498, this corresponds to neutron density of $n = 3.43\times10^{14}\,\mathrm{cm}^{-3}$ and an exposure of $\tau = 1.06\,\mathrm{mbarn}^{-1}$. Figure 2.28 shows that fit. The reason why I wanted to look at this fit was to see if the light element abundance pattern, including the P, could be reproduced given the poor fit of the light elements in the original models. We can see that the elements beyond P fit a little better in comparison to Figure 2.27. There is still the pronounced peak at Sc that is not echoed in the observed abundances. The fact that Sc is not present in the stellar abundance of 2M22045404 means making a prediction about what the progenitor of this star is may be difficult. We do see more

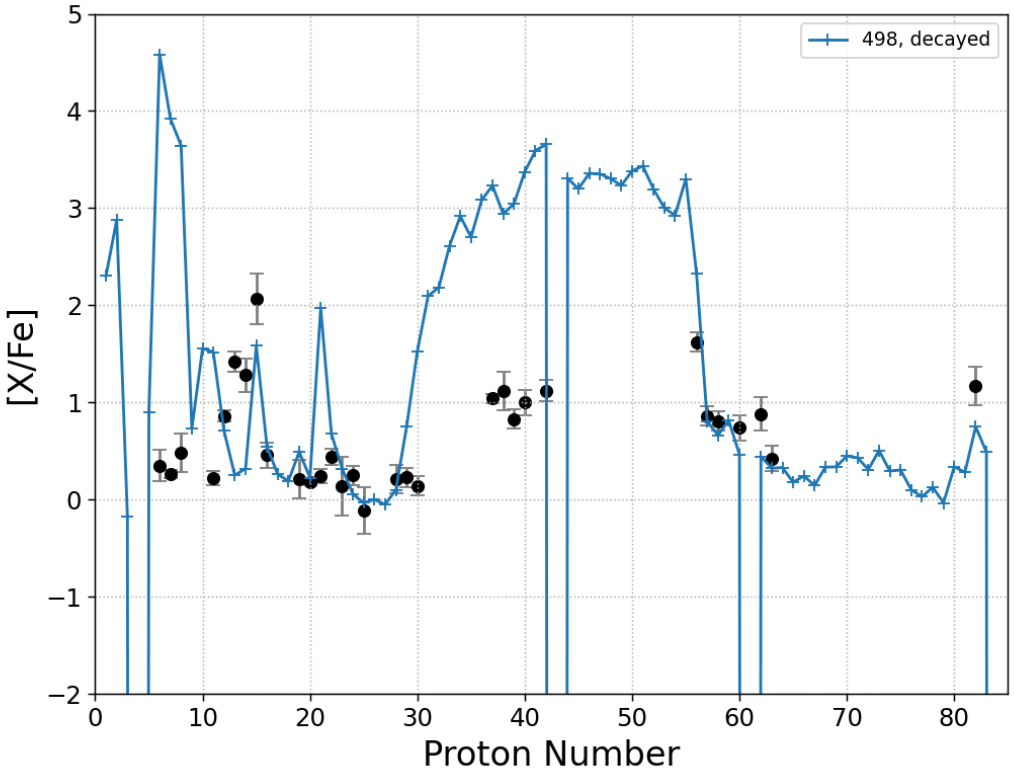

Figure 2.28: Best one-zone model fit to 2M22045404 between $10 \leq Z < 30$. The fitting parameters are d = 0.599 at cycle 498, resulting in $\chi^2 = 656.4$. The observations are shown in black with the error bars in grey.

i-process-like values in terms of the cycle and dilution factor of this fit but we can see that the χ^2 is high and the heavy element pattern isn't reproduced at all.

Koch et al. (2019) found they could fit the abundances of peculiar bulge star J183003.87-333423.6 (Star ID #10464) by considering a double i-process enrichment scenario. This is when two proton ingestion events have occurred thereby exposing the stellar interior to two separate i-process events. The fit that they found was made up of two distinctly different i-process exposures of $\tau = 0.30\,\mathrm{mbarn}^{-1}$ and $\tau = 0.96\,\mathrm{mbarn}^{-1}$. The combination of the two different exposures allowed Koch et al. (2019) to simultaneously fit both the ls and hs peaks of this star, which has previously been difficult, as well as the high [Rb/Fe]. I decided that 2M22045404 may be a good candidate for double i-process enrichment because Masseron et al. (2020b) concluded that perhaps a new mode of operation for the s process could be responsible for the heavy element abundance pattern, so why not consider an unusual operation

for the i process, especially given the success of Koch et al. (2019). It is also a good candidate because finding a single enrichment scenario proved difficult both for the i process and s process (Masseron et al., 2020b). The idea being that the first exposure would build up the heavy element pattern, while the second would then be able to enhance the abundances of the lighter-heavy and light elements, including the phosphorus peak. To create a double enrichment scenario, we need to consider two exposures of i process in different proportions along with the solar-scaled material to dilute the abundances. This can be achieved as follows:

$$X = aX_{\tau_1} + bX_{\tau_2} + cX_{\text{scaled}} \tag{2.3}$$

where X_{τ_1} and X_{τ_2} are the abundances of the first and second i-process exposures and X_{scaled} is the solar scaled material. The dilution factors a, b and c are associated with each component of the dilution where $a + b + c = 1$. To compute the abundances of every combination of cycles with every possible combination of a, b and c is computationally expensive and extremely time consuming. Therefore, to be able to find the combination of cycles and dilution factors that would provide the smallest χ^2, I narrowed down the search in increments. First I made the conditions broad by taking every 10 cycles between 400 and 580 (cycles with i-process neutron density) for X_{τ_1} and X_{τ_2} and limiting a, b and c to a range of values between 0-1 in steps of 0.1. For every set of abundances found with these parameters, a χ^2 fit for the heavy elements was calculated and the smallest value found was $\chi^2 = 182.9$. This yielded $\tau_1 = 1.296\times10^{-5}$ mbarn $^{-1}$ (cycle 400) and $\tau_2 = 0.129$ mbarn^{-1} (cycle 470) with a = 0, b = 1 and c = 0 which is exactly the same as the original best fit (Figure 2.26a).

I continued to narrow down the range of cycles and values that a, b and c could take. The final part of this was to take every cycle between 460 and 485 with a, b and c being able to take any value between 0-1 in steps of 0.01. The fit to the heavy elements yielded a value of $\chi^2 = 162$, $\tau_1 = 0.31$ mbarn^{-1} (cycle 480) and $\tau_2 = 0.12$ mbarn^{-1} (cycle 469) and a = 0.06, b = 0.94 and c = 0. This best double i-process enrichment fit is shown in Figure 2.29. Though we see a difference in χ^2 value, we don't immediately see a difference between the original best fit and the double i-process fit on visual inspection (Figure 2.30).

The goal of the double i-process fitting in the present work was to replicate the success of Koch et al. (2019) by having two distinctly different neutron exposures, that combined would

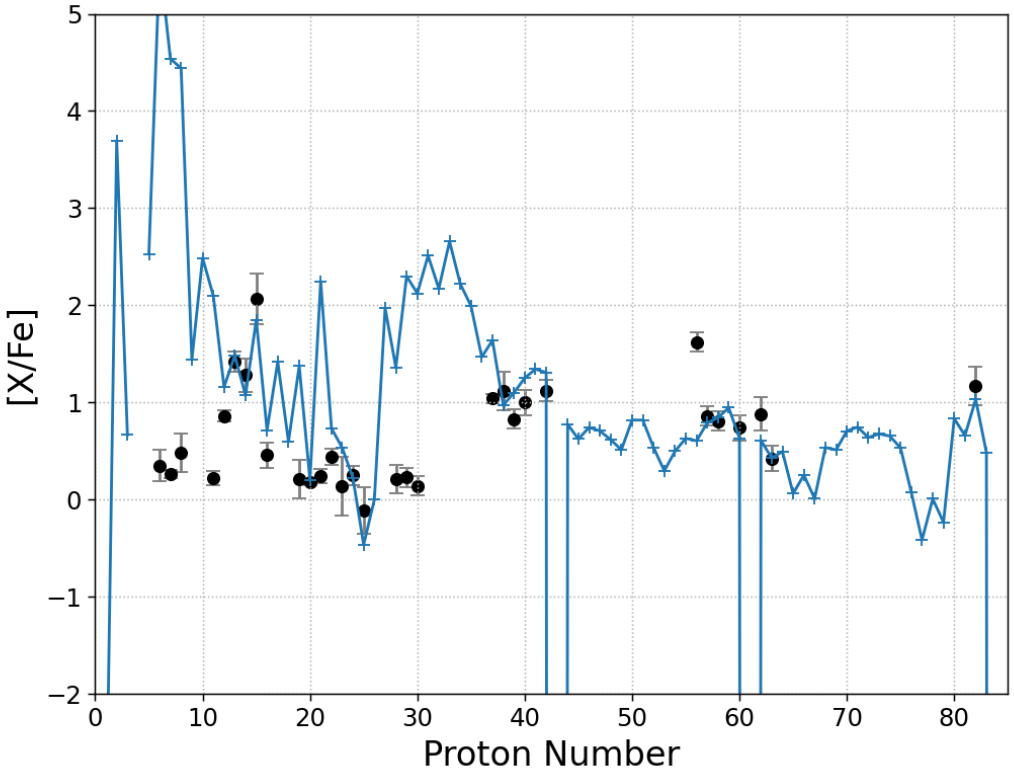

Figure 2.29: Best double i-process enrichment fit with dilution factors a = 0.06, b = 0.94 and c = 0. This results in $\chi^2 = 162.3$. The observations are shown in black with the error bars in grey.

give a good fit to the abundances. The aim was to see if the P-rich peak could be met along with the heavy element pattern, which is not the case. This fit has a lot of the same problems as others in that we have a peak at Sc, high [Ba/La] ratio that cannot be replicated and low Zn, Cu and Ni that cannot be reproduced.

Denissenkov et al. (2021) investigated the (n,γ) reaction rates of 164 isotopes which affect the abundances of elements from Ba to W (Z = 56 - Z = 74). Given the aim with this abundance fitting is to see if the heavy element abundances can be reproduced, I decided to see if varying the reaction rate of Ba could mean the model matches the high [Ba/La] ratio. Denissenkov et al. (2021) states that the most important (n,γ) reaction for Ba production is ^{135}I(n,γ)^{136}I and that the abundance of Ba could vary by up to 1 dex (their figures 7 and 10) based on the reaction rate uncertainty. However, even for the 'best' double i-process enrichment model (Figure 2.29), the observed Ba abundance is approximately 1 dex higher than the model

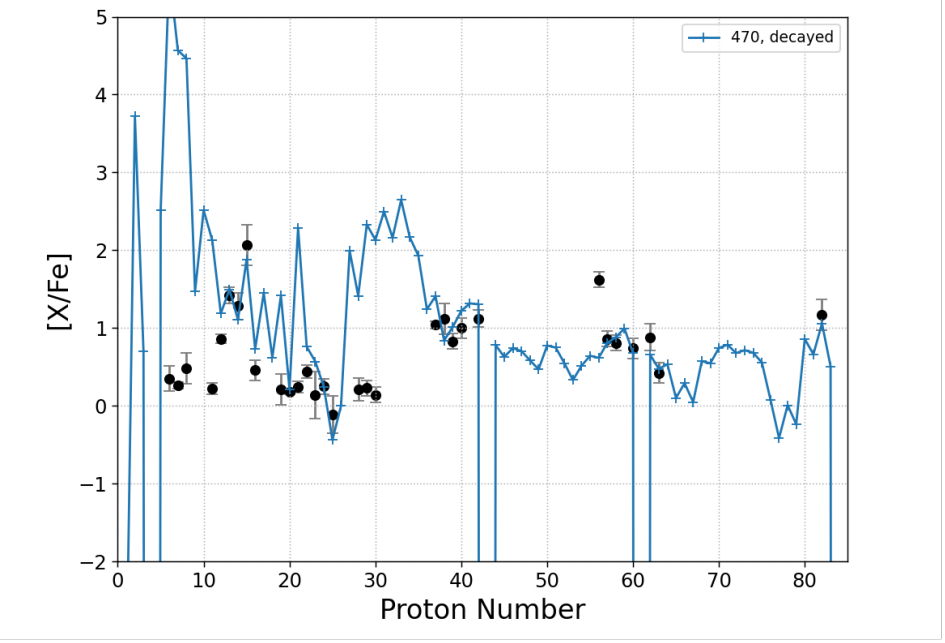

(a) Same as Figure 2.26a. With fitting parameters d = 1.0 at cycle 470 with $\chi^2 = 182$.

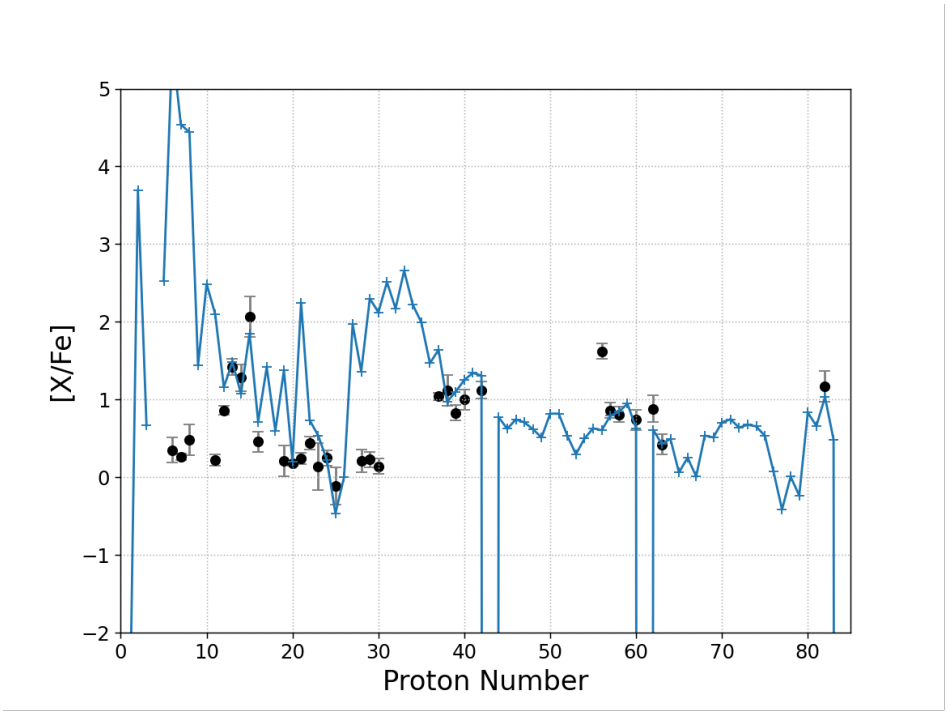

(b) Best double i-process fit to 2M22045404 using the one-zone model. The values for a, b and c are 0.06, 0.94 and 0.0 respectively, resulting in a $\chi^2 = 162.3$.

Figure 2.30: A comparison of the best fit to the abundances of 2M22045404 with a single exposure (a) and two exposures (b). The observations are shown in black with the error bars in grey.

prediction. Therefore, it is unlikely the Ba abundance could ever be reproduced along with the rest of the heavy element pattern of 2M22045404. A discussion on how reaction rate uncertainties could impact the work done in this thesis as a whole can be found in chapter 4.

Ultimately, the i process cannot fully explain the abundances for these particular stars. The fitting for 2M13535604 leads me to concur with Masseron et al. (2020b) that these abundances are likely the result of an unusual mode of neutron capture nucleosynthesis. It is still unclear if this is also the case for 2M22045404 given how well an i-process model matches the P-rich peak that is so unusual about these stars. That being said, it would also seem that the i process is not the whole solution for explaining the abundance pattern of 2M22045404, even after considering a double i-process exposure scenario.

2.2.5 Using χ^2 fitting to make predictions

Lead (Pb) is the end of the s-process path because it is the final element with stable isotopes, though there is a quasi-stable isotope of bismuth that can be produced in the s process (^{209}Bi). A quasi-stable isotope is an isotope that has a half life of the order of gigayears. The i process occurs at higher neutron densities than the s process and can therefore reach much further from the valley of stability, giving the i process the potential to produce Th (Z = 90) and U (Z = 92), which are normally considered r-process elements (Burbidge et al., 1957). Thorium has one quasi-stable isotope (^{232}Th) while uranium has two (^{235}U and ^{238}U). These are the heaviest quasi-stable isotopes. Neutron captures onto lead would be required to produce these elements and therefore we would hope to see Th and U present in stars that have both high lead abundance and have undergone the i process. Figure 2.31 shows the evolution of Th, U and Pb over time relative to iron for the one-zone model. The grey line on this figure marks the point of maximum neutron density. We can see that all three of the elements in question peak after this point, with the green dashed line marking the peak of [Pb/Fe] and the [Th/Fe] and [U/Fe] peaking slightly afterwards. The peaks at this point are likely due to neutron capture during the period of high neutron density.

One of the reasons we are interested in i-process production of Th and U is because if we can find Th and U abundances in stars we can do cosmochronometry. Cosmochronometry is

the process of age-dating a star based on the abundances of a particular elements. Typically, this age-dating is performed on very old stars that are enriched with r-process elements. The idea was originally proposed by Butcher (1987) and came into prominence when we started being able to take Th abundance measurements of stars. Cosmochronometry requires an element with quasi-stable isotopes and one element with dominant r-process isotopes. [Th/Eu] is the ratio most commonly used (e.g Sneden et al. 1996, Cowan et al. 1997, Gull et al. 2018, Gull et al. 2021). However, due to the large mass number gap between europium and thorium, it has been suggested that [Th/U] may be a better ratio to use for age-dating r-process enriched stars Cayrel et al. (2001). In the context of this work, if we observe a star that we think has undergone the i process and we have a Th observation for this star we can find out how long it has been since the i-process event took place. We can do this because if we know how much Th we expect to find produced by the i process, knowledge of the production ratio of Th relative to i-process elements and we know the decay rate of Th, then we know from the observed abundance how long Th has existed in that star.

CEMP-i stars show i-process enrichment and I have shown that the one-zone AGB intershell i-process model can reproduce the abundances very well in a lot of cases (section 2.2.2.1). Across the whole sample, the heaviest element observed is lead but the model that we fit the observations to goes further. Therefore, for a given star we can use the best fitting model to predict the Th and U abundance we may expect to find.

To do this I take the best fitting cycle number and decay the abundances for 10 Gyr at a temperature of 1×10^7 K. As we do not know the length of time that passes between an i-process event and the point at which its signatures are observed, we allow the decay sequence to run for 10 Gyrs. This seems a plausible upper limit on the time available. Though this will allow all elements to decay, what I am interested in by doing this decay are the quasi-stable Th and U isotopes. The decay performed here is different to the decay described in section 2.2.1. Here, I am using `ppn` to decay the abundances of the chosen cycle. The network for the decayed run is extended to californium (Cf) The data is again outputted in cycles and the fixed factor that increases the timestep between cycles is 1.5. Both methods of decaying the abundances yield the same results for elements up to and including Pb. The only exception

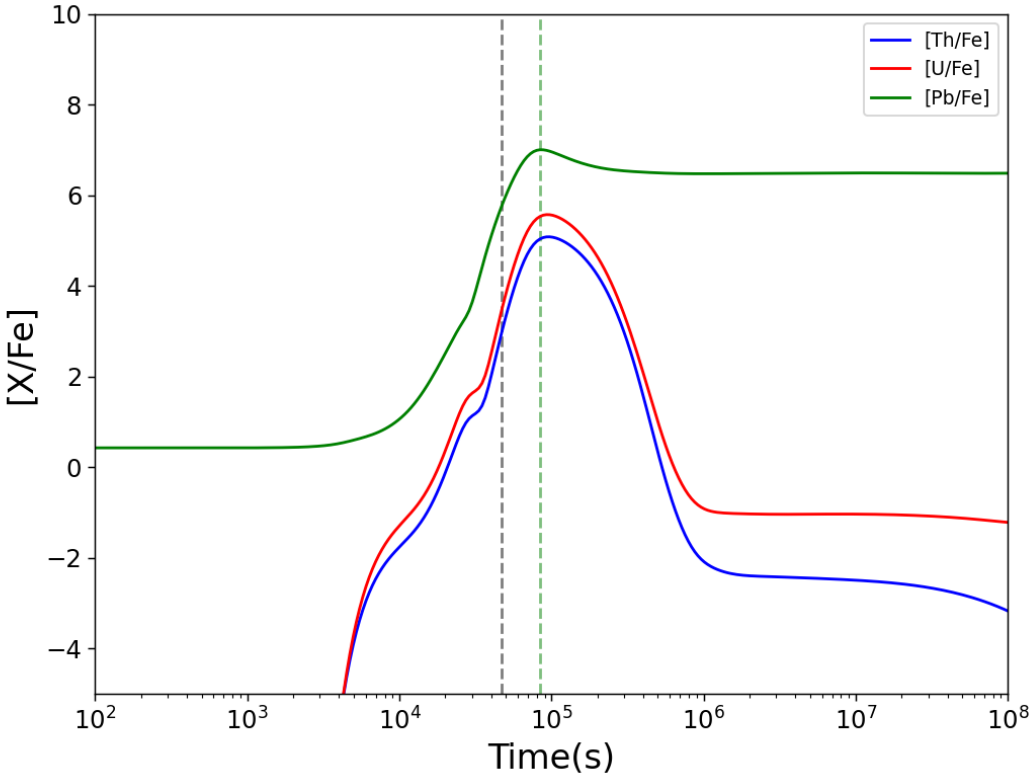

Figure 2.31: Evolution of [Th/Fe], [U/Fe] and [Pb/Fe] over time. The grey dashed line marks the point of maximum neutron density and the green dashed line shows the point at which [Pb/Fe] peaks.

is Cs due to the long half life of ^{135}Cs, see later in this chapter (section 2.2.5.1) for more information.

Six CEMP-i stars were selected from the sample of 17. To select these stars, I looked for stars with a lead abundance of [Pb/Fe] ≈ 3 to start with because the higher the lead abundance, the more seeds we have to capture neutrons onto and produce trans-lead elements. Next, I had to be confident that the abundances of the stars selected could have come from an AGB intershell proton ingestion event. In principle, the i-RAWD stystem could also produce Th and U but we don't have a larger network run for the RAWD model. That being said, RAWD models tend to produce less Pb and therefore, would likely also produce less Th and U. The latter selection criteria removed HE2148-1247 because it had a smaller χ^2 value for the RAWD model and HE0338-3945 because the double feature in Figure 2.17d means the model has two reasonable best fit models. In order to make a prediction of Th and U for each

Star	[Pb/Fe]	Cycle number
CS29497-030	3.517	532
CS29526-110	3.38	532
CS31062-050	2.913	520
HD187861	3.11	566
HD224959	3.11	530
HE0143-0441	3.372	534

Table 2.5: Lead abundance and best fit cycle number for the six selected CEMP-i stars.

Star	χ^2	d	t (yrs)	[Th/Fe]	[U/Fe]
CS29497-030	8.03	0.046	5.58×10^{6}	2.22	3.69
CS29526-110	7.74	0.033	2.48×10^{6}	1.57	3.39
CS31062-050	15.3	0.034	1.65×10^{6}	0.72	2.35
HD187861	1.51	0.014	9.83×10^{1}	0.25	0.05
HD224959	6.22	0.036	2.48×10^{6}	1.53	3.35
HE0143-0441	8.44	0.047	5.58×10^{6}	2.30	3.76

Table 2.6: Properties of the best fitting model after the abundances have been decayed for each of the six stars. Column one is the star whose abundances have been decayed, column two is the χ^2 achieved by the best fitting decayed cycle, column three is the dilution factor, column 4 is the time since initial production of Th and U that the model fits best and columns 5 and 6 are the corresponding [Th/Fe] and [U/Fe].

star, I took the abundances at the best fitting cycle and decayed them by using them as input for a decayed run (as described above). I then used the decayed abundances to recompute the best fitting conditions, using a χ^2 fit (see section 2.2.2.1). Table 2.5 shows the Pb abundances for each star and the cycle of the one-zone intershell model that was decayed. Table 2.6 shows the properties of the best fitting cycle of the decayed run, including the Th and U predictions from those fits.

In order to predict the abundances of Th (Z = 90) and U (Z = 92) produced by the i process we extended the [X/Fe] vs proton number plots to include Th and U (see the six panels in Figure 2.32). The modelled fit lines shows a predicted abundance for Th and U. From these

plots, the range of predicted Th is 0.25 < [Th/Fe] < 2.30 and U is 0.05 < [U/Fe] < 3.76. The individual predictions for each star can be found in Table 2.6.

Table 2.6 shows that HD187861 predicts lower values of [Th/Fe] and [U/Fe] than the other selected stars. This is because the time since initial production for the best fitting cycle is not long enough for some of the more unstable isotopes to have decayed to quasi-stable Th and U. Therefore, the abundance of these elements will remain low until there has been more time for the elements to decay.

This work shows that stellar models also have predicting power. Often we need to use stellar models to explain a set of abundances after they have already been observed. However, by using these best fitting models as an indicator of what an i-process pattern looks like, we can predict a range of Th and U we may expect to observe and see if we can find stars with these properties. That being said, there are observational difficulties in measuring these elements, especially uranium. This is because only one weak line of uranium (U II) is available in the optical spectrum (Frebel & Kratz, 2009). This is also why it is difficult to use [Th/U] as the ratio involved in cosmochronometry.

2.2.5.1 HE0338-3945

Jonsell et al. (2006) give observational abundance measurements for star HE0338-3945, which at the time was classified as an s+r star. Now we classify that star as a CEMP-i and it is included in my sample. Jonsell et al. (2006) give upper limit abundance measurements for Th and U as well as for Ag (Z = 47), Tb (Z = 65), Ho (Z = 67) and Lu (Z = 71). These measurements are not included in the sample of Abate et al. (2015) because upper limits were not used in that work. In this section, I will not be using the upper limit measurements for Ag, Tb, Ho or Lu but I will be using them for Th and U because even an upper limit is helpful in giving an estimate for how much time has passed between production and observation. The upper limits on Th and U for this star are [Th/Fe] < 2.57 and [U/Fe] < 2.82.

As stated in section 2.2.5, this particular star was rejected from my initial study on the predictive power of χ^2 fitting because the fits for the two models were too close together to make a conclusive decision on which model fit best. However, for the purposes of the

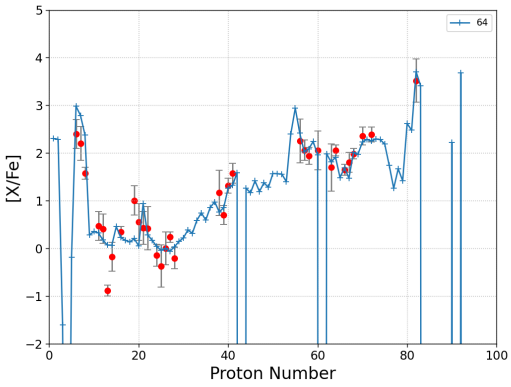

(a) Best decayed fit to CS29497-030, t = 5.58×10^{6} yrs after production.

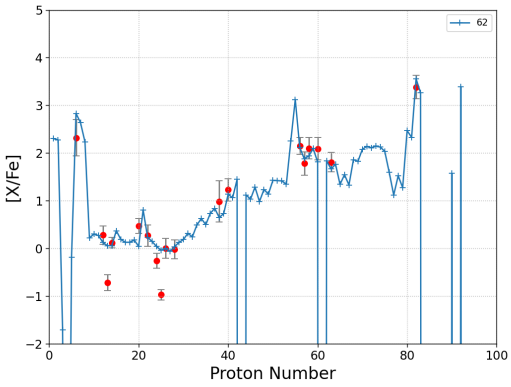

(b) Best decayed fit to CS29526-110, t = 2.48×10^{6} yrs after production.

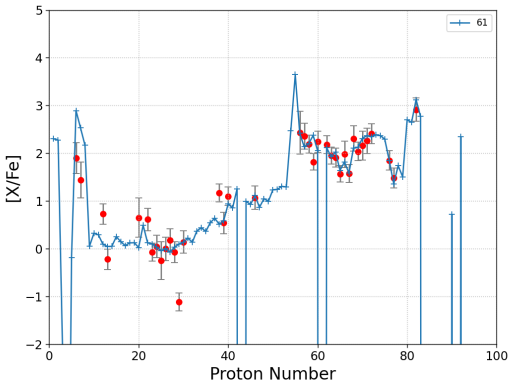

(c) Best decayed fit to CS31062-050, t = 1.65×10^{6} yrs after production.

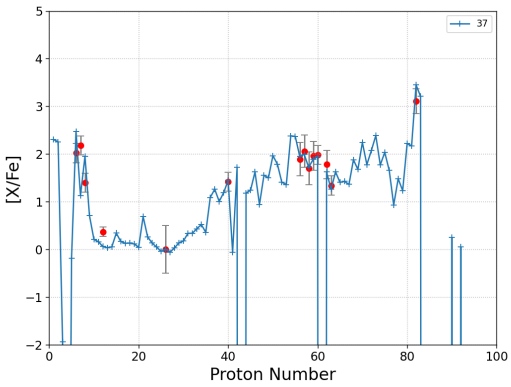

(d) Best decayed fit to HD187861, t = 9.83×10^{1} yrs after production.

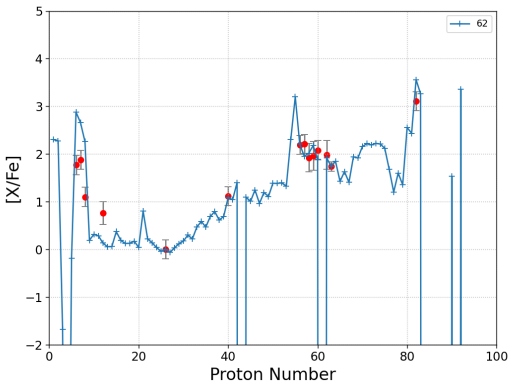

(e) Best decayed fit to HD224959, t = 2.48×10^{6} yrs after production.

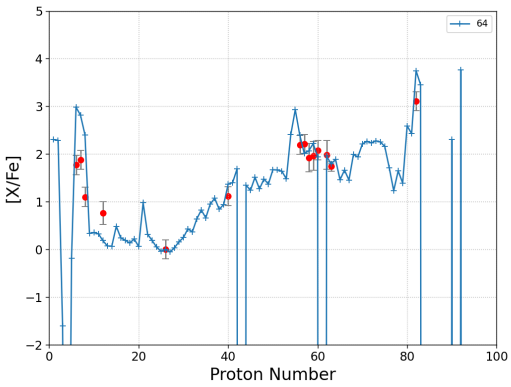

(f) Best decayed fit to HE0143-0441, t = 5.588×10^{6} yrs after production.

Figure 2.32: Best fitting decayed abundance models for each of the stars selected, including predictions of [Th/Fe] and [U/Fe] values. The observations are shown in red with the error bars in grey. The properties of each of these fits can be found in table 2.6.

following analysis, the one-zone intershell model will be used as the abundances can be more easily decayed and we are more interested in the i-process production of Th and U as a whole rather than the particular i-process site.

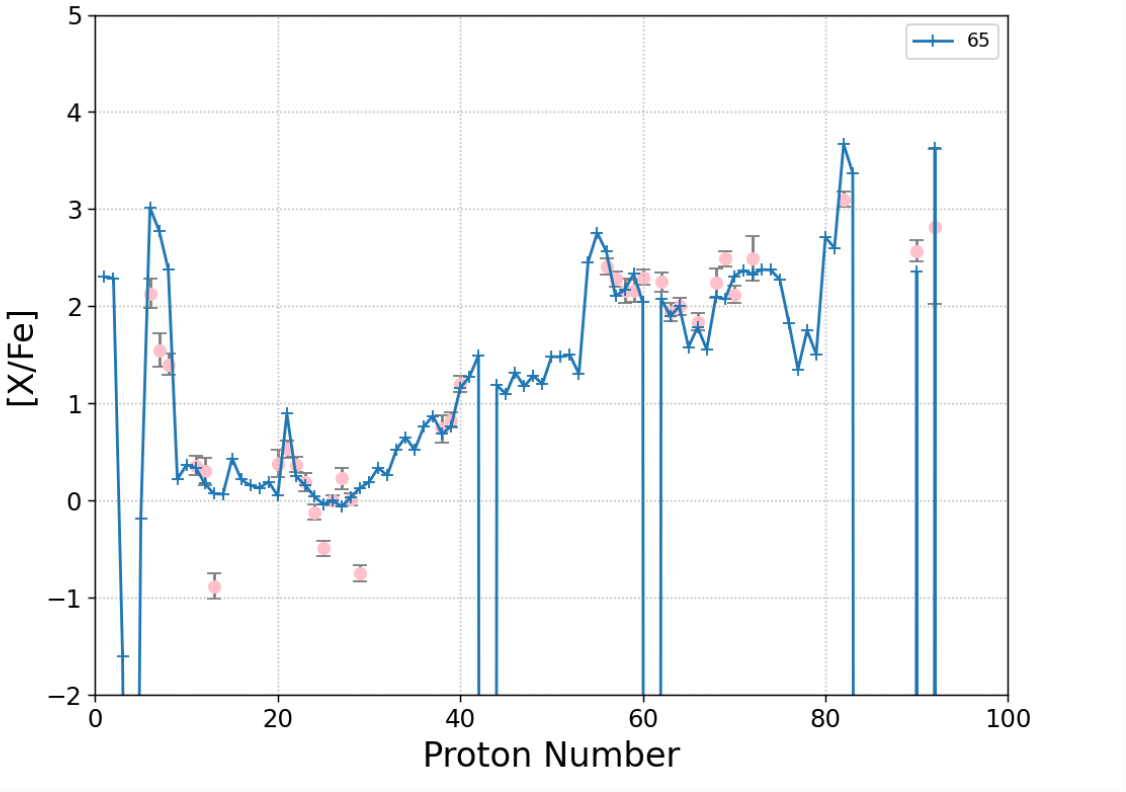

Figure 2.33: Best fit for the Jonsell et al. (2006) abundances of HE0338-3945 with thorium and uranium, t = 1.26×10^7 yrs after production. The fitting parameters are d = 0.048 with χ^2 = 182.3. The observations are shown in pink with grey error bars.

To find a best fitting decayed model for this star, the same method described in 2.2.5 will be used. Here, the best fitting cycle is 529. This cycle was decayed and the best fitting model, including the Th and U, was found to be cycle 65 (t = 1.26×10^7 yrs after initial production), d = 0.048 and χ^2 = 182.3. Figure 2.33 shows that fit. We can see that the Th is underproduced by the model by around 0.2 dex and the U is overproduced. The overproduction of U shows that the upper limit on the uranium abundance can be produced by the i process because the uranium will eventually decay back to that value. The underproduction of the Th shows that the i process can achieve close to the upper limits on the observations.

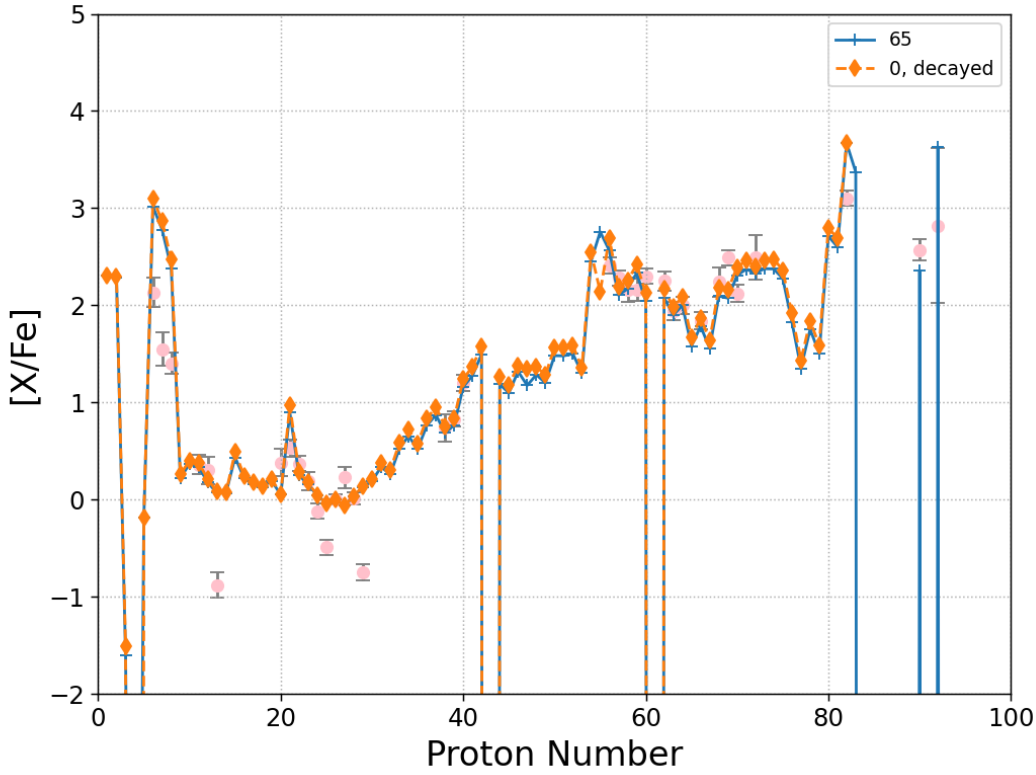

Figure 2.34: Best fit for the decayed run (blue line with crosses) compared to the original best fit (orange line with diamonds). The observations are shown in pink with grey error bars.

Figure 2.34 shows the new fit compared to the original best fit model of Figure 2.17a. The Th and U have been removed from the original best fit as we know that the decay done for the original model (orange line) does not treat the upper portion of the network correctly as it assumes everything β decays, which is not the case here. The main difference between the two models is Cs (Z = 55). The Cs in the decayed run is higher than the original best fit because ^{135}Cs has a half life of 2.3 Myr and therefore has not had time to decay yet at this point in the decayed run.

What we want to understand by doing this is how much time has passed between when the model fits the rest of the observed abundances (the original fit) and when it also fits the Th and U (the best fit from the decayed run). This tells us how much time has passed between initial production of Th and U and the observations. Figure 2.35 shows the evolution of elemental thorium and uranium with respect to time throughout the period of 10 Gyr over

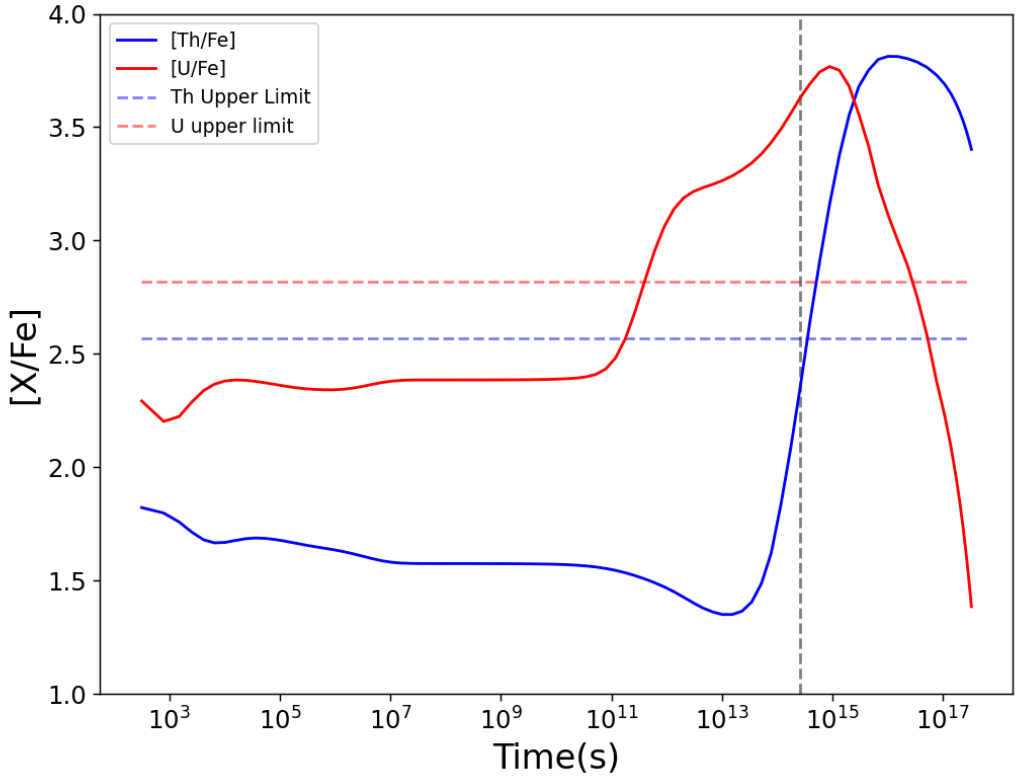

Figure 2.35: Abundances of thorium and uranium relative to iron as they decay, where the time shown here is the time that has passed since production. The upper limit observations taken by Jonsell et al. (2006) are marked by the blue (Th) and red (U) dashed lines. The grey dashed line indicates the best fitting cycle from the decayed abundances.

which the abundances are allowed to decay. The abundances here have been diluted by a factor of d = 0.048 in order to replicate the best fit model of Figure 2.33. This shows us that [U/Fe] peaks just after the best fitting model (grey dashed line) while the [Th/Fe] continues to rise, going beyond the upper limit. The horizontal lines on this figure show the upper limit on the observed Th (blue dashed line) and U (red dashed line). There is a point at which both of these ratios match the observational 'upper limit' therefore, we know it is possible to get abundances of [Th/Fe] and [U/Fe] as high as this, or higher, from an i-process event. The increase in Th comes from α decays of ^{236}U, Figure 2.36 shows the abundance by mass fraction of ^{232}Th and ^{236}U (as well as other isotopes of uranium) against time for the decayed run. We can see that after the ^{236}U peaks and falls off, the ^{232}Th continues to increase and

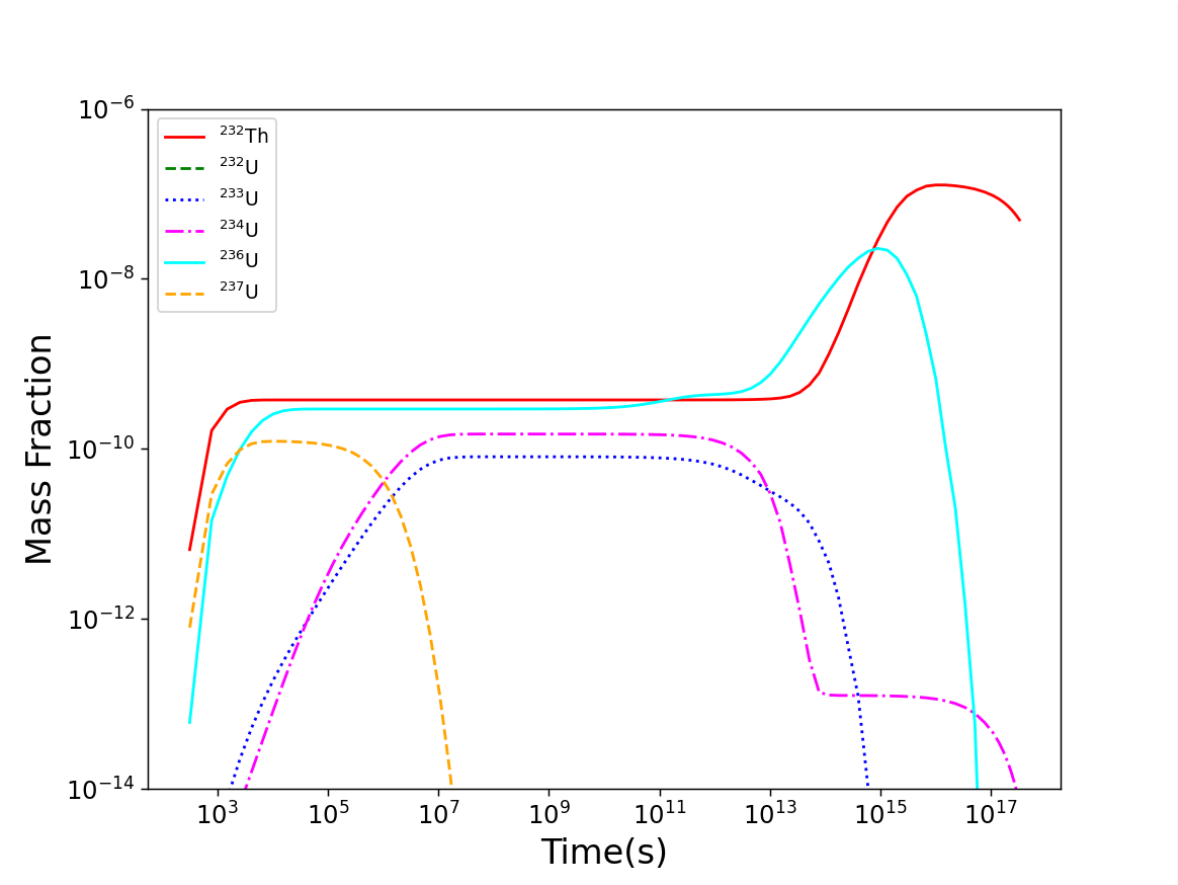

Figure 2.36: Evolution of the abundance by mass fraction of ^{232}Th (red line) and ^{236}U (light blue line) as well as ^{232}U, ^{233}U, ^{234}U, and ^{237}U while the decays are occurring.

peaks higher and later than ^{236}U. Other unstable isotopes, such as ^{232}U, ^{233}U, ^{234}U, and ^{237}U, do not provide as strong of a contribution, being produced early and decaying quickly becoming uninteresting to us as.

Figure 2.35 shows that at any time up to around 4×10^{11} s the model produces an abundance of [Th/Fe] and [U/Fe] that is within this upper limit and therefore reproduces the abundances well. However, after this point where the value of [Th/Fe] matches the upper limit (around $t = 3.5\times10^{14}$ s), [U/Fe] is about to peak and at the two points where [U/Fe] matches the upper limit (around $t = 4\times10^{11}$ s and $t = 2.8\times10^{16}$ s) the Th is either too low or too high. However, the nuclear network used to create the one-zone i-process models was never designed to produce isotopes and elements as heavy as Th and U so this may be an issue with the network itself rather than the inability of the i process to reproduced these two upper limits at the same time.

2.2.5.2 Gull et al 2018: 's+r' star, J0949-1617

Gull et al. (2018) state they have found the first ever true CEMP - s+r star (J0949-1617). This is a star which has first been enriched with r-process material, due to the composition of the gas cloud it was formed in, and then has undergone the s process in order to enrich it with s-process material. In pre-enrichment scenarios such as this, Abate et al. (2016) showed that the final abundances depend on the material transferred from the AGB companion rather than on both the companion and the pre-enrichment. However, the s process cannot produce elements as heavy as Th. Therefore, the abundances of thorium and uranium would remain unaffected by any s-process abundance build-up, hence the claim that this star is 's+r'. On the other hand, any simultaneous s- and r-process enrichment in metal-poor stars is generally attributed to the i process (e.g. CEMP-r/s stars). Therefore it is interesting to see how these abundances compare to an i-process model.

Figure 2.37 shows the comparison of the abundances of J0949-1617 with the one-zone intershell and RAWD models. The abundances considered here do not include Th in the fitting. The χ^2 value of the fits for the one-zone and RAWD model are 111.7 and 144.4 respectively. The one-zone model fit is at cycle 547 ($\tau = 9.83$), dilution factor 0.002 and neutron density 6.08×10^{13} cm^{-3}. The RAWD model best fit occurs at cycle 1700 and dilution 0.001. Given the neutron density of the one-zone intershell model fit, I would expect an i-process like pattern. However, the dilution factor is the second lowest possible dilution factor that can be chosen, so the modelled abundances do not contain a high fraction of pure i-process material. The one-zone model does not match the elements Ru, Rh and Ba by about 0.5, 0.4 and 0.2 dex respectively but appears to replicate the rest of the abundances well up until lead. The RAWD model gives a poor fit around Ba, overproducing it by around 0.5 dex, and La, overproducing it by around 0.3 dex, and the trans-europium elements. Neither model can replicate the abundances of Lu (Z = 71) and Hf (Z = 72). The one-zone model overproduces these elements by around 0.15 dex and 0.3 dex for Lu and Hf respectively. The RAWD model also overproduces Lu and Hf but by 0.35 dex and 0.5 dex respectively. Neither model has a good fit around the lead abundance, which as previously discussed, appears to be the deciding factor in reducing the χ^2 value and providing a good fit.

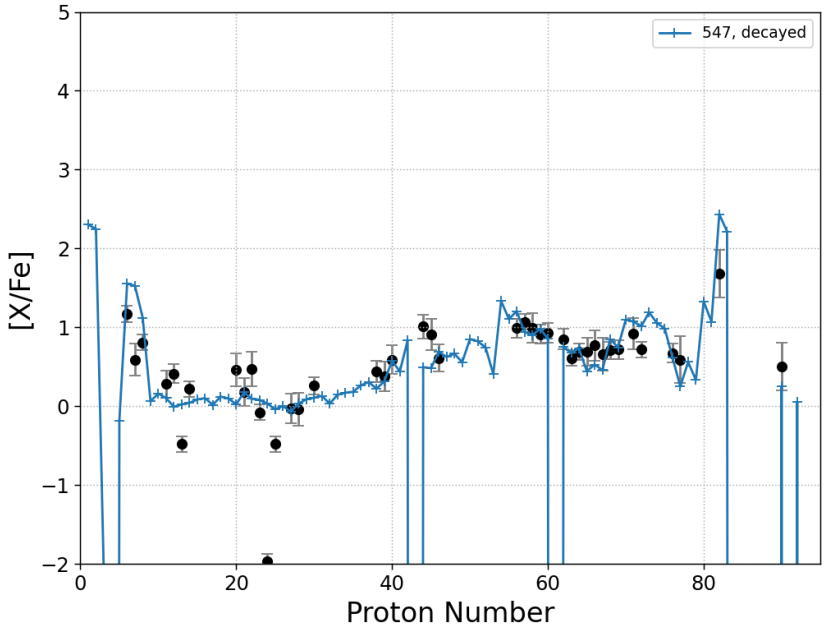

(a) Best fitting one-zone AGB intershell model with fitting parameters d = 0.002 at cycle 547, resuting in $\chi^2 = 111.7$.

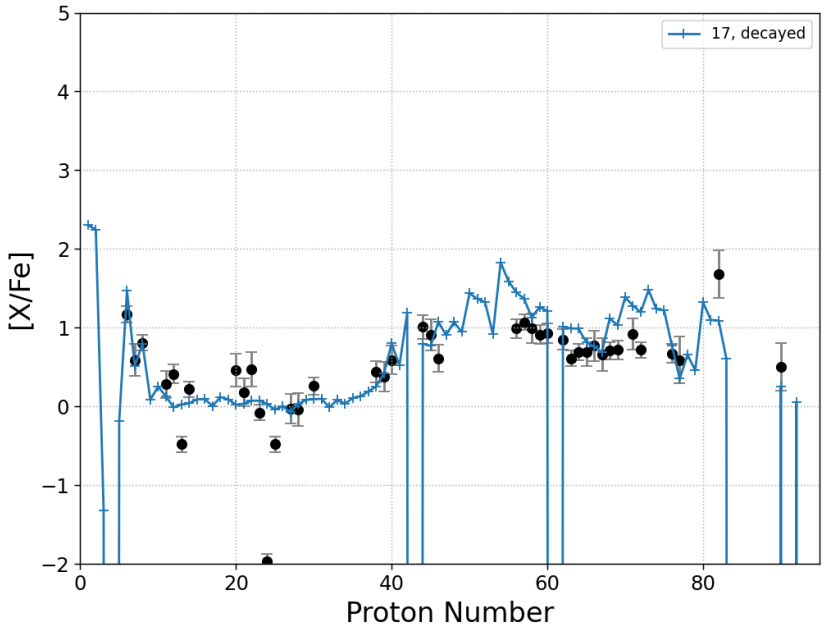

(b) Best fitting RAWD model with fitting parameters d = 0.001 at cycle 1700, resulting in $\chi^2 = 144.4$

Figure 2.37: Best [X/Fe] fits for the 's+r' star J0949-1617. The observations are the black circles with grey error bars.

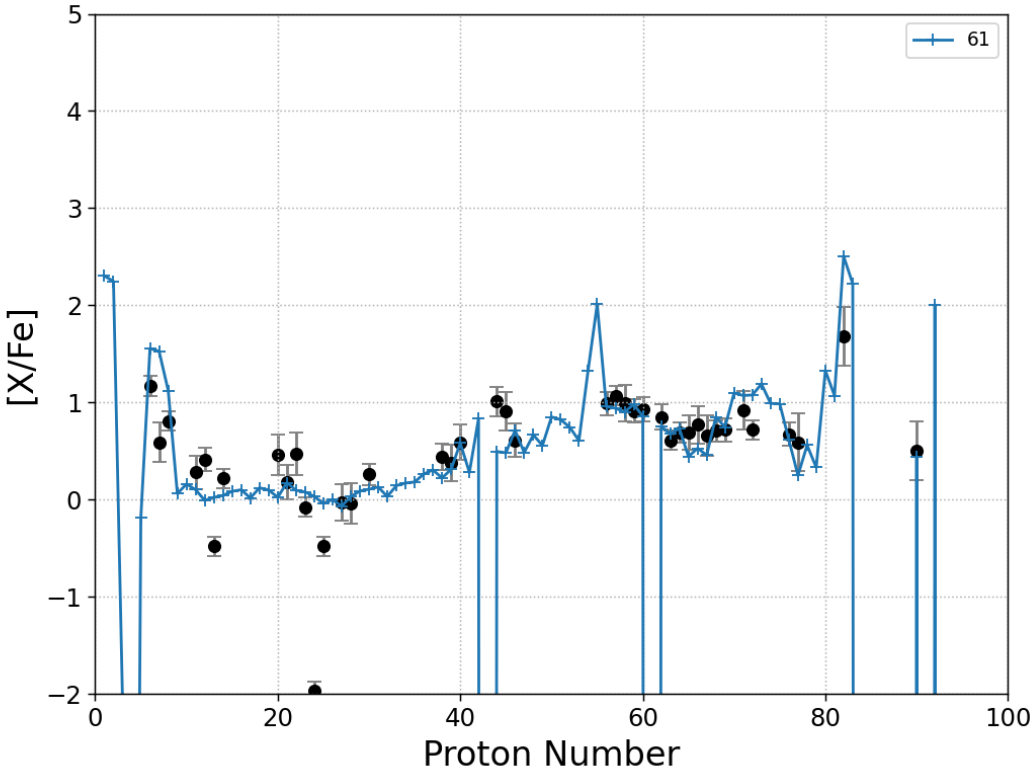

Figure 2.38: Best fitting model to the abundances of J0949-1617 for the decayed run. With fitting parameters d = 0.002, 1.65×10^6 yrs after initial production, resulting in $\chi^2 = 120.0$. The observations are the black circles with grey error bars.

Given there is a thorium abundance measurement for this star, it is more appropriate to find the best fitting model using the same technique as in section 2.2.5.1 because the Th measurement can be incuded in the χ^2 fit. Cycle 547 is decayed and the best fitting model was found to be cycle 61 (t = 1.65×10^6 yrs from production), d = 0.002 and $\chi^2 = 120.0$. Figure 2.38 shows this fit. We can see that Th is reproduced closely by this model and the Ba is now also replicated by the model. However, the fit still has the problems of not replicating the Ru, Rh, Lu or Hf as previously discussed. Figure 2.39 shows the evolution of the abundance of [Th/Fe] as decays occur, with a dilution factor of d = 0.002 applied to the abundances. The blue dashed line shows the observational measurement from Gull et al. (2018). The [Th/Fe] matches within error until 2.6×10^6 yrs (8.2×10^{13} s) due to the flat abundance profile. At this point the [Th/Fe] begins to increase due to the decay of ^{236}U discussed earlier. Therefore, if

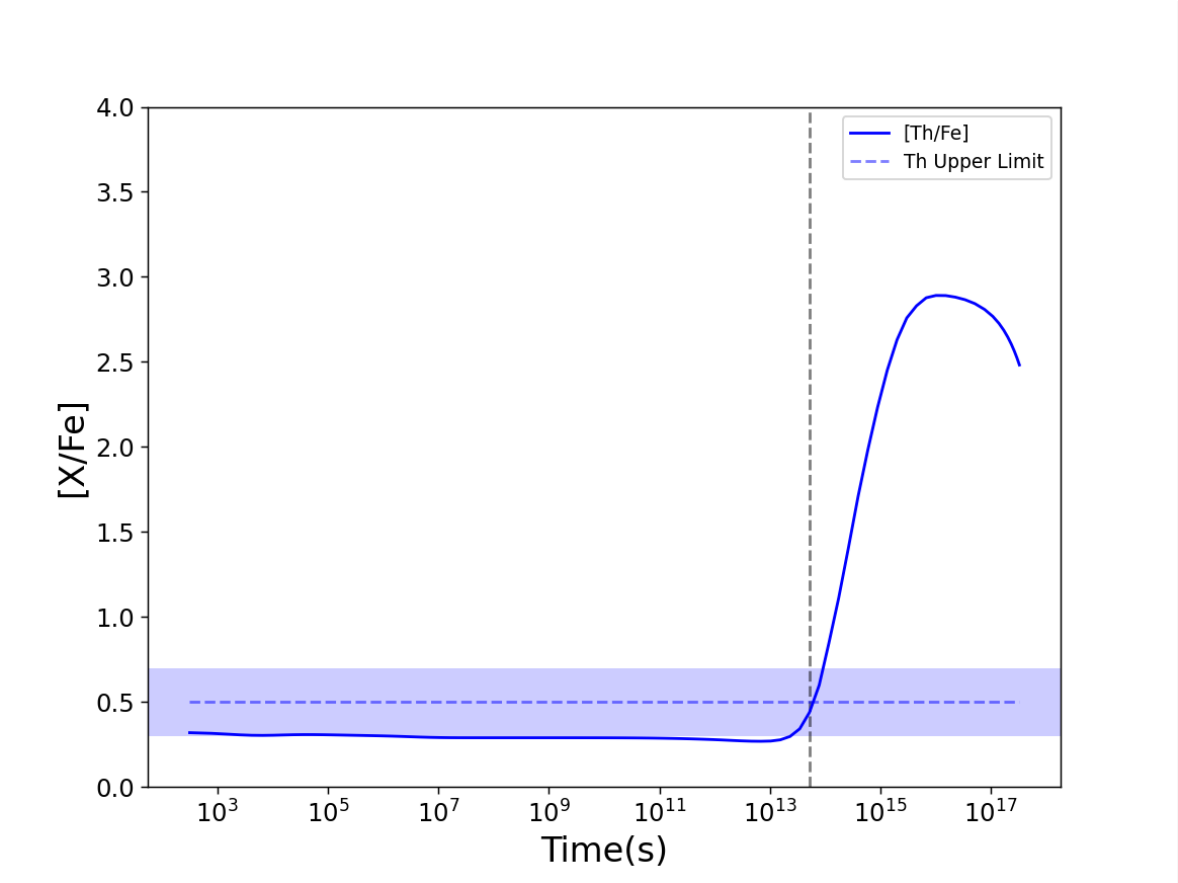

Figure 2.39: Abundance of [Th/Fe] through time as the abundances are left to decay. The grey dashed line denotes the best fit model while the blue dashed line is the measurement of [Th/Fe] from Gull et al. (2018) with the shaded region around it representing the range the measurement could be taking error into account.

the Th has been produced via the i process, it has been observed within 3 Myr of production. However, given the poor fit to the other elements and the low dilution factor, it is more likely that this star is 's+r' and that the Th abundance can be attributed to an r-process event.

Overall, this section (section 2.2.5) has shown that is it possible to produce thorium and uranium in the i process. Not only that, we can also replicate abundances of Th and U that have been previously attributed to the r process, with i-process models. My calculations show that plausible ranges for i-process production of thorium and uranium are $0.25 < [\text{Th/Fe}] < 2.30$ and U is $0.05 < [\text{U/Fe}] < 3.76$. This is backed up by the fact that the Th and U abundances for HE0339-3945 found by Jonsell et al. (2006) are well within that range and are easily replicated by the one-zone i-process model.

3. Determining other i-process signatures

We can try to understand the nucleosynthesis that is occurring in stars through other means than just χ^2 fits of models to detailed abundance patterns of individual stars. We can also look at individual elemental abundance ratios. These ratios can give us information about how one element is made relative to the others and therefore give us clues about the processes that could be occurring in the interior of stars. It is important to gather information on the kind of elemental signatures we may expect from the i process. It would be useful to find some ratios or some anomalous abundances that are unique to, and therefore indicative of, the i process. Finding these abundance signatures is useful because we do not have a complete abundance inventory of all stars and wouldn't necessarily need one if we could find a signature that could easily distinguish the s process from the i process.

3.1 Three-element plots

We can investigate the elemental abundance ratios of the CEMP-i sample by using three-element plots. A three element plot, shows two abundance ratios with the same reference element, for example [Ba/Fe] versus [La/Fe]. The three-element plot [Ba/Fe] versus [Eu/Fe] lead to the classification of CEMP stars based on the groupings that appeared in this space. In this work, I want to find out how well the observations match the models in various three-element spaces. I want to look for regions where the models fit the observations closely and regions where the models do not fit the observations and investigate why that might be the case. This will give us an insight, both into the abundance signatures of the i process we should be looking out for and also the signatures that our models are not replicating.

3.1.1 Constraining the choice of elements

Of all the CEMP-i stars in the sample (section 2.2.2), there are 45 elements that had a measurement in at least one star. This gives a possible 14190 combinations of three elements

that could be plotted. To narrow the number of possible combinations further, it was stipulated that there had to be at least three stars with a given element so that there were at least three points on the three-element plots. This brings the potential combinations of three elements down to 4932. This is still a lot of potential three-element plots, therefore I needed a method to figure out which elemental ratios are going to be most interesting to look at. To do this I used a number of steps:

1. For each abundance ratio in question, I took the available stars and found the mean average of that abundance ratio. This allowed me to find the 'average' point of a CEMP-i star on the three element plot I was interested in.

2. For each point on the modelled line (the AGB intershell i-process model) I found the distance between the point on the line and the average abundance point previously calculated. The distance was calculated using equation 3.1,

$$r = \sqrt{(\text{model}_y - \text{obs}_y)^2 - (\text{model}_x - \text{obs}_x)^2} \tag{3.1}$$

   where model_x and model_y are the x and y-axis values for the point on the modelled line and obs_x and obs_y are the x and y values of the average CEMP-i point.

3. Of the distances calculated at the previous step, the smallest distance between the average CEMP-i abundance and the modelled line is becomes r_{min}

Figure 3.1 illustrates this concept. We can see that in this case $r_2 = r_{\text{min}}$ because it is the shortest distance from the blue average point to the line. In reality, the distance from the average point would be calculated for each point on the line but for ease of understanding, this has naturally not been included in this figure. A similar method was used by Choplin et al. (2021) (their equation 5). They calculate a distance d_{RMS}, which is the average abundance distance to the solar-scaled r process, by summing the distance squared between the abundances and the r-process abundance and taking the square root, whereas the method in this work takes the minimum distance rather than the sum of the distances.

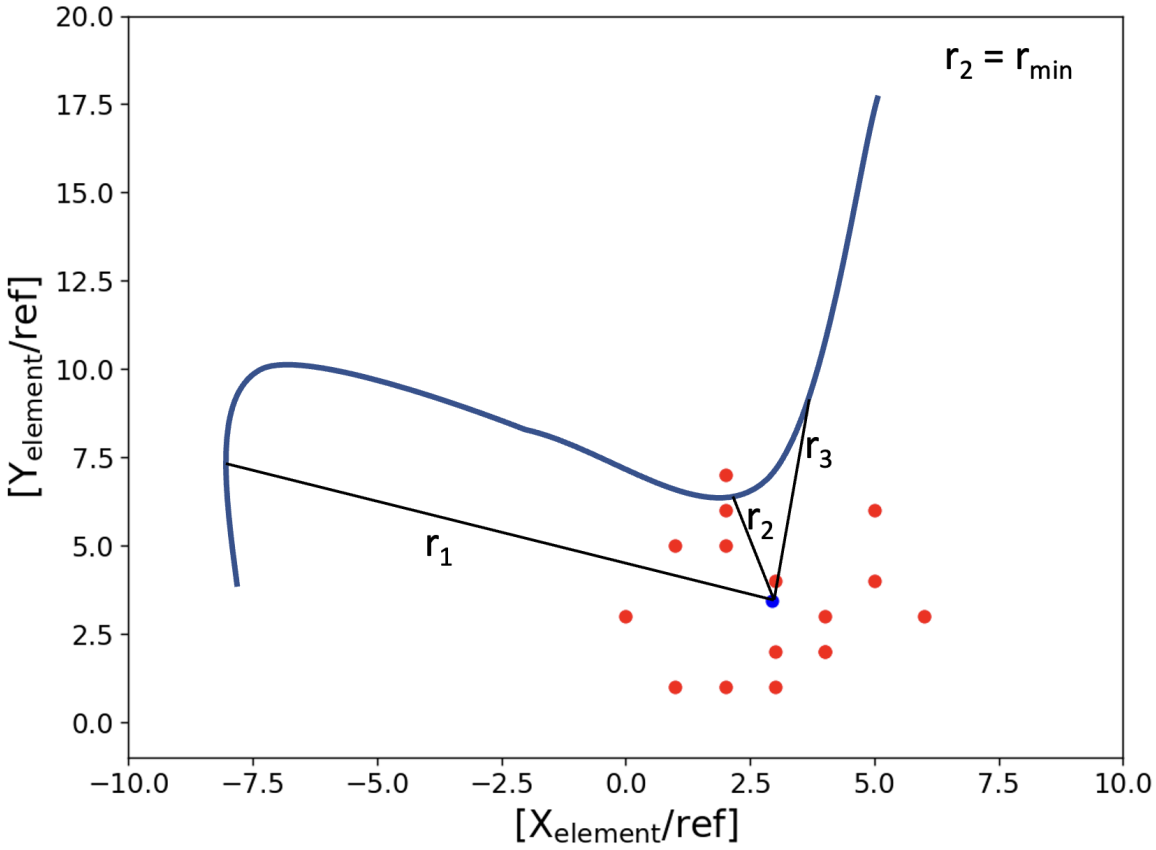

Figure 3.1: A hypothetical three-element plot to demonstrate how the calculation of r_{min} works. The red points represent a hypothetical CEMP-i sample, the blue line is a hypothetical modelled line. The blue point is the average position of all the CEMP-i stars, with the black lines representing three different distances from the point to the modelled line.

Table 3.1: The 100 smallest r_{min} values and the combination of three elements considered, where the first element is the element on the y-axis, the second is the element on the x-axis and the third is the reference element. Combinations highlighted in blue are the combinations that are investigated in more detail (see section 3.3.1).

Combination of Elements	r_{min}
Sr, Ce, Yb	0.0006100
Sm, Gd, Tm	0.0007699
Ce, Sm, Hf	0.001722
Eu, Pb, Gd	0.002000

Continued on next page

Table 3.1 – continued from previous page

Combination of Elements	$r_{\min}$
Sm, Er, Tm	0.002267
La, Nd, Tm	0.002302
Er, Gd, Tm	0.002616
Eu, Yb, Tm	0.002858
Ti, Y, Cr	0.003444
Ni, Dy, Gd	0.003816
Nd, Dy, Gd	0.004191
Nd, Sm, Gd	0.004299
La, Eu, Sc	0.004343
Ba, Dy, Yb	0.004345
Ce, Sm, Er	0.004399
Fe, Eu, Dy	0.004418
La, Er, Pb	0.004693
Mg, Ni, Sc	0.004732
Eu, Dy, Pb	0.005044
Nd, Gd, Tm	0.005087
Nd, Dy, Zn	0.005203
Ba, La, Yb	0.005860
Eu, Ce, Tm	0.005996
La, Er, Yb	0.006015
Dy, Sc, Tm	0.006476
La, Nd, Er	0.006584
La, Gd, Tm	0.006932
Mg, Sm, Tm	0.007410
Eu, Gd, Tm	0.007891
Y, Zr, Sc	0.008194

Continued on next page

Table 3.1 – continued from previous page

Combination of Elements	$r_{\min}$
Nd, Sm, Tm	0.008249
Nd, Er, Yb	0.008587
Dy, Yb, Tm	0.008630
Ce, Sm, Dy	0.008789
Ce, Yb, Tm	0.008934
La, Dy, Gd	0.009064
Nd, Dy, Er	0.009300
La, Nd, Dy	0.009361
Fe, Dy, Yb	0.009450
Eu, Sm, Pb	0.009898
Sm, Er, Pb	0.009945
La, Er, Gd	0.009957
Fe, Ce, Sm	0.01035
Pb, Yb, Tm	0.01077
Pb, Gd, Yb	0.01079
Er, Gd, Yb	0.01081
Na, Mg, Zn	0.01124
Nd, Sc, Gd	0.01140
Sr, Si, Co	0.01147
Eu, Ce, Dy	0.01171
Y, Eu, Ce	0.01196
La, Sm, Er	0.01228
Sr, Dy, Yb	0.01232
Eu, Pb, Tm	0.01252
Y, Zr, Ce	0.01255
Er, Pb, Yb	0.01271

Continued on next page

Table 3.1 – continued from previous page

Combination of Elements	$r_{\min}$
Dy, Er, Tm	0.01311
Sc, Gd, Yb	0.01368
La, Sm, Tm	0.01385
Sr, Ba, Eu	0.01387
Ce, Gd, Tm	0.01396
Ce, Pb, Tm	0.01402
Ni, Si, Sc	0.01504
Mn, Ni, Gd	0.01509
Sm, Dy, Tm	0.01514
Mn, Dy, Gd	0.01540
Ce, Gd, Yb	0.01552
Y, Nd, Er	0.01552
Y, Zr, Dy	0.01564
Gd, Yb, Tm	0.01569
Nd, Er, Tm	0.01588
Nd, Sm, Er	0.01596
Eu, Ce, Er	0.01625
Dy, Gd, Tm	0.01631
Fe, Sm, Er	0.01655
Zr, Eu, Ce	0.01662
Zr, Eu, Tm	0.01675
La, Sm, Gd	0.01677
Zr, Er, Yb	0.01686
Dy, Pb, Gd	0.01704
Er, Hf, Tm	0.01706
La, Er, Tm	0.01738

Continued on next page

Table 3.1 – continued from previous page

Combination of Elements	r_{min}
Sm, Pb, Yb	0.01742
Zr, Yb, Tm	0.01770
Ba, Gd, Tm	0.01790
Ce, Er, Yb	0.01800
Sm, Gd, Yb	0.01807
Sm, Dy, Er	0.01811
Y, La, Sm	0.01814
La, Dy, Tm	0.01828
Nd, Dy, Tm	0.01839
Dy, Pr, Hf	0.01843
Ba, Nd, Sm	0.01849
La, Nd, Gd	0.01857
Er, Pb, Gd	0.01886
Ba, Eu, Ce	0.01914
Ba, Ce, Dy	0.01914
Y, Zr, Pr	0.01920
Ba, Eu, Dy	0.01925
Sm, Pb, Tm	0.01955

Table 3.2: The 100 largest r_{min} values and the combination of three elements considered, where the first element is the element on the y-axis, the second is the element on the x-axis and the third is the reference element. Combinations highlighted in blue are the combinations that are investigated in more detail (see section 3.3.2)

Combination of Elements	r_{min}
Mg, Ca, O	2.800
Na, Fe, Eu	2.806

Continued on next page

Table 3.2 – continued from previous page

Combination of Elements	$r_{\min}$
Na, Fe, Ce	2.819
Ti, Ni, O	2.822
Ti, Mn, O	2.824
Cr, Ni, O	2.838
Fe, Sc, Hf	2.841
N, Ce, Co	2.866
N, Ba, Co	2.868
N, Dy, Co	2.869
N, Eu, Ni	2.871
Fe, Pb, Zn	2.871
N, Eu, Co	2.873
Na, Fe, La	2.880
C, Fe, Hf	2.889
Fe, Sc, Gd	2.890
Fe, O, Hf	2.905
Mg, Ni, O	2.926
N, Nd, Co	2.927
N, Nd, Ni	2.931
C, Fe, Sm	2.933
N, La, Co	2.935
N, Er, Co	2.936
Ni, Sm, O	2.938
N, La, Ni	2.947
N, Ba, Mn	2.962
C, Fe, Gd	2.965
Na, Ca, O	2.965

Continued on next page

Table 3.2 – continued from previous page

Combination of Elements	$r_{\min}$
Mn, Sm, O	2.967
C, Fe, Sr	2.979
Fe, Sc, Yb	2.985
C, Fe, Y	2.988
N, Eu, Mn	2.988
Fe, Sc, Tm	2.992
Fe, O, Gd	2.995
N, La, Mn	3.011
C, Fe, Eu	3.018
C, Ti, Fe	3.019
N, Nd, Mn	3.020
Na, Mn, O	3.033
C, Fe, Dy	3.036
C, Ca, Fe	3.040
C, Na, Fe	3.043
Mg, Mn, O	3.050
C, Fe, Ce	3.051
C, Mg, Fe	3.056
Fe, O, Tm	3.058
C, Fe, Tm	3.063
C, Fe, Er	3.100
N, Fe, Sm	3.111
C, Pb, Co	3.121
C, N, Mn	3.123
C, Fe, Zr	3.140
C, Fe, Ba	3.148

Continued on next page

Table 3.2 – continued from previous page

Combination of Elements	$r_{\min}$
N, Fe, Hf	3.163
C, N, Ca	3.165
C, Fe, Nd	3.174
N, Fe, Ce	3.189
Fe, O, Yb	3.195
N, Fe, Eu	3.202
C, Fe, Pr	3.204
N, Fe, Gd	3.216
Pb, O, Co	3.221
Na, Fe, O	3.243
C, Fe, Yb	3.251
C, Fe, La	3.253
N, Fe, Dy	3.267
N, Fe, Ba	3.278
N, Fe, Nd	3.295
Mn, Ni, O	3.306
N, Pb, Co	3.312
Ca, Ni, O	3.314
Ca, Mn, O	3.317
N, Fe, La	3.330
N, Fe, Er	3.334
N, Fe, Yb	3.348
N, Fe, Pr	3.360
Fe, Cr, O	3.383
N, Fe, Tm	3.388
Fe, Mn, O	3.421

Continued on next page

Table 3.2 – continued from previous page

Combination of Elements	$r_{\min}$
Fe, Ni, O	3.481
N, Fe, Pb	3.510
Mg, Fe, O	3.557
C, Fe, Pb	3.574
Fe, Er, O	3.664
Fe, Dy, O	3.678
C, N, Fe	3.708
Fe, Zr, O	3.792
Ti, Fe, O	3.821
Fe, Y, O	3.855
Fe, Sr, O	3.856
Ca, Fe, O	3.898
Fe, Pb, O	3.942
Fe, Pr, O	4.009
Fe, La, O	4.019
Fe, Nd, O	4.021
Fe, Ba, O	4.028
Fe, Ce, O	4.048
Fe, Eu, O	4.064
Fe, Sm, O	4.100

From all the $r_{\min}$ values, I picked out the 100 smallest and the 100 largest. The 100 smallest values correspond to the three element plots where the one-zone AGB intershell model line runs closest to the observations. The 100 largest values correspond to the plots where the modelled line runs farthest from the observed abundances, where we have a minimum of three data points to plot. Tables 3.1 and 3.2 show the 100 smallest and largest $r_{\min}$ values and

their corresponding three-element combinations. I am most interested in these combinations because the 100 smallest $r_{\rm min}$ values show where the models run closest to the observations and the 100 largest may show interesting discrepancies between the models and observations.

3.2 A typical three element plot

This section will briefly describe what a 'typical' three-element plot will look like through the rest of this work. On each three-element plot, there are three models that are plotted: the one-zone AGB intershell model described in section 2.1.1 restricted to those parts of the run that have neutron densities between $10^{12}\,{\rm cm}^{-3}$ and $10^{15}\,{\rm cm}^{-3}$ (cycles 400 - 570), the RAWD model described in section 2.1.2 and an s-process model at neutron densities $10^{6}\,{\rm cm}^{-3} < n < 10^{8}\,{\rm cm}^{-3}$. The s-process model is another one-zone model made using ppn. It is the ^{13}C pocket trajectory from Pignatari et al. (2016) with metallicity $Z = 1\times10^{-4}$, matching the metallicity used for the i-process model. The initial abundances by mass fraction for the key isotopes here are: $^{1}H = 1.04\times10^{-2}$, $^{12}C = 3.64\times10^{-1}$ and $^{13}C = 1.0\times10^{-1}$. The initial temperature and density for this model are $T = 5.5\times10^{7}$ K and $\rho = 1\times10^{2}\,{\rm g\,cm}^{-3}$.

Under the assumption that observation is taking place long after nucleosynthesis has ceased, all modelled abundances are decayed. On each plot, there are also two diluted versions of the one-zone intershell model. The dilution factors used are d = 0.0334 and 0.088, where d = 0.0334 is the average dilution factor of the five smallest χ^2 models in section 2.2.2.1 and d = 0.088 is the largest dilution factor of any of the models (this is the dilution factor for star LP625-44). Also included alongside these models is a black cross along the one-zone i-process model line. The cross represents the cycle where maximum neutron density is reached which is cycle 512 with a neutron density of $4.08\times10^{14}\,{\rm cm}^{-3}$.

Also included on each plot are two sets of observational data. First, the sample of CEMP-i stars from Abate et al. (2015) used throughout this work and described in section 2.2.2 and second a sample of CEMP-s stars. For this work, the sample of CEMP-s stars was collected from the JINAbase[1] (Abohalima & Frebel, 2018) and details of the selection criteria can be found in section 3.2.1.

[1]https://jinabase.pythonanywhere.com/

Finally, included in these plots are s-process yields from Lugaro et al. (2012). The yields here are 1.9$M_\odot$ AGB yields at metallicity $Z = 1\times10^{-4}$ and the width of the partial mixing zone is $M_{mix} = 2\times10^{-3} M_\odot$. These yields have been calculated for a detailed model at a specific mass and metallicity and therefore are likely to be more accurate in comparison to a one-zone s-process trajectory, hence they have also been included on the plots. Given this work is a study of the i process, one may ask why so much s-process data has been included on the three-element plots. The reason is so that we can find signatures that are distinctly different between the two processes. This will help us to separate s- and i-process signatures, given that their modes of operation are similar. It will also help us to understand where we may have mis-classified or misunderstood an i-process signature.

3.2.1 CEMP-s JINAbase sample

The CEMP-s sample of stars was collected from the JINAbase, which is a database for metal-poor stars. The sample of CEMP-s stars are selected from all stars in the JINAbase that match the following criterion: [Eu/Fe] < 1, [Ba/Fe] > 1, [Ba/Eu] > 0 and [C/Fe] > 0.9, this is the Masseron et al. (2010) definition of a CEMP-s star. This gave me a sample of 20 CEMP-s stars from various authors. Of the 20 stars, 3 were repeated entries due to abundance measurements being collected by two different authors, namely the objects HE2158-0348, HD196944 and CS22881-036.

- The abundances of HE2158-0348 were calculated by Cohen et al. (2006) and Cohen et al. (2013). For this work, I will take the abundances of this star from Cohen et al. (2013) as it is the most up-to-date analysis of this object, given the later paper has largely the same authors as the earlier work.

- The abundances of HD196944 were calculated by Roederer et al. (2014) and Aoki et al. (2002). Here, I have selected the abundances of Roederer et al. (2014) because the abundances of 7 other stars in this sample come from this paper, whereas no others come from Aoki et al. (2002).

- CS22881-036 appears in the CEMP-s sample with two measurements, one from Preston & Sneden (2001) and another from Roederer et al. (2014). Preston & Sneden (2001)

gives a value of [Eu/Fe] of 0.99, while Roederer et al. (2014) finds [Eu/Fe] of 0.55. However, it also appears as a CEMP-i star in the sample of Abate et al. (2015) and Hampel et al. (2016), which are the samples I am using in this work. Here, this star has an [Eu/Fe] of 1.045. Therefore, for this work I will continue to classify this star as CEMP-i and remove the two appearances of CS22881-036 from my CEMP-s sample.

After selecting these stars, the size of the CEMP-s sample is 16. Table 3.3 shows the properties of each star, including T_{eff}, log g, abundances of C, Ba and Eu and the reference paper for the abundances.

3.3 Resulting three-element plots

3.3.1 'Good' fits

Table 3.1 shows the combinations of elements with the smallest r_{min} value and therefore the combinations for which the modelled line matches the observational data the closest. However, 100 plots is still a lot to analyse, so this number needed to be narrowed further, in order to find the plots which are of the most interest. The plots that were rejected had the following features:

1. The CEMP-i and CEMP-s sample occupied the same space on visual inspection. These plots got rejected because we cannot spot trends unique to the i-process if the observations for the selected elements overlap for the two groups of stars. An example of this can be found in Figure A.1.1

2. The trajectories of the models do not show significant variations across the phase space. These plots got rejected because there is no significant nucleosynthesis, and so no clear trends can be distinguished. An example of this can be found in Figure A.1.2.

3. The combination of elements contains a light element, which here is any element lighter than iron. These plots were rejected because when we study neutron capture processes we are mainly interested in the heavy element production. Other processes are primarily responsible for the production of light elements e.g. CNO cycle or alpha-capture. As

Star	T_{eff} (K)	$\log_{10}$ g	Number of Elements Measured	[C/Fe]	[Ba/Fe]	[Eu/Fe]	Reference
HE0202-2204	5280	1.65	20	1.12	1.35	0.48	2
HE1135+0139	5487	1.8	19	1.16	1.08	0.33	2
CS22880-074	6050	4	12	1.60	1.29	0.54	6
CS29495-042	5180	2.55	30	1.07	1.79	0.61	7
HE2158-0348	5215	2.5	21	1.90	1.68	0.74	3
CS22945-024	5120	2.35	36	2.30	1.43	0.44	7
CS22879-029	5920	3.7	37	1.46	1.39	0.59	7
CS22896-136	6190	3.85	37	1.30	1.44	0.81	7
CS22947-187	5300	1.4	38	1.25	1.53	0.55	7
CS22956-102	6220	3.85	28	2.21	1.99	1.0	7
CS29512-073	5560	3.44	16	1.67	1.55	0.55	1
CS29513-014	5440	1.55	38	1.03	1.38	0.24	7
HE0054-2542	5300	2.7	28	2.13	1.52	0.78	4
HD196944	5310	1.75	38	1.19	1.47	0.12	7
HD201626	5175	2.8	29	1.48	1.73	0.95	5
HE1045+0226	5077	2.2	18	1.09	1.19	0.22	3

Table 3.3: CEMP-s sample details including the name of the star, the abundance relative to iron of carbon, barium and europium and the paper from which the measurement has come from. References: (1) Allen et al. (2012), (2) Barklem et al. (2005), (3) Cohen et al. (2013), (4) Hansen et al. (2015), (5) Placco et al. (2015), (6) Preston & Sneden (2001), (7) Roederer et al. (2014)

previously discussed in section 2.2.4, we also have reasons to distrust very light element production in one-zone models.

4. If the modelled lines produced a straight horizontal or vertical line. This was most common with combinations containing elements $63 \leq$ Z- ≤ 71 (Eu to Lu). An example of this can be found in Figure A.1.3. These elements are close together on the nuclide chart, therefore we expect these elements to be produced in similar quantities for both the s and i process. The straight lines in these plots is as a consequence of the similar abundances of the elements in this range. Though there are some of the 'bad' fit plots with interesting features around these elements, which will be discussed in section 3.3.2.

After using the above selection criteria four combinations of elements remained, these combinations are coloured in blue in Table 3.1. Where there is a combination containing a heavy-s element, light-s element and Eu, the combination has been ordered so that [ls/Eu] versus [hs/Eu] is plotted. The combinations selected are [La/Tm] versus [Nd/Tm], [Eu/Tm] versus [Yb/Tm], [Y/Eu] versus [Ce/Eu] and [Sr/Eu] versus [Ba/Eu]. The corresponding three-element plots for these combinations are in Figures 3.2, 3.3, 3.6 and 3.7. These combinations can be split into two groups: a group for which the combination is [ls/Eu] versus [hs/Eu] and a group for which the reference element is Tm. I will first discuss the plots containing combinations of light-s, heavy-s and Eu, then combinations containing Tm as the reference element.

Figures 3.2 ([Y/Eu] versus [Ce/Eu]) and 3.3 ([Sr/Eu] versus [Ba/Eu]): Given that the elements in question here are Y, Sr, Ba, Ce and Eu, which can all be used as signatures of i-process nucleosynthesis, it makes sense that the models would, at points, be close to or run through both the CEMP-i and CEMP-s observations. We know that both the s and i process will produce the first peak elements Y and Sr and the second peak elements Ba and Ce. However, we also know that the i process will produce more europium than the s process, hence the CEMP-i sample being placed lower in the plots than the CEMP-s sample.

For both Figures 3.2 and 3.3 the shape of the i-process model suggests that we start by building up the abundance of the first peak element, then the second and finally europium.

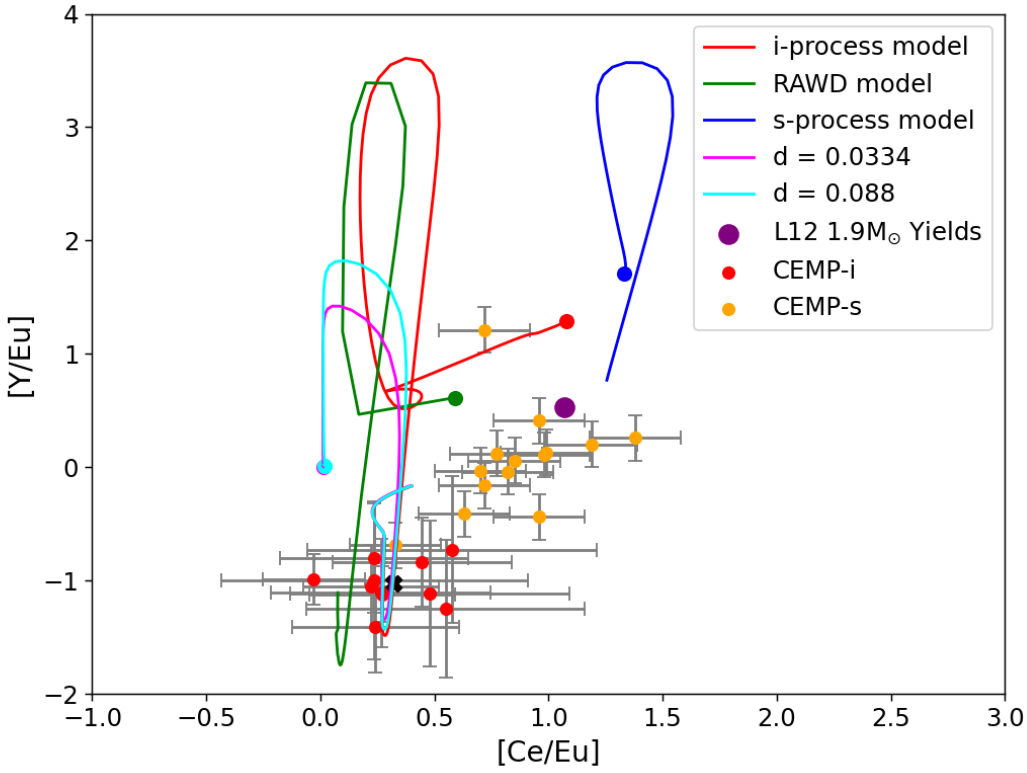

Figure 3.2: Three-element plot of [Y/Eu] versus [Ce/Eu] showing the trajectories traced by the one-zone i-process model, the RAWD model, a one-zone s-process model and two diluted one-zone i-process models. The circle attached to each trajectory denotes the start of the track. The black cross marks cycle 512, the point of maximum neutron density. The purple circle shows the yields of Lugaro et al. (2012). The CEMP-i and CEMP-s sample are represented by red and orange circles.

This build up of elements is what we expect from the i-process and is illustrated in Figure 3.4. This figure shows the abundances of Sr, Y, Ba and Ce relative to Eu during the period where i-process neutron densities are occurring, which is the same interval shown on the three-element plots in this section. We can see that the first peak elements Sr and Y peak at the same time which makes sense given we expect the abundances of these elements to be similar during neutron captures, while the Ba and Ce peak slightly later, as expected considering the shape of the i-process curves in Figures 3.2 and 3.3. The Ba peak is almost 2 dex higher than the peak of Ce (see below for a discussion on this). This explains why the shape of curve in Figure 3.2 is so much steeper than Figure 3.3 because [Ce/Eu] stays fairly constant through time, while [Ba/Eu] peaks to create a curved shape in the trajectory.

Cycle	Isotope 1	Contribution	Isotope 2	Contribution	Isotope 3	Contribution	Isotope 4	Contribution	Isotope 5	Contribution
500	^{135}I	0.977	^{135}Xe	0.010	^{137}Cs	0.006	^{137}Xe	0.003	^{138}Cs	0.001
530	^{135}I	0.880	^{137}Cs	0.057	^{138}Ba	0.021	^{138}Cs	0.014	^{137}Xe	0.012
550	^{135}I	0.636	^{138}Ba	0.144	^{137}Cs	0.143	^{135}Xe	0.049	^{138}Cs	0.021
570	^{138}Ba	0.598	^{137}Cs	0.337	^{135}Xe	0.031	^{135}Cs	0.018	^{136}Cs	0.012

Table 3.4: The isotopes that primarily contribute to the total decayed abundance of Ba at the cycles specified should the abundance pattern at that cycle be allowed to decay. The contributions are represented as a fraction of the total Ba.

Cycle	Isotope 1	Contri-bution	Isotope 2	Contri-bution	Isotope 3	Contri-bution	Isotope 4	Contri-bution	Isotope 5	Contri-bution
500	^{140}Ba	0.698	^{142}Ba	0.240	^{140}Cs	0.046	^{142}La	0.014		
530	^{140}Ba	0.751	^{142}Ba	0.209	^{142}La	0.020	^{140}Cs	0.016	^{142}Ce	0.002
550	^{140}Ba	0.901	^{142}La	0.035	^{142}Ba	0.028	^{142}Ce	0.025	^{140}La	0.010
570	^{142}Ce	0.547	^{140}Ba	0.330	^{140}La	0.062	^{140}Ce	0.052	^{142}La	0.010

Table 3.5: The unstable isotopes that primarily contribute to the total decayed abundance of Ce at the cycles specified should the abundance pattern at that cycle be allowed to decay. The contributions are represented as a fraction of the total Ce.

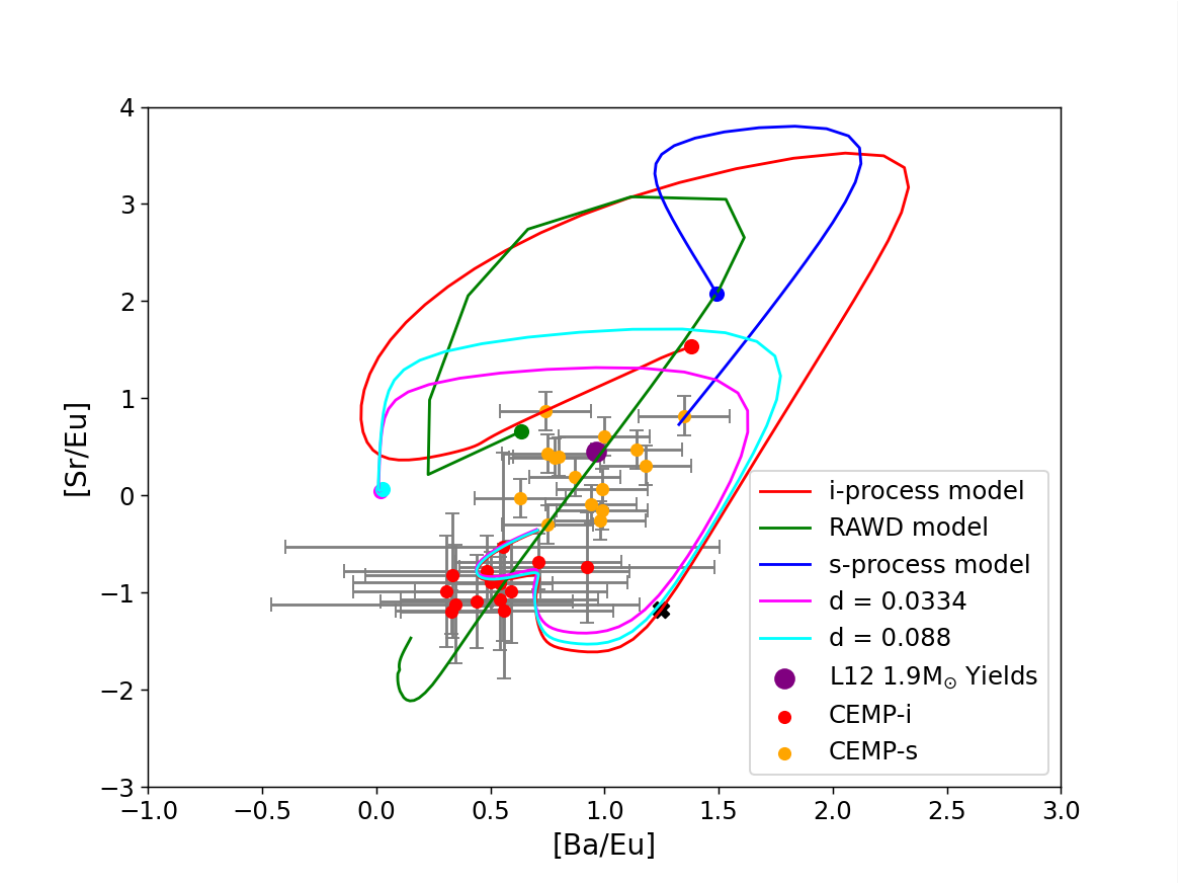

Figure 3.3: Same as Figure 3.2 but for [Sr/Eu] versus [Ba/Eu].

[Ce/Eu] does not peak as highly as [Ba/Eu] because the abundance of Ba is built-up due to decays from highly abundant ^{135}I, whereas the abundance of ^{140}Ce comes from the β decays of ^{140}La and ^{140}Ba which are low in abundance because the low neutron-capture cross-sections of the stable neutron magic isotopes inhibit the production of their heavier counterparts. Figure 3.5 shows four different nuclide charts in this region at cycles 500, 530, 550 and 570 which correspond to t = 2.6×10^4, 1.1×10^5, 3.0×10^5 and 7.9×10^5 seconds through the evolution respectively and shows the abundances of the isotopes in this sections of the nuclide chart pre-decay. The abundance of ^{135}I builds up through cycles 500-550, as does the Ba abundance. The high ^{135}I will contribute to an even higher abundance of ^{135}Ba once the isotopes have decayed. However, two stable Ce isotopes (^{138}Ce and ^{139}Ce) are shielded by stable Ba and La respectively which means most of the Ce abundance has to come from β decays of isotopes of Ba and La that are more neutron-rich than the neutron magic number and so will not build up as much Ce as the Ba peak. Table 3.4 shows the eventual contribution

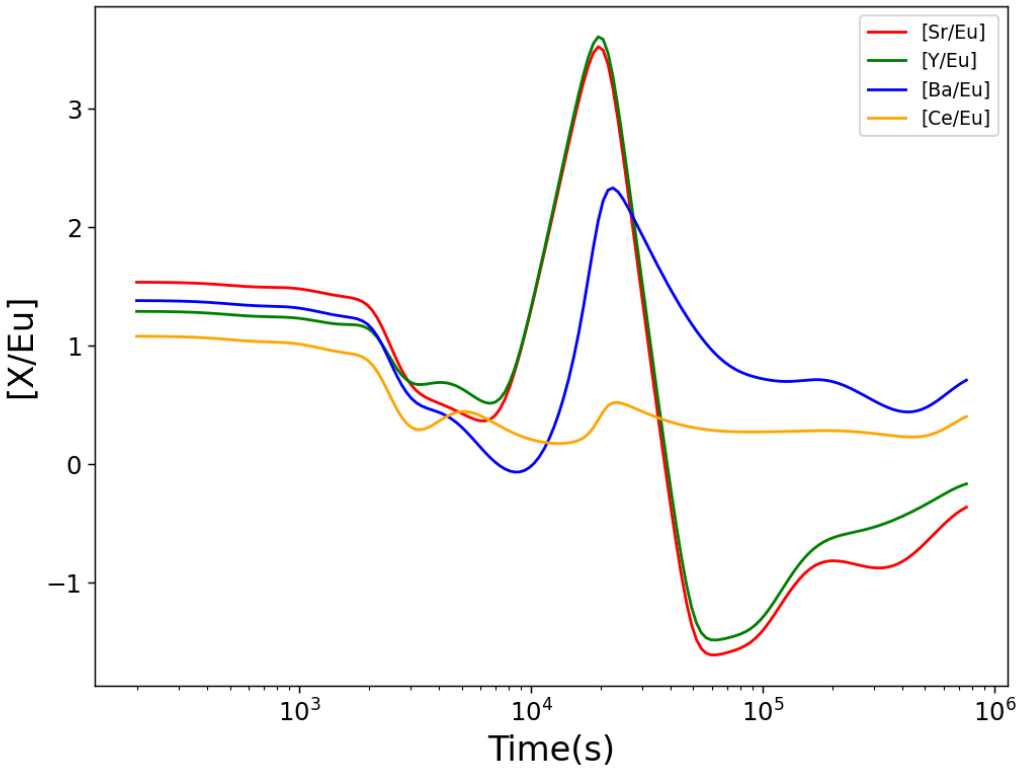

Figure 3.4: Abundances of Sr, Y, Ba and Ce with respect to europium during the time of i-process neutron densities occurring (cycles 400-570).

of each isotope to the elemental abundance of barium, if the isotopic pattern at that cycle is allowed to fully decay. We can see that as we expect ^{135}I is what contributes the most to the decayed elemental Ba abundance, contributing 97.7% at cycle 500, 88% at cycle 530 and 63.6% at cycle 550. Other isotopes with mass numbers 135, 136 and 137 make up smaller fractions due to β decays, as expected. At cycle 570, there is a transition to s-process like signatures with the dominant contribution to Ba coming from ^{138}Ba. Table 3.5 contains the contribution of each isotope to the elemental abundance of cerium, if the isotopic pattern at that cycle is allowed to fully decay. The dominant contributions to Ce comes from ^{140}Ba at cycles 500, 530, 550 with contributions of 69.8%, 75.1% and 90.1% respectively, with ^{142}Ce contributing 54.7% at cycle 570. Smaller contributions come from other isotopes of mass number 140 and 142. All of this together helps build a picture of why the i-process trajectories in Figures 3.2 and 3.3 look the way they do. All ratios in Figure 3.4 eventually

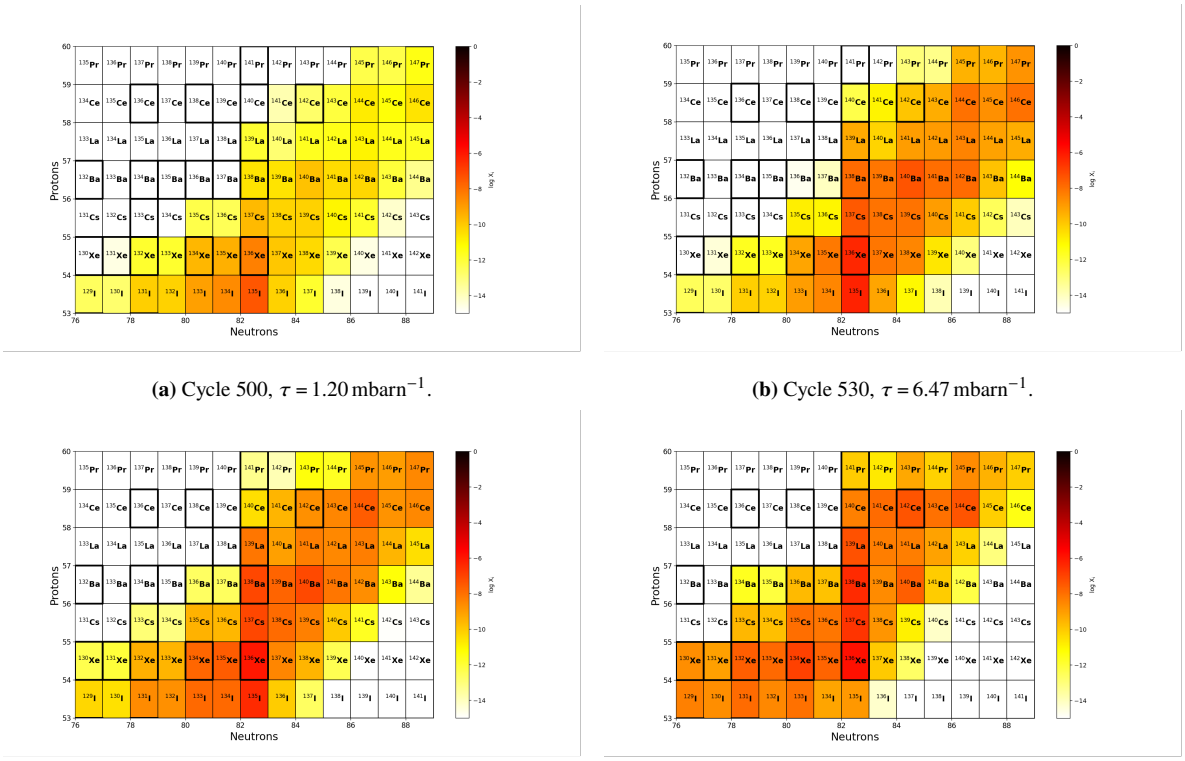

(a) Cycle 500, $\tau = 1.20\,\mathrm{mbarn}^{-1}$.

(b) Cycle 530, $\tau = 6.47\,\mathrm{mbarn}^{-1}$.

(c) Cycle 550, $\tau = 10.2\,\mathrm{mbarn}^{-1}$.

(d) Cycle 570, $\tau = 11.2\,\mathrm{mbarn}^{-1}$.

Figure 3.5: Section of the nuclide chart showing the high i-process abundance of ^{135}I and how that effects the other elements as it decays. The abundance of each isotope is indicated by the colour, the darker the colour the more abundant the isotope.

decline as Eu becomes more abundant at later times which is again reflected in the trajectories of Figures 3.2 and 3.3. In both these figures we can see that the s-process model doesn't come close to running through the CEMP-s sample. This is likely because this is a pure ^{13}C pocket s-process trajectory, which would need diluting in order to be in the region of the CEMP-s sample. In both figures we see that the diluted models cross the CEMP-i sample, which is to be expected given that the diluted models in section 2.2.2.1 often matched the observations closely. These results confirm what we expect of i-process nucleosynthesis and suggest that the three element plots could be useful tools.

Figures 3.6 ([La/Tm] versus [Nd/Tm]) and 3.7 ([Eu/Tm] versus [Yb/Tm]) : Figures 3.6 and 3.7 both use Tm as the reference element but the shape of the trajectories are different. Figure 3.6 shows that the i-process model trajectory starts high in both [La/Tm] and [Nd/Tm] abundance. Both the ratios decrease, before increasing slightly and finally decreasing until

both ratios finish lower in abundance than where they started. Figure 3.7 starts high in [Yb/Tm] and with a negative abundance of [Eu/Tm]. The trajectory of the i-process model line varies throughout the period of i-process neutron density. [Yb/Tm] ends at around [Yb/Tm] = 0, showing that the abundance of these elements are similar at the end of the period of i-process neutron densities. While the [Eu/Tm] abundance increases overall through the evolution of the model, the [Eu/Tm] ratio remains negative throughout, showing that Tm is more highly abundant than the Eu throughout.

Though these are the only two 'good fit' plots selected with Tm as one of the elements, Tm appeared many times in the list of good combinations (Table 3.1). Figure 3.8 shows four nuclide charts at cycles 500, 530, 550 and 570 ($t = 2.6\times10^4$, 1.1×10^5, 3.0×10^5 and 7.9×10^5 seconds through the evolution respectively) for the region around Tm. The arrows on these figures show the flux of the reactions from the start element to the finish element. These nuclide charts demonstrates how Tm is produced. We can see that the abundance of Tm is built up via β decays occurring due to neutron captures onto elements with lower Z. We see from each panel that the abundance of thulium's only stable isotope ^{169}Tm is built up slowly as stable ^{166}Er, ^{167}Er and ^{168}Er will not decay to produce lighter isotopes of Tm that could neutron capture to make ^{169}Tm. The abundance of ^{169}Tm is built-up solely by decays from ^{169}Er which has a relatively long half life of 9.4 days. However, we can see by cycle 570 that ^{169}Tm starts to build due to β decays from ^{169}Er and ^{169}Ho. This is reflected in Table 3.6 which shows the isotopic contributions to Tm at each cycle should it be allowed to decay. From this table we can see that ^{169}Tm is entirely produced via β decay of isotopes with the same mass number with the dominant contribution being 57.5% from ^{169}Dy at cycle 500, 50.8% from ^{169}Ho at cycle 530, 59.2% from ^{169}Ho at cycle 550 and 99.5% from ^{169}Er at cycle 570. From this we know that ^{169}Tm can be made via intermediate neutron capture. The Tm measurement for all of the CEMP-s stars was an upper limit, so there is a possibility that the sample in each of the figures is placed lower than it could be. The CEMP-s stars with Tm upper limit abundances are CS22945-024, CS22879-029, CS22947-187, CS29513-014 and HD196944 from Roederer et al. (2014). The Tm upper limits come from the fact that the lines are not detected or not detected strongly enough in the spectra. Therefore a 3σ upper

limit was found by fitting a Gaussian profile to the weak line by using the properties of the pixels in the spectra (formula presented on page 590 of Frebel et al. 2008).

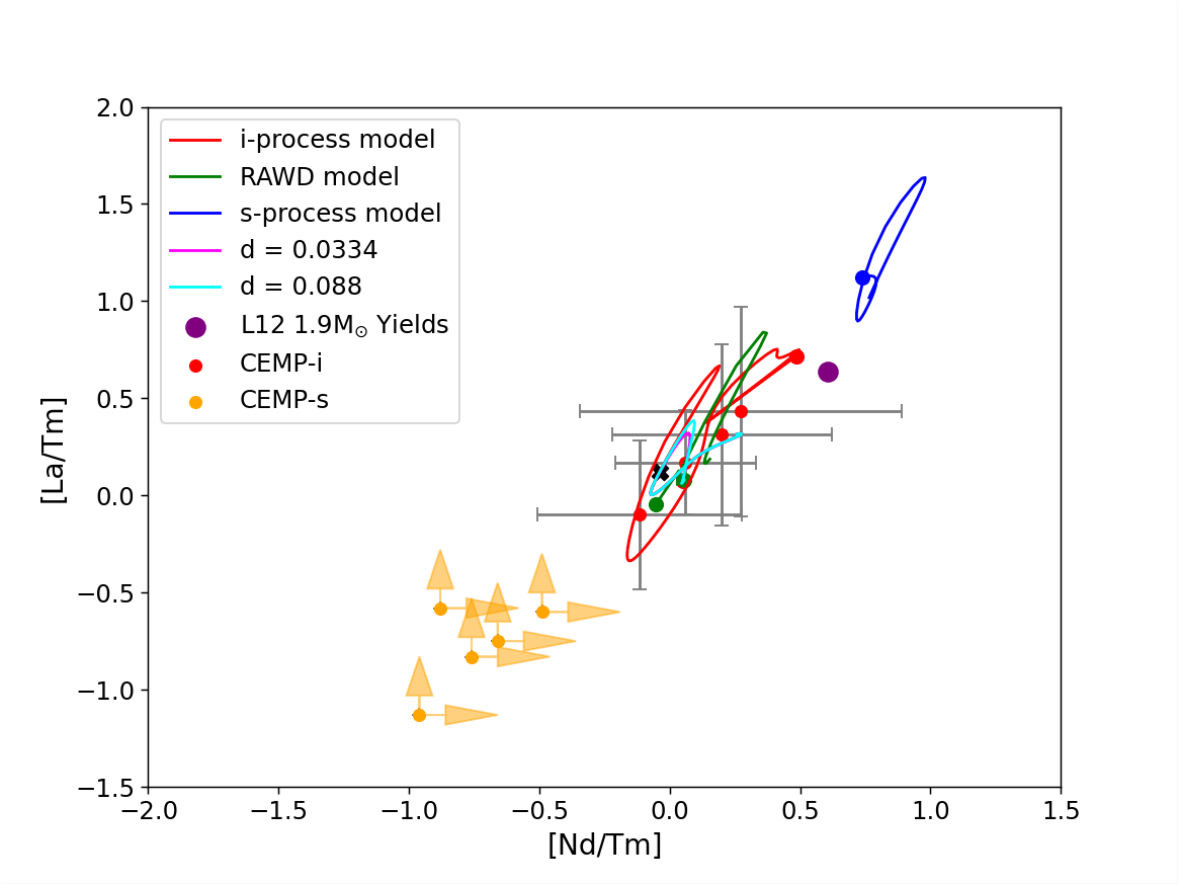

Figure 3.6: Same as Figure 3.2 but for [La/Tm] versus [Nd/Tm].

La and Nd are both second peak elements produced by the i-process. Figure 3.9 shows the evolution of La, Nd, Eu and Yb relative to Tm during the period where i-process neutron densities are occurring. The [Nd/Tm] abundance is lower than the [La/Tm] abundance for most of the time, apart from a small trough between around $t = 7\times10^3$ s and 1.6×10^4 s. However, the shape of these curves is largely the same. Therefore, Figure 3.6 doesn't give us a lot of insight into potential signatures of the i-process. From this, all we know is that second peak neutron capture elements are more abundant than an element with a single stable isotope also made via the i-process.

However, Figure 3.7 may give us some information that may be useful in identifying an i-process. The shape of this curve suggests that both the Eu and Yb are not as abundant as Tm at the start of the i-process period. Then, we start to see an increase in Eu and Yb relative to

Cycle	Isotope 1	Contribution	Isotope 2	Contribution	Isotope 3	Contribution	Isotope 4	Contribution
500	^{169}Dy	0.575	^{169}Ho	0.386	^{169}Er	0.020	^{169}Tb	0.019
530	^{169}Ho	0.508	^{169}Dy	0.442	^{169}Er	0.043	^{169}Tb	0.007
550	^{169}Ho	0.592	^{169}Er	0.356	^{169}Dy	0.052		
570	^{169}Er	0.995	^{169}Tm	0.003	^{169}Ho	0.002		

Table 3.6: The unstable isotopes that primarily contribute to the total decayed abundance of Tm at the cycles specified should the abundance pattern at that cycle be allowed to decay. The contributions are represented as a fraction of the total Tm.

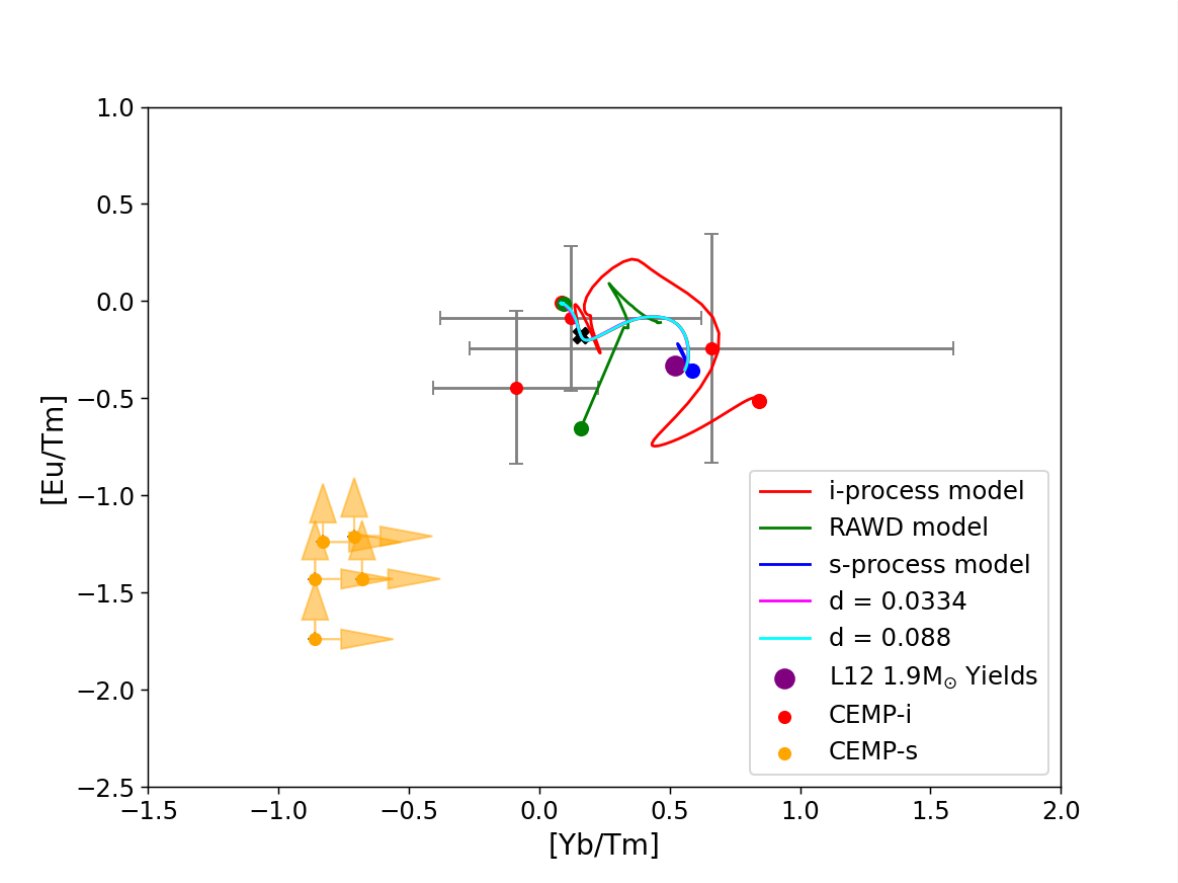

Figure 3.7: Same as Figure 3.2 but for [Eu/Tm] versus [Yb/Tm].

Tm but while the Eu continues to rise, the Yb abundance decreases relative to Tm. This trend can be seen more clearly in Figure 3.9 where we can see the [Eu/Tm] and [Yb/Tm] initially decrease before they both peak at around 3.5×10^3 s. Then, we see that the [Eu/Tm] peaks at $t = 2.4\times10^4$ s where the Yb remains more constant before both ratios go on to increase. The reason for this second spike in Eu where we don't see one in Yb is likely because Yb and Tm are next to each other on the nuclide chart. Both Yb and Tm are made via β decays of isotopes further down the chart and therefore, will be produced at somewhat similar rates at this point. Figure 3.8 shows that β decays of unstable isotopes of Er are critical in producing Yb, along with some isotopes of Ho and Tm. Table 3.7 shows eventual isotopic contributions to Yb should each cycle be allowed to decay. The majority of the material started out as unstable isotopes of Er with ^{174}Er contributing 37.6% to the total elemental Yb at cycle 500 and ^{172}Er contributing 33.6%, 47.2% and 31.6% at cycles 530, 550 and 570. These Er isotopes β decay to Tm before a final β decay to stable Yb. This means Tm is crucial in producing Yb.

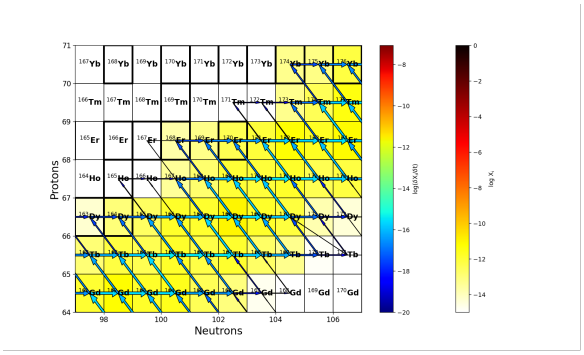

(a) Cycle 500, $\tau = 1.20\,\mathrm{mbarn}^{-1}$.

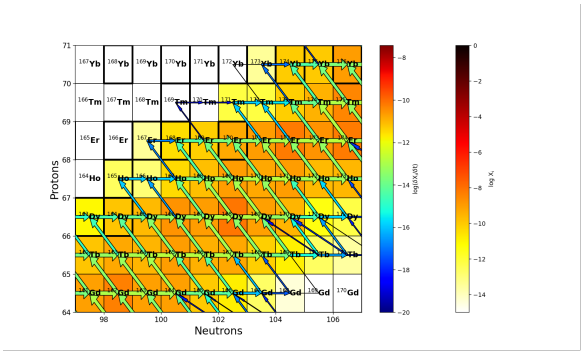

(b) Cycle 530, $\tau = 6.47\,\mathrm{mbarn}^{-1}$.

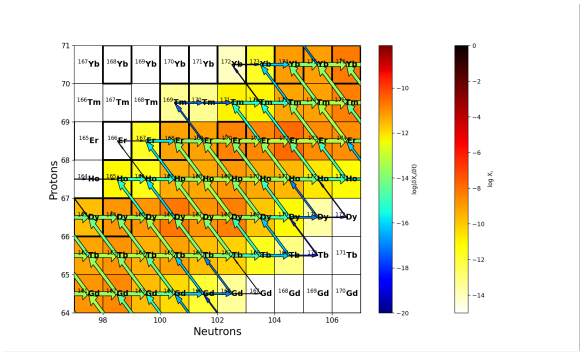

(c) Cycle 550, $\tau = 10.2\,\mathrm{mbarn}^{-1}$.

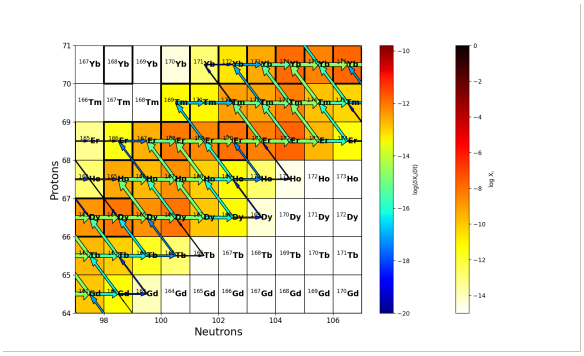

(d) Cycle 570, $\tau = 11.2\,\mathrm{mbarn}^{-1}$.

Figure 3.8: Sections of the nuclide chart showing production of Tm (and Yb) at cycles 500, 530, 550 and 570. The abundance of each isotope is indicated by the colour, the darker the colour the more abundant the isotope. The arrows represent the nuclear reactions taking place, while the colour of the arrows indicates the strength of the flux of the reaction.

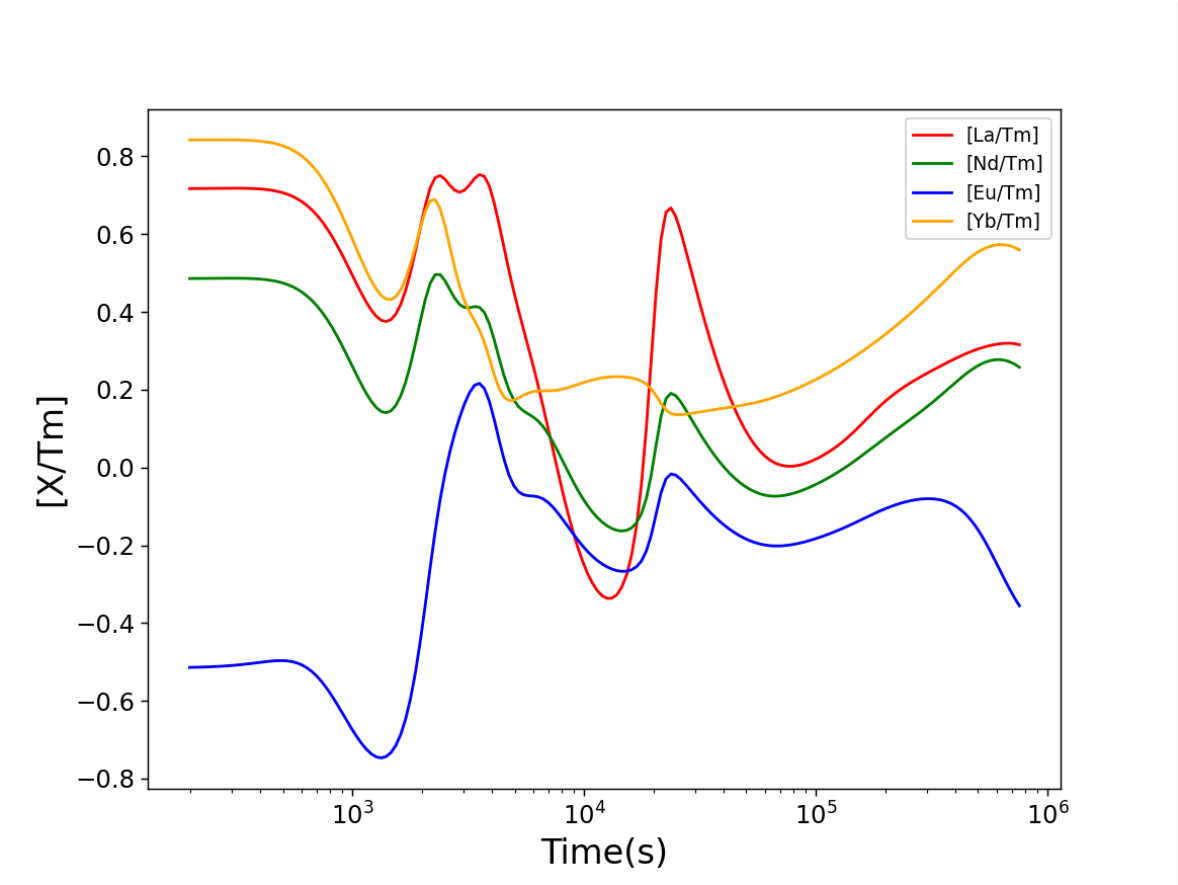

Figure 3.9: Abundances of La, Nd, Eu and Yb with respect to Tm during the period of i-process neutron densities (cycles 400-570).

Therefore, the information contained within Figure 3.7, may give us a ratio which may help us identify an i process from an s process.

The stars in the CEMP-i sample which have a Tm or Yb measurement can be found in Table 3.8. From section 2.2.2.1 we know that best fit models for these stars fit the Tm and Yb abundances within error bars for all but one of the stars. HE0338-3945 underproduced Tm by 0.2 dex but did reproduce the Yb within error bars. Overall, this is a good modelled fit to the abundances. Therefore, given the split between the two sets of abundances perhaps an abundance ratio of [Yb/Tm] > 0 could be indicative of an i-process. However, as previously stated, the Tm abundances are all upper limits, thus if we had more definite abundance measurements for Tm, the [Yb/Tm] split in Figure 3.7 may not be so prominent.

Cycle	Isotope 1	Contribution	Isotope 2	Contribution	Isotope 3	Contribution	Isotope 4	Contribution	Isotope 5	Contribution
500	^{174}Er	0.376	^{172}Er	0.268	^{173}Er	0.088	^{171}Ho	0.072	^{171}Er	0.042
530	^{172}Er	0.336	^{174}Er	0.311	^{173}Er	0.094	^{176}Yb	0.057	^{171}Ho	0.054
550	^{172}Er	0.472	^{176}Yb	0.186	^{171}Er	0.094	^{173}Er	0.082	^{174}Er	0.067
570	^{172}Er	0.316	^{176}Yb	0.285	^{174}Yb	0.210	^{171}Er	0.076	^{173}Tm	0.070

Table 3.7: The unstable isotopes that primarily contribute to the total decayed abundance of Yb at the cycles specified should the abundance pattern at that cycle be allowed to decay. The contributions are represented as a fraction of the total Yb.

Star	[Tm/Fe]	[Yb/Fe]	[Yb/Tm]	χ^2	model
CS29497-030	-	2.357±0.187	-	6.1	one-zone
CS31062-050	2.04±0.196	2.160±0.304	0.12±0.5	15.9	one-zone
HE0338-3945	2.397±0.158	2.307±0.158	-0.09±0.316	0.9759	one-zone
HE2258-6358	1.70±0.158	-	-	49.3	one-zone
LP625-44	2.121±0.275	2.781±0.652	0.66±0.927	7.8	RAWD

Table 3.8: Properties of CEMP-i stars that have a Tm or Yb measurement, their best χ^2 fit and the model that produced it.

3.3.2 'Bad' fits

Table 3.2 shows the combinations of elements with the largest r_{min} value and therefore the combinations for which the modelled line matches the observational data the least. Again, the 100 plots needed to be narrowed down to a number that is more manageable to be analysed. The rejection criteria for these plots was largely the same as the criteria laid out in section 3.3.1 but there were some differences. The plots that were rejected in this case had the following features:

1. The CEMP-i and CEMP-s sample occupied the same space.
2. The modelled line was so small that they cannot be seen or distinguished well from one another.
3. The combination of elements contains two or more light elements.

It is notable that the final two points from the list in section 3.3.1 are missing from the above list. Point 4 was removed because there were no straight lines in the modelled data to need to reject them. Point 3 was changed because in the whole sample, there were no combinations which did not contain at least one light element. Any combinations with one light element were kept unless that element was carbon, nitrogen or oxygen as we know they are produced primarily in the CNO cycle and therefore will likely not be useful in helping to find signatures of neutron capture processes, as well as the fact that we know that the model cannot reliably predict these abundances. After using the above selection criteria six

combinations remained which are coloured blue in Table 3.2. Where iron is present in the combination, the order of the elements has been changed so that Fe is the reference element. The selected combinations are [Na/Fe] versus [La/Fe], [Na/Fe] versus [Eu/Fe], [Sc/Fe] versus [Gd/Fe], [Sc/Fe] versus [Yb/Fe], [Sc/Fe] versus [Tm/Fe] and [Sc/Fe] versus [Hf/Fe]. The corresponding three-element plots for these combinations are in Figures 3.10, 3.11, 3.15, 3.16, 3.17 and 3.18. These figures can also be split into two groups: the combinations containing Na and the combinations containing Sc.

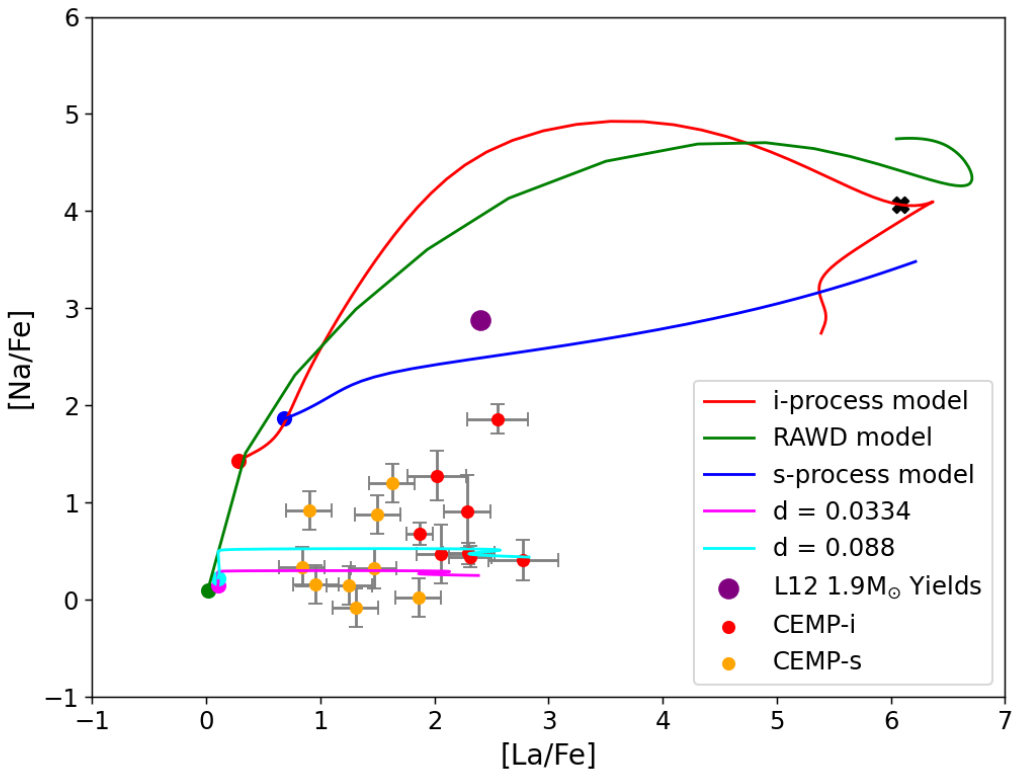

Figure 3.10: Same as Figure 3.2 but for [Na/Fe] versus [La/Fe].

Figures 3.10 ([Na/Fe] versus [La/Fe]) and 3.11 ([Na/Fe] versus [Eu/Fe]): Here we can see that the CEMP-s and CEMP-i samples have similar [Na/Fe] and are split only by the [La/Fe] or [Eu/Fe] ratios. Given we expect more La and Eu to be produced in the i process than the s process, this separation is to be expected. What is interesting about these figures is the significantly high [Na/Fe] in the i-process models compared to the s-process model, which poses the question: could high Na be in any way indicative of neutron captures having

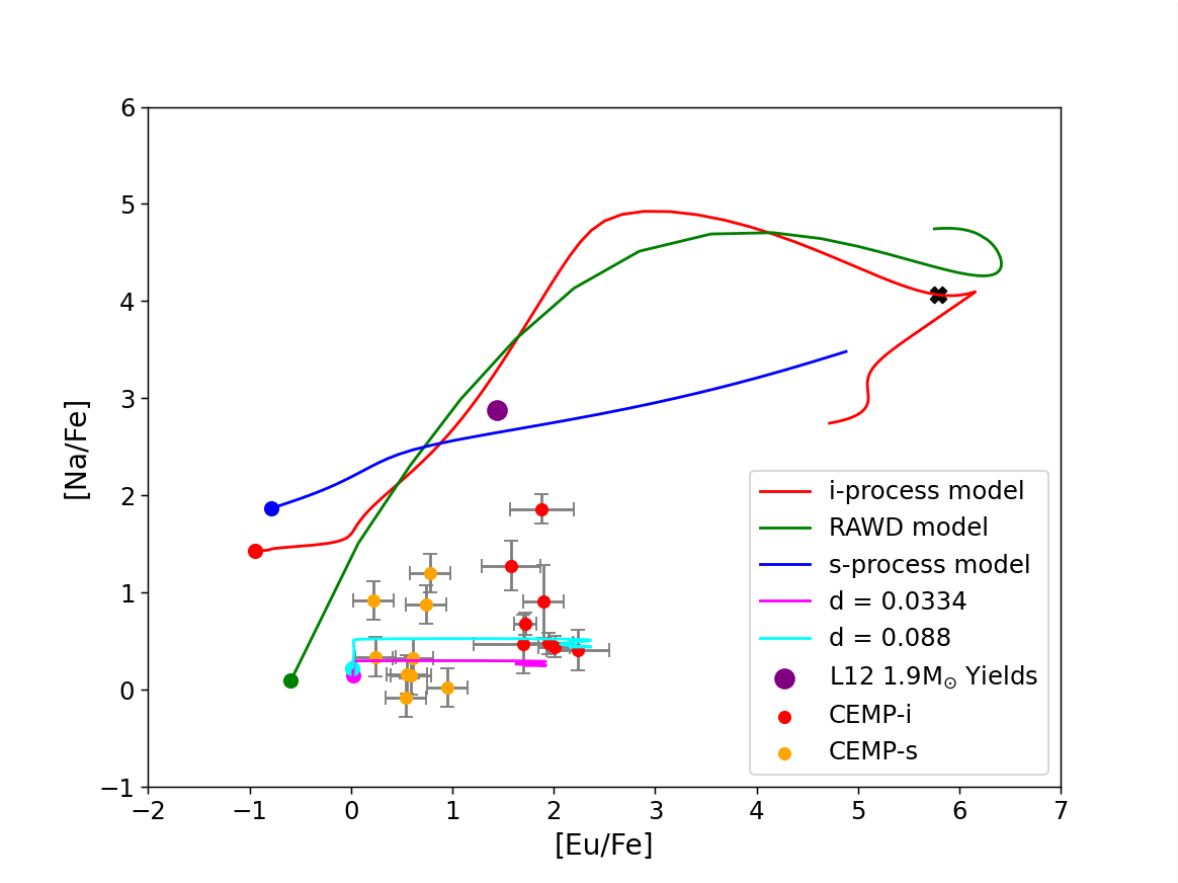

Figure 3.11: Same as Figure 3.2 but for [Na/Fe] versus [Eu/Fe].

taken place?

Figure 3.13 shows the abundance and production of sodium at i-process neutron densities. We can see that during this period, sodium is primarily produced via neutron captures through the following series of reactions: $^{22}\mathrm{Ne}\,(\mathrm{n},\,\gamma)\,^{23}\mathrm{Ne}\,(\beta)\,^{23}\mathrm{Na}$. We can see from the diluted models (pink and light blue lines Figures 3.10, 3.11) that the high abundance of sodium we see in the one-zone and RAWD models will dilute to a lower [Na/Fe] abundance and replicate the abundances of CEMP-s and i stars more closely. The undiluted i-process models sit higher than the s-process model in Figures 3.10 and 3.11 but that is not to say that a high abundance of sodium relative to iron is indicative of an i process over an s process. Sodium is primarily a product of hydrogen-burning during an interpulse phase of an AGB star's evolution which is then mixed into the envelope during the next third dredge up (Karakas & Lattanzio, 2014). Therefore, it is likely that much of the high sodium abundance was already present pre-neutron captures occurring. How much sodium is made during this phase is dependent on a

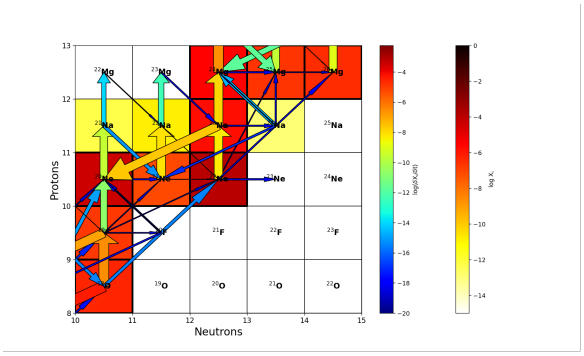

(a) Cycle 100 $\tau = 4.82\times10^{-16}$ mbarn^{-1}.

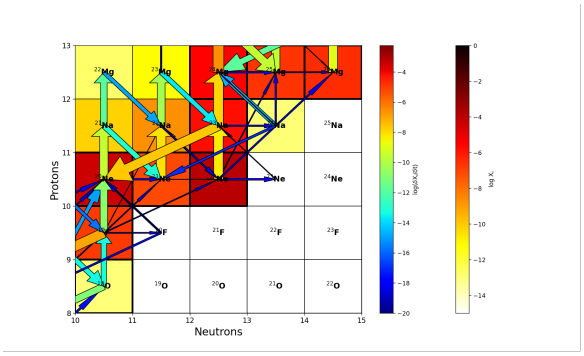

(b) Cycle 200 $\tau = 6.33\times10^{-14}$ mbarn^{-1}.

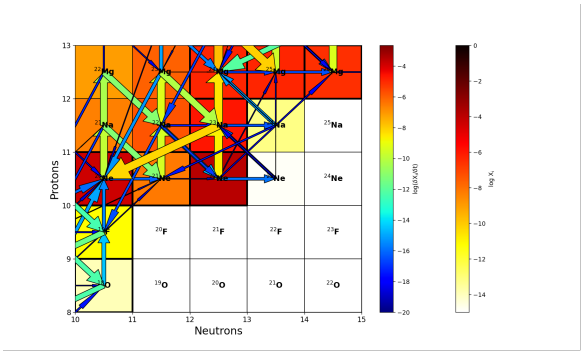

(c) Cycle 300 $\tau = 3.17\times10^{-10}$ mbarn^{-1}.

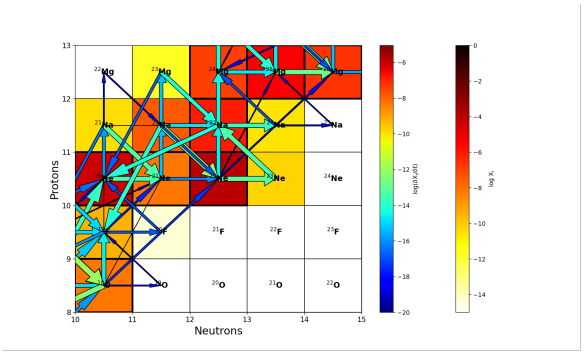

(d) Cycle 400 $\tau = 1.30\times10^{-5}$ mbarn^{-1}.

Figure 3.12: Same as Figure 3.8 but showing production of Na at cycles 100, 200, 300 and 400.

number of factors such as the chemical composition before the pulse, the mass of the star, the duration of the pulse and the peak temperature and density. Therefore, there is no definitive answer for the abundance of sodium we would expect to see from this process. However, Figure 3.12 shows the abundance and production of sodium at early cycles, 100, 200, 300 and 400 (t = 8.65×10^{-5} s, 0.011 s, 1.51 s and 198 s respectively) and shows the high abundance of Na for this particular intershell model. At all cycles, the abundance of ^{23}Na is already high relative to the isotopes surrounding it, coupled with a strong contribution from ^{22}Ne (p, γ) ^{23}Na. This is further highlighted by Figure 3.14 where we can see [Na/Fe] peak at around 2.1×10^{4} s (approximately cycle 500), the neutron density at this point is 3.54×10^{14} cm^{-3} and the exposure is only 1.20 mbarn^{-1}. The neutron density here is only just beginning to peak and the exposure is low, therefore it is unlikely that the peak in sodium abundance can be attributed to neutron captures. Though there is somewhat of a split between the two groups of CEMP stars, it is not strong enough to make any definitive conclusions on neutron capture signatures.

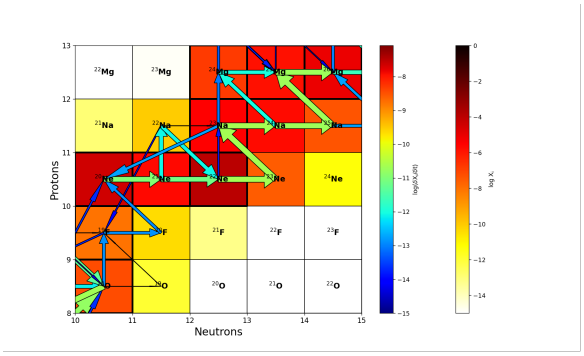

(a) Cycle 500, $\tau = 1.20\,\mathrm{mbarn}^{-1}$.

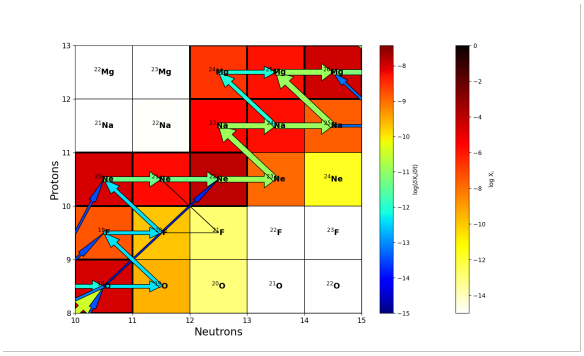

(b) Cycle 530, $\tau = 6.47\,\mathrm{mbarn}^{-1}$.

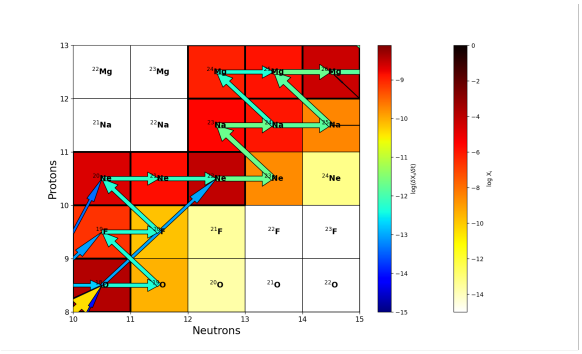

(c) Cycle 550, $\tau = 10.2\,\mathrm{mbarn}^{-1}$.

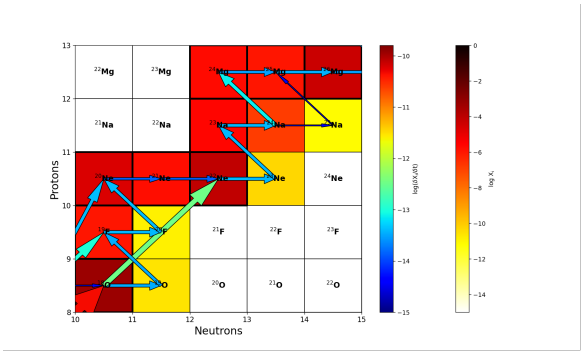

(d) Cycle 570, $\tau = 11.2\,\mathrm{mbarn}^{-1}$.

Figure 3.13: Same as Figure 3.8 but showing production of Na at cycles 500, 530, 550 and 570.

Figures 3.15 to 3.18 - [Sc/Fe] versus [Gd/Fe], [Sc/Fe] versus [Yb/Fe], [Sc/Fe] versus [Tm/Fe] and [Sc/Fe] versus [Hf/Fe]: In all of these figures, we see a similar effect with Sc to that of Na in Figures 3.10 and 3.11 where the i-process models sit much higher than the s-process models. ^{45}Sc is the only stable isotope of scandium and is produced via proton captures at early cycles as illustrated by Figure 3.19 and β decay due to neutron captures at later cycles as illustrated by Figure 3.20. Both Figures 3.19 and 3.20 show the abundance and production of ^{45}Sc at the specified cycles. At early cycles we see a small contribution to the abundance of ^{45}Sc due to proton captures, but it is not as strong as the flux of the proton capture reactions that produce ^{23}Na at these early times. At cycle 400, the transition from dominant proton captures to neutron captures starts to occur before neutron captures fully dominate from cycle 500, therefore we can say that Sc is predominately made via neutron capture.

Figure 3.21 shows the evolution of Sc, Gd, Yb, Tm and Hf relative to iron over cycles 400-570. We can see that Sc peaks at 2.2×10^4 seconds (approximately cycle 500). Cycle 500

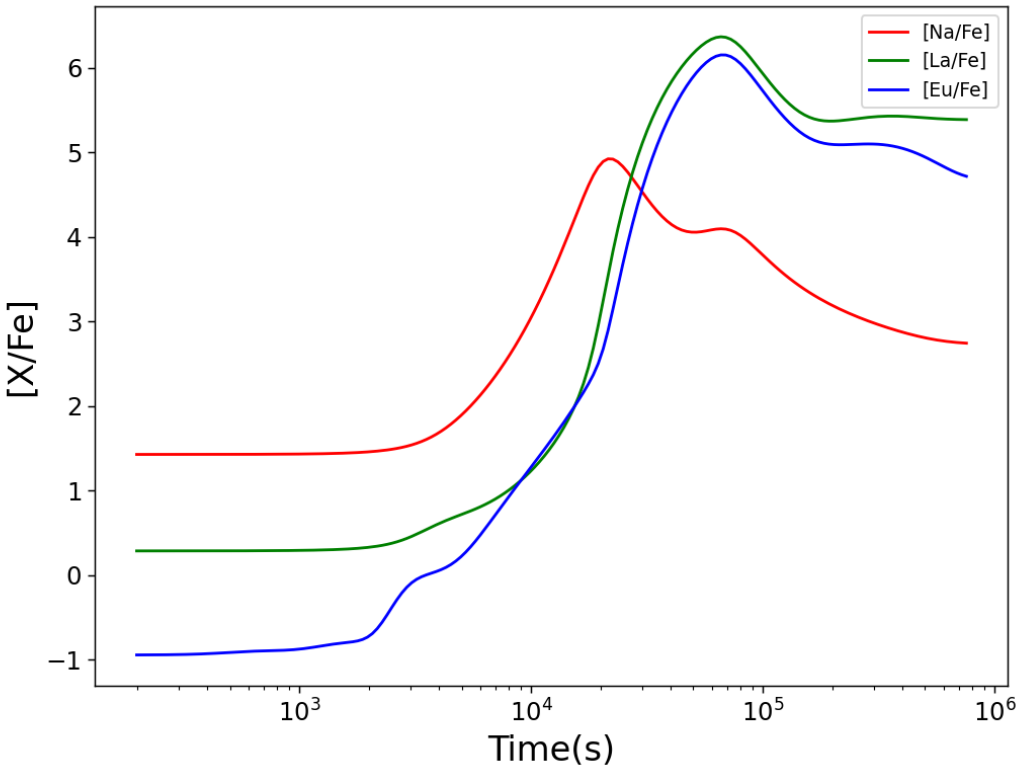

Figure 3.14: [Na/Fe], [La/Fe] and [Eu/Fe] with respect to time for the period of the evolution where i-process neutron densities are occurring (cycles 400-570, t = 198 seconds - 7.92×10^5 seconds).

has a neutron density and exposure of 3.54×10^{14} cm^{-3} and 1.20 mbarn^{-1} as stated previously. Figure 3.20a shows that neutron captures around Sc are strong at this point even though peak neutron density hasn't been reached yet because neutron captures can still occur lower down the nuclide chart at low exposure, which is what we are seeing here. Therefore, this initial peak is likely as a result of a combination of both proton and neutron capture driving a peak in Sc abundance as well as the depletion of the iron seeds causing this ratio to spike. There is a second smaller peak in the [Sc/Fe] at approximately cycle 524 (t = 8.4×10^4 seconds), which occurs at a similar time to the peaks in Gd, Yb, Tm and Hf. Therefore, it is likely that this smaller peak in [Sc/Fe] of about 4.6 is due to i-process nucleosynthesis. The [Sc/Fe] ratio of the one-zone i-process model in Figures 3.15, 3.16, 3.17 and 3.18 (red line) is high. However, we would not observe an abundance of scandium as high as this in a star due to the dilution of the abundances (as discussed in section 2.2.1). The diluted models fit the

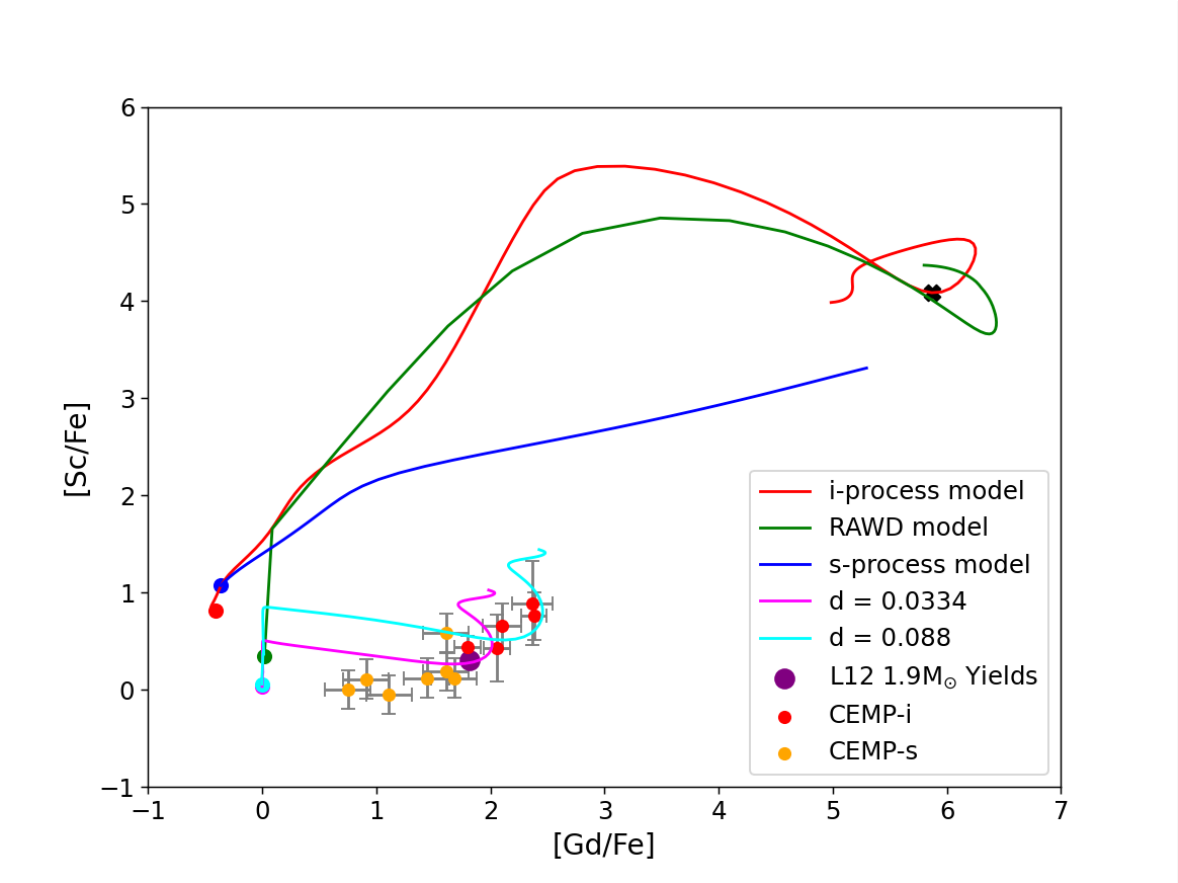

Figure 3.15: Same as Figure 3.2 but for [Sc/Fe] versus [Gd/Fe].

[Sc/Fe] ratio much closer than the undiluted models. The figures also show somewhat of a split between the CEMP-i and CEMP-s sample. The split in [Sc/Fe] at around [Sc/Fe] = 0.5 could become a distinguishing signature between the s and i process. However, to confirm this more abundance measurements of Sc are required to confirm the split in the data.

Figure 3.15 shows [Sc/Fe] versus [Gd/Fe]. Looking at the observed data we can see a small split between the CEMP-s and CEMP-i sample where the CEMP-s population appears fairly flat, while the CEMP-i population shows an upturn in both Sc and Gd. Gd is primarily produced via neutron captures, as demonstrated by Figure 3.22. We can see that all the stable isotopes of Gd are being produced by either neutron captures or β decays, therefore we know that Gd can be produced by the i process. The isotopes that would primarily contribute to the abundance of Gd at each cycle should it be allowed to decay can be found in Table 3.9. We can see that for cycles 500, 530 and 550 the majority of the Gd is being produced via decays of ^{158}Sm to ^{158}Eu to ^{158}Gd. ^{155}Sm, ^{156}Sm, ^{157}Sm and ^{158}Sm contribute a combined 82.6%,

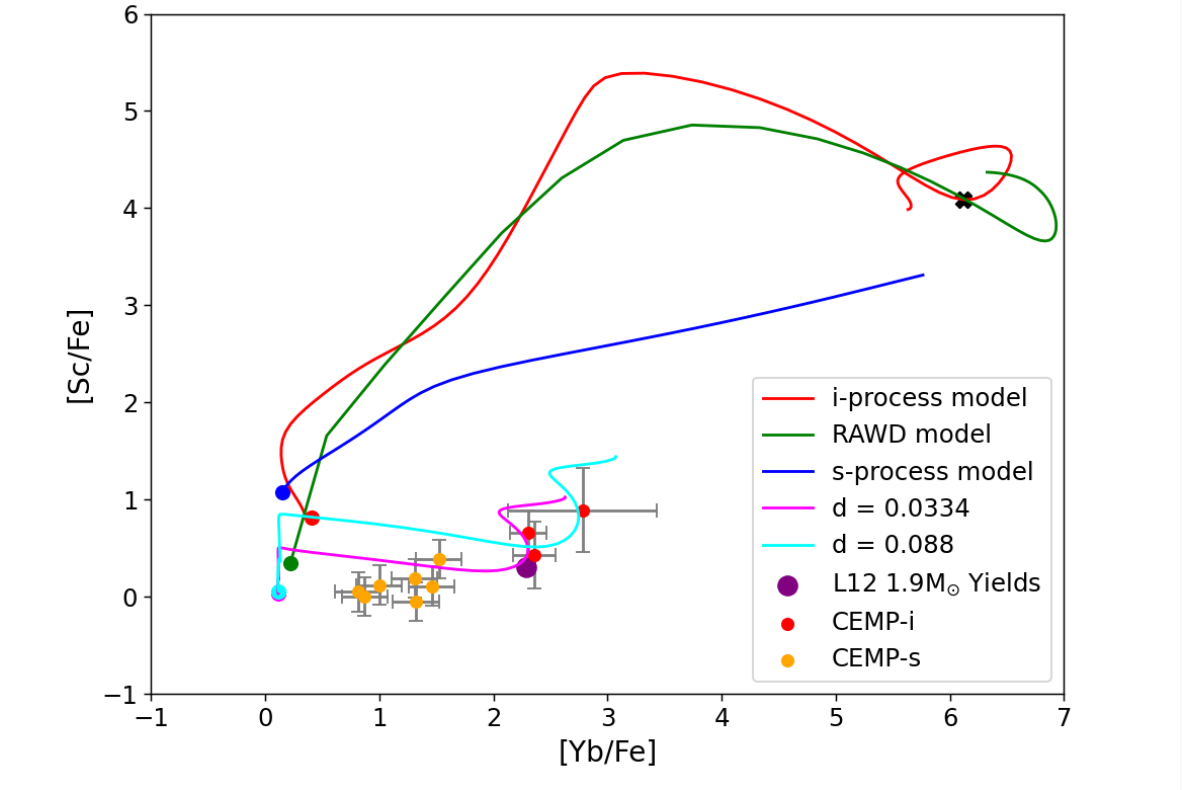

Figure 3.16: Same as Figure 3.2 but for [Sc/Fe] versus [Yb/Fe].

85.2% and 78.3% to the decayed abundance of Gd at cycle 500, 530 and 550 respectively. These isotopes of Sm β-decay to Eu and then to Gd. This demonstrates a strong i-process origin of Gd. There is a split in [Gd/Fe] between the two groups of data around [Gd/Fe] > 1.8. However, it is not as clear as some of the other splits in this work and it would not be justified to say that a [Gd/Fe] abundance over this value is definitely indicative of an i process. More observations of Gd in CEMP-i and CEMP-s stars would be required to make sure that this split is seen more widely.

Figure 3.16 shows a clear split between the CEMP-s and CEMP-i sample. It has already been shown that Yb can be produced in the i process via β decays of unstable isotopes of Tm and that a [Yb/Tm] ratio greater than zero may be indicative of an i process. Here, we could say the same with the [Yb/Fe] ratio, whereby a [Yb/Fe] > 2.1 could be indicative of an i process. I find this idea to be more robust than the [Yb/Tm] i-process prediction because none of the measurements here are upper limits. The reason for this split could be due to

Cycle	Isotope 1	Contribution	Isotope 2	Contribution	Isotope 3	Contribution	Isotope 4	Contribution	Isotope 5	Contribution
500	^{158}Sm	0.489	^{156}Sm	0.175	^{157}Sm	0.112	^{155}Pm	0.099	^{155}Sm	0.050
530	^{158}Sm	0.448	^{156}Sm	0.224	^{157}Sm	0.118	^{155}Pm	0.077	^{155}Sm	0.062
550	^{156}Sm	0.408	^{158}Sm	0.139	^{155}Sm	0.124	^{160}Gd	0.119	^{157}Sm	0.112
570	^{160}Gd	0.488	^{158}Gd	0.167	^{156}Sm	0.065	^{156}Gd	0.063	^{157}Eu	0.061

Table 3.9: The unstable isotopes that primarily contribute to the total decayed abundance of Gd at the cycles specified should the abundance pattern at that cycle be allowed to decay. The contributions are represented as a fraction of the total Gd.

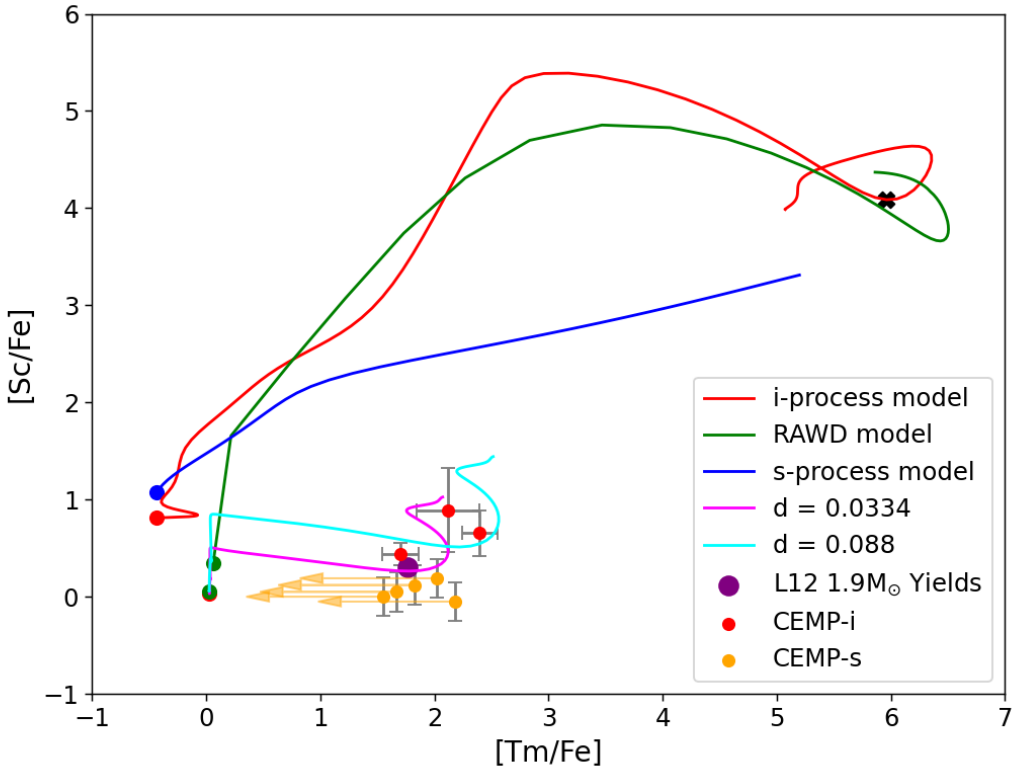

Figure 3.17: Same as Figure 3.2 but for [Sc/Fe] versus [Tm/Fe].

the differences between the s- and i-process path. Table 3.7 shows us that the majority of Yb is being produced via β decays from ^{171}Er, ^{172}Er, ^{173}Er and ^{174}Er. These are all isotopes that are produced due to β decays of unstable isotopes further down the nuclide chart. The unstable isotopes which decay to make ^{171}Er, ^{172}Er, ^{173}Er and ^{174}Er are far enough from stability that it is unlikely the s-process path will produce these isotopes. Therefore, the decay of these isotopes to unstable Er eventually leads to a higher abundances of Yb than is able to be achieved by the s process. This idea can be illustrated in Figure 3.23 which is a nuclide chart showing the production of Yb and the reactions that are occurring at t = 0.0095 yrs (2.99×10^5 seconds) through the evolution of the model (cycle 550, $\tau = 10.2$ mbarn^{-1}). We can see that decays of unstable Ho and Dy leads to the production of unstable Er. These isotopes of Ho and Dy could not be made in the s process because they are 9 and 7 isotopes away from stability respectively. However, the split between the two samples could also be down to a lack of observational data for objects containing Yb, therefore more observations

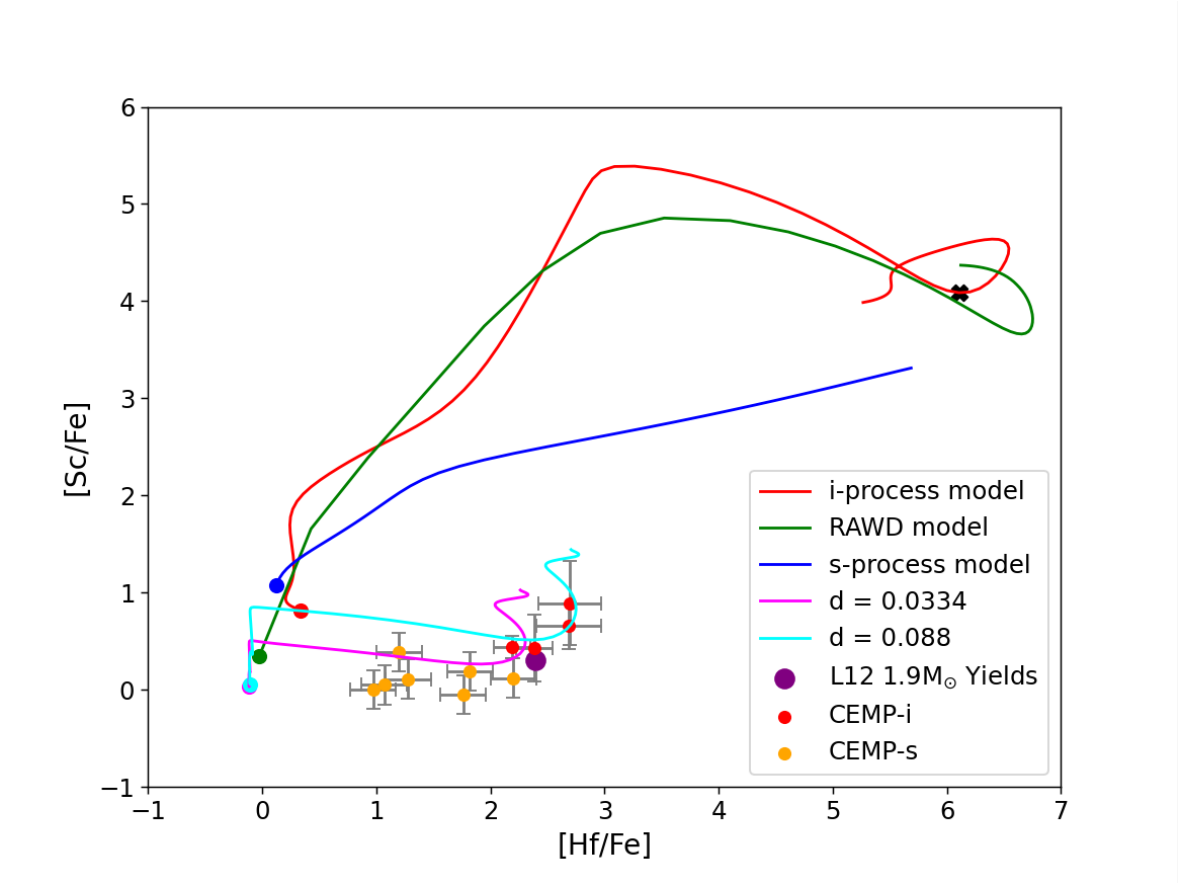

Figure 3.18: Same as Figure 3.2 but for [Sc/Fe] versus [Hf/Fe].

of Yb would be helpful to confirm this split.

Figure 3.17 shows there isn't a particular split between the CEMP-s and CEMP-i sample in [Tm/Fe] space. Therefore, there are no potential i-process indicators or signatures to comment on here. Given the CEMP-s measurements of Tm are upper limits, there is the potential that the [Tm/Fe] of the CEMP-s sample is not quite as high. Therefore, if we had more robust measurements of Tm for this sample, perhaps a more firm conclusion could be made here.

Figure 3.18 shows a similar split in the samples to Figure 3.15. Hf is primarily produced by β decays due to neutron captures as shown in Figure 3.24. Table 3.10 shows the isotopes which contribute the most to the abundances of Hf at each cycle should that cycle be allowed to decay. The majority of Hf comes from unstable isotopes of Yb. ^{177}Yb, ^{178}Yb, ^{179}Yb and ^{180}Yb contribute 83.5%, 87% and 86% to the decayed abundances of Hf at cycles 500, 530 and 550 respectively. These isotopes of Yb will decay to Lu. However, there is not a clear enough split between the CEMP-i and CEMP-s sample in [Hf/Fe] to make any robust

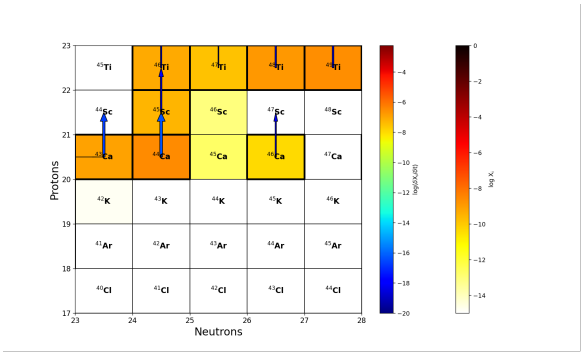

(a) Cycle 100 $\tau = 4.82\times10^{-16}$ mbarn^{-1}.

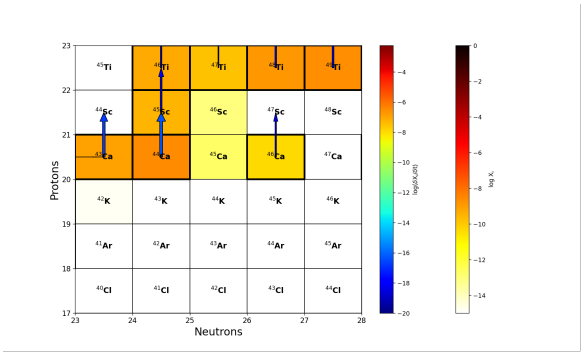

(b) Cycle 200 $\tau = 6.33\times10^{-14}$ mbarn^{-1}.

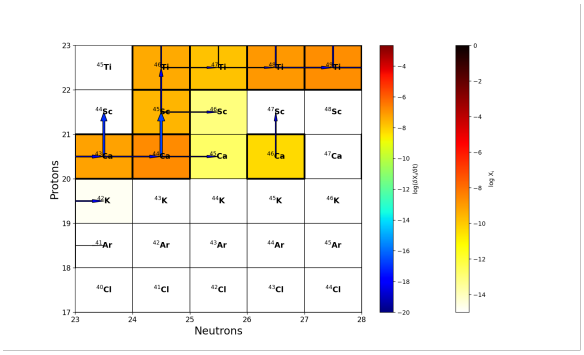

(c) Cycle 300 $\tau = 3.17\times10^{-10}$ mbarn^{-1}.

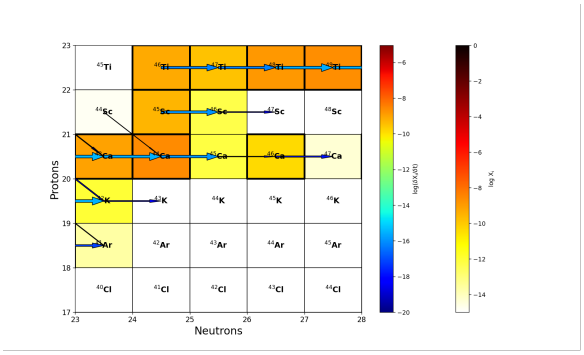

(d) Cycle 400 $\tau = 1.30\times10^{-5}$ mbarn^{-1}.

Figure 3.19: Same as Figure 3.8 but showing the production of Sc at cycles 100, 200, 300 and 400.

conclusions on i-process signatures as some of the stars in the CEMP-i sample sit on top of the CEMP-s sample.

It should be noted that the reason the combinations of elements were selected as 'bad' fits for this section is because the one-zone i-process model runs far from the abundances. However, the two selected diluted models seem to run close enough to the CEMP-i sample that the ratios discussed in this section could be observed in stars.

3.3.3 Other three-element plots of interest

Figure 3.25 shows [Ba/La] versus [Ba/Eu] for the various models and samples. Here, the element in common (barium) between the two ratios isn't the reference element. This was done as a sanity check for the three-element plots to make sure that ratios we are confident in, look how we think they should. The CEMP-i sample has a smaller [Ba/Eu] ratio, which makes sense given the fact that the i process should produce more Eu than the s process thereby reducing this ratio. The i-process models have a larger maximum value of [Ba/La] compared

Cycle	Isotope 1	Contribution	Isotope 2	Contribution	Isotope 3	Contribution	Isotope 4	Contribution	Isotope 5	Contribution
500	^{178}Yb	0.355	^{180}Yb	0.325	^{179}Yb	0.117	^{177}Tm	0.088	^{177}Yb	0.038
530	^{178}Yb	0.444	^{180}Yb	0.252	^{179}Yb	0.126	^{177}Tm	0.066	^{177}Yb	0.048
550	^{178}Yb	0.617	^{177}Yb	0.111	^{179}Yb	0.093	^{180}Hf	0.042	^{180}Yb	0.039
570	^{180}Hf	0.500	^{178}Hf	0.177	^{177}Yb	0.092	^{179}Hf	0.066	^{177}Lu	0.059

Table 3.10: The unstable isotopes that primarily contribute to the total decayed abundance of Hf at the cycles specified should the abundance pattern at that cycle be allowed to decay. The contributions are represented as a fraction of the total Hf.

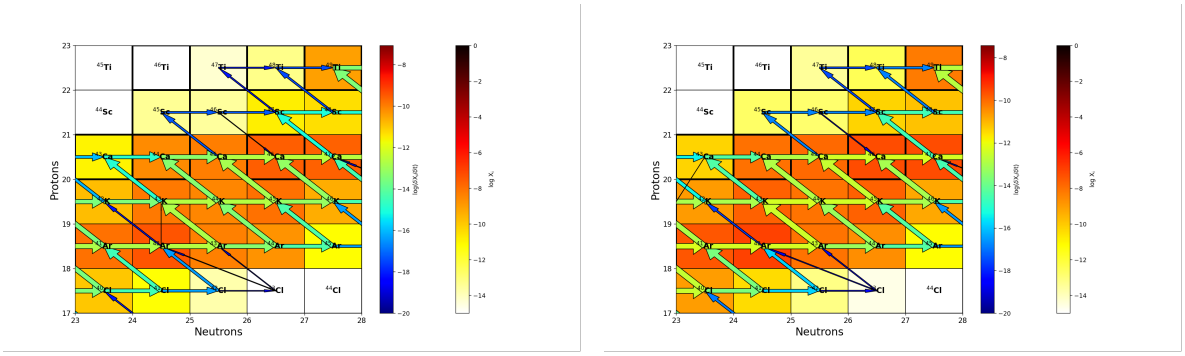

(a) Cycle 500, $\tau = 1.20\,\mathrm{mbarn}^{-1}$.

(b) Cycle 530, $\tau = 6.47\,\mathrm{mbarn}^{-1}$.

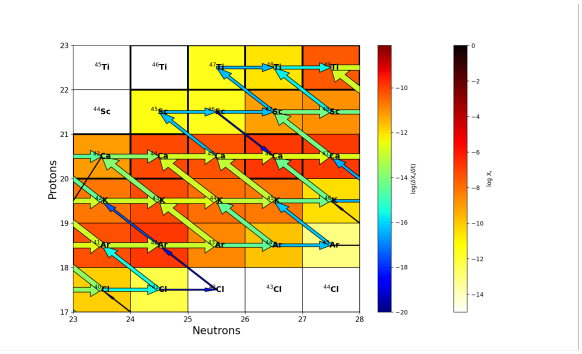

(c) Cycle 550, $\tau = 10.2\,\mathrm{mbarn}^{-1}$.

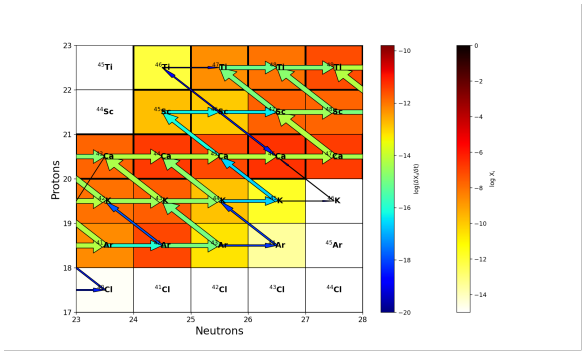

(d) Cycle 570, $\tau = 11.2\,\mathrm{mbarn}^{-1}$.

Figure 3.20: Same as Figure 3.8 but showing the production of Sc at cycles 500, 530, 550 and 570.

to the s-process model, while the CEMP-i and CEMP-s samples show similar [Ba/La] ratios, which makes sense as these abundances will have been observed post-dilution of the material. As with all of the three-element plots in this chapter, the s-process model appears farther away from the CEMP-s sample. However, this is because the s-process model here is pure ^{13}C pocket trajectory material, so no dilution has occurred yet.

Something notable about the three-element plots throughout this section is that there are multiple plots for which either the s-process model, the Lugaro et al. (2012) detailed AGB model or both do no match the CEMP-s sample. This is because these abundances haven't been diluted by solar scaled material in order to replicate the transfer of the s-process material to the companion (e.g. Stancliffe et al. 2007 Stancliffe 2009, Stancliffe 2021). Therefore, should dilution to these models occur, they would come closer to matching the CEMP-s sample.

Overall, this study into elemental ratios where i-process models run close to CEMP-i observations and where they do not has yielded some promising ratios which could be useful

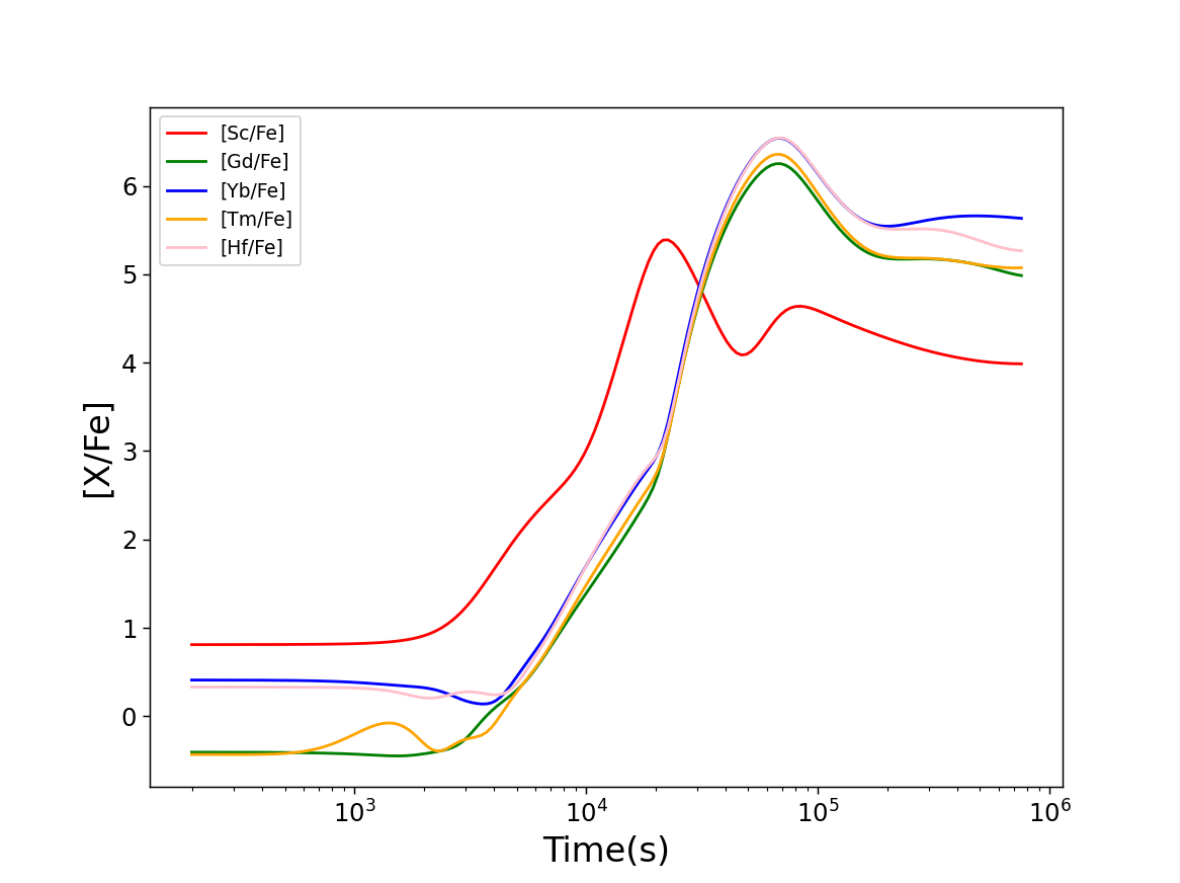

Figure 3.21: [Sc/Fe], [Gd/Fe], [Tm/Fe], [Yb/Fe] and [Hf/Fe] with respect to time for the period of the evolution where i-process neutron densities are occurring (cycles 400-570, t = 198 seconds - 7.92×10^5 seconds).

in distinguishing a star which has been polluted with s- or i-process rich material. In section 3.3.1, it was identified that [Yb/Tm] > 0 could indicate an i process. However, the Tm measurements of Roederer et al. (2014) for the CEMP-s stars are upper limit measurements so more robust measurements of Tm in CEMP-s stars will be needed to confirm this ratio as a signature. In section 3.3.2, it was identified that [Sc/Fe] > 0.5, [Gd/Fe] > 1.8 and [Yb/Fe] > 2.1 could be indicative of the i process. The ratios of [Sc/Fe] and [Gd/Fe] need more observations in both CEMP-s and CEMP-i stars in order to confirm this small split in the data and ensure new data would not cause the two groups to completely overlap. The ratio of [Yb/Fe] is much more convincing that that of [Yb/Tm] as the Yb and Fe observations do not have any limits associated with them. That being said, though the split between the CEMP-i and CEMP-s sample in Figure 3.16 is definite, the Yb data is sparse and it would be preferable to have a few more data points to confirm this trend.

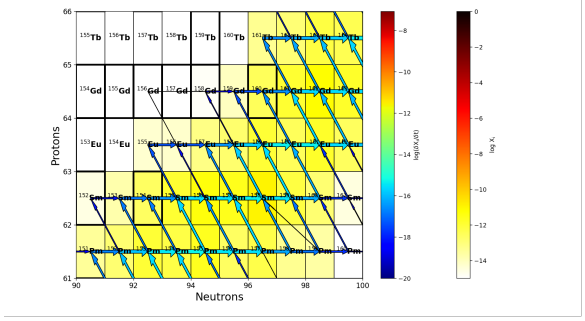

(a) Cycle 500, $\tau = 1.20\,\mathrm{mbarn}^{-1}$.

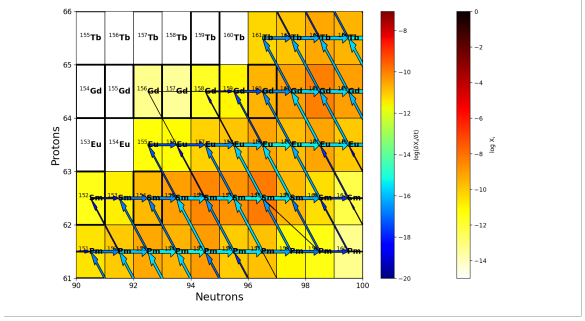

(b) Cycle 530, $\tau = 6.47\,\mathrm{mbarn}^{-1}$.

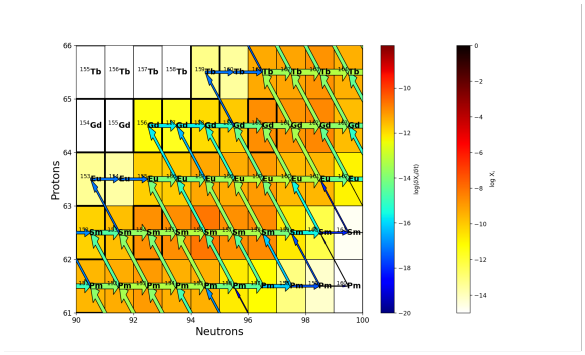

(c) Cycle 550, $\tau = 10.2\,\mathrm{mbarn}^{-1}$.

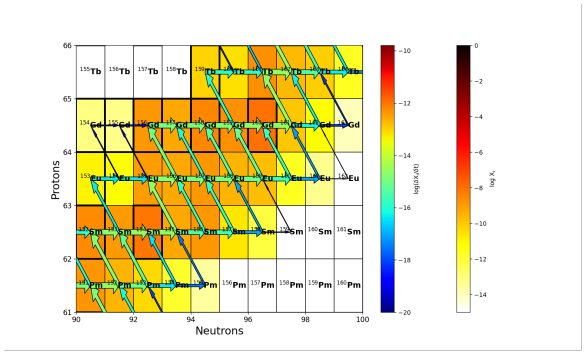

(d) Cycle 570, $\tau = 11.2\,\mathrm{mbarn}^{-1}$.

Figure 3.22: Same as Figure 3.8 but for the production of Gd at cycles 500, 530, 550 and 570.

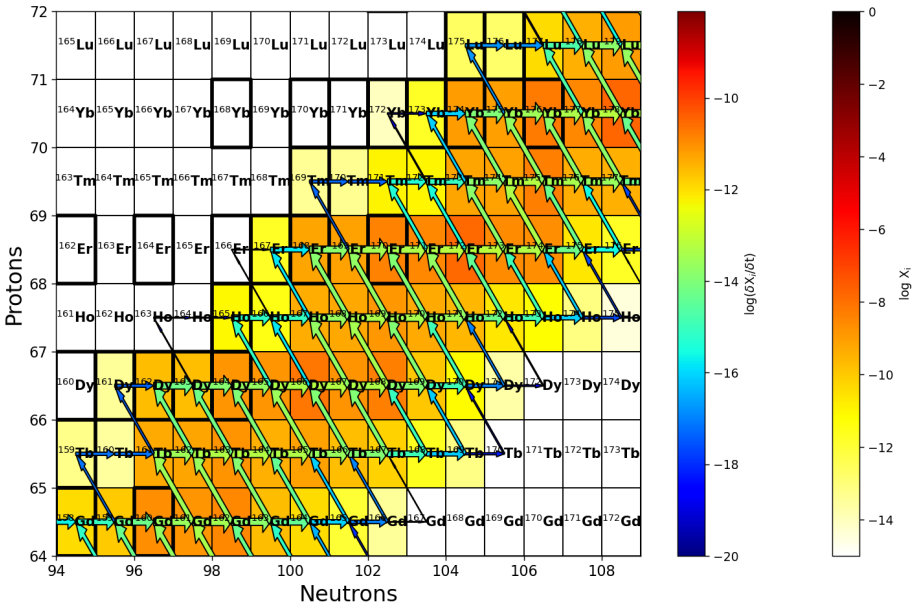

Figure 3.23: Section of the nuclide chart showing production of Yb at cycle 550. The colour of each isotope indicates how abundant it is, the darker the colour the more abundant it is. The arrows represent the nuclear reactions taking place, the colour of the arrows represent the strength of the flux of the reaction.

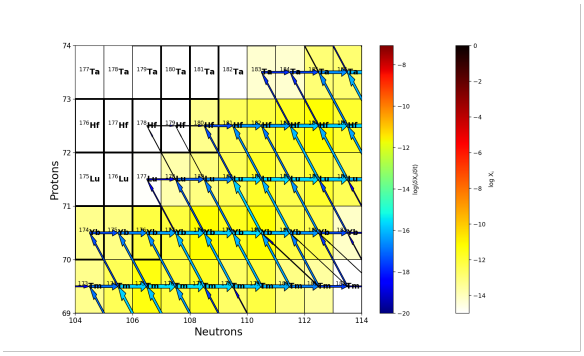

(a) Cycle 500, $\tau = 1.20\,\mathrm{mbarn}^{-1}$.

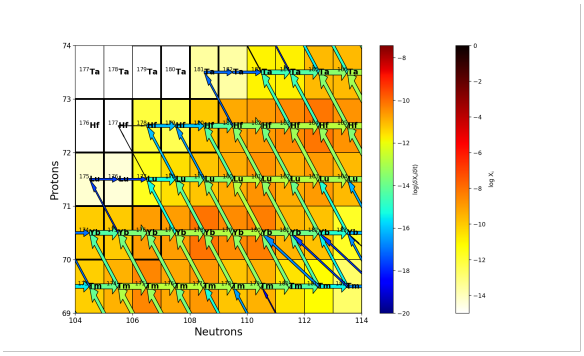

(b) Cycle 530, $\tau = 6.47\,\mathrm{mbarn}^{-1}$.

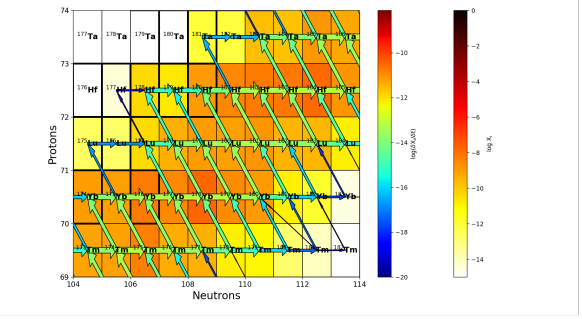

(c) Cycle 550, $\tau = 10.2\,\mathrm{mbarn}^{-1}$.

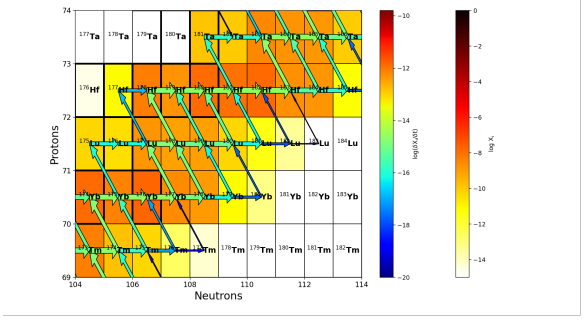

(d) Cycle 570, $\tau = 11.2\,\mathrm{mbarn}^{-1}$.

Figure 3.24: Same as Figure 3.8 but for the production of Hf at cycles 500, 530, 550 and 570.

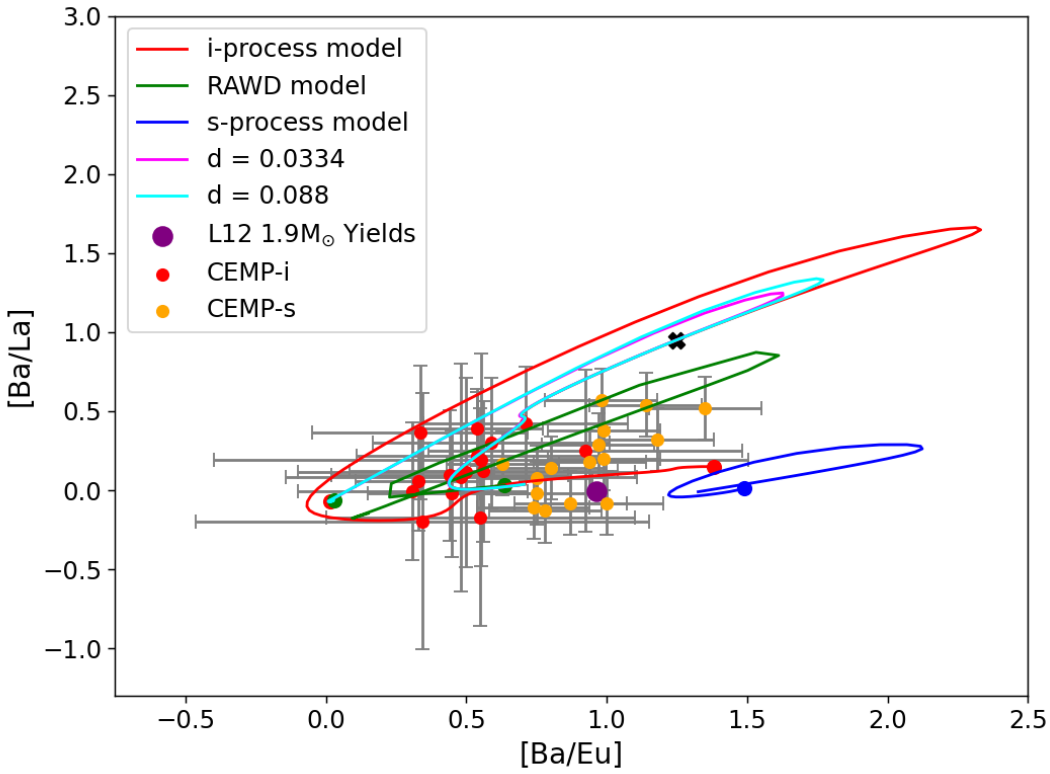

Figure 3.25: Same as Figure 3.2 but for [Ba/La] versus [Ba/Eu].

4. Discussion, Conclusions and Future Work

This work used two different models to study signatures of i-process nucleosynthesis. The fit to various CEMP-i stars using each of these models were found using χ^2 fitting and a comparison made between the two models. The same χ^2 technique was used in order to try to explain the anomalous abundances of phosphorus-rich stars and make predictions of the abundances of thorium and uranium we would expect to see produced in the i process. The one-zone AGB intershell model was then also used to try to find abundance ratios that could distinguish an i-process abundance from an s-process abundance.

By using χ^2 fitting, it was found that the model that best fit the [Pb/Fe] abundance of a star was more likely to provide the closer fit to the heavy element abundances as a whole and that the [Pb/hs] ratio was higher in stars where the one-zone model fit best. The resulting fits were also compared to fits achieved by other authors to the same stars. A comparison to the modelled fits of Choplin, Siess & Goriely (2021) showed that simple one-zone models can reproduce i-process abundances just as well, if not better than, more complex models. This highlights again that one-zone models can be sufficient when looking at AGB nucleosynthesis and performing abundance comparisons, especially given how quick these models are to run, they are a useful tool for successful abundance comparisons before introducing complexity into the models. Added complexity such as using multiple zones or hydrodynamics allows for increased uncertainty in the models as well as longer running times, so though it could be argued that they better represent the situation physically, they are not always ideal for modelling some scenarios. Although, it is still important to find multi-zone and multi-dimensional models that can treat convection and mixing properly and consistently in order to confirm our findings. A comparison to the work of Hampel et al. (2019) found that the modelled fits of their work and the present work were very similar in shape, even if some of the fitting properties such as neutron density and exposure were different. This can give us an idea of the kind of uncertainties that arise when doing abundance fitting in this manner. The

comparison of the abundances of Abate et al. (2015) to Karinkuzhi et al. (2021) for the same stars (HD187861 and HD224959) highlighted that the properties of the model fit to the same star is dependent on the way the abundances are derived in the first place. If the abundances have been derived in two different ways by two different groups of authors the properties of the fits can be very different, so much so that they would suggest that the two fits are for two different objects entirely.

Unfortunately the anomalous abundances of the P-rich stars of Masseron et al. (2020b) could not be entirely explained by the i process. The abundances of 2M13535604 could not be replicated by the i-process models and likely is due to an unusual mode of neutron capture nucleosynthesis. The abundance of 2M22045404 also couldn't be entirely reproduced by the i-process model, even when considering a double i-process exposure. The best fit to the abundances came from two i-process exposures: $\tau_1 = 0.31$ mbarn^{-1} (cycle 480) and $\tau_2 = 0.12$ mbarn^{-1} (cycle 469) with dilution factors a = 0.06, b = 0.94 and c = 0, yielding $\chi^2 = 162$. The aim of the double i-process fit was to replicate the success of Koch et al. (2019) and find two distinctly different exposures that would combine to provide a good fit to the data, which was not the case here. Baratella et al. (2021) studied the chemical abundances of young open clusters and found a super solar [Ba/Fe] of 0.25 dex - 0.75 dex. High Ba is also a feature of the P-rich star 2M22045404. These authors state that this overabundance cannot be replicated by an s-process model and note that perhaps these abundances could provide a clue to the site of the i process. However, from the work carried out in this thesis, we know that it is difficult to reproduce the abundances of the P-rich stars with just an i-process model alone. Therefore, perhaps these abundances could be a combination of the s and i process, in a similar fashion to the double i-process exposure tried in this work and the work of Koch et al. (2019). However, any good solution to the abundance pattern would have to reconcile the high phosphorus abundance with the low scandium abundance, which is particularly hard to do given we expect to see the two produced at the same time.

Using χ^2 fitting to predict the i-process abundances of thorium and uranium gave us a range of potential values for these elements of: $0.25 <$ [Th/Fe] < 2.30 and $0.05 <$ [U/Fe] < 3.76. An example of a star with a measurement of Th and U to try and fit to was HE0338-3945 (Jonsell

et al., 2006). The same χ^2 fitting technique was used to fit the abundances of this star, including the Th and U, using an i-process model where the abundances have been allowed to decay. The best fit decayed abundances were at t = 1.26×10^7yrs after initial production (cycle 66) with d = 0.0046, producing χ^2 = 619.2. However, what was notable was that the [Th/Fe] value was reproduced exactly, while the [U/Fe] was overproduced and therefore, would be able to decay back to the upper limit observation. It was found that both upper limits of [Th/Fe] and [U/Fe] can be reached by the i-process models but they cannot be reproduced simultaneously. A similar analysis was done on the abundances of J0949-1617, which were derived by Gull et al. (2018). However, it was found that the abundance pattern as a whole fits better with an 's+r' scenario. Overall, to be able to apply this more widely, more i-rich or 's+r' stars will need to be observed with measured thorium and uranium abundances. This will allow verification of the predictions made and further show that the i process can produce thorium and uranium. More abundance measurements will also show that χ^2 fitting and abundance fitting in general is also useful to make predictions as well as explaining anomalous or strange abundance patterns.

The analysis of the three-element plots found four abundance ratios that could be indicative of the i process. These ratios were: [Yb/Tm] > 0.0, [Sc/Fe] > 0.5, [Gd/Fe] > 1.8 and [Yb/Fe] > 2.1. These ratios could be used to decide whether an object displaying neutron capture signatures belongs to the s or the i process and could also be useful to narrow down a site for the i process should these ratios be observed. Finding abundance ratios are useful to help determine the processes that may have taken place in order to produce there ratios. Elemental and isotopic abundance ratios can also be useful when studying things such as pre-solar grains. By studying the isotopic ratios of pre-solar grains we can get an idea of where in the universe these grains may have originally been formed. For example, Lugaro et al. (2020) used the ratio δ (^{88}Sr/^{86}Sr) as a representative s-process signature and compared it to [Ce/Fe] from Ba stars (which show s-process signatures) to show that larger silicon-carbide (SiC) pre-solar grains originate from AGB stars of higher metallicity than smaller SiC grains.

It is important to consider the effects of reaction rate uncertainties when working with nuclear networks and nucleosynthesis calculations. Changing a reaction rate can cause a

change in the abundances that the network calculates. Therefore, it is important to be aware of any changes that are possible when the rates are varied within their uncertainties. This has already been briefly discussed in this work in section 2.2.4 when looking at if altering the reaction rate most significant to the production of Ba (^{135}I (n,γ) ^{136}I) could allow us to replicate the [Ba/La] ratio of the P-rich star 2M22045404. Uncertainties of the abundances of the models have not been quantified for the χ^2 fitting or for the three element plots. In order to quantify the uncertainties, we would have to take into account the uncertainties on the rates of all the reactions included in the network. When using a network of 67,377 reactions, this level of calculation is not feasible. However, we can still take a look at the reaction rate uncertainties included in the literature for the elements and isotopes that we are interested in or that will have the biggest impact on the work. The works of Denissenkov et al. (2018, 2021) show the reaction rates which, if changed, have the most impact on the final abundances of elements on the first peak and from Ba-W respectively. For the present work, uncertainty in reaction rates adds another layer of uncertainty to the method of fitting models to abundances. As has already been discussed, how well a model fits a set of abundances is dependent on a number of factors. Changing the reaction rates could make the modelled abundances fit more closely to some objects and not for others. Denissenkov et al. (2018) shows potential variations of around 1 dex for the abundance of both Sr and Zr, this can be seen in their figure 8. The observational data sits around 1 dex outside the red area of the plot for each of these elements, this shows that the majority of the monte-carlo (MC) runs predict an i-process abundance for these elements that is not matched by observational data, in this case the abundance of Sakurai's object. Figure 7 of Denissenkov et al. (2021) shows potential variations of around 1 dex for Pr. Again, the observational abundance of Pr (this time from star CS31062-050) does not sit in the region where most of the MC runs predict the Pr to be. The uncertainties in the reaction rates could also change the shape of the models in the three-element plots of chapter 3. Given the selection of which combinations of elements are of interest to us are based on the shape of the three-element plots, changing the reaction rates could have an impact on which ratios give us an i-process model that run close to the CEMP-i sample and which do not. The elements of interest from chapter 3 are Yb, Tm, Gd and Sc.

Denissenkov et al. (2021) states that the two isotopes most significant to the production of Gd, Tm and Yb are: ^{156}Sm and ^{158}Sm, ^{169}Dy and ^{169}Ho and ^{172}Er and ^{174}Er respectively. The variation caused by the uncertainty in these rates is around 0.7 dex for [Gd/Fe], around 0.5 dex for [Tm/Fe] and around 0.4 dex for [Yb/Fe]. These changes would not significantly affect the results of Figures 3.15, 3.16 and 3.17 because the reason the modelled lines do not run close to the observations is due to the high [Sc/Fe]. However, these changes could have an impact on Figure 3.7 because the ratio of [Yb/Tm] could be affected.

Another factor that could be considered a source of uncertainty in the models is the effect of the abundances of the models prior to the onset of the i process. However, the total [X/Fe] for each element, X, during the i process increases by many orders of magnitude. Therefore, it is unlikely that there are large uncertainties associated with the abundances prior to the i process taking place.

In future, it would be helpful to have more detailed models of proton ingestion episodes in the intershell regions of AGB stars. This work uses a one-zone representation of an AGB intershell proton ingestion by using the intershell abundances of a low-mass low-metallicity AGB star with high initial ^{1}H and ^{12}C abundance which, as explained above, has been shown to work well at modelling an i-process event. However, true proton ingestion requires convection, which is a 3D process. Therefore, it would be helpful to have more 3D hydrodynamics simulations of proton ingestion in metal-poor AGB stars (e.g. Stancliffe et al. 2011). On the other hand, to create these simulations and properly model the convection is extremely computationally expensive and complex so making these models work is challenging. It would be especially useful to have more detailed models of AGB nucleosynthesis because the one-zone model in this work and the RAWD model F of Denissenkov et al. (2019) fit each of the different stars in the CEMP-i sample reasonably well and in some cases it is difficult to differentiate between the two.

The RAWD model is a detailed model but with that comes advantages and disadvantages. The ingestion rate and convective boundary mixing parameters of the RAWD model are found using hydrodynamics simulations which is advantageous because hydrodynamics models can take into account the convection and mixing processes that take place which makes them

more detailed. However, the model includes multiple thermal pulses and only one is selected and post-processed. Therefore, if any conditions change from pulse-to-pulse, it will not be captured in the model. For the RAWD scenario to be the one responsible for the i-process abundances of CEMP-i stars, a triple-system would have to occur. We do not know if we get enough triple-systems for RAWDs to be primarily responsible for the abundances we see on CEMP-i stars. We also do not know if the CEMP being in a triple system will change its orbital properties. A more detailed model of proton-ingestion in an AGB intershell would allow a more direct comparison between the two CEMP-i formation scenarios.

In future, the methodology of section 3.1.1 could be improved by considering the spread in the observational data. A modelled line that is far away from a tight cloud of observations is a worse fit than a modelled line that is far from the observational data simply because the data is spread out. By taking into account the spread, this effect can be minimised. Finally, as previously discussed, in future it would be beneficial to have more abundance measurements for Sc, Tm, Yb and Gd in order to confirm the indicative abundance ratios that have been put forward in this work.

Bibliography

Abate C., Pols O. R., Izzard R. G., Karakas A. I., 2015, Astronomy and Astrophysics, 581, A22

Abate C., Stancliffe R. J., Liu Z. W., 2016, Astronomy and Astrophysics, 587, A50

Abbott B., et al., 2017a, Physical Review Letters, 119, 161101

Abbott B., et al., 2017b, The Astrophysical Journal Letters, 848, L12

Abohalima A., Frebel A., 2018, The Astrophysical Journal Supplement Series, 238, 36

Allen D., Ryan S., Rossi S., Beers T., Tsangarides S., 2012, Astronomy & Astrophysics, 548, A34

Aoki W., et al., 2002, Publications of the Astronomical Society of Japan, 54, 427

Aoki W., Beers T. C., Christlieb N., Norris J. E., Ryan S. G., Tsangarides S., 2007, The Astrophysical Journal, 655, 492

Asplund M., Lambert D. L., Kipper T., Pollacco D., Shetrone M. D., 1999, Astronomy and Astrophysics, 343, 507

Asplund M., Grevesse N., Sauval A., Scott P., 2009, Annual Review of Astronomy and Astrophysics, 47, 481

Baratella M., D'Orazi V., Sheminova V., Spina L., Carraro G., Gratton R., Al. 2021, Astronomy and Astrophysics, ArXiv:2107.12381

Barklem P. S., et al., 2005, Astronomy and Astrophysics, 439, 129

Beers T. C., Christlieb N., 2005, Annual Review of Astronomy and Astrophysics, 43, 531

Bisterzo S., Gallino R., Straniero O., Cristallo S., Käppeler F., 2011, Monthly Notices of the Royal Astronomical Society, 418, 284

Bisterzo S., Travaglio C., Gallino R., Wiescher M., Käppeler F., 2014, Astrophysical Journal, 787, 10

Burbidge E. M., Burbidge G. R., Fowler W. A., Hoyle F., 1957, Reviews of Modern Physics, 29, 547

Busso M., Gallino R., Wasserburg G. J., 1999, Annual Review of Astronomy and Astrophysics, 37, 239

Butcher H. R., 1987, Nature, 328, 127

Campbell S., 2007, PhD thesis, Monash University

Campbell S. W., Lugaro M., Karakas A. I., 2010, Astronomy and Astrophysics, 522, 10

Cayrel R., et al., 2001, Nature, 409, 691

Cescutti G., Matteucci F., Caffau E., François P., 2012, Astronomy and Astrophysics, 540, 4

Choplin A., Siess L., Goriely S., 2021, Astronomy and Astrophysics, 648, A119

Clarkson O., Herwig F., Pignatari M., 2018, Monthly Notices of the Royal Astronomical Society: Letters, 474, L37

Coc A., Vangioni E., 2017, International Journal of Modern Physics E, 26, 1

Cohen J. G., et al., 2006, The Astronomical Journal, 132, 137

Cohen J. G., Christlieb N., Thompson I., McWilliam A., Shectman S., Reimers D., Wisotzki L., Kirby E., 2013, Astrophysical Journal, 778, 56

Côté B., O'Shea B. W., Ritter C., Herwig F., Venn K. A., 2017, The Astrophysical Journal, 835, 128

Côté B., Denissenkov P., Herwig F., Ruiter A. J., Ritter C., Pignatari M., Belczynski K., 2018a, The Astrophysical Journal, 854, 105

Côté B., et al., 2018b, The Astrophysical Journal, 855, 99

Cowan J. J., Rose W. K., 1977, The Astrophysical Journal, 14, 149

Cowan J. J., Thielemann F. K., 2004, Physics Today, 57, 47

Cowan J. J., McWilliam A., Sneden C., Burris D. L., 1997, The Astrophysical Journal, 480, 246

Cristallo S., Piersanti L., Straniero O., Gallino R., Dominguez I., Kappeler F., 2009, Publications of the Astronomical Society of Australia, 26, 139

Dardelet L., et al., 2015, in Proceedings of XIII Nuclei in the Cosmos — PoS(NIC XIII). Sissa Medialab, Trieste, Italy, p. 145

Denissenkov P. A., Herwig F., Battino U., Ritter C., Pignatari M., Jones S., Paxton B., 2017, The Astrophysical Journal, 834, L10

Denissenkov P., et al., 2018, Journal of Physics G: Nuclear and Particle Physics, 45, 055203

Denissenkov P. A., Herwig F., Woodward P., Andrassy R., Pignatari M., Jones S., 2019, Monthly Notices of the Royal Astronomical Society, 488, 4258

Denissenkov P., Herwig F., Perdikakis G., Schatz H., 2021, Monthly Notices of the Royal Astronomical Society, 503, 3913

Dillmann I., Heil M., Käppeler F., Plag R., Rauscher T., 2006, AIP Conference Proceedings, 819, 123

Frebel A., Kratz K.-L., 2009, in Proceedings of the International Astronomical Union, IAU Symposium. p. 449

Frebel A., Collet R., Eriksson K., Christlieb N., Aoki W., 2008, The Astrophysical Journal, 684, 588

Fujimoto M. Y., Iben I., Hollowell D., 1990, The Astrophysical Journal, 349, 580

Fujiya W., Hoppe P., Zinner E., Pignatari M., Herwig F., 2013, Astrophysical Journal Letters, 776, L29

Garcia-Berro E., Iben Jr I., 1994, The Astrophysical Journal, 434, 306

Goswami P. P., Goswami A., 2020, Journal of Astrophysics and Astronomy, 41, 47

Goswami P. P., Rathour R. S., Goswami A., 2021, Astronomy and Astrophysics, 649, A49

Gulick A., 1955, American Scientist, 43, 479

Gull M., et al., 2018, The Astrophysical Journal, 862, 174

Gull M., Frebel A., Hinojosa K., Roederer I. U., Ji A. P., Brauer K., 2021, The Astrophysical Journal, 912, 52

Hampel M., Stancliffe R. J., Lugaro M., Meyer B. S., 2016, The Astrophysical Journal, 831, 171

Hampel M., Karakas A. I., Stancliffe R. J., Meyer B. S., Lugaro M., 2019, Astrophysical Journal, 887, 11

Hansen T., et al., 2015, Astrophysical Journal, 807, 173

Hansen T. T., Andersen J., Nordström B., Beers T. C., Placco V. M., Yoon J., Buchhave L. A., 2016, Astronomy and Astrophysics, 588, 1

Heil M., et al., 2008, The Astrophysical Journal, 673, 434

Herwig F., et al., 2009, in Proceedings of 10th Symposium on Nuclei in the Cosmos — PoS(NIC X). Sissa Medialab, Trieste, Italy, p. 023

Herwig F., Pignatari M., Woodward P. R., Porter D. H., Rockefeller G., Fryer C. L., Bennett M., Hirschi R., 2011, Astrophysical Journal, 727, 89

Herwig F., Woodward P. R., Lin P. H., Knox M., Fryer C., 2014, Astrophysical Journal Letters, 792, L1

Hollowell D., Iben I., Fujimoto M. Y., 1990, The Astrophysical Journal, 351, 245

Iliadis C., 2015, Nuclear physics of stars. Wiley-VCH

Ishimaru Y., Wanajo S., Prantzos N., 2015, Astrophysical Journal Letters, 5, L35

Ivanova N., et al., 2013, Astronomy and Astrophysics Review, 21, 59

Jadhav M., Pignatari M., Herwig F., Zinner E., Gallino R., Huss G. R., 2013, Astrophysical Journal Letters, 777, L27

Jaeger M., Kunz R., Mayer A., Hammer J., Staudt G., Kratz K., Pfeiffer B., 2001, Physical Review Letters, 87, 202501

Ji A. P., Frebel A., Simon J. D., Chiti A., 2016, The Astrophysical Journal, 830, 93

Jones S., Ritter C., Herwig F., Fryer C., Pignatari M., Bertolli M. G., Paxton B., 2016, Monthly Notices of the Royal Astronomical Society, 455, 3848

Jonsell K., Barklem P. S., Gustafsson B., Christlieb N., Hill V., Beers T. C., Holmberg J., 2006, Astronomy and Astrophysics, 451, 651

Käppeler F., Beer H., Wisshak K., 1999, Reports on Progress in Physics, 52, 945

Käppeler F., Gallino R., Bisterzo S., Aoki W., 2011, Reviews of Modern Physics, 83, 157

Karakas A. I., Lattanzio J. C., 2014, Publications of the Astronomical Society of Australia, 31, e030

Karinkuzhi D., Van Eck S., Goriely S., Siess L., Jorissen A., Merle T., Escorza A., Masseron T., 2021, Astronomy and Astrophysics, 645, A61

Kilpatrick C. D., et al., 2017, Science, 358, 1583

Kobayashi C., Karakas A. I., Lugaro M., 2020, The Astrophysical Journal, 179, 900

Koch A., Reichert M., Hansen C. J., Hampel M., Stancliffe R. J., Karakas A., Arcones A., 2019, Astronomy and Astrophysics, 622, A159

Lattimer J. M., Schramm D. N., 1974, The Astrophysical Journal, 192, 663

Liu N., et al., 2014, Astrophysical Journal, 786, 66

Lugaro M., 2005, Stardust From Meteorites: An Introduction to Presolar Grains. World Scientific

Lugaro M., Campbell S. W., De Mink S. E., 2009, Publications of the Astronomical Society of Australia, 26, 322

Lugaro M., Karakas A. I., Stancliffe R. J., Rijs C., 2012, Astrophysical Journal, 747, 2

Lugaro M., et al., 2020, The Astrophysical Journal, 898, 96

Malaney R., 1986, Monthly Notices of the Royal Astronomical Society, 223, 683

Masseron T., Johnson J. A., Plez B., Van Eck S., Primas F., Goriely S., Jorissen A., 2010, Astronomy and Astrophysics, 509, A93

Masseron T., García-Hernández D. A., Santoveña R., Manchado A., Zamora O., Manteiga M., Dafonte C., 2020a, Nature Communications, 11, 1

Masseron T., García-Hernández D. A., Zamora O., Manchado A., 2020b, Astrophysical Journal Letters, 904, L1

McClure R. D., Woodsworth A. W., 1990, The Astrophysical Journal, 352, 709

Merrill P., 1952, Astrophysical Journal, 116, 21

Mishenina T., et al., 2014, Monthly Notices of the Royal Astronomical Society, 446, 3651

National Nuclear Data Centre B. N. L., 2021, https://www.nndc.bnl.gov/nudat2/

Nishimura N., Takiwaki T., Thielemann F., 2015, The Astrophysical Journal, 810, 109

Nishimura N., Sawai H., Takiwaki T., Yamada S., Thielemann F.-K., 2017, The Astrophysical Journal, 836, L21

Nomoto K., 1982, The Astrophysical Journal, 253, 798

Ono M., Hashimoto M. A., Fujimoto S. I., Kotake K., Yamada S., 2012, Progress of Theoretical Physics, 128, 741

Paxton B., Bildsten L., Dotter A., Herwig F., Lesaffre P., Timmes F., 2011, The Astrophysical Journal Volume Supplement, 192, 3

Paxton B., et al., 2013, Astrophysical Journal, Supplement Series, 208, 4

Pignatari M., et al., 2016, The Astrophysical Journal Supplement Series, 225, 24

Placco V. M., et al., 2015, Astrophysical Journal, 812, 109

Prantzos N., Abia C., Limongi M., Chieffi A., Cristallo S., 2018, Monthly Notices of the Royal Astronomical Society, 476, 3432

Preston G. W., Sneden C., 2001, The Astronomical Journal, 122, 1545

Rauscher T., Thielemann F. K., 2000, Atomic Data and Nuclear Data Tables, 75, 1

Ritter C., Herwig F., Jones S., Pignatari M., Fryer C., Hirschi R., 2018, Monthly Notices of the Royal Astronomical Society, 480, 538

Roederer I. U., Preston G. W., Thompson I. B., Shectman S. A., Sneden C., Burley G. S., Kelson D. D., 2014, Astronomical Journal, 147, 136

Schönberner D., 1979, Astronomy & Astrophysics, 79, 108

Sneden C., McWilliam A., Preston G., Cowan J., Burris D., Armosky B., 1996, The Astrophysical Journal, 467, 819

Sneden C., Cowan J. J., Gallino R., 2008, Annual Review of Astronomy and Astrophysics, 46, 241

Stancliffe R. J., 2009, Monthly Notices of the Royal Astronomical Society, 394, 1051

Stancliffe R. J., 2021, Monthly Notices of the Royal Astronomical Society, 505, 5554

Stancliffe R. J., Glebbeek E., Izzard R. G., Pols O. R., 2007, Astronomy and Astrophysics, 464, L57

Stancliffe R. J., Dearborn D. S., Lattanzio J. C., Heap S. A., Campbell S. W., 2011, Astrophysical Journal, 742, 121

Suda T., et al., 2008, Publications of the Astronomical Society of Japan, 60, 1159

Thielemann F., Eichler M., Panov I. V., Wehmeyer B., 2017, Annual Review of Nuclear and Particle Science, 67, 1

Thompson I. B., et al., 2008, The Astrophysical Journal, 677, 556

Travaglio C., Gallino R., Arnone E., Cowan J., Jordan F., Sneden C., 2004, The Astrophysical Journal, 601, 864

Winteler C., Käppeli R., Perego A., Arcones A., Vasset N., Nishimura N., Liebendörfer M., Thielemann F. K., 2012, Astrophysical Journal Letters, 750, L22

A. Appendix

A.1 Three Element Plots - Supplementary Information

Here each figure represents an example of a three-element plot that was rejected for each rejection criteria.

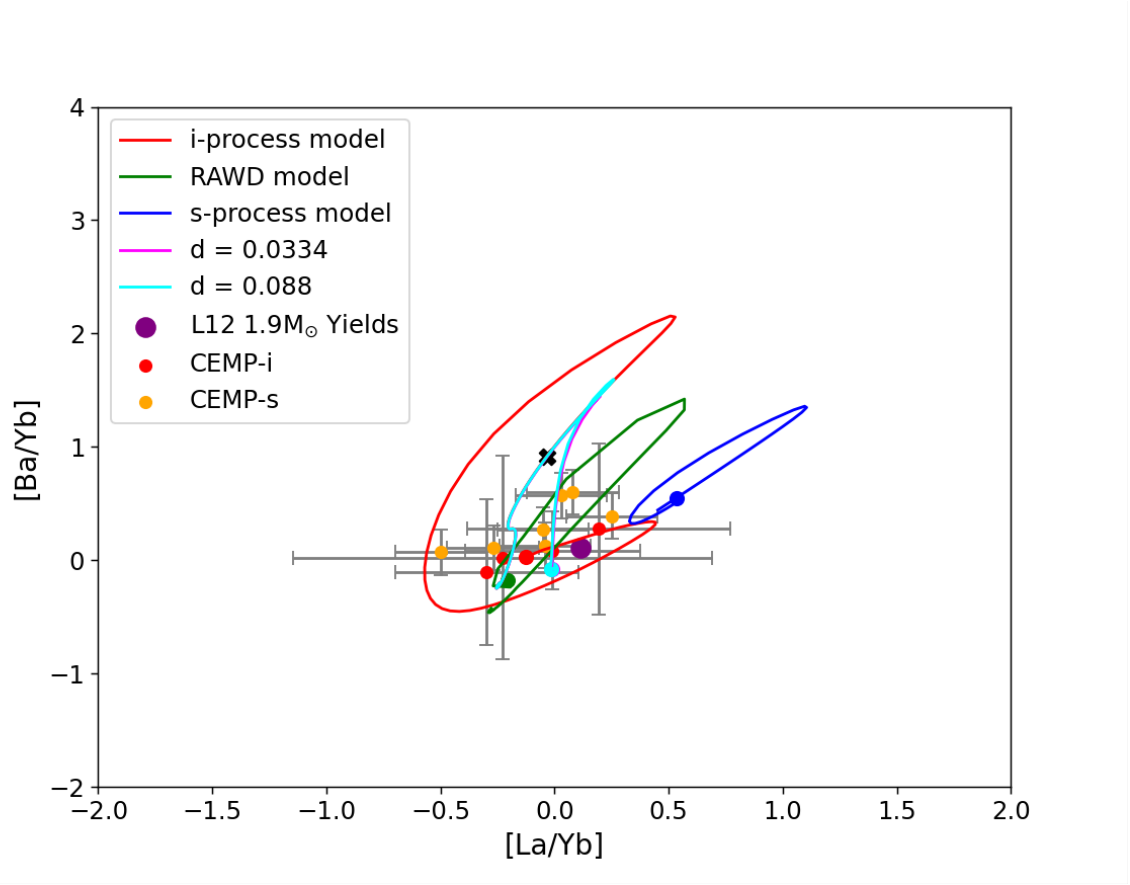

Figure A.1.1: [Ba/Yb] versus [La/Yb]. An example of a plot where the CEMP-i and CEMP-s sample occupy the same space.

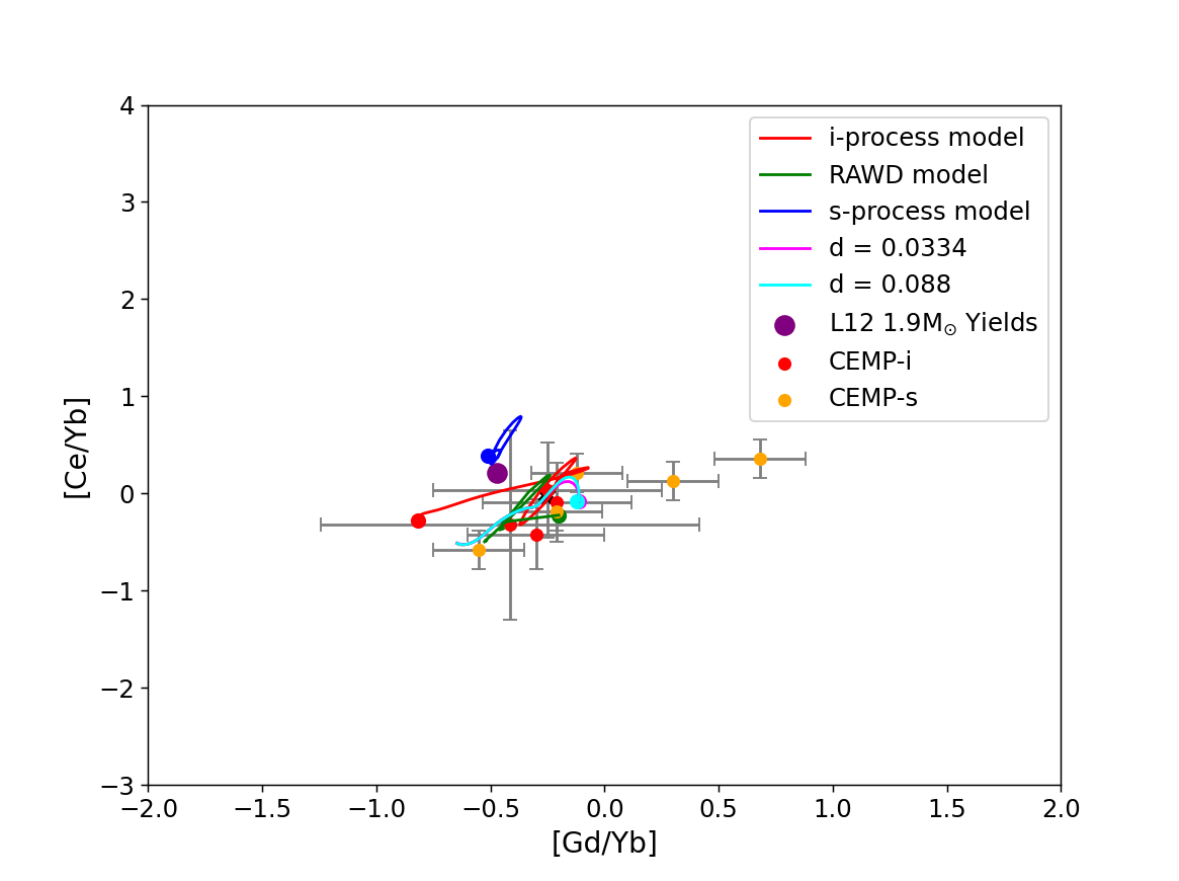

Figure A.1.2: [Ce/Yb] versus [Gd/Yb]. An example of a plot where the modelled lines are small enough that it's hard to distinguish any trends.

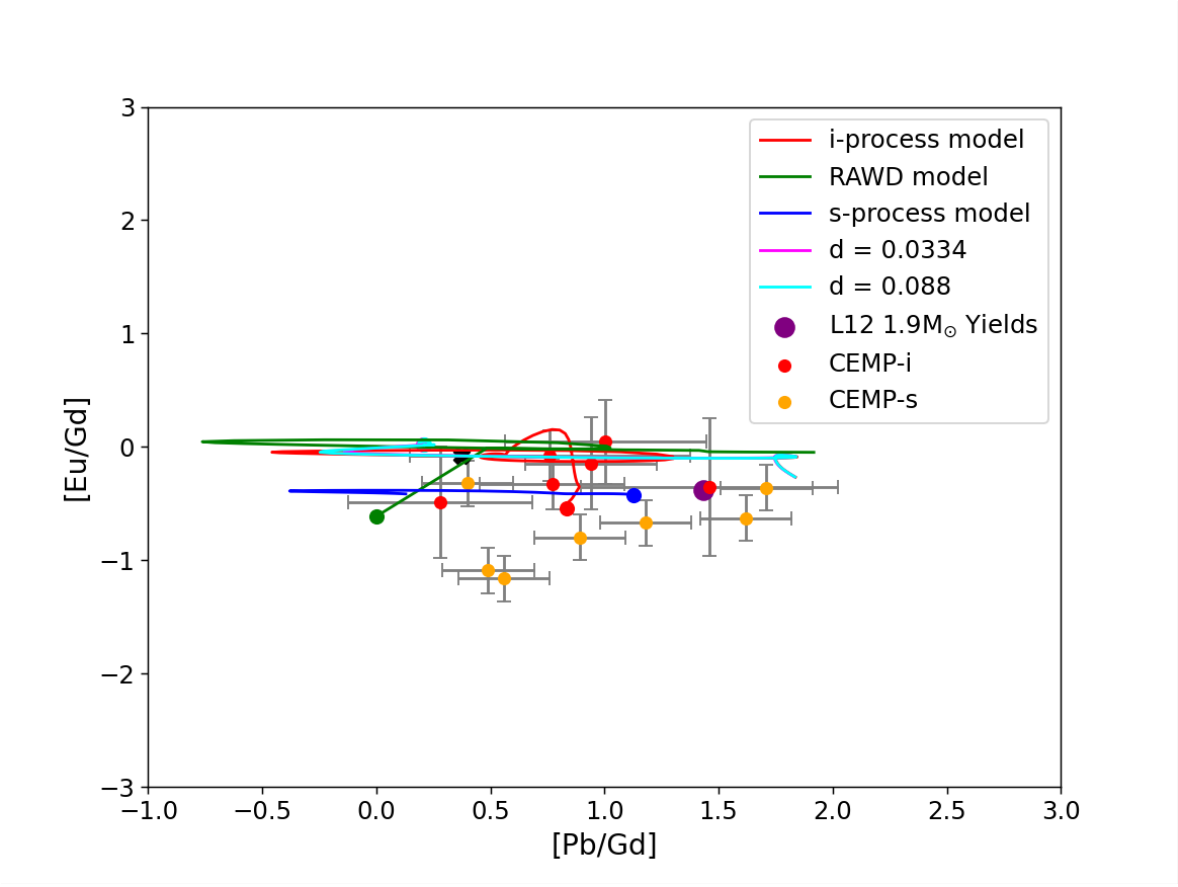

Figure A.1.3: [Eu/Gd] versus [Pb/Gd] An example of a plot where the modelled lines produce straight horizontal or vertical lines.